Liège University

Doctoral Thesis

Enhanced creation of many-body entanglement via geodesic counterdiabatic driving

Author:
Simon Dengis

Supervisor:
Prof. Peter Schlagheck

A thesis submitted in fulfillment of the requirements for the degree of Doctor of Philosophy in Science

in the

Statistical Quantum Physics group
Department of Physics

February 9, 2026

Jury

Prof. Thierry Bastin	President
Prof. John Martin	Secretary
Prof. Peter Schlagheck	Supervisor
Prof. Nathan Goldman	
Prof. Françoise Remacle	
Prof. Sandro Wimberger	

"*Il faut imaginer Sisyphe heureux.*"

Albert Camus

Abstract

This thesis investigates the fast and controlled generation of highly entangled many-body quantum states in systems of ultracold bosonic atoms. We focus in particular on the preparation of NOON states and their multimode generalizations, which constitute central resources for quantum metrology due to their enhanced sensitivity to parameter estimation. Working within Bose-Hubbard models in the self-trapping regime, where interaction effects dominate the dynamics, we exploit collective tunneling phenomena to isolate effective subspaces suitable for state engineering. To overcome the intrinsic slowness of adiabatic protocols, we introduce a control strategy based on the combined use of geodesic control and counterdiabatic driving, referred to as *geodesic counterdiabatic driving*. This approach enables accelerated state preparation using time-independent and experimentally accessible control parameters, while reaching the quantum speed limit. We demonstrate the efficiency and robustness of the method for generating high-fidelity NOON states in optical lattices. Finally, we extend the framework to the creation of NOON states with vortices in two-dimensional harmonic traps and discuss applications to quantum-enhanced metrology, highlighting the feasibility of rotation sensing beyond classical limits.

Résumé

Cette thèse étudie la génération rapide et contrôlée d'états quantiques fortement intriqués dans des systèmes composés d'atomes bosoniques ultrafroids. En particulier, l'accent est mis sur la préparation d'états NOON et de leurs généralisations multimodes, qui constituent des ressources centrales pour la métrologie quantique en raison de leur grande sensibilité à l'estimation de paramètres. En travaillant avec des modèles de Bose-Hubbard en régime de self-trapping, où les effets d'interaction dominent la dynamique, nous exploitons des phénomènes de tunneling collectif afin d'isoler des sous-espaces effectifs favorables à l'ingénierie d'états quantiques. Afin de surmonter la lenteur intrinsèque des protocoles adiabatiques, nous introduisons une stratégie de contrôle reposant sur l'utilisation conjointe d'un contrôle géodésique et de termes contre-diabatiques, appelée *geodesic counterdiabatic driving*. Cette approche permet d'accélérer la préparation d'états à l'aide de paramètres de contrôle indépendants du temps et accessibles expérimentalement, tout en atteignant la limite de vitesse quantique. Nous démontrons l'efficacité et la robustesse de cette méthode pour la génération d'états NOON de haute fidélité dans des réseaux optiques. Enfin, nous étendons ce cadre théorique à la création d'états NOON de vortex dans des pièges harmoniques bidimensionnels et discutons de leurs applications en métrologie quantique, en mettant en évidence la faisabilité de la détection de rotations au-delà des limites classiques.

Remerciements

Quel voyage. Voilà maintenant 10 ans que je suis arrivé à l'Université de Liège les yeux pleins d'espoir et, surtout, animé par l'ambition de comprendre le monde qui m'entourait. Des équations ornaient les murs de ma chambre dont je n'en saisissais pas encore la substance, accompagnées de desseins de grandeur et de l'aspiration à élucider tous les mystères de l'univers. Eh bien, jeune Simon de 19 ans, saches qu'à 29 ans je n'ai toujours pas la moindre idée de ce qui se trame là-dehors. Mais la certitude que j'ai, c'est que tout ce que tu vas vivre, perché là-haut sur la colline du Sart-Tilman, te forgera et t'amènera un jour à pouvoir écrire tes propres équations sur les murs de ta chambre. Avant de remercier rétrospectivement tous ceux qui ont été là durant toutes ces années, merci à toi d'avoir tenu bon. Ça valait le coup, non ?

La première personne que je souhaite remercier est mon promoteur, Prof. Peter Schlagheck, qui m'a donné l'opportunité de commencer un doctorat il y a trois ans. Je ne saurais compter le nombre de fois où sa connaissance et son intuition de la physique m'ont permis de sortir du brouillard, que ce soit durant mon stage, mon mémoire ou ma thèse. Merci pour la confiance et la liberté qu'il m'a accordées au cours de ces dernières années, pour sa disponibilité à toute épreuve, ainsi que pour sa sagesse et son humanité à chaque instant. Je suis très reconnaissant d'avoir pu apprendre le métier de chercheur auprès d'un mentor d'une telle qualité.

I would also like to thank Prof. T. Bastin, Prof. N. Goldman, Prof. J. Martin, Prof. F. Remacle, and Prof. S. Wimberger for accepting to be part of my thesis jury. I hope that this thesis will be as pleasing to read as it was for me to carry out. Beyond this, I would like to warmly thank Sandro for welcoming me twice in Parma. It was a real pleasure to visit you and to gain a different perspective on how to do physics. In particular, with the simple sentence, "when I have a doubt, I look at the gap", you enabled me to resolve the issue with the $N = 5$ particles. If Peter is my physics father, you are certainly my physics cool uncle! I look forward to continuing our collaboration.

Bien sûr, un grand merci aux collègues qui ont rendu ces années de doctorat aussi légères qu'un temps de midi qui s'éternise à la machine à café. Merci à Thomas et Jona pour les canapés et les débriefs hebdomadaires du scan de One Piece. Merci à Colin d'avoir terminé la physique avec moi. Plus généralement, merci aux compagnons du B15b et du B15c pour l'exode au B5 et ses afters du dîner de Noël. Merci aux doctorants du DocPhyzMeal : on a tellement régalé les finances de Pizza à Papa qu'ils se sont barrés avec la caisse. Un très grand merci à Baptiste, avec qui les discussions physiques, philosophiques ou politiques comptent parmi mes meilleurs souvenirs de

ce doctorat. Merci aussi pour tous les souvenirs oubliés, les quelques fois où l'on a frôlé la mort, le traquenard derrière le bar de la fête des fous, Windsor, et toutes les autres bonnes mauvaises idées que l'on a eues. J'espère sincèrement que nos chemins continueront à se croiser au détour d'un tableau noir.

Durant toutes ces années à l'Université, j'ai eu l'occasion de rencontrer de nombreuses personnes et de vivre mille vies différentes. Merci au CB Sciences pour la culture parallèle et le traditionnel resto entre vieux copains, le dernier vendredi de la saison du Q1. De rien pour la Renaisciences. Merci à la MEL pour ces cinq années passées à apprendre comment on administre un bâtiment de deux millions d'euros. Merci à la Questure d'avoir élevé ma plume et de constituer un repère de bons copains. J'ai pu m'épanouir au sein de ces infrastructures, qui m'ont permis de devenir la personne que je suis aujourd'hui.

Merci aux Beavers, aux barrages, au mini-golf et autres jeux de cartes qu'il m'est impossible de réexpliquer. Merci à Maud pour tous les conseils, l'écoute attentive et tous les bons souvenirs. Merci pour tous les cafés, assis sur ton coussin rouge sciemment placé dans le coin inférieur gauche de ton tapis.

Je remercie évidemment mes parents pour leur soutien tout au long de ces années. Je n'aurais pas pu arriver là où j'en suis sans la certitude de vous avoir toujours à mes côtés, quels que soient mes choix. J'espère vous avoir rendus fiers ! Promis, les études, c'est terminé.

S'il y a bien quelqu'un qui m'a accompagné tout au long de ce voyage, c'est mon frère d'armes Matteo (qui n'a rien à voir avec le Mathéo remercié dans mon mémoire), avec lequel j'ai vécu ces mille vies dans la bonne humeur, l'ambition et l'empathie. Merci pour tous ces instants hors du temps où tout semblait léger. Merci pour ton écoute à chaque fois que ça n'allait pas. Merci pour tout ce que nous avons vécu, et tous ces souvenirs qui m'accompagneront le reste de ma vie. Merci pour ton amitié et pour tout ce qu'elle m'a apporté. Pour citer un grand scientifique, je mesure la chance de t'avoir rencontré.

Enfin, je conclus ces remerciements par le plus grand coup de chance de ma vie, Titziana. Je ne sais comment te remercier pour tout ton amour et ton soutien indéfectible en toutes circonstances. J'ai hâte de découvrir ce que la vie nous réserve. Merci d'être la plus belle chose qui me soit arrivée.

Publications

The research presented in this manuscript has led to the following publications:

- S. Dengis, S. Wimberger and P. Schlagheck, *Accelerated creation of NOON states with ultracold atoms via counterdiabatic driving*, Phys. Rev. A **111**, L031301 (2025).

- S. Dengis, S. Wimberger and P. Schlagheck, *Multimode NOON-state generation with ultracold atoms via geodesic counterdiabatic driving*, Phys. Rev. A **112**, 042610 (2025).

- S. Dengis, N. Dupont, P. Schlagheck and N. Goldman, *NOON states of vortices in a 2D harmonic trap for rotation sensing*, in preparation (2026).

Contents

Introduction

The first time one encounters quantum mechanics, whether in a classroom or through a standard textbook, it feels like a child discovering a new toy. Matrix algebra seems to be the "grown-up" version of the vector calculus used when first learning Newton's equations. One begins by uncovering a few oddities, ranging from state superposition to the first quantizations of a system's energy. However, the first real shock a physicist experiences when analytically exploring the microscopic world comes from the phenomenon of quantum entanglement.

When quantum physics tells us that a system is more than merely the sum of its components, a fascinating consequence follows: measuring one component, such as the position of one particle in a bipartite system, immediately fixes the state of the other component. What Einstein famously referred to as "spooky action at a distance" is a strong result of quantum mechanics and cannot be explained by an incompleteness of the information at our disposal, as our intuition might suggest [1]. On the contrary, several experiments have shown [2] that quantum mechanics is not a local hidden-variable theory, and that the entangled photons that were observed indeed exhibit non-local behavior.

There exist several types of entangled states. Among them, Bell states are examples of maximal entanglement, meaning that their quantum correlations are maximal [3]. In such states, precise knowledge of one particle provides all the accessible information about the state of the other. Bell states can be generalized to systems of N bosonic particles, for instance with NOON states that correspond to superpositions of N particles occupying two orthogonal states.

And yet, in everyday life, we do not observe entangled states. A mismatched sock does not fix the position of its counterpart when it is found under the couch. Although observations of entangled crystalline systems have been reported [4, 5], the realization of macroscopic entanglement remains an open challenge. Nevertheless, significant progress has been made in recent years, in particular in the realization of NOON states with photons and phonons [6, 7]. Producing such a state with massive particles, such as neutral atoms, however, remains to be achieved.

In particular, interatomic interactions strongly modify the dynamics compared to what one might observe with particles of light. Trapping techniques are also fundamentally different. For example, a NOON state could be created with bosonic particles trapped in a potential that renders them nearly immobile. This immobility translates into a system temperature close to absolute zero, causing the bosons to behave as a giant matter wave: a Bose-Einstein condensate. However, particles are difficult to trap

even at low temperatures, and several phenomena come into play that severely limit the lifetime of a condensate, to the order of one second [8]. Thus, in order to hope to create an entangled state of matter waves, the timescale required for its creation must be short compared to the lifetime of the system.

This thesis aims to propose an experimentally viable state-preparation protocol. By theoretically investigating the Bose-Hubbard model describing a set of ultracold bosons trapped in an optical lattice, we show that it is possible to generate entanglement within such systems on experimentally achievable timescales.

Trapping ultracold atoms

The first step when one wishes to study an ensemble of atoms is to determine how to trap them. In particular, alkali atoms such as ^{87}Rb are very commonly used to study ultracold matter, owing to the magnetic moment associated with the spin of their unpaired valence electron [9]. This property makes it possible to trap such systems in potentials created by magnetic fields. They can also be trapped in optical lattices via the dipole transition between the ground state and the first excited state of the valence electron, which lies in the optical regime and is therefore accessible with lasers. In particular, optical potentials can be arranged in periodic structures so as to form a lattice of minima in which the atoms can be localized. Such lattices are extremely useful, as they make it possible to emulate crystalline lattices and the dynamics that occur within them [8, 10].

The addition of another laser beam with a wavelength at least twice as large as the one forming the first lattice makes it possible to create what is known as a superlattice. For example, superimposing two harmonic traps with very different wavelengths allows one to generate a superlattice composed of double wells, where each pair is isolated from the others [11]. Loading an ultracold atomic gas into such an optical lattice makes it possible to observe many phenomena that we will detail later, in particular by tuning the well depths and barrier heights [12]. More exotic structures can also be realized, for instance by superimposing a hexagonal lattice with a triangular lattice, which allows one to isolate a so-called “star” system in which one site is symmetrically connected to three others [10, 13–15].

In the protocol we propose, all atoms are placed in such a lattice, and more specifically in the site that is symmetrically coupled to the others. Once this state is stabilized, the energy of the central well is modified in such a way that the evolution of the system ends in a NOON state composed of the L other sites surrounding the central well. This also holds for a double-well lattice, where there is only one external site.

NOON states with ultracold atoms

NOON states are defined as coherent superpositions of the form

$$|\mathrm{NOON}\rangle = \frac{1}{\sqrt{2}} \left(|N, 0\rangle + |0, N\rangle \right) \tag{1}$$

and represent a class of highly entangled states that are particularly sought after in metrology. Their extreme sensitivity to phase differences (for example) makes them central resources for parameter estimation, even allowing one to surpass the standard quantum limit and to reach the Heisenberg limit. The larger the number of particles N, the greater their metrological relevance.

While such states have been realized with photons, phonons, or superconducting qubits, their creation with ultracold atoms remains a contemporary challenge and has been intensively discussed [16–25]. A notable feature of atomic gases is the interaction between particles, which allows certain states to be isolated within the energy spectrum of the system. For instance, when particles interact, states where all particles are localized in the same mode tend to cluster together, separated from the rest of the spectrum. This suppresses sequential tunneling and thus gives rise to the phenomenon of collective tunneling [26–29], where particles undergo tunneling between different modes collectively. This behavior has enabled the first creation of NOON like states in systems of atoms trapped in a perfectly symmetric double-well potential [30], albeit with a rather limited purity.

In the deep self-trapping regime [31], where particle interactions significantly exceed the hopping rate between sites, a NOON state is formed after half the time required for complete tunneling. However, this method poses a challenge: since the tunneling time is inversely proportional to the energy difference between the two modes, the time required to observe the creation of a NOON state far exceeds the lifetime of a Bose-Einstein condensate. To address this limitation, a faster process was proposed, leveraging chaos-assisted and resonance-assisted tunneling [32–34], which reduced the time required for NOON states creation by several orders of magnitude [35]. This same method has been applied to create triple-NOON states in three-site systems [36], but the time needed to entangle the system is still long ($\sim$ 1s for ultracold ^{87}Rb gases with $N = 5$). Our method provides an alternative approach to generating the entangled state on a more realistic timescale.

Adiabatic driving

Adiabatic transport of a system is well understood in terms of classical physics. When carrying a glass filled a bit too generously with water, one must slow down one's motion in order not to spill it. Our instinct tells us that if the perturbation applied to the glass by our movement is too strong, the state of the glass will change from full to partially emptied. This observation is of course not restricted to human walking; drivers also slow down when approaching a turn that is a bit too sharp.

This principle of driving carries over directly to the quantum world. When a system is modified abruptly, the time evolution of its state is likewise strongly perturbed. In particular, rather than being merely a nuisance, this effect can be exploited to steer the system toward a desired state. By initializing the system in an easy-to-prepare state and then gradually modifying its energy so as to gently bring it toward the target state, the adiabatic theorem guarantees that the path will be followed without difficulty [37–41]. In the context of ultracold atoms in optical lattices, adiabatic transport can be achieved through a slow modification of the depth of the optical lattice in which the bosons are trapped.

Although adiabatic transport provides a relatively simple way to prepare a specific state, it is by nature slow, sometimes too slow to be experimentally viable in its basic form. Typically, the adiabatic driving of a cloud of ultracold atoms trapped in an optical lattice requires a timescale much longer than the typical lifetime of a condensate. It is therefore necessary to apply methods that accelerate adiabatic driving, in order to avoid exciting the system, which would result in populations of atoms occupying energy levels corresponding to unwanted states.

Beyond adiabatic theorem

To overcome the intrinsic limitations of the adiabatic theorem, many different techniques have been developed under the umbrella term Shortcuts to Adiabaticity (STA) [42]. The goal of these methods is to reach the same outcome as in the infinitely slow driving limit, while allowing the system to evolve on much shorter timescales. Among these techniques are the fast-forward approach, the Lewis-Riesenfeld invariant method, and the fast quasiadiabatic (FAQUAD) approach. The method we will employ is known as counterdiabatic driving (CD), also referred to as transitionless quantum driving [43].

The approach underlying this technique is based on a simple idea: if we know precisely which perturbations excite the system into unwanted states, we can construct a "remedy" that cancels them at every instant. By adding to the Hamiltonian a term exactly equivalent to the one responsible for nonadiabatic transitions, a perfectly adiabatic evolution is guaranteed by construction.

In practice, defining a counterdiabatic (CD) term can raise several difficulties. In particular, for many-body systems with a very large and sometimes dense energy spectrum, it is impossible to obtain the exact form of the CD. Even when an approximate form can be derived, it may contain nonlocal terms that render its experimental implementation unrealistic. Nevertheless, many approximation schemes exist that make counterdiabatic driving feasible, sometimes at the cost of a reduced state fidelity, but one that remains sufficient for practical use [44–46].

Other methods to go beyond the adiabatic theorem exist, which focus on optimizing the way the system is driven rather than on canceling the disturbing terms. In particular, the search for an optimal protocol can be carried out using optimal control techniques, or analytically by exploring the intrinsic geometry of the system. Geodesic driving is based on the Riemannian geometry underlying the manifold defined by the family of Hamiltonians that depend on a parameter such as time [47]. From this perspective, it is possible to identify the path that, at each instant, brings the state of the system as close as possible to the desired target state [48]. This idea, which is relatively recent, is still rarely used in the literature, although it provides a low-resource way to drive a system more efficiently than standard driving schemes [38–41].

Although these two approaches may appear disjoint at first glance, their combined use reveals fundamental properties of the system's geometry. In particular, geodesic counterdiabatic driving enables counterdiabatic control using time-independent terms [49, 50]. This new method, in addition to offering clear experimental advantages due

to its low control cost, highlights the shared geometric properties of counterdiabatic driving and geodesic driving, and even makes it possible to establish a connection to the quantum speed limit [51].

The central idea of this thesis is to combine geodesic driving with the application of counterdiabatic terms. The resulting method (GCD) makes it possible to rapidly achieve fidelities close to unity using experimentally accessible and low-cost controls. Beyond being demonstrated as valid for any system related to a Landau-Zener model, this method naturally extends to many-body systems, whether interacting or not.

Outline of the chapters

This thesis is organized into five main chapters, first detailing the theoretical framework that is developed and then applying it to the creation of various NOON states in ultracold atoms described by the Bose-Hubbard Hamiltonian.

Chapter 1 introduces the physics of ultracold atoms, starting from the physical intuition behind Bose-Einstein condensation and progressing to its proper mathematical formalization through the contact potential describing interactions between particles in such a gas. Techniques for trapping these systems are presented in order to define the Bose-Hubbard model, which serves as the theoretical framework throughout the thesis.

Chapter 2 develops the geometric framework underlying quantum control. In particular, we make explicit the adiabatic theorem and how it can be visualized in a driven quantum system. By introducing the concept of the adiabatic gauge potential, we define the counterdiabatic Hamiltonian that allows one to accelerate adiabatic driving. Building on differential geometry, we develop the idea of geodesic driving by searching for optimal trajectories defined on the manifold representing the system as it evolves in time. Finally, we unify these two approaches within the framework of geodesic counterdiabatic driving, presenting this new method and the fundamental implications it entails.

Chapter 3 applies the formalism developed in Chapter 2 to the creation of NOON states in a three-site Bose-Hubbard system. We then derive, using perturbation theory, a reduced Hamiltonian that accurately describes the system's evolution when it is placed in a so-called self-trapping regime. We subsequently show how the GCD protocol can be implemented in an interacting many-body system and apply it to the generation of highly entangled NOON states with very high final fidelity.

The second part of Chapter 3 extends these methods to the creation of multimode NOON states, building on the geometry inherent to so-called "star" optical lattices, in which a central well is symmetrically connected to L outer sites. We generalize the reduced Hamiltonian by exploiting a symmetry of the system that allows one to consider an arbitrary number of modes while reducing the dynamics to two orthogonal modes. We then show how the GCD protocol enables the rapid creation of L-NOON states, and apply the method to the generation of triple-, quadruple-, and quintuple-NOON states. We also present several possible schemes for generating an optical lattice optimized for the application of our method.

Chapter 4 explores a slightly different physical system in which NOON states can emerge from vortex dynamics within a two-dimensional harmonic trap. We develop a Bose-Hubbard model describing the two-mode vortex dynamics, and once again define a reduced Hamiltonian that faithfully captures the many-body system. The GCD protocol is applied to the creation of vortex NOON states, as well as to the emulation of counterdiabatic terms via Floquet engineering.

Finally, Chapter 5 details the metrological advantage of NOON states by highlighting their sensitivity to phase-difference measurements. In particular, we show that triple-NOON states reach the Heisenberg limit, enabling enhanced phase resolution. We then propose an experimental protocol that exploits vortex NOON states for the measurement of an external rotation. We establish the sensitivity window of the protocol for different parameters and show that, in principle, it is possible to detect the Earth's rotation using the generated NOON states.

1

Physics with ultracold atoms

1.1 Bose-Einstein condensates

The wave-particle duality is probably one of the earliest revolutions in quantum physics marking the rupture between our intuition and experimental reality. While classical physics clearly distinguished waves (electromagnetic waves described by Maxwell's equations) from particles (atoms and electrons in Newtonian mechanics), several experimental results challenged this separation. In 1905, Albert Einstein interpreted the photoelectric effect by introducing the idea that light, traditionally considered as a wave, could behave as a flux of energy quanta, or photons [52]. A few years later, in 1924, Louis De Broglie proposed that this duality was not specific to light, but also applied to matter: any material particle with momentum p could be associated with a wave of wavelength $\lambda = h/p$ [53]. The wave-particle duality, later formalized by Heisenberg [54] and Schrödinger [55], became, after its observation through the diffraction of electrons on a nickel crystal [56], one of the foundational pillars of quantum mechanics and remains today at the heart of modern physics.

Particles can therefore be interpreted as having a spatial extent on the order of h/p, inversely proportional to their momentum. Slow bodies thus have a priori a larger wavelength λ than those with a high momentum. This notion of momentum is directly related to the temperature of the particles by identifying the kinetic energy $p^2/2m$ of a particle of mass m with its energy expressed in temperature units $k_B T$. The momentum can therefore be rewritten as $p \sim \sqrt{2mk_BT}$, and by inserting this expression into the wavelength λ, one obtains a relation between the latter and the temperature of the bodies:

$$\lambda_{\mathrm{DB}} = \sqrt{\frac{2\pi\hbar^2}{mk_BT}}\,, \tag{1.1}$$

called the thermal De Broglie wavelength [57]. From this, it is clear that cooling a gas of particles will increase the spatial extent of each constituent body, up to a critical point where the different waves begin to overlap (see Fig. 1.1 for an illustrative picture). If all the particles composing the gas are bosons, described by a fully symmetric wavefunction, then exchanging two constituents leaves the system invariant, unlike the case where the particles are fermionic in nature. This simple fact leads to the exclusion principle stating that two fermions cannot occupy the same quantum state, which is not the case for bosonic particles.

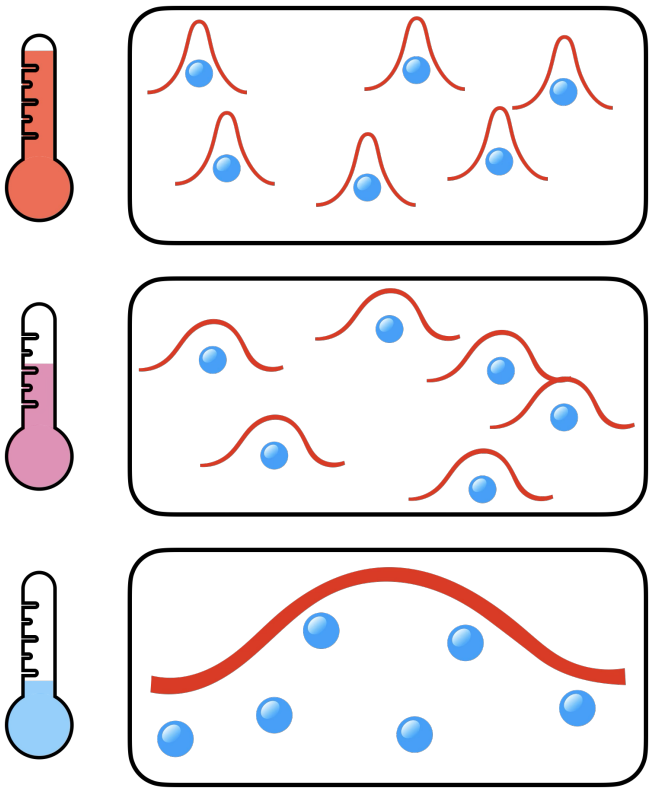

FIGURE 1.1: Illustrative sketch of the intuitive notion of a Bose-Einstein condensate. Since the De Broglie wavelength of the particles is inversely proportional to the temperature of the gas (itself related to the momentum of the bosons), there exists a critical temperature at which all the wavefunctions overlap and the gas forms a single gigantic matter wave.

In particular, returning to the De Broglie wavelength, there exists a critical temperature at which all the bosons in a gas occupy the same quantum state corresponding to the lowest-energy mode, the ground state. An ideal bosonic gas is described by the Bose-Einstein distribution, which characterizes how particles populate the various energy levels ϵ_k as a function of the temperature T of the gas:

$$\langle n_k \rangle = \frac{1}{\exp\left(\dfrac{\epsilon_k - \mu}{k_B T}\right) - 1} \tag{1.2}$$

with μ the chemical potential of the system, that is, the energy required to remove a particle from its energy level. If all the bosons experience a drop in temperature, their energy will decrease accordingly and tend toward the ground state of energy ϵ_0. At that point, the chemical potential μ will itself tend toward the ground-state energy, yielding a zero argument in the exponential and a divergence in the average number of particles $\langle n_0 \rangle$ populating the ground state. This phenomenon was named Bose-Einstein condensation (BEC), and describes the sudden occupation of the ground state by a large number of particles in a bosonic gas.

Bose-Einstein condensation was theoretically predicted in 1925 by Albert Einstein, building on Satyendra Nath Bose's statistical work on light [58, 59]. Einstein and Bose showed that an ideal gas of bosons exhibits, below a critical temperature, a macroscopic occupation of the ground state [59]. It was only with the development of laser cooling in the 1980s [60] and evaporative cooling in magnetic traps [61] that the necessary

experimental conditions could finally be achieved. In 1995, two independent teams succeeded in creating the first BEC with dilute atomic gases: the group of Cornell and Wieman at JILA with rubidium-87 atoms [62], and the group of Ketterle at MIT with sodium [63]. These experiments marked a historic milestone in modern physics, demonstrating that a macroscopic system could be described by a single coherent quantum wavefunction. This discovery earned Cornell, Wieman, and Ketterle the 2001 Nobel Prize in Physics. Numerous realizations of Bose-Einstein condensates were achieved experimentally in the following years [64–70]. Since then, BECs have become an essential platform for studying quantum coherence phenomena, phase transitions, and the engineering of nonclassical states of matter.

1.1.1 Non-interacting bosonic gas

Let us now describe Bose-Einstein condensation in a more rigorous way. To do so, we first consider the behavior of a gas of bosonic atoms in free space and highlight how the population is distributed among the different energy levels of the system. Let us first assume a collection of atoms in free space in $D = 3$ dimensions. The N particles have a mass m, and the kinetic Hamiltonian describing the single-particle physics of the system reads

$$H = -\frac{\hbar^2}{2m}\frac{\partial^2}{\partial \mathbf{r}^2}, \tag{1.3}$$

where the vector $\mathbf{r}$ denotes the position of a particle. The bosons are free to move throughout the entire space, and it becomes necessary to introduce a renormalization volume in order to avoid the obvious divergence that appears when considering an infinite space. To do so, we study the gas in a renormalization volume $V = L^3$, where L is the side length of a cube. Within this volume, one defines a wavefunction ψ describing the gas, which must be periodic across the different cubes, meaning that it satisfies $\psi(\mathbf{r}_j) = \psi(\mathbf{r}_j + L)$. Imposing this condition amounts to assuming that we have chosen an arbitrary volume and that the physics would remain unchanged had we chosen another cube.

The eigenfunctions of the Hamiltonian (1.3) are well known and consist of plane waves of the form

$$\phi_{\mathbf{k}}(\mathbf{r}) = \frac{1}{\sqrt{V}} e^{i\mathbf{k}\cdot\mathbf{r}}, \tag{1.4}$$

associated with the energies

$$E_{\mathbf{k}} = \frac{\hbar^2 \mathbf{k}^2}{2m}, \tag{1.5}$$

where $\mathbf{k}$ is the wave vector. As mentioned previously, bosonic particles obey the Bose-Einstein distribution, so it is possible to obtain the mean average total population $\langle \bar{N} \rangle$, which can be expressed as a sum over the average particle numbers in the different energy levels. In particular, the population that will interest us the most is that of the ground state and how it behaves with temperature, that is, with the kinetic energy of the system. One can show that, in the case of a free Bose gas in the thermodynamic limit in dimension $D = 3$, the ground-state population N_0 satisfies

$$\frac{N_0}{N} = 1 - \left(\frac{T}{T_c}\right)^{3/2}, \tag{1.6}$$

where critical temperature T_c is expressed as

$$T_c = \frac{2\pi\hbar^2}{mk_B}\left(\frac{\bar{n}}{\zeta(3/2)}\right)^{3/2}, \tag{1.7}$$

with $\bar{n} = \langle\bar{N}\rangle/V$ and $\zeta(p) = \sum_{l=1}^{\infty} l^{-p}$ the Riemann zeta function. The behavior of the ratio N_0/N is characteristic of a second-order phase transition, similar to that appearing in the case of ferromagnetism. When the temperature T of the system is cooled below a critical temperature T_c, the population of the ground state becomes macroscopically large. All the bosons tend to occupy the ground state, a behavior that could never occur in a fermionic system. Saying that the particles all occupy the same state amounts to saying that they all behave in the same way, which justifies the sometimes-used term "gigantic matter wave." Indeed, the bosons all share the dynamics of the ground state and their De Broglie wavelength keeps increasing with decreasing temperature; it then becomes impossible to distinguish their wavefunctions, and only a single collective behavior remains: this is Bose-Einstein condensation.

If we consider a more realistic system consisting of a set of bosonic particles not in free space but confined by a harmonic trap of frequencies $\omega_j, j \in \{1, 2, 3\}$, the Hamiltonian of the system becomes [71, 72]

$$H = -\frac{\hbar^2}{2m}\frac{\partial^2}{\partial\mathbf{r}^2} + \frac{m}{2}\sum_{j=1}^{3}\omega_j^2 r_j^2. \tag{1.8}$$

Once again, this is a well-known system, and the eigenenergies of the Hamiltonian are given by

$$E_{\mathbf{n}} = \sum_{j=1}^{3}(n_j + 1/2)\hbar\omega_j, \tag{1.9}$$

where $\mathbf{n} \equiv (n_1, n_2, n_3)$ and $n_j \in \{0, 1, 2, \ldots\}$ for all $j \in \{1, 2, 3\}$. The same type of behavior for the ground-state population can be obtained by defining the critical temperature this time as

$$T_c = \frac{\hbar\bar{\omega}}{k_B}\left(\frac{N}{\zeta(3)}\right)^{1/3}, \tag{1.10}$$

with $\bar{\omega} = \left(\prod_{j=1}^{3}\omega_j\right)^{1/3}$ the geometric mean of the trap oscillation frequencies. In this case, the ground-state population follows the relation

$$\frac{N_0}{N} = 1 - \left(\frac{T}{T_c}\right)^3. \tag{1.11}$$

This behavior once again describes a second-order phase transition, although with a dimensional dependence different from the free-space case. In a three-dimensional trap, the critical temperature T_c depends explicitly on the confinement parameters of the potential through the geometric mean $\bar{\omega}$: tightening the trap, corresponding to higher frequencies, increases the density of states and lowers the transition temperature. In other words, switching to a confined potential "compresses" the energy spectrum in a way that favors a macroscopic occupation of the ground state. This behavior lies at the heart of the experimental physics of Bose-Einstein condensates: in almost all experiments, condensation is achieved not in a homogeneous gas but in magnetic or optical harmonic traps, where the precise determination of T_c is possible and in

good agreement with theoretical predictions. It thus becomes clear that Bose-Einstein condensation results from a combination of quantum statistics and the structure of the energy spectrum imposed by confinement. When the temperature becomes sufficiently low, the particles stop individually exploring the many excited levels of the trap and instead gather collectively in the ground state, realizing a coherent macroscopic state whose emergent properties, such as superfluidity [73] or the Mott insulating phase [74], will be important in the remainder of this thesis. This transition marks the emergence of quantum behavior on a mesoscopic scale, justifying the description of the condensate as a single macroscopically occupied matter wave.

1.2 Interacting bosonic gases

1.2.1 Atomic interactions

A realistic model for describing a gas of ultracold atoms cannot be limited to the case of the ideal Bose gas: interactions between particles play an essential role. Under typical experimental conditions, the average distance between atoms is on the order of 100 nm, sufficiently large for three-body collisions to be strongly suppressed [72, 75]. It is therefore justified to retain only two-body processes. The associated dynamics can be obtained from the two-particle Schrödinger equation

$$i\hbar\partial_t\psi(\mathbf{r}_1,\mathbf{r}_2,t) = -\frac{\hbar^2}{2m}\left(\partial^2_{\mathbf{r}_1}+\partial^2_{\mathbf{r}_2}\right)\psi(\mathbf{r}_1,\mathbf{r}_2,t) + U(\mathbf{r}_1-\mathbf{r}_2)\psi(\mathbf{r}_1,\mathbf{r}_2,t), \tag{1.12}$$

where $\partial_t \equiv \partial/\partial t$, describing the dynamics between two particles of mass m interacting through the potential U, which depends on the interatomic distance. By switching to center-of-mass coordinates $\mathbf{R} = (\mathbf{r}_1+\mathbf{r}_2)/2$ and $\mathbf{r} = \mathbf{r}_1-\mathbf{r}_2$, the wavefunction $\psi(\mathbf{R}+\mathbf{r}/2,\mathbf{R}-\mathbf{r}/2,t)$ can be expressed through its Fourier components $\int d^3\mathbf{K}\psi_{\mathbf{K}}(\mathbf{r},t)e^{i\mathbf{K}\cdot\mathbf{R}}$. Therefore, equation (1.12) can then be rewritten as an effective single-particle equation with a reduced mass $m_r = m/2$:

$$i\hbar\partial_t\psi_{\mathbf{K}}(\mathbf{r},t) = \left(-\frac{\hbar^2}{2m_r}\partial^2_{\mathbf{r}} + U(\mathbf{r}) + \frac{\hbar^2K^2}{4m}\right)\psi_{\mathbf{K}}(\mathbf{r},t) \tag{1.13}$$

Using a gauge-transform $\psi(\mathbf{r},t) \equiv \psi_{\mathbf{K}}(\mathbf{r},t)e^{-i\hbar^2K^2t/4m}$ to eliminate the K^2 term, one obtain

$$i\hbar\partial_t\psi(\mathbf{r},t) = -\frac{\hbar^2}{2m_r}\partial^2_{\mathbf{r}}\psi(\mathbf{r},t) + U(\mathbf{r})\psi(\mathbf{r},t) \tag{1.14}$$

which describes the evolution of the wavefunction ψ in the presence of a central potential, assumed to vanish asymptotically for $r \to \infty$. Initially, the incoming wave is completely uncorrelated with the interaction potential, which acts only when the two bodies are close to one another. We can therefore consider an incoming wavefunction as a superposition of plane waves $\psi(\mathbf{r},t_0) = \int d^3\mathbf{k}\alpha(\mathbf{k})e^{i\mathbf{k}\cdot\mathbf{r}}e^{-iE_kt_0/\hbar}$, where the $\alpha(\mathbf{k})$ are the Fourier coefficients of the wavefunction and $E_k = \hbar^2k^2/2m_r$. The evolution of this wavefunction is then described as a combination of a plane wave and the set of waves scattered by the potential, in the form of a scattering wavefunction

$$\psi_{\mathbf{k}}(\mathbf{r}) \approx e^{i\mathbf{k}.\mathbf{r}} - \frac{a_s}{r}e^{ikr} \tag{1.15}$$

with a_s the s-wave scattering length describing scattering at low energy [76, 77]. In particular, this quantity allows one to define a contact effective potential :

$$U(\mathbf{r}-\mathbf{r}') = g\delta(\mathbf{r}-\mathbf{r}'), \tag{1.16}$$

where

$$g = \frac{4\pi\hbar^2 a_s}{m}. \tag{1.17}$$

This contact potential constitutes the central approximation in the description of two-body interactions in ultracold atomic gases [72, 78]. It replaces the complexity of the real potential, generally a combination of attractive long-range van der Waals forces and a short-range repulsive core, by a point-like interaction entirely characterized by the scattering length a_s. This simplification is particularly relevant in the low-energy regime, where only s-wave collisions contribute significantly to the dynamics: higher partial waves, subjected to a centrifugal barrier, are strongly suppressed as $k \to 0$. The replacement of the real interatomic potential by the contact potential thus forms one of the cornerstones of the dilute Bose gas model. In this framework, the complex microscopic effects of the interaction are condensed into a single parameter: the coupling constant g. The value of a_s, and therefore of g, can moreover be tuned experimentally using Feshbach resonances [79], allowing one to explore different interaction regimes, from an almost ideal gas ($a_s \approx 0$) to a strongly correlated regime (large $|a_s|$). This experimental flexibility has made it possible to investigate a wide variety of quantum phases and collective phenomena.

When this effective term is introduced into the Hamiltonian of a system of N identical particles, the interaction between all pairs of atoms can be described by

$$\hat{H}_{\text{int}} = \frac{g}{2}\int d^3\mathbf{r}\ \hat{\psi}^\dagger(\mathbf{r})\hat{\psi}^\dagger(\mathbf{r})\hat{\psi}(\mathbf{r})\hat{\psi}(\mathbf{r}), \tag{1.18}$$

where $\hat{\psi}(\mathbf{r})$ is the bosonic field operator. This term expresses the fact that, in the contact model, two particles interact only when they are located at the same point in space. Combined with the kinetic Hamiltonian and the external potential, it allows one to describe the full physics of the dilute bosonic gas, including the Gross-Pitaevskii equation, collective excitations, and superfluid phenomena. Thus, introducing interactions through the scattering length a_s provides a unified and remarkably efficient framework for modeling ultracold bosonic gases. Despite the apparent simplicity of the contact potential, its implications are profound and fundamentally determine the structure, stability, and dynamics of the Bose-Einstein condensate.

1.2.2 Gross-Pitaevskii equation

Let us consider a gas of N bosonic particles trapped in an optical or magnetic potential. We assume that all particles are in the same state, which amounts to working at very low temperature and in the presence of a Bose-Einstein condensate of ^{87}Rb atoms. In the formalism of second quantization, the Hamiltonian of this system is given by

$$\hat{H} = \int d^3\mathbf{r}\,\hat{\psi}^\dagger(\mathbf{r})\Big[-\frac{\hbar^2}{2m}\nabla^2 + V(\mathbf{r})\Big]\hat{\psi}(\mathbf{r}) \tag{1.19}$$

$$+\frac{g}{2}\int d^3\mathbf{r}\,\hat{\psi}^\dagger(\mathbf{r})\hat{\psi}^\dagger(\mathbf{r})\hat{\psi}(\mathbf{r})\hat{\psi}(\mathbf{r}) \tag{1.20}$$

in terms of the bosonic field annihilation ($\hat{\psi}(\mathbf{r})$) and creation ($\hat{\psi}^\dagger(\mathbf{r})$) operators, with atomic mass m and trapping potential $V(\mathbf{r})$ [80]. The interatomic interaction $U(\mathbf{r}-\mathbf{r}')$ is a contact potential defined by Eq. 1.16.

To obtain a description of the dynamics of the ground state of the system governed by the Hamiltonian 1.19, we must resort to approximations. Indeed, while in the non-interacting model the ground state is simply the Fock state defined in the basis of single-particle states $\phi_k \in (\phi_0, \phi_1, \ldots)$, where all particles occupy the lowest-energy state, namely $|\mathrm{GP}\rangle = |N, 0, 0, \ldots\rangle$, the presence of the term proportional to U modifies the dynamics. The Hartree ansatz [81] consists in assuming that the condensate wavefunction can be written as $\psi_0(\mathbf{r}) = \sqrt{N}\,\phi_0(\mathbf{r})$, where ϕ_0 is the orbital corresponding to the ground state. The field annihilation (respectively creation) operator being defined in terms of the annihilation (creation) operators of a bosonic particle, we have

$$\hat{\psi}(\mathbf{r})|N, 0, 0, ...\rangle = \psi_0(\mathbf{r})|N-1, 0, 0, ...\rangle. \tag{1.21}$$

This last definition allows us to obtain the form of the Hamiltonian (1.19) in the context of an isolated Bose-Einstein condensate, and in particular to obtain the expression of the energy associated with the state $|\mathrm{GP}\rangle$. Concretely, we are assuming here that the ground state is slightly modified compared with that of the non-interacting system and we will determine which energy corresponds to the lowest one, this is the variational principle. Let us first establish the expression of the energy relative to the state $|\mathrm{GP}\rangle$:

$$\langle \mathrm{GP}|\hat{H}|\mathrm{GP}\rangle = \int d^3\mathbf{r} \left[\psi_0^*(\mathbf{r}) \left(-\frac{\hbar^2}{2m}\nabla^2 + V(\mathbf{r}) \right) \psi_0(\mathbf{r}) + \frac{g}{2}|\psi_0(\mathbf{r})|^4 \right] \tag{1.22}$$

$$\equiv E_{\mathrm{GP}}[\psi_0], \tag{1.23}$$

where we have assumed that the number of particles is very large, allowing the approximation $N - 1 \approx N$. The variational principle will now be applied to the energy E_{GP}: we seek the wavefunction ψ_0 that minimizes this energy. To do so, we additionally impose the condition that the number of particles is conserved and equal to

$$N = \int d^3\mathbf{r}\ |\psi_0(\mathbf{r})|^2, \tag{1.24}$$

meaning that all particles indeed occupy the lowest-energy orbital. Using the Lagrange multiplier μ, the variational principle applied to ψ_0^*, that is, solving the equation

$$\frac{\delta}{\delta\psi_0^*(\mathbf{r})} \left[E_{\mathrm{GP}}[\psi_0] - \mu \left(\int d^3\mathbf{r}|\psi_0(\mathbf{r})|^2 - N \right) \right] = 0, \tag{1.25}$$

yields the dynamics of the wavefunction ψ_0, the Gross-Pitaevskii equation [82, 83]:

$$\left(-\frac{\hbar^2}{2m}\nabla^2 + V(\mathbf{r}) + g|\psi_0(\mathbf{r})|^2 \right) \psi_0(\mathbf{r}) = \mu\psi_0(\mathbf{r}). \tag{1.26}$$

Equation (1.26) closely resembles a time-independent Schrödinger equation, with a kinetic term $-\hbar^2\nabla^2/2m$, a trapping potential $V(\mathbf{r})$, and a total energy μ, known as the chemical potential of the gas, i.e., the energy required to add or remove a particle from the gas. However, a new nonlinear term $g|\psi_0(\mathbf{r})|^2$ appears and acts as an effective potential defined by the interaction constant g and the probability density $|\psi_0(\mathbf{r})|^2$, thus encoding the influence of particles on one another. This nonlinearity introduces

a physics fundamentally different from that usually described by the Schrödinger equation, and it makes the derivation of analytical solutions more difficult. We will nevertheless detail here the solution that can be obtained in the case of a spatially constant potential $V(\mathbf{r}) \equiv V_0$, in order to provide a first intuition of the wavefunction of a Bose-Einstein condensate.

In the case of a constant potential V_0, Eq.(1.26) is satisfied by the perfectly homogeneous condensate wavefunction $\psi_0(\mathbf{r}) = \sqrt{n}$, where n is the atomic density. Injecting this wavefunction into the Gross-Pitaevskii equation, we obtain a condition on n:

$$gn = \mu - V_0. \tag{1.27}$$

Thus, the atomic density of the condensate, weighted by the interaction scale g, is linked to the difference between the chemical potential of the gas and the constant trapping potential. Assuming hard-wall boundaries in the (x, y) planes at $z = 0$ and $z = L$ (with L taken to be much larger than any characteristic length scale of the system), the condensate wavefunction depends only on the coordinate z and satisfies a one-dimensional Gross-Pitaevskii equation:

$$-\frac{\hbar^2}{2m}\partial_z^2\psi_0(z) + g|\psi_0(z)|^2\psi_0(z) = (\mu - V_0)\psi_0(z), \tag{1.28}$$

where we impose the boundary conditions $\psi_0(0) = \psi_0(L) = 0$. A solution for $L \to \infty$ is given by

$$\psi_0(z) \simeq \sqrt{n}\,\tanh\left(\frac{z}{\sqrt{2}\xi}\right)\,\tanh\left(\frac{L-z}{\sqrt{2}\xi}\right), \tag{1.29}$$

where $\xi = \hbar/\sqrt{2mgn}$ is the condensate healing length [84]. This characteristic length ξ plays a central role: it represents the spatial scale over which the condensate wavefunction recovers after being perturbed. Physically, ξ measures the compromise between kinetic energy, which tends to smooth out rapid variations of $\psi_0(z)$, and interaction energy, which instead favors a uniform density. In the limit $L \gg \xi$, the resulting hyperbolic solution shows that edge effects are localized in regions of extent on the order of ξ, while the core of the system remains perfectly homogeneous, confirming that interactions stabilize an almost constant density far from the boundaries. The effect of interactions is to "flatten" the condensate wavefunction at the center of the system, as can be seen in Fig. 1.2. This behavior contrasts sharply with that of a non-interacting gas: the ground-state wavefunction in a well of width L normally adopts the sinusoidal form $\psi(z) \propto \sin(\pi z/L)$, dominated by kinetic energy. Introducing a nonlinear term into the Gross-Pitaevskii equation radically modifies this structure, allowing the condensate to locally adjust its profile to minimize the total energy.

1.3 Traps and lattices

The manipulation and control of ultracold atoms rely crucially on our ability to confine them in a stable and reproducible way. Magnetic traps enabled the first observations of Bose-Einstein condensation [62, 63], and subsequently, the use of light as a trapping tool established itself as an extremely versatile method. Optical traps and optical lattices indeed make it possible to shape periodic or quasi-arbitrary potentials by exploiting the fundamental interaction between an oscillating electromagnetic field and the internal structure of the atoms. This interaction, which shifts the electronic

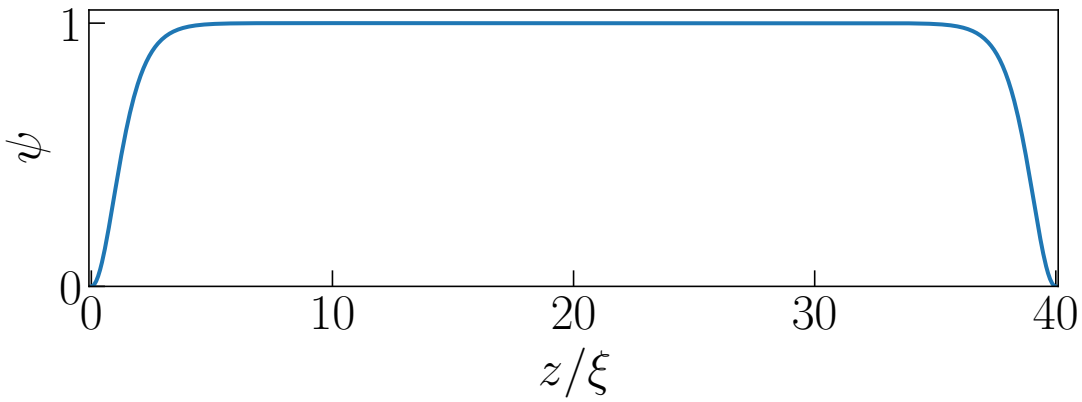

FIGURE 1.2: Wavefunction solving Gross-Pitaevskii equation in the case of a constant trapping potential and hard-wall boundary conditions for $n = 1$ and $L = 40\xi$. A Bose-Einstein condensate in such a context resembles the usual sinusoidal wavefunction of the non-interacting case, but with a flattening at the center of the trap. The interaction between bosons has the effect of confining the density to an almost uniform region, leaving significant variations only at the edges, where the characteristic coherence lengths of the system develop.

energy levels, can be used to create attractive or repulsive forces leading to the spatial confinement of the particles. Optical lattices play a central role today in quantum simulation, as they provide a direct analogy with crystalline lattices in condensed matter while offering a level of control unattainable in real materials. The geometry, depth, dimensionality, and even the topology of the lattice can be adjusted simply by modifying the laser beam parameters. Thus, shifting a potential minimum, isolating a site, or creating superlattices or exotic geometries become routine experimental operations.

Two of the main ways to trap atoms rely on their hyperfine structure, which results from the interaction between the magnetic moments of the nucleus and of its bound electron. First observed in 1891 by Michelson [85], hyperfine splitting could only be explained once Pauli proposed the existence of an intrinsic magnetic moment for the nucleus [86]. This interaction causes the splitting of the energy levels defined by the fine structure. To understand how the hyperfine structure makes it possible to define atomic traps, we will consider a simple model of the interaction between the two magnetic moments associated with the spins of the electron and the nucleus, denoted respectively by $\mathbf{S}$ and $\mathbf{I}$. Let A be the constant setting the energy scale of the interaction; the Hamiltonian describing this phenomenon is written [9, 87]:

$$\hat{H}_{\mathrm{HF}} = A\hat{\mathbf{I}} \cdot \hat{\mathbf{S}}. \tag{1.30}$$

The eigenenergies of the hyperfine Hamiltonian (1.30) are obtained by diagonalizing it, which can be done by defining the total spin operator $\hat{\mathbf{F}} = \hat{\mathbf{I}} + \hat{\mathbf{S}}$ and expanding the expression for $\hat{\mathbf{F}}^2$. The Hamiltonian can then be rewritten

$$\hat{H}_{\mathrm{HF}} = \frac{A}{2}\left(\hat{\mathbf{F}}^2 - \hat{\mathbf{I}}^2 - \hat{\mathbf{S}}^2\right), \tag{1.31}$$

and takes a diagonal form in the basis of eigenstates $|I, F, m_F\rangle$, defined through the quantum numbers of nuclear spin I, total spin F, and total magnetic moment m_F. The eigenenergies are known and can be written, in terms of the quantum numbers I,

F, and S,

$$E_F = \frac{A}{2}\left(F(F+1) - I(I+1) - S(S+1)\right). \tag{1.32}$$

Assuming that the atomic species under consideration is ^{87}Rb, whose nuclear spin quantum number is $I = 3/2$, and inserting the electron spin quantum number $S = 1/2$, we obtain the selection rule imposing that F can only take the values 1 or 2. In this case, the ground state of the fine structure is split into two energies corresponding to the values $F = 1$ and $F = 2$, respectively

$$E_{\mathrm{F=1}} = -\frac{5A}{4} \tag{1.33}$$

$$E_{\mathrm{F=2}} = \frac{3A}{4}. \tag{1.34}$$

A trap designed to confine atoms in a specific region of space must modify these energy levels in such a way that a minimum appears at the desired configuration. Typically, in the case of an inhomogeneous magnetic trap, one seeks to ensure that the ground state of the system lies at the minimum of the magnetic field, which can be controlled experimentally using Helmholtz coils.

1.3.1 Magnetic trap

The application of a magnetic field $\mathbf{B}$ to the system described by the Hamiltonian (1.30) adds two terms to it, accounting for the interaction of this magnetic field with the nuclear spin and the electronic spin. The hyperfine system under a magnetic field is described by the Hamiltonian

$$\hat{H}_{\mathrm{HF,B}} = A\hat{\mathbf{I}}\cdot\hat{\mathbf{S}} + g_e\mu_B\mathbf{B}\cdot\hat{\mathbf{S}} - g_N\mu_N\mathbf{B}\cdot\hat{\mathbf{I}}, \tag{1.35}$$

where g_e and g_N are the Landé factors of the electron and the nucleus, respectively, and μ_B and μ_N are the Bohr magneton and the nuclear magneton, respectively. In this model, we will neglect the effect of the last term compared with that describing the interaction between the magnetic field and the electronic spin. This approximation is justified by the ratio $\mu_N/\mu_B \sim 10^{-4}$, which reflects the fact that, given the mass difference between the nucleus and the electron, it is much more difficult to affect with a magnetic field the motion of the central nucleus than that of the electron. Within this approximation, and considering a magnetic field oriented along the z axis, the Hamiltonian becomes

$$\hat{H}_{\mathrm{HF,B}} = A\hat{\mathbf{I}}\cdot\hat{\mathbf{S}} + g_e\mu_B\big|\mathbf{B}\big|\hat{S}_z, \tag{1.36}$$

where $\hat{S}_z = \hbar\hat{\sigma}_z/2$. In the limit of a magnetic field small compared with the hyperfine energy scale A (i.e. $|\mathbf{B}| \ll A$) the energy levels take on a clear form regarding the action of the magnetic field and allow one to immediately understand its influence. For the case of ^{87}Rb, we have:

$$E_{F=1,m_F} = -\frac{5A}{4} - \frac{m_F g_e\mu_B\big|\mathbf{B}\big|}{4} \tag{1.37}$$

$$E_{F=2,m_F} = \frac{3A}{4} + \frac{m_F g_e\mu_B\big|\mathbf{B}\big|}{4}. \tag{1.38}$$

This additional splitting of the energy levels is called the Zeeman effect, the analogue of the Stark effect in the case of an electric field. This modification is proportional to the magnetic field intensity and thus allows one to measure, through the difference

$E_{\mathrm{F}=2,m_F} - E_{\mathrm{F}=1,m_F}$, the magnitude of the magnetic field $|\mathbf{B}|$ [88, 89].

What will interest us here, however, is a different situation: the case in which the external magnetic field is controlled and we wish to separate the two energy levels so as to isolate the ground state of lowest energy. To achieve this, since the level $E_{\mathrm{F}=1,m_F}$ decreases with the decrease of the magnetic field intensity when $m_F > 0$, a local minimum of $|\mathbf{B}|$ will correspond to a local minimum of the ground-state energy. In the Zeeman regime of a magnetic field small compared with the hyperfine interaction energy scale, the modification of the energy levels can be rewritten as the effect of an effective potential

$$V(\mathbf{r}) = \frac{m_F g_e \mu_B}{2I+1} \big|\mathbf{B}(\mathbf{r})\big|, \tag{1.39}$$

where m_F is the magnetic quantum number. This potential places its minimum where the amplitude of the magnetic field is minimal, and it enables the construction of traps for ultracold atoms, such as the Ioffe-Pritchard trap [90, 91].

1.3.2 Laser-induced optical trap

In its ground state, a neutral atom is unpolarized. However, when placed in an external electric field $\mathbf{E}$, the electronic cloud of the atom can deform and induce an electric dipole moment that depends on the field

$$\mathbf{d}_{\mathrm{ind}} = \alpha(\omega)\mathbf{E}, \tag{1.40}$$

where $\alpha(\omega)$ is the atomic polarizability at the frequency ω of the external field (see Fig. 1.3). Let us consider the case of a monochromatic and linearly polarized field of the form

$$\mathbf{E}(\mathbf{r},t) = \mathbf{E}_0(\mathbf{r})\cos\left(\omega t - \varphi\right), \tag{1.41}$$

with a phase φ and an amplitude $\mathbf{E}_0(\mathbf{r})$. The action of such an electric field will modify the energy levels of the system, and in particular time-dependent perturbation theory allows one to obtain the shift ΔE_0 experienced by the ground-state energy E_0:

$$\Delta E_0 = -\frac{|\langle 1|(\mathbf{r}_e - \mathbf{r})\cdot\mathbf{e}_z|0\rangle|^2}{E_1 - E_0 - \hbar\omega}\frac{I(\mathbf{r})}{2\epsilon_0 c}, \tag{1.42}$$

where $\mathbf{r}_e$ and $\mathbf{r}$ are the position vectors of the electron and the nucleus, respectively, ϵ_0 the vacuum permittivity, c the speed of light and where $I(\mathbf{r})$ is the laser intensity at the position $\mathbf{r}$ of the atom. The spatial intensity profile of the laser can thus be interpreted as an effective potential $V(\mathbf{r})$ that will attract or repel the atom depending on the sign of the difference between the excitation frequency $\omega_0 = (E_1 - E_0)/\hbar$ and the oscillation frequency of the electric field ω. The two possible cases are:

$$\omega < \omega_0 : V(\mathbf{r}) < 0 \longrightarrow \text{red-detuned}, \tag{1.43}$$

$$\omega > \omega_0 : V(\mathbf{r}) > 0 \longrightarrow \text{blue-detuned}. \tag{1.44}$$

In the first case, the energy is minimal where the light intensity is maximal. The laser is said to be red-detuned with respect to the atom, and the particles are attracted to regions of high light intensity. In the second case, the laser is blue-detuned, and the particles are attracted to dark regions because the energy is maximized at the intensity maxima.

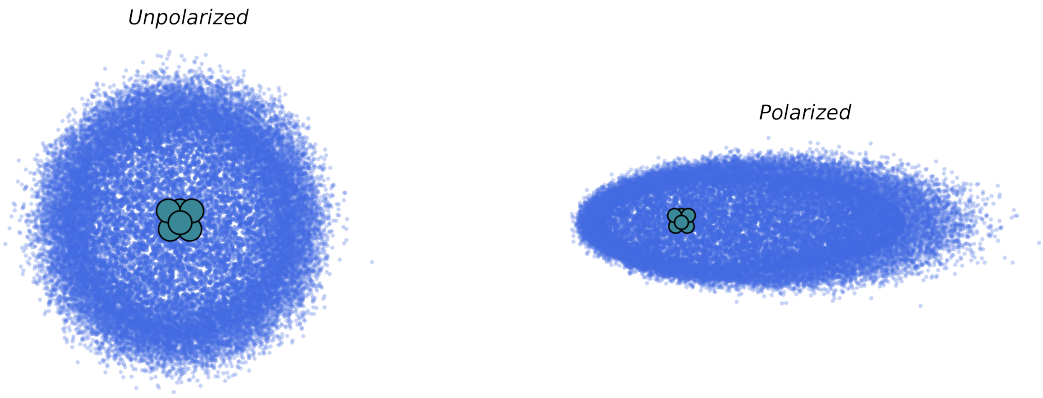

FIGURE 1.3: Effect of an external electric field on the electronic cloud of an atom. Left: in the absence of a field, the electronic distribution remains isotropic and unpolarized around the nucleus. Right: the application of an electric field induces a polarization, deforming the electronic density and creating an effective electric dipole. This polarizability makes it possible, in particular, to confine atoms in electromagnetic traps.

Thus, the interaction between an oscillating electric field and a neutral atom gives rise to an optical dipole potential proportional to the local intensity of the light field:

$$V(\mathbf{r}) = -\frac{1}{2}\mathrm{Re}\{\alpha(\omega)\}|\mathbf{E}_0(\mathbf{r})|^2. \tag{1.45}$$

This potential reflects the induced deformation of the electronic cloud and the linear response of the atom to the applied field. The imaginary part of $\alpha(\omega)$ accounts for absorption processes, and in particular for the probability that the atom absorbs a photon and is subsequently excited, leading to spontaneous scattering. The spatial dependence of the light intensity therefore directly translates into a modulation of the effective potential acting on the atoms. By adjusting the laser frequency, its intensity, and its geometry, it becomes possible to shape at will the potential landscape in which the particles evolve [92]. In the case of a focused beam, the maximum light intensity is located at the center of the beam. For a red-detuned laser, the atoms are trapped in this central region, realizing a Gaussian-shaped optical dipole trap. This type of confinement is particularly robust and has the advantage of depending only weakly on the internal state of the atom, unlike magnetic traps. More generally, by superimposing several coherent beams, one can produce optical interference patterns whose fringes create a periodic modulation of the intensity. The minima (or maxima) of this intensity correspond to minima (or maxima) of the dipole potential, giving rise to optical lattices. These structures, analogous to the crystalline lattices of solid-state systems, enable atoms to be confined at well-defined lattice sites and allow precise control of the quantum system parameters (trap depth, geometry, dimensionality, etc.).

1.3.3 Optical lattice

Up to this point, we have shown how a light field can create a dipole potential capable of trapping an atom in a localized region of space. By extending this principle, it is possible to reproduce this structure periodically in space in order to form an optical lattice. These lattices, consisting of a succession of minima and maxima of light intensity, allow a large number of atoms to be confined in equivalent sites and make it possible to study the collective dynamics arising from quantum tunneling between neighboring sites. Such systems constitute an ideal platform for simulating models

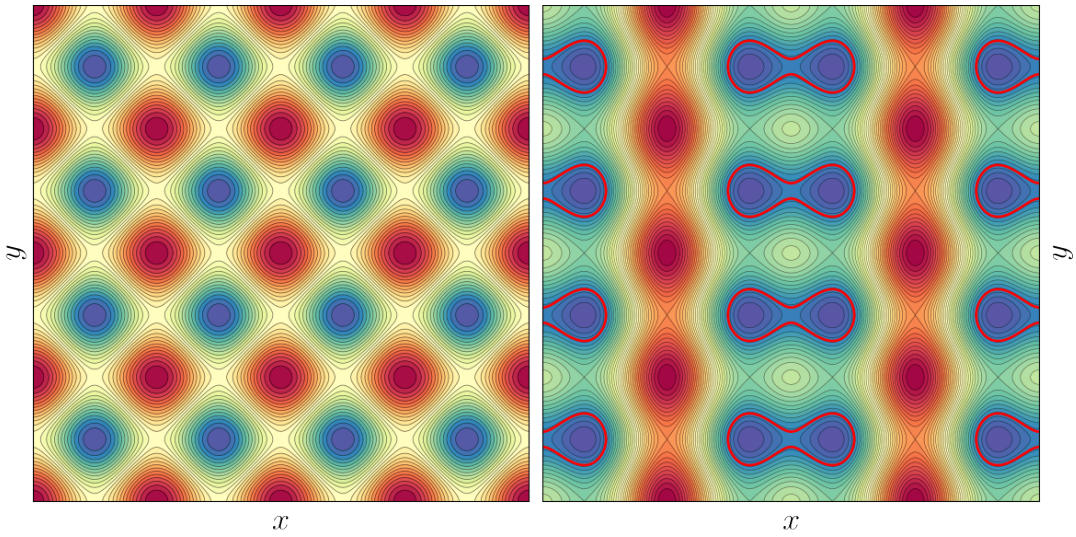

FIGURE 1.4: Left: Potential of a two-dimensional square optical lattice formed by the interference of two pairs of orthogonal laser beams. The potential minima are periodic and equally spaced, creating a regular array of identical sites. Right: Superlattice obtained by adding a second spatial modulation, producing double wells within each minimum of the primary lattice. This configuration allows fine control over the local structure of the potential. In both panels, minima are shown in blue shades and maxima in red shades. A red contour highlights the double-well-shaped minima.

from solid-state physics, such as the Bose-Hubbard model or electronic crystalline structures [8, 10, 12]. As a first approach, let us consider a one-dimensional (1D) optical lattice formed by the interference of two laser beams of the same wavelength λ, with the same polarization, propagating in opposite directions along the x axis. The corresponding electric fields can be written:

$$\mathbf{E}_1(x,t) = E_0 e^{-i(kx+wt+\varphi_1)}\mathbf{e}_\perp \tag{1.46}$$

$$\mathbf{E}_2(x,t) = E_0 e^{-i(-kx+wt+\varphi_2)}\mathbf{e}_\perp \tag{1.47}$$

where $k = 2\pi/\lambda$ is the wave vector and $\mathbf{e}_\perp$ is a unit vector perpendicular to the propagation direction. The superposition of the two beams creates a standing wave whose spatial intensity is given by:

$$I(x) \propto |\mathbf{E}_1 + \mathbf{E}_2|^2 = 4|E_0|^2 \cos^2(kx + \varphi/2), \tag{1.48}$$

noting $\varphi \equiv \varphi_1 - \varphi_2$ the relative phase difference. This periodic modulation of the light intensity directly translates into a periodic potential for the atoms:

$$V(x) = V_0 \cos^2(k_L x + \varphi), \tag{1.49}$$

with V_0 the lattice depth, proportional to the beam intensity, and $k_L = 2\pi/\lambda$. The minima of the potential correspond to positions where the atoms are trapped (for a red-detuned laser). The lattice period is therefore $\lambda/2$, i.e. half the wavelength of the laser. By combining several one-dimensional lattices along orthogonal axes, it is possible to obtain two-dimensional (2D) or three-dimensional (3D) lattices. For instance, the potential

$$V(x,y) = V_x \cos^2(k_x x) + V_y \cos^2(k_y y) \tag{1.50}$$

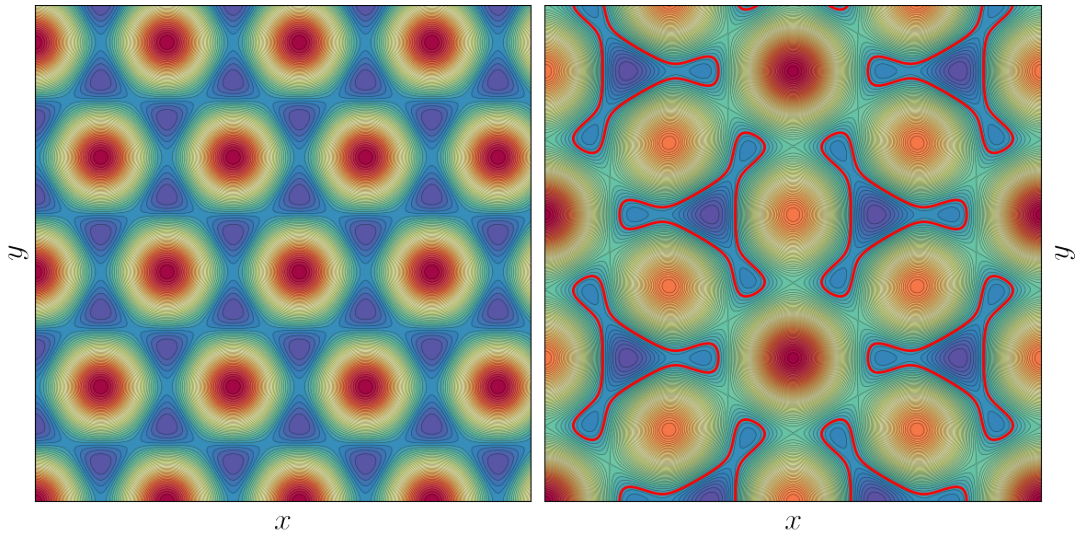

FIGURE 1.5: Left: potential of a two-dimensional hexagonal optical lattice produced by the interference of three laser beams inclined at 120°. The resulting structure exhibits triangular symmetry and equally spaced minima forming a regular hexagonal lattice. Right: hexagonal superlattice obtained by adding an additional modulation, which locally modifies the depth of the sites and introduces substructures within each cell. This refined geometry allows one to engineer complex potential landscapes, useful for studying phenomena such as frustration, topological phases, or directed dynamics in nontrivial lattices. In both panels, minima are shown in blue shades and maxima in red shades. A red contour highlights the star-shaped minima.

forms a square lattice in the (x, y) plane, as illustrated in Fig. 1.4(a) for $k = \pi$. In particular, it is possible to create what is called a superlattice by adding an other laser whose wavelength is exactly twice the first one. In the case of an initial square lattice, one can create a square superlattice where it is possible to isolate double wells systems within (see Fig. 1.4(b)). It is also possible to realize more exotic optical lattices. In particular, two optical lattices can be superimposed in order to precisely manipulate the depth of certain wells. The superposition of a hexagonal lattice and a triangular lattice can produce a "star-shaped" superlattice, in which a central well is connected to three neighboring wells. In Fig. 1.5(a), a hexagonal lattice is formed by the potential

$$V_{\text{hex}} = V_0 \left(\cos^2(\mathbf{k}_1.\mathbf{r}) + \cos^2(\mathbf{k}_2.\mathbf{r}) + \cos^2(\mathbf{k}_3.\mathbf{r})\right). \tag{1.51}$$

Adding a triangular lattice of the form

$$V_{\text{tri}} = V_1 \left(\cos(\mathbf{k}_1.\mathbf{r}) + \cos(\mathbf{k}_2.\mathbf{r}) + \cos(\mathbf{k}_3.\mathbf{r})\right) \tag{1.52}$$

makes it possible to define a hexagonal superlattice $V_{\text{hex}} + V_{\text{tri}}$, where the depth of a central well connected to three other minima can be controlled by the intensity of the additional triangular lattice (see Fig. 1.5(b)), for $k_1 = (2\pi, 0), k_2 = (-\pi, \sqrt{3}\pi)$ and $k_3 = -k_2$. By adjusting the relative intensity of the beams forming these lattices, one can control the depth of particular wells and the local connectivity of the lattice, opening the way to the realization of novel artificial geometries.

1.4 Bose-Hubbard model

Now that we defined what is an ultracold gas and how to trap it within an optical lattice, we can describe its behavior in the latter. Let $\hat{\psi}^\dagger(\mathbf{r})$ and $\hat{\psi}(\mathbf{r})$ be the creation and annihilation field operators of a bosonic field located at position $\mathbf{r}$. In the framework of second quantization, the Hamiltonian describing such a gas is written [8]:

$$\hat{H} = \int d\mathbf{r}\ \hat{\psi}^\dagger(\mathbf{r})\Big[-\frac{\hbar^2}{2m}\nabla^2 + V(\mathbf{r})\Big]\hat{\psi}(\mathbf{r}) + \frac{1}{2}\int d\mathbf{r}\int d\mathbf{r}'\hat{\psi}^\dagger(\mathbf{r})\hat{\psi}^\dagger(\mathbf{r}')U(\mathbf{r}-\mathbf{r}')\hat{\psi}(\mathbf{r}')\hat{\psi}(\mathbf{r}) \tag{1.53}$$

The first term describes the kinetic energy of the particles as well as their interaction with the external potential $V(\mathbf{r})$, which in our case corresponds to an optical lattice. The second term accounts for interactions between particles, modeled by an interaction potential $U(\mathbf{r}-\mathbf{r}')$. As we have seen, for collisions at very low energies, the interaction term can be replaced by a contact interaction $U(\mathbf{r}-\mathbf{r}') = g\delta(\mathbf{r}-\mathbf{r}')$ with $g = 4\pi\hbar^2 a_s/m$, where a_s is the s-wave scattering length.

The dynamics of a particle trapped in a periodic optical lattice $V(\mathbf{r})$ is described by the time-independent Schrödinger equation

$$\Big[-\frac{\hbar^2}{2m}\nabla^2 + V(\mathbf{r})\Big]\phi_n(\mathbf{r}) = E_n\phi_n(\mathbf{r}) \tag{1.54}$$

where $\phi_n(\mathbf{r})$ is the wavefunction associated with the energy E_n. According to Bloch's theorem [93], these functions can be written as a plane wave modulated by a periodic function that has the same symmetry as the optical lattice. To analyze localized systems, it is more convenient to introduce a basis of Wannier functions w_n [94], which are obtained as linear combinations of Bloch functions and are maximally localized in space:

$$w_n(\mathbf{r}) = \frac{1}{\sqrt{L}}\sum_{q} e^{-i\mathbf{q}.\mathbf{r}}\phi_n(\mathbf{r}). \tag{1.55}$$

These Wannier functions make it possible to rewrite the field operators in terms of contributions localized on the lattice sites. In particular, since we are considering a gas of ultracold atoms at low temperature, only the lowest band is significantly populated. We can therefore write

$$\hat{\psi}(\mathbf{r}) = \sum_i w_0(\mathbf{r}-\mathbf{r}_i)\hat{a}_i \tag{1.56}$$

where $\hat{a}_i$ annihilates a particle located in site i.

Let us now examine the different terms of the Hamiltonian in this basis. The kinetic term becomes

$$\hat{H}_1 = \sum_{i,j}\int d\mathbf{r}\ w_0^*(\mathbf{r}-\mathbf{r}')\Big[-\frac{\hbar^2}{2m}\nabla^2 + V(\mathbf{r})\Big]w_0(\mathbf{r}-\mathbf{r}')\hat{a}_i^\dagger\hat{a}_j. \tag{1.57}$$

Since the Wannier functions are well localized around each site, this term can be interpreted as a coupling between sites i and j that decreases rapidly with the distance between them:

$$\hat{H}_1 = \sum_i J_0\hat{a}_i^\dagger\hat{a}_i - \sum_{i,j=i\pm1} J_1\hat{a}_i^\dagger\hat{a}_j - \sum_{i,j=i\pm2} J_2\hat{a}_i^\dagger\hat{a}_j + \dots \tag{1.58}$$

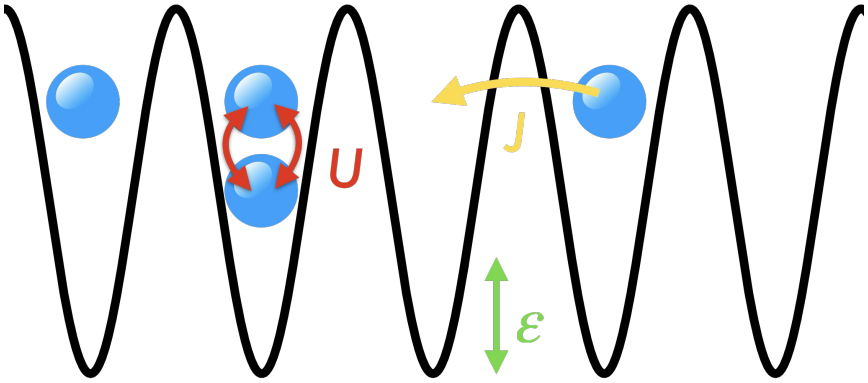

FIGURE 1.6: Illustration of the one-dimensional Bose-Hubbard model. The bosons are confined in a periodic lattice whose minima define the sites. The local interaction energy $U > 0$ penalizes the presence of multiple particles on the same site, while the tunneling coupling J allows the coherent transfer of a boson from one site to the next. The on-site energy ε may also be controlled, modifying the relative energy of the sites and influencing the system's dynamics.

The coefficients J_m represent the hopping amplitudes between sites separated by m lattice spacings:

$$J_m = \int d\mathbf{r}\ w_0^*(\mathbf{r})\Big[V(\mathbf{r}) - \frac{\hbar^2}{2m}\nabla^2\Big]w_0(\mathbf{r}-\mathbf{r}_m) \tag{1.59}$$

The first term (J_0) corresponds to the local on-site energy, while J_1 describes the tunneling amplitude between two neighboring sites. If the lattice is sufficiently deep, hopping beyond nearest neighbors becomes negligible and the Hamiltonian simplifies to:

$$\hat{H}_1 = \varepsilon \sum_i \hat{a}_i^\dagger \hat{a}_i - J \sum_{\langle i,j\rangle} \hat{a}_i^\dagger \hat{a}_j \tag{1.60}$$

where we noted $J_0 \equiv \varepsilon$. For the interaction term, we define

$$U_{i,j,k,l} = g \int d\mathbf{r}\ w_0^*(\mathbf{r}-\mathbf{r}_i) w_0^*(\mathbf{r}-\mathbf{r}_j) w_0(\mathbf{r}-\mathbf{r}_k) w_0(\mathbf{r}-\mathbf{r}_l). \tag{1.61}$$

Due to the strong localization of the Wannier functions, the dominant contribution comes from on-site interactions (two particles occupying the same well). Thus, the leading interaction Hamiltonian takes the form

$$\hat{H}_2 = \frac{U}{2} \sum_i \hat{a}_i^\dagger \hat{a}_i^\dagger \hat{a}_i \hat{a}_i \tag{1.62}$$

where U is the on-site interaction energy.

By gathering all terms together, we finally obtain the Bose-Hubbard Hamiltonian, which is the effective model describing a bosonic gas in an optical lattice [10, 12]

$$\hat{H} = \frac{U}{2} \sum_i^L \hat{a}_i^\dagger \hat{a}_i^\dagger \hat{a}_i \hat{a}_i + \sum_i^L \varepsilon_i \hat{a}_i^\dagger \hat{a}_i - J \sum_i^{L-1} (\hat{a}_{i+1}^\dagger \hat{a}_i + \hat{a}_i^\dagger \hat{a}_{+1}) \tag{1.63}$$

This Hamiltonian describes a system of N bosons trapped in an optical lattice with L sites of on-site energies ε_i and on-site interaction U (see Fig. 1.6). The particles can

move from one site to another through a hopping term proportional to the parameter J.

Several parametric regimes exist depending on the ratio between interaction and hopping [12, 73, 74]. Indeed, the ratio U/J characterizes the competition between on-site interaction and the kinetic energy associated with inter-site hopping. For a ratio $U/J \to \infty$, inter-site tunneling is suppressed and the particles become completely localized in their energy levels. Such a regime defines what is known as a Mott insulator. Conversely, when $U/J \to 0$, the particles can tunnel very easily and their wavefunctions delocalize over the entire lattice. In this regime, the excitation spectrum is gapless and displays a linear (phonon-like) dispersion at low momentum, which corresponds to the behavior of a superfluid phase.

The parametric zone of interest in this thesis lies between these extremes. The self-trapping regime, where $U/J \gg 1$, describes a system in which particles cannot tunnel independently [27, 95]. The dominant interaction causes the wavefunctions to be mostly localized, but the nonzero hopping rate $J \neq 0$ allows the system to tunnel in a particular way, known as collective tunneling. In this case, the particles can only tunnel together, inducing an effective coupling between the states in which all N particles are located in the same site.

1.5 Two-site Bose-Hubbard model

To grasp the behavior of a Bose-Hubbard system, we introduce a first approach in the case of a two-site model corresponding to a ensemble of N bosonic particles trapped in a double-well potential [26, 27]:

$$\hat{H} = \frac{U}{2}(\hat{a}_1^\dagger \hat{a}_1^\dagger \hat{a}_1 \hat{a}_1 + \hat{a}_2^\dagger \hat{a}_2^\dagger \hat{a}_2 \hat{a}_2) - J(\hat{a}_1^\dagger \hat{a}_2 + \hat{a}_2^\dagger \hat{a}_1) + \varepsilon(\hat{a}_1^\dagger \hat{a}_1 - \hat{a}_2^\dagger \hat{a}_2) \tag{1.64}$$

This minimal model, sometimes called the Josephson dimer, is one of the simplest systems for exploring the interplay between interactions, hopping, and quantum tunneling phenomena [27]. Despite its reduced structure, the two-site model already reveals a rich variety of physical behaviors. In the weak-interaction regime, the bosons delocalize over the two wells and form a coherent superfluid state, analogous to the behavior of Josephson oscillations between the two modes. When interactions become strong, the dynamics change radically: the system can enter a macroscopic quantum self-trapping regime, characterized by a strongly imbalanced population between the two sites.

At the quantum level, the competition between interaction energy and tunnel coupling also leads to the formation of highly nonclassical states, such as NOON states, resulting from collective tunneling between two macroscopically distinct configurations. The study of this model, both in its mean-field version and in its exact quantum formulation, thus provides a privileged entry point for understanding emergent phenomena in optical lattices, bosonic junctions, and strongly correlated mesoscopic systems. In what follows, we analyze the dynamics of the two-site system within the mean-field approximation, and then examine the purely quantum effects, in particular the emergence of collective tunneling and the natural generation of NOON states in the strongly correlated regime.

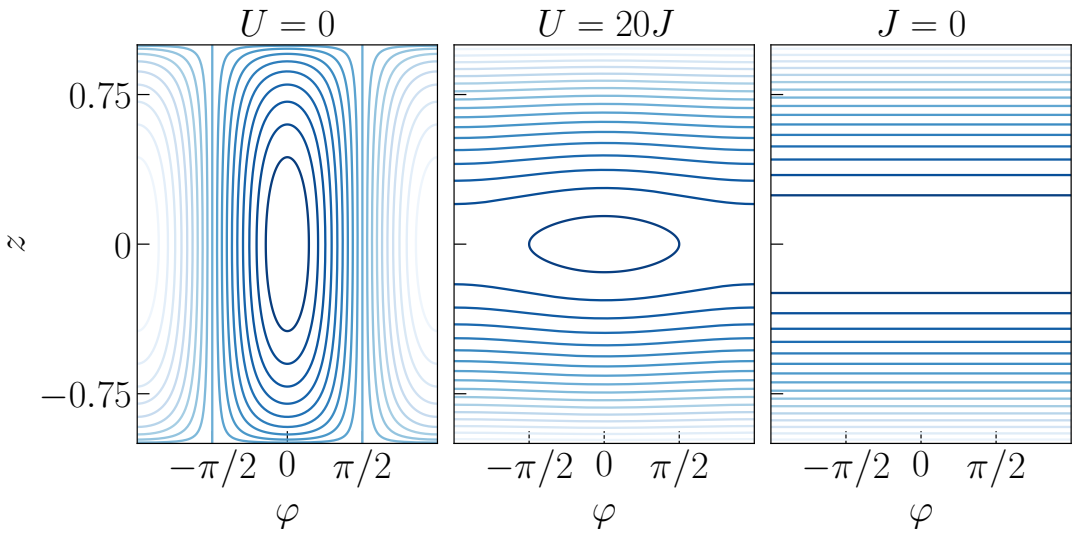

FIGURE 1.7: Phase portraits of the two-mode Hamiltonian $H(z, \varphi)$ of the Bose-Hubbard model for different interaction ratios and $N = 5$. Left: noninteracting regime ($U = 0$), where the dynamics are purely Josephson-like and the trajectories are elliptical. Center: intermediate strongly interacting regime ($U = 20J$), exhibiting separatrix orbits and a hyperbolic fixed point, characteristic of the transition toward the self-trapping regime. Right: case $J = 0$, where tunneling is suppressed and the phase dynamics are frozen, producing horizontal trajectories corresponding to constant values of the imbalance z.

1.5.1 Macroscopic quantum self-trapping

In a double-well potential the phenomenon of macroscopic quantum self-trapping was observed in the 2000s [96, 97]. Shortly afterward, correlated pair tunneling was observed in an optical lattice, a clear signature of collective dynamics beyond simple single-particle tunneling [11]. These works were followed by further observations, notably in double-well dynamics with controlled atomic occupation, confirming that barrier crossing can result from a correlated quantum process [98]. These experimental results, made possible by fine control of interactions via Feshbach resonances, constitute direct demonstrations of the existence of collective tunneling in ultracold atomic systems [96]. In this section, we will detail how the two-site Bose-Hubbard Hamiltonian, in a self-trapping parametric regime, naturally allows the generation of NOON states during the time evolution of a suitably prepared initial state.

One way to visualize the different parametric regimes depending on the ratio NU/J is to use the mean-field approximation, in which the bosonic operators are replaced by their coherent expectation values [99]. This approach provides a semiclassical description of the system, where one is no longer concerned with individual quantum fluctuations but rather with the evolution of global quantities such as populations and macroscopic phases. In this framework we introduce a complex amplitude $\psi_j = \langle \hat{a}_j \rangle$ for each site j, interpreted as the local condensate wavefunction. The two-site Bose-Hubbard Hamiltonian (1.64) then takes the form

$$H(\psi_j, \psi_j^*, t) = \frac{U}{2} \sum_{j=1}^{2} |\psi_j|^4 - J\left(\psi_1^* \psi_2 + \psi_2^* \psi_1\right) + \varepsilon\left(|\psi_1|^2 - |\psi_2|^2\right), \tag{1.65}$$

which of course reminds us of the Gross-Pitaevskii equation. By writing $\psi_j = \sqrt{I_j}\, e^{i\theta_j}$ with $I_j = n_j$ the number of particles on each site (and $I_1 + I_2 = N$), and performing

the canonical change of variables $z = (I_1 - I_2)/N$ and $\varphi = \theta_1 - \theta_2$ while ignoring constant terms, we obtain

$$H(z, \varphi, t) = \frac{UN^2}{2} z^2 - JN\sqrt{1 - z^2}\cos(\varphi) + N\varepsilon z. \tag{1.66}$$

The Hamiltonian (1.66) depends parametrically on the imbalance z and on the phase difference φ between the two sites, and describes the effective dynamics of a nonlinear pendulum, whose nonlinearity is entirely controlled by the ratio NU/J. The associated equations of motion, obtained using the usual canonical relations, are given by

$$\dot{z} = -NJ\sqrt{1 - z^2}\sin\varphi, \tag{1.67}$$

$$\dot{\varphi} = \frac{UN^2}{2} + NJ\frac{z}{\sqrt{1 - z^2}}\cos\varphi + N\varepsilon. \tag{1.68}$$

For an unperturbed system with $\varepsilon = 0$, these equations are analogous to those governing a bosonic Josephson junction and possess a rich dynamical structure that depends only on the dimensionless parameter

$$\Lambda = \frac{NU}{J}. \tag{1.69}$$

For $\Lambda \ll 1$, the tunneling term dominates and the system exhibits typical Josephson oscillations, characterized by a regular alternating flow of population between the two sites (see Fig. 1.7). In this regime, the relative phase remains confined around $\varphi \approx 0$, and the population oscillates symmetrically around $z = 0$, indicating a balanced sharing between the two wells. Conversely, when $\Lambda \gg 1$, the interactions become strong enough to qualitatively modify the topology of the phase space. The system can then enter the so-called macroscopic quantum self-trapping regime: the imbalance $z(t)$ remains of fixed sign over time, meaning that the particles remain essentially localized in one of the two wells despite the presence of tunnel coupling, as depicted in Figure 1.7(b)(c).

The mean-field dynamics indeed predict that in the self-trapping regime, the system will not move from its initial state if the imbalance z is strong. What the semiclassical approach cannot capture is that when two close states, for example $|N, 0\rangle$ and $|0, N\rangle$ are almost degenerate, nothing prevents the system from quantum tunneling between them. As a result, if the system is initially prepared in the state $|N, 0\rangle$, only collective tunneling can occur toward the state $|0, N\rangle$. The self-trapping regime ensures that sequential tunneling, particle-by-particle transfer, is forbidden. Thus, the phenomenon of collective tunneling can be partially understood in the sense that any individual particle tunneling is impossible due to the mismatch between the chemical potentials, whereas collective tunneling is allowed because of the near-degeneracy of the two states in which all particles occupy the same site. Figure 1.8(a) shows the population dynamics of a two-site Bose-Hubbard system described by the Hamiltonian (1.64), in the self-trapping regime for $N = 5$ particles and $U = 20J$, where the initial state is one in which all particles occupy the left well, namely $|5, 0\rangle$. In this figure, it is clearly visible that only the state $|0, 5\rangle$ appears during the evolution, providing direct evidence of a genuine collective tunneling effect: the bosons all cross the potential barrier together. In particular, halfway through the population inversion, the system is in a coherent superposition $|5, 0\rangle + |0, 5\rangle$, a 5-particle NOON state.

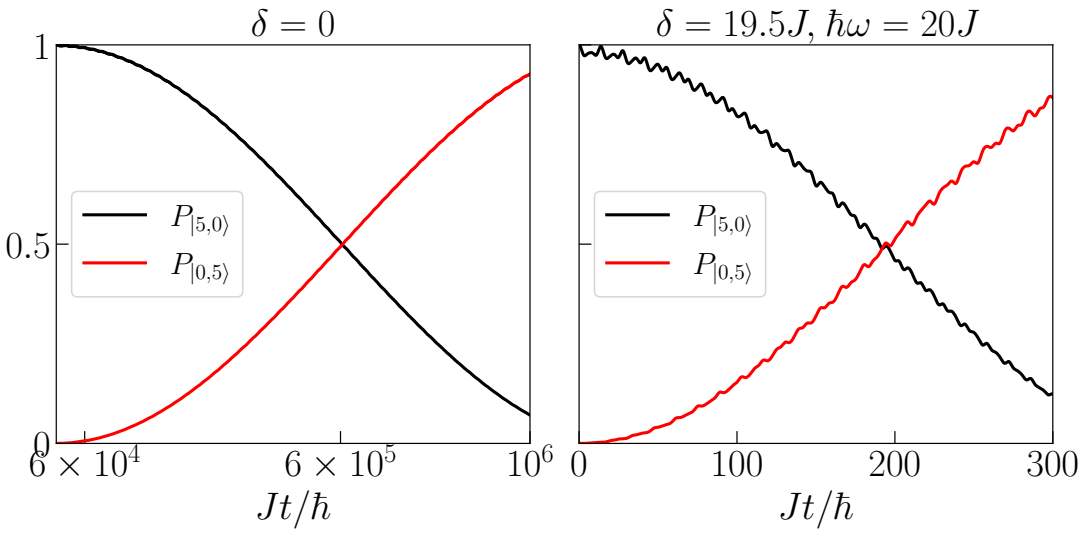

FIGURE 1.8: Time evolution of the populations $P_{|5,0\rangle}$ and $P_{|0,5\rangle}$ of a two-site Bose-Hubbard system with $N = 5$ bosons and strong interactions $U = 20J$. Left: undriven dynamics ($\delta = 0$), where single-particle tunneling is suppressed and the system evolves through slow collective tunneling, transferring all particles simultaneously between the two sites; a NOON superposition appears around $T \simeq 6 \times 10^5 \hbar/J$. Right: driven dynamics with periodic modulation of the tunneling ($\delta = 19.5J$, $\hbar\omega = 20J$), where chaos-assisted tunneling enables a dramatically faster transfer between the two macroscopically occupied states. The periodic drive couples the system to chaotic regions of phase space, strongly enhancing the collective tunneling rate compared with the undriven case.

1.5.2 NOON states via chaos-assisted tunneling

Although the self-trapping regime indeed allows Rabi oscillations between the states $|N, 0\rangle$ and $|0, N\rangle$, the characteristic time for this phenomenon to occur is extremely long. To understand this let us consider the unperturbed ($\varepsilon = 0$) Hamiltonian (1.64), in the case where tunneling is completely switched off, i.e. $J = 0$. The eigenstates are fully determined by the Fock basis, and their energies E_U result only from the interaction between bosons of the same site:

$$E_U = \frac{U}{2}\left(n_1(n_1 - 1) + n_2(n_2 - 1)\right), \tag{1.70}$$

where n_1 and n_2 are respectively the number of particles in the left and right well. In this regime, the eigenstates are exactly the Fock states and no tunneling can occur between the states $|N, 0\rangle$ and $|0, N\rangle$ which are perfectly degenerate. However, in the regime $J \neq 0$, the eigenstates are no longer exactly the Fock states. Tunneling between the states $|N, 0\rangle$ and $|0, N\rangle$ becomes allowed through perturbative corrections, but on a timescale inversely proportional to these small contributions. In particular, by numerically diagonalizing the Hamiltonian (1.64), one can identify the two highest eigenvalues and compute their difference to obtain the gap directly associated with the timescale of collective tunneling. Concretely, for parameters $N = 5$ and $U = 20J$, the time required for collective tunneling is on the order of $T \approx 10^6 \hbar/J$, which far exceeds the typical lifetime of a Bose-Einstein condensate, usually around $T \approx 2.5 \times 10^3 \hbar/J$.

To reduce the creation time, which is far too long to allow any realistic experimental implementation, it was proposed to use a periodic modulation of the two sites in order to increase the tunneling rate via the phenomenon of chaos-assisted tunneling [32, 35,

36]. Concretely, one considers a periodic tilting of the wells of the form

$$\varepsilon(t)(\hat{a}_1^\dagger \hat{a}_1 - \hat{a}_2^\dagger \hat{a}_2) = \delta \cos(\omega t)(\hat{a}_1^\dagger \hat{a}_1 - \hat{a}_2^\dagger \hat{a}_2), \tag{1.71}$$

which will induce chaotic dynamics in the system. In particular, by selecting appropriate values for the amplitude δ and the frequency ω of the perturbation, a chaotic sea will appear at the center of phase space creating a large number of accessible states that connect $|N, 0\rangle$ and $|0, N\rangle$. This will accelerates tunneling as can be seen in the population as a function of time depicted in Figure 1.8(b). In this context, the role of chaos-assisted tunneling is precisely to provide an efficient pathway between the two quasi-degenerate macroscopic configurations by exploiting the chaotic structure of phase space induced by the periodic driving. In the absence of modulation, the states $|N, 0\rangle$ and $|0, N\rangle$ are isolated at the top of two regular islands, widely separated by a forbidden region in phase space. Their direct coupling is then purely perturbative and decreases exponentially with the number of particles, which explains the extremely slow collective tunneling.

2

Geometric quantum control

In this section, we address the control of a quantum system by shaping the Hamiltonian that governs its time evolution. Within this framework, controlling the system consists in modifying the parameters entering the definition of the Hamiltonian in order to steer the system's state toward a target configuration, typically chosen according to experimental or informational goals. In particular, geometric quantum control relies on the idea that the state space of a quantum system possesses a rich mathematical structure that can be exploited to construct efficient trajectories between initial and final states. Rather than focusing exclusively on dynamical amplitudes or phases, this approach emphasizes the global properties of the projective state space, such as curvature, connections, or intrinsic geometric constraints. These considerations make it possible to identify not only the achievable paths in state space, but also the optimal strategies in terms of duration, robustness, or sensitivity to imperfections.

2.1 Adiabatic theorem

2.1.1 Time-dependent Hamiltonian

Let us consider a quantum system described by a Hamiltonian $H(t)$ that depends explicitly on time. A concrete example is the total spin of an atom subjected to an oscillating magnetic field, as in magnetic resonance imaging (MRI), where the interaction between the magnetic moment of the electron and the modulated external field enables control over the system's dynamics [88]. In the absence of time dependence, the system's energy is conserved and the dynamics are said to be conservative. In this setting, the time-independent Schrödinger equation is sufficient to determine the evolution of the state, which can be expressed as a linear combination of the eigenstates of the Hamiltonian. When H is time-dependent, the situation becomes more subtle. The eigenstates of the Hamiltonian no longer form a fixed stationary basis: they themselves evolve in time, leading to a continuous reorganization of the system's energy structure. The system's state can no longer be described as a simple accumulation of dynamical phases associated with constant energy levels, but is instead carried along by the evolution of the instantaneous eigenbasis [39–41, 76].

The time-dependent Schrödinger equation provides the fundamental tool for describing the evolution of a quantum state. It reflects how changes in $H(t)$ directly influence the temporal variation of the system's state vector $|\psi(t)\rangle$:

$$i\hbar\frac{d}{dt}|\psi(t)\rangle = H(t)|\psi(t)\rangle. \tag{2.1}$$

This equation thus governs the full dynamics and serves as the starting point for many approaches in quantum control, where the objective is to design control functions, that is, time dependencies of $H(t)$ that make it possible to implement targeted operations such as the creation of nonclassical states [100, 101].

The Hamiltonian $H(t)$ describing the system possesses a time-dependent eigenbasis $\{|n(t)\rangle\}$ associated with the instantaneous energies $E_n(t)$. The state of the system $|\psi(t)\rangle$ can always be expanded in the eigenbasis of $H(t)$:

$$|\psi(t)\rangle = \sum_n c_n(t)|n(t)\rangle. \tag{2.2}$$

Substituting this expression into the Schrödinger equation (2.1) yields

$$i\hbar\left(\sum_n \dot{c}_n(t)|n(t)\rangle + c_n(t)|\dot{n}(t)\rangle\right) = \sum_n c_n(t)E_n(t)|n(t)\rangle, \tag{2.3}$$

where the notation $\dot{c}_n \equiv dc_n/dt$ is used. By projecting the resulting equation onto an eigenstate $\langle k|$ of the Hamiltonian, we obtain

$$i\hbar\dot{c}_k(t) = \left(E_k(t) - i\hbar\langle k|\dot{k}\rangle\right)c_k(t) - i\hbar\sum_{n\neq k} c_n(t)\langle k|\dot{n}\rangle, \tag{2.4}$$

which describes the time evolution of the coefficient $c_k(t)$ associated with the state $|k\rangle$. For readability, we omit the explicit time dependence of the eigenstates.

Let us now focus on the last term, which accounts for a nonzero transition probability toward the state $|n\rangle$. By differentiating with respect to time the instantaneous eigenvalue equation of $H(t)$,

$$H(t)|n(t)\rangle = E_n(t)|n(t)\rangle, \tag{2.5}$$

and projecting onto the bra $\langle k| \neq \langle n|$, one easily finds

$$\begin{aligned} & H|\dot{n}\rangle + \dot{H}|n\rangle = \dot{E}_n|n\rangle + E_n|\dot{n}\rangle \\ \Leftrightarrow\ & \langle k|H|\dot{n}\rangle + \langle k|\dot{H}|n\rangle = \dot{E}_n\cancelto{0}{\langle k|n\rangle} + E_n\langle k|\dot{n}\rangle \\ \Rightarrow\ & \langle k|\dot{n}\rangle = \frac{\langle k|\dot{H}|n\rangle}{E_n - E_k}, \end{aligned} \tag{2.6}$$

where we have used the orthogonality of the eigenstates of $H(t)$. Substituting this expression into the previous equation, we obtain:

$$i\hbar\dot{c}_k(t) = \left(E_k(t) - i\hbar\langle k|\dot{k}\rangle\right)c_k(t) + i\hbar\sum_{n\neq k}\frac{\langle k|\dot{H}|n\rangle}{E_n(t) - E_k(t)}c_n(t). \tag{2.7}$$

The last term, proportional to $\langle k|\dot{H}|n\rangle$, is a coupling term between instantaneous energy levels. It accounts for the fact that a temporal variation of $H(t)$ may induce transitions between eigenstates, even in a perfectly isolated system [37]. This phenomenon will play a central role in the discussion of the adiabaticity criterion. For now, if the initial state of the system is an eigenstate of the Hamiltonian and the variation of $H(t)$ is sufficiently slow for the system to remain close to that state, this contribution may

be considered negligible. Under this temporary omission, the solution of the equation governing the time evolution of the coefficient c_k can be written as

$$c_k(t) = c_k(0) \exp\left(-\frac{i}{\hbar}\int_0^t E_k(t')dt'\right) \exp\left(-\int_0^t \langle k|\dot{k}\rangle dt'\right). \tag{2.8}$$

The first exponential factor corresponds to the well-known dynamical phase, $\phi_{dyn} \equiv -\frac{1}{\hbar}\int_0^t E_k(t')dt'$, which depends solely on the instantaneous energy of the state under consideration and on the time spent in that state. This contribution is "local" in the sense that it does not depend on the path followed by the system: only the instantaneous energy level matters. The second contribution, $\phi_{geo} \equiv -i\int_0^t \langle k|\dot{k}\rangle dt'$, appears instead because the eigenvectors of $H(t)$ evolve over time [102, 103]. Even if the system remains associated with the same energy level $E_n(t)$, the eigenvector representing it "moves" in the state space, leading to the accumulation of an additional phase whose value depends on the path taken, and not on the rate at which this path is traversed. This geometric phase is therefore entirely determined by the geometry of the motion in parameter space, rather than by the temporal dynamics as such. An important consequence is that this geometric phase can give rise to measurable physical signatures. A paradigmatic example is the Aharonov-Bohm effect, in which a particle acquires a phase depending on a potential even in a region where the physical field is zero [104–106]. More generally, this contribution highlights the intrinsic geometric structure of the eigenstate manifold of a quantum system.

The crucial point for what follows is the role of the term previously neglected: if this term is indeed small compared with the diagonal contributions (which in particular means that transitions between eigenstates remain strongly suppressed), then the quantum state evolves by following the eigenvector to which it was initially associated. The system remains "locked" to this level, accumulating only the dynamical and geometric phases described above. This phenomenon constitutes the essence of the **adiabatic theorem** [37, 103], according to which a quantum system prepared in a non-degenerate eigenstate of a slowly varying Hamiltonian will remain associated with that eigenstate over time, up to the accumulation of an overall phase.

The adiabatic theorem can be rigorously stated as follows:

> *A physical system remains in its instantaneous eigenstate if a given perturbation is acting on it slowly enough and if there is a gap between the eigenvalue and the rest of the Hamiltonian's spectrum.*

If a perturbation acts on a system *slowly*, that is, when the quantity $\langle k|\dot{H}|n\rangle$ remains very small compared with the energy difference $E_n - E_k$ between the two eigenstates $|n\rangle$ and $|k\rangle$, then the evolution of the eigenvectors of H takes place on a sufficiently long timescale for the state of the system to readjust continuously and remain associated with the same instantaneous eigenstate [107–109]. In other words, no significant transition toward other energy levels occurs, as long as the spectral separation remains sufficiently large to prevent any mixing between neighbouring states. Intuitively, this phenomenon is not in the least exotic. It is a familiar situation to anyone who has ever tried to carry an overfilled cup of coffee: to avoid spilling, one naturally walks more slowly. The motion of the walker plays the role of the

perturbation: when it is gentle, the surface of the coffee remains calm and the liquid stays in its "ground state", namely the bottom of the cup. If on the other hand one starts to accelerate abruptly, the perturbation becomes too strong and the coffee becomes "excited": it spills over. This is, in essence, the logic of the adiabatic theorem: when a system is subjected to a sufficiently slow evolution and its energy levels are well separated, it remains in the eigenstate in which it was initially prepared. In other words, no one spills coffee.

2.2 Counterdiabatic driving

The adiabatic theorem guarantees that a quantum system initially prepared in an eigenstate of a slowly varying Hamiltonian remains in that state throughout the evolution, provided that the change is sufficiently gradual so as not to induce transitions between energy levels. However, its practical applicability is severely limited by the intrinsically long times required to suppress unwanted transitions when the spectral gap becomes small. In experimental situations, where dissipation, noise, and instabilities constrain the coherence time, such ideal adiabatic evolutions often become unfeasible.

To overcome these limitations, several strategies collectively referred to as Shortcuts to Adiabaticity (STA) have been developed [42, 110–115]. Their goal is to perfectly reproduce the outcome of an adiabatic evolution, but in an arbitrarily short time, by adding an appropriate control term to the original Hamiltonian. Among these methods, Counterdiabatic Driving (CD) plays a central role [43, 116, 117]. Initially introduced by Demirplak and Rice and later generalized by Berry, this approach relies on the simple yet profound idea that one can exactly cancel nonadiabatic transitions by adding an extra term to the Hamiltonian, constructed so as to force the system to follow its instantaneous eigenstates regardless of the rate at which the control parameter evolves.

The fundamental idea is the following: for a Hamiltonian that depends explicitly on time through an external parameter $\lambda(t)$, diabatic transitions arise from the fact that the instantaneous eigenbasis changes over time. The natural question is therefore: can one analytically identify the term responsible for these transitions, and eliminate it? The answer is yes, and it leads to the geometric formalism underlying the theory of counterdiabatic driving. Indeed, when the evolution is expressed in the frame that instantaneously diagonalizes the Hamiltonian, an additional term (analogous to an inertial force in classical mechanics, see Fig. 2.1) appears in the Schrödinger equation. This term contains complete information about the rate of change of the parameter and about the geometry of the eigenstates as a function of λ. It is entirely responsible for nonadiabatic transitions. This inertial term is proportional to a central operator in the theory: the Adiabatic Gauge Potential (AGP), a geometric object that quantifies the sensitivity of the eigenbasis to variations of λ [118, 119].

The goal of the next section is precisely to define this operator rigorously, to explain its role in time-dependent quantum dynamics, and to show how it leads to the systematic construction of the counterdiabatic Hamiltonian.

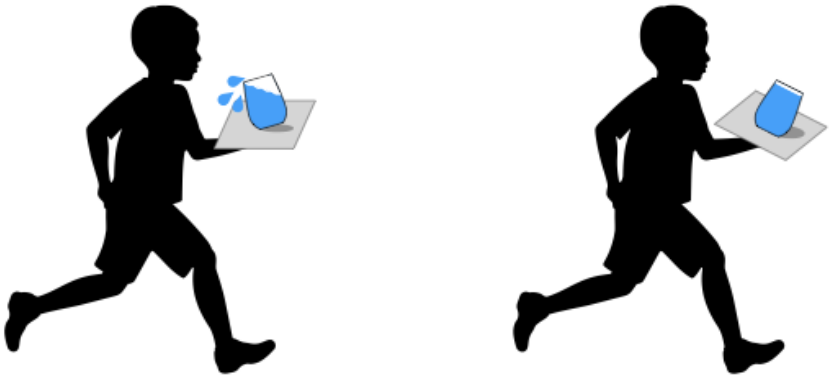

FIGURE 2.1: Illustration of counterdiabatic driving. When the tray is moved rapidly (left), the water begins to slosh and overflow: the system is driven out of its instantaneous ground state. By adding a compensating motion (right), the water remains perfectly still in its glass despite the speed: this is the analogue of counterdiabatic driving, where an additional term is applied to the dynamics to prevent any transition and keep the system in its instantaneous eigenstate.

2.2.1 Adiabatic Gauge Potential

Let us start again from the Schrödinger equation to derive, in full generality, the term responsible for unwanted transitions [120]. In particular, we assume that the time dependence of the system enters through a parameter $\lambda(t)$. Using chain rule, the state of the system $|\psi(\lambda)\rangle$ then evolves according to

$$i\hbar\dot{\lambda}\partial_\lambda|\psi(\lambda)\rangle = H(\lambda)|\psi(\lambda)\rangle. \tag{2.9}$$

We decompose the system's state in the eigenbasis of the Hamiltonian. Denoting by $U(\lambda)$ the unitary operator such that

$$\tilde{H}(\lambda) = U^\dagger(\lambda)H(\lambda)U(\lambda), \tag{2.10}$$

is purely diagonal, we can rewrite $|\psi(\lambda)\rangle = U(\lambda)|\tilde{\psi}(\lambda)\rangle$. We then obtain

$$\begin{aligned} i\hbar\dot{\lambda}\partial_\lambda\big[U(\lambda)|\tilde{\psi}(\lambda)\rangle\big] &= H(\lambda)U(\lambda)|\tilde{\psi}(\lambda)\rangle \\ \Leftrightarrow i\hbar\dot{\lambda}\partial_\lambda|\tilde{\psi}(\lambda)\rangle &= \big[U^\dagger(\lambda)H(\lambda)U(\lambda) - i\hbar\dot{\lambda}U^\dagger\partial_\lambda U(\lambda)\big]|\tilde{\psi}(\lambda)\rangle. \end{aligned} \tag{2.11}$$

The new Hamiltonian appearing in the Schrödinger equation in the co-moving frame is then given by

$$\tilde{H}(\lambda) - i\hbar\dot{\lambda}U^\dagger(\lambda)\partial_\lambda U(\lambda), \tag{2.12}$$

where, by definition, $\tilde{H}(\lambda)$ is diagonal. Thus, any off-diagonal element coupling the initial state of the system to another must be contained in the term

$$\tilde{\mathcal{A}}_\lambda \equiv i\hbar U^\dagger(\lambda)\partial_\lambda U(\lambda) \tag{2.13}$$

Going back to the lab frame, we define the Adiabatic Gauge Potential (AGP) as

$$\mathcal{A}_\lambda \equiv i\hbar\partial_\lambda U(\lambda)U^\dagger(\lambda). \tag{2.14}$$

The AGP is a connection that measures how the eigenbasis of H changes under variations of λ. By describing the geometry of the eigenstates in parameter space, this connection quantifies the quantum inertia of the system when the Hamiltonian is

changed. The AGP is a Hermitian operator[1] which can be defined in terms of its matrix elements. Let us consider an arbitrary λ-independent basis of Hilbert-space vectors $|k\rangle$. This basis can be rewritten in the eigenbasis $|m(\lambda)\rangle$ of $H(\lambda)$ as $|m(\lambda)\rangle = U(\lambda)|k\rangle$. We now expand the AGP in the eigenbasis:

$$\begin{aligned}\langle m(\lambda)|\mathcal{A}_\lambda|n(\lambda)\rangle &= \langle m(\lambda)|i\hbar\partial_\lambda U(\lambda)U^\dagger(\lambda)|n(\lambda)\rangle \\ &= \langle k|U^\dagger(\lambda)(i\hbar\partial_\lambda U(\lambda)U^\dagger(\lambda))U(\lambda)|k'\rangle \\ &= \langle k|i\hbar U^\dagger(\lambda)\partial_\lambda U(\lambda)|k'\rangle. \end{aligned} \tag{2.15}$$

Now, since $|n(\lambda)\rangle = U(\lambda)|k\rangle \Leftrightarrow \partial_\lambda|n(\lambda)\rangle = \partial_\lambda U(\lambda)|k\rangle$, the right-hand side of Eq. (2.15) can be rewritten as $-i\hbar\langle m(\lambda)|\partial_\lambda|n(\lambda)\rangle$. Finally, we obtain

$$\langle m(\lambda)|\mathcal{A}_\lambda|n(\lambda)\rangle = i\hbar\langle m(\lambda)|\partial_\lambda|n(\lambda)\rangle. \tag{2.16}$$

In the instantaneous eigenbasis, the matrix elements of $\mathcal{A}_\lambda$ and of the operator $i\hbar\partial_\lambda$ are equivalent. Indeed, in this basis the AGP acts as a derivation on operators in the same way as a connection, in perfect analogy with the connections that appear in general relativity or in quantum field theory, where they introduce the notion of parallel transport. The Christoffel symbols $\Gamma^\nu_{\mu\alpha}$ define the covariant derivative of a four-vector v^ν as $D_\mu v^\nu = \partial_\mu v^\nu + \Gamma^\nu_{\mu\alpha}v^\alpha$, which "corrects" the path by taking into account the curvature of spacetime. In quantum electrodynamics, the covariant derivative of an electron evolving in an electromagnetic field is defined as $D_\mu \equiv \partial_\mu - ieA_\mu$, where A_μ is the four-potential and e the electron charge. From these examples, one understands that the role of a connection is to correct a trajectory in parameter space (spacetime in general relativity), which is modified by the action of an external field (the gravitational field inducing a curvature field).

Here, the connection $\mathcal{A}_\lambda$ corrects the moving eigenbasis of the Hamiltonian. Returning to Eq. (2.16), which gives the matrix elements of the AGP in the instantaneous eigenbasis of the Hamiltonian, we have

$$(\mathcal{A}_\lambda - i\hbar\partial_\lambda)|n(\lambda)\rangle = 0. \tag{2.17}$$

In other words, by defining the covariant derivative $D_\lambda \equiv \partial_\lambda + i\mathcal{A}_\lambda/\hbar$, one can understand the fundamental geometric role of the AGP:

$$D_\lambda|n(\lambda)\rangle = 0. \tag{2.18}$$

This very strong equation tells us that the AGP makes it possible to define the parallel transport of the Hamiltonian's instantaneous eigenvectors. In other words, the connection $\mathcal{A}_\lambda$ contains the information about the curvature of the geometry arising from the variation of the Hamiltonian with respect to the parameter λ. In the co-moving frame, the Schrödinger equation then takes the form

$$i\hbar D_\lambda|\tilde{\psi}(\lambda)\rangle = \tilde{H}(\lambda)|\tilde{\psi}(\lambda)\rangle, \tag{2.19}$$

where $\tilde{H}$ is purely diagonal. By reintroducing the explicit time dependence through the chain rule, $\partial_t = \dot{\lambda}\partial_\lambda$, the Schrödinger equation in the co-moving frame becomes:

$$i\hbar\,\partial_t|\tilde{\psi}(t)\rangle = [\tilde{H}(\lambda(t)) - \dot{\lambda}(t)\tilde{\mathcal{A}}_\lambda]|\tilde{\psi}(t)\rangle. \tag{2.20}$$

[1] $(\mathcal{A}_\lambda)^\dagger = (i\hbar(\partial_\lambda U)U^\dagger)^\dagger = (-i\hbar U\partial_\lambda U^\dagger) = (i\hbar\partial_\lambda UU^\dagger) = \mathcal{A}_\lambda$, where we have used the unitarity of U: $\partial_\lambda(1) = 0 = \partial_\lambda(UU^\dagger) = \partial_\lambda UU^\dagger + U\partial_\lambda U^\dagger$.

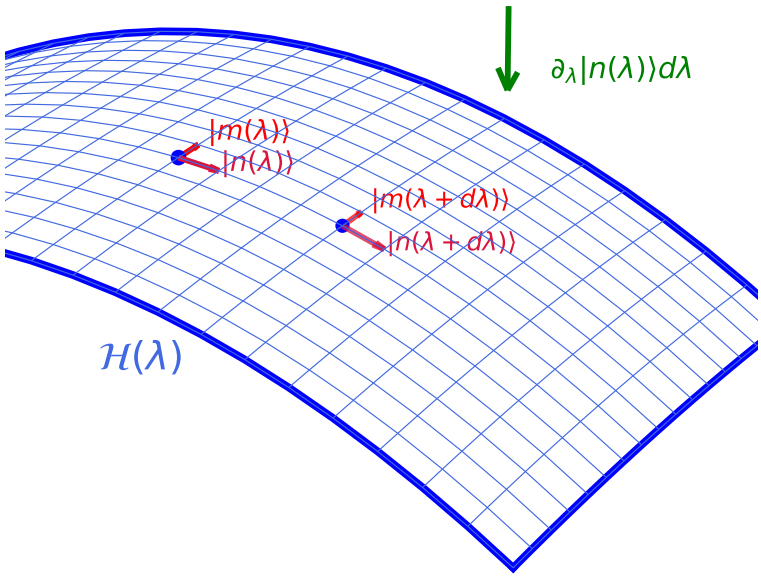

FIGURE 2.2: Geometric representation of the instantaneous eigenbasis. The blue surface represents the manifold $\mathcal{H}(\lambda)$ of Hamiltonians $H(\lambda)$. At each point, a local basis $\{|n(\lambda)\rangle, |m(\lambda)\rangle\}$ is defined (red arrows). After an infinitesimal change of the parameter to $\lambda + d\lambda$, the transported basis $\{|n(\lambda+d\lambda)\rangle, |m(\lambda+d\lambda)\rangle\}$ is located at a different point of the manifold. The green arrow indicates the infinitesimal variation of the eigenstate $|n(\lambda)\rangle$. Parallel transport is implemented thanks to the corrective term $\mathcal{A}_\lambda|n(\lambda)\rangle$, which encapsulates the variation of the eigenstate.

The term $-\dot{\lambda}\tilde{\mathcal{A}}_\lambda$ is immediately identified as the sole source of diabatic transitions. It plays exactly the role of an inertial term: it arises solely from the fact that the eigenstate basis itself depends on the parameter λ. In the strictly adiabatic regime, where $\dot{\lambda} \to 0$, this term naturally disappears, so that the system remains in an instantaneous eigenstate of $H(\lambda)$. However, as soon as one attempts to speed up this evolution, this inertial term becomes non-negligible and induces transitions out of the targeted eigenstate.

The core idea of Shortcuts to Adiabaticity is to cancel this term exactly by adding to the original Hamiltonian an artificial term that compensates for its effect [42]. One thus defines the counterdiabatic (CD) Hamiltonian:

$$H_{\mathrm{CD}} = \dot{\lambda}\mathcal{A}_\lambda \tag{2.21}$$

in such a way that the Hamiltonian $H + H_{\mathrm{CD}}$ produces a perfectly adiabatic evolution in finite time: the term $\dot{\lambda}\tilde{\mathcal{A}}_\lambda$ cancels the inertial term $-\dot{\lambda}\tilde{\mathcal{A}}_\lambda$ in the co-moving frame. Thus, in the instantaneous eigenbasis, the system's evolution becomes strictly diagonal, even for rapid variations of the control parameter. This is a remarkable result: it is possible to reproduce exactly the adiabatic dynamics without ever satisfying the standard adiabatic condition.

2.2.2 Counterdiabatic terms

The geometric form of the AGP, obtained previously through equation (2.16), is conceptually powerful: it clearly identifies the geometric origin of diabatic transitions and justifies the introduction of a control Hamiltonian of the form $H_{\mathrm{CD}} = \dot{\lambda}\mathcal{A}_\lambda$. However, this expression is not yet directly usable in practice. To obtain an operational formula, it is necessary to express the derivative $\partial_\lambda|n(\lambda)\rangle$ in terms of more accessible quantities such as derivatives of the Hamiltonian and energy gaps between levels. We start from the eigenvalue equation

$$H(\lambda)|n(\lambda)\rangle = E_n(\lambda)|n(\lambda)\rangle. \tag{2.22}$$

By differentiating this relation with respect to λ, one obtains

$$\partial_\lambda H|n(\lambda)\rangle + H(\lambda)\partial_\lambda|n(\lambda)\rangle = \partial_\lambda E_n|n(\lambda)\rangle + E_n(\lambda)\partial_\lambda|n(\lambda)\rangle. \tag{2.23}$$

Projecting this equation onto $\langle m(\lambda)|$ with $m \neq n$ leads to

$$\langle m(\lambda)|\partial_\lambda n(\lambda)\rangle = \frac{\langle m(\lambda)|\partial_\lambda H(\lambda)|n(\lambda)\rangle}{E_n(\lambda) - E_m(\lambda)}. \tag{2.24}$$

By inserting this expression into the definition of the AGP (Eq. (2.16)), one then obtains the off-diagonal elements of $\mathcal{A}_\lambda$ in the form

$$\langle m(\lambda)|\mathcal{A}_\lambda|n(\lambda)\rangle = i\hbar\frac{\langle m(\lambda)|\partial_\lambda H(\lambda)|n(\lambda)\rangle}{E_n(\lambda) - E_m(\lambda)}, \tag{2.25}$$

still for $m \neq n$. Reintroducing the implicit time dependence and using the definition of H_{CD}, one finally obtains the general expression of the counterdiabatic term in the eigenbasis of the Hamiltonian:

$$H_{\mathrm{CD}}(t) = i\hbar \sum_{n,m\neq n} \frac{\langle m(t)|\dot{H}(t)|n(t)\rangle}{E_n(t) - E_m(t)}|m(t)\rangle\langle n(t)|. \tag{2.26}$$

This is the exact expression of the counterdiabatic Hamiltonian, unmistakably similar to the term initially neglected in equation (2.7). When added to the original Hamiltonian, it guarantees the complete cancellation of transitions out of the instantaneous eigenbasis, thereby ensuring a perfectly adiabatic evolution regardless of the rate at which the parameter $\lambda(t)$ varies.

The expression above highlights several essential aspects of the counterdiabatic term. First, the presence of the time derivative $\dot{H}$ in the numerator shows that the term H_{CD} depends only on the components of the Hamiltonian that evolve in time: if H does not change, then $\dot{H} = 0$ and no control is required. The numerator therefore selects only the part of the dynamics that is capable of inducing diabatic transitions. The denominator $E_n(t) - E_m(t)$ plays a fundamental role: it strongly enhances the counterdiabatic term when two energy levels approach each other. In other words, the smaller the gap becomes, the larger the inertia, and the more likely the system is to leave its instantaneous eigenstate. This structure captures the physics of the phenomenon perfectly: it is precisely in the regions where the spectrum exhibits quasi-degeneracies that the strongest control is needed to prevent diabatic transitions [38–41].

2.2.3 Approximating CD terms: Floquet engineering

The exact expression (2.26) of the counterdiabatic term in principle provides the universal solution to cancel all diabatic transitions. However, this form becomes unusable as soon as one moves away from very low-dimensional systems. Indeed, computing H_{CD} requires explicit knowledge of the instantaneous eigenbasis of H, that is, the full diagonalization of the Hamiltonian at every instant. For many-body quantum systems, this operation quickly becomes prohibitive: the spectrum is too complex, and even its local structure may be extremely complex. To bypass these limitations, several strategies have been developed to approximate, rather than exactly compute, the adiabatic gauge potential $\mathcal{A}_\lambda$ [44–46, 121, 122]. The goal is to obtain approximate counterdiabatic terms that are sufficiently accurate to suppress most unwanted transitions, while remaining both computable and experimentally feasible. In this thesis, we will use two approaches in particular: a variational expansion of the gauge potential, and effective protocols based on Floquet engineering.

A first general approximation scheme was introduced in Ref. [45]. It is based on the idea that the adiabatic gauge potential can be expanded as a series of nested commutators of the form

$$\mathcal{A}_\lambda^{(l)} = i \sum_{k=1}^{l} \alpha_k \, [\underbrace{H, [H, ..., [H}_{2k-1}, \partial_\lambda H]]], \tag{2.27}$$

where l denotes the order of the expansion. The coefficients α_k are determined through a variational principle, obtained by minimizing the action [118]:

$$S_l = \mathrm{Tr}[G_l^2] \qquad\qquad G_l = \partial_\lambda H - i[H, \mathcal{A}_\lambda^{(l)}], \tag{2.28}$$

so that the condition $\delta S = 0$ guarantees that the constructed operator $\mathcal{A}_\lambda^{(l)}$ provides the best possible approximation to the true AGP. In the instantaneous eigenbasis of H, the elements of $\mathcal{A}_\lambda^{(l)}$ have the form

$$\langle m|\mathcal{A}_\lambda^{(l)}|n\rangle = i \sum_{k=1}^{l} \alpha_k \langle m|[H, [H, \dots, [H, \partial_\lambda H]]|n\rangle \tag{2.29}$$

$$= i \sum_{k=1}^{l} \alpha_k (E_m - E_n)^{2k-1} \langle m|\partial_\lambda H|n\rangle. \tag{2.30}$$

In the particularly simple case where the system has only a single excitation frequency (typically a two-level system), this expansion becomes exact at first order:

$$\langle m|\mathcal{A}_\lambda^{(1)}|n\rangle = i \frac{\langle m|\partial_\lambda H|n\rangle}{E_n - E_m}. \tag{2.31}$$

One thus recovers the exact expression of the counterdiabatic term simply by multiplying by $\dot{\lambda}(t)$.

This approach also reveals a crucial property of counterdiabatic Hamiltonians. Let us consider for example

$$H(t) = \epsilon(t)\sigma_z + J(t)\sigma_x \tag{2.32}$$

where σ_z and σ_x are the Pauli matrices. First order expansion leads to

$$\mathcal{A}_\epsilon^{(1)} = i\alpha_1[H, \partial_\epsilon H] = -2\alpha_1 J\sigma_y \tag{2.33}$$

$$\mathcal{A}_J^{(1)} = i\alpha_1'[H, \partial_J H] = 2\alpha_1'\epsilon\,\sigma_y. \tag{2.34}$$

In both cases, the AGP is proportional to σ_y, a spin direction that is absent from the original Hamiltonian. This illustrates a common difficulty: the exact counterdiabatic term may require operators that do not belong to the set of experimentally accessible controls. This is precisely where Floquet engineering becomes relevant [44–46, 123]. By rapidly modulating the accessible parameters, it becomes possible to generate, in an effective manner, control terms that do not exist in the static Hamiltonian. In other words, periodic drives make it possible to emulate the missing components of the gauge potential, thereby enabling the practical implementation of STA protocols even in systems where the available control directions are, a priori, insufficient.

Let us now consider a Hamiltonian enriched by the addition of oscillating terms, designed to generate, via Floquet engineering, the desired counterdiabatic contributions. To this end, we introduce an oscillating Hamiltonian :

$$H_{\mathrm{FE}}(t) = \Big[1 + \frac{\omega}{\omega_0}\cos(\omega t)\Big]H(\lambda) + \dot{\lambda}\Big[\sum_{k=1}^{\infty}\beta_k\,\sin\big((2k-1)\omega t\big)\Big]\partial_\lambda H(\lambda), \tag{2.35}$$

where the first term introduces a rapid modulation of the static Hamiltonian with the driving frequency ω and a reference frequency ω_0 linked to the energy scale of the system [45], while the second modulates the direction $\partial_\lambda H$ using odd harmonics [45]. According to Floquet theory, there then exists an effective time-independent Hamiltonian H_F that exactly reproduces the evolution generated by $H_{\mathrm{FE}}(t)$ at stroboscopic times [124, 125]. It is implicitly defined by

$$e^{-iH_F T} \;\equiv\; \mathcal{T}\exp\left[-i\int_t^{t+T} H_{\mathrm{FE}}(t')\,dt'\right], \tag{2.36}$$

where $T = 2\pi/\omega$ is the period of the drive, and $\mathcal{T}$ the time ordering operator which enforces time ordering in the exponential, ensuring a well-defined evolution operator when the Hamiltonian varies in time and does not commute with itself at different instants. In the infinite-frequency limit $\omega \to \infty$, the Floquet-Magnus expansion shows that the effective Hamiltonian takes the form

$$H_F \approx H + i\dot{\lambda}\alpha_1[H, \partial_\lambda H] + i\dot{\lambda}\alpha_2[H, [H, [H, \partial_\lambda H]]] + \cdots. \tag{2.37}$$

The coefficients α_k depend explicitly on the drive parameters, and in particular on the amplitudes β_k. By adjusting these coefficients, it is therefore possible to ensure that the effective Hamiltonian H_F reproduces (at least to the first orders of the Floquet-Magnus expansion) the contributions of the variational series of the adiabatic gauge potential. In other words, the appropriate choice of the amplitudes β_k allows the oscillating terms to emulate the essential components of the counterdiabatic Hamiltonian, thus providing an experimental method to implement STA protocols stroboscopically even when the required operators are not directly accessible.

2.3 Geodesic control

Up to this point, we have focused on simply compensating the inertial terms in order to drive our system at the desired speed. This strategy, which corresponds to the so-called counterdiabatic driving approach, in principle allows one to follow exactly the instantaneous adiabatic state, but at the price of introducing additional terms into the Hamiltonian. These control terms, often fast and highly nontrivial, are in many cases difficult to implement experimentally: they may depend explicitly on time, require access to operators that are not available in the setup, or demand coupling regimes that are incompatible with technological limitations. It is therefore natural to ask whether there exists a way to steer a quantum system without cancelling the inertial terms exactly, but instead making them sufficiently small so that the conditions of the adiabatic theorem are respected as closely as possible. Rather than forcing the system to rigidly follow a single eigenstate, the idea is to determine the optimal way of varying the control parameters so that the evolution remains, at every instant, as adiabatic as possible.

This approach relies on a simple intuition: in the parameter space of the Hamiltonian, certain motions strongly affect the eigenstate of the system, while others modify it only weakly. It follows that not all trajectories connecting two points in state space are equivalent from the viewpoint of adiabatic dynamics. To reduce excitations to higher states, one must choose the trajectory that “deforms" the state as little as possible, or, more rigorously, the one that minimizes the infinitesimal change of the state in Hilbert space. To make this idea precise, we introduce the language of Riemannian geometry applied to quantum state space. Each parametrization of the Hamiltonian defines an immersion of the parameter space into the projective space of states [47]. The latter is endowed with a Riemannian geometry defining a metric, which provides a measure of infinitesimal distance between neighboring states and which quantifies the sensitivity of the eigenstates to variations of the parameters [119, 126].

The goal of this section is to show how this geometric structure allows one to define a geodesic driving. This consists in choosing a trajectory in parameter space such that, at every instant, the quantity measuring nonadiabatic excitation is minimized [48, 127]. In other words, we aim for the regime where the adiabatic theorem is “saturated": excitations do not vanish completely (as in ideal counterdiabatic driving), but they are reduced to the strict minimum allowed by the geometry of the system. This purely geometric approach to adiabatic dynamics turns out to be particularly powerful: it requires no additionnal controls of the Hamiltonian, it relies on geometric objects (metric, curvature), and it provides intrinsic optimal trajectories. In what follows, we will introduce the Riemannian geometry of parameter space, the quantum geometric tensor and the notion of geodesic, and we will show how these ingredients naturally lead to an optimal adiabatic control strategy.

2.3.1 Riemannian geometry

Suppose a very general case where a Hamiltonian $H(\lambda)$ depends on a set of parameters $\lambda = (\lambda^1, \lambda^2, \ldots)$. Following the conventions of differential geometry, we denote the components of the vector $(\lambda^1, \lambda^2, \ldots)$ using a Greek index $\mu \in 1, 2, \ldots$, that is, λ^μ. This set of parameters represents coordinates in parameter space, which associates to each λ a vector $|\psi(\lambda)\rangle$. We wish to define the notion of distance between two infinitesimally close states $|\psi(\lambda)\rangle$ and $|\psi(\lambda + d\lambda)\rangle$ in this space.

First, we expand $|\psi(\lambda+d\lambda)\rangle$ to second order around each infinitesimal displacement $d\lambda^\mu$:

$$|\psi(\lambda+d\lambda)\rangle = |\psi(\lambda)\rangle + |\partial_\mu\psi(\lambda)\rangle d\lambda^\mu + \frac{1}{2}|\partial_\mu\partial_\nu\psi(\lambda)\rangle d\lambda^\mu d\lambda^\nu + \mathcal{O}(d\lambda^\mu d\lambda^\nu d\lambda^\sigma), \quad (2.38)$$

where we have used the notation $\partial_\mu \equiv \partial/\partial\lambda^\mu$ and the implicit Einstein summation convention:

$$|\partial_\mu\psi(\lambda)\rangle\, d\lambda^\mu \equiv \sum_{\mu=1}^{D} \partial_\mu|\psi(\lambda)\rangle d\lambda^\mu = \frac{\partial|\psi(\lambda)\rangle}{\partial\lambda^1}\, d\lambda^1 + \frac{\partial|\psi(\lambda)\rangle}{\partial\lambda^2} d\lambda^2 + \dots, \quad (2.39)$$

where, whenever a Greek index appears once in a lower position and once in an upper position, one must sum over it. Let us now expand the scalar product between two infinitesimally close states

$$\begin{aligned}\langle\psi(\lambda)|\psi(\lambda+d\lambda)\rangle &= 1 + \langle\psi(\lambda)|\partial_\mu\psi(\lambda)\rangle d\lambda^\mu + \frac{1}{2}\langle\psi(\lambda)|\partial_\mu\partial_\nu\psi(\lambda)\rangle d\lambda^\mu d\lambda^\nu + \mathcal{O}(d\lambda^3) \\ &\equiv 1 + A_\mu d\lambda^\mu + B_{\mu\nu} d\lambda^\mu d\lambda^\nu + \mathcal{O}(d\lambda^3) \end{aligned} \quad (2.40)$$

where we defined $A_\mu = \langle\psi(\lambda)|\partial_\mu\psi(\lambda)\rangle$ and $B_{\mu\nu} = \langle\psi(\lambda)|\partial_\mu\partial_\nu\psi(\lambda)\rangle/2$. At the second order, the overlap is given by

$$\begin{aligned}|\langle\psi(\lambda)|\psi(\lambda+d\lambda)\rangle|^2 &= (1 + A_\mu d\lambda^\mu + B_{\mu\nu} d\lambda^\mu d\lambda^\nu)(1 + A^*_\mu d\lambda^\mu + B^*_{\mu\nu} d\lambda^\mu d\lambda^\nu) \\ &= 1 + (A_\mu + A^*_\mu)\, d\lambda^\mu + (B_{\mu\nu} + B^*_{\mu\nu} + A_\mu A^*_\nu)\, d\lambda^\mu d\lambda^\nu \end{aligned} \quad (2.41)$$

Now, the quantity $A_\sigma = \langle\psi|\partial_\sigma\psi\rangle$ is purely imaginary[2] [128]. Thus, no linear term in $d\lambda^\mu$ can occur, since the overlap $|\langle\psi(\lambda)|\psi(\lambda+d\lambda)\rangle|^2$ is real. Since $\partial_\mu\partial_\nu(\langle\psi|\psi\rangle) = 0$, the second order terms can be written as

$$B_{\mu\nu} + B^*_{\mu\nu} = -\mathrm{Re}\{\langle\partial_\mu\psi|\partial_\nu\psi\rangle\} \quad (2.42)$$

We therefore have the following quantity as a measure of distance:

$$ds^2 = 1 - |\langle\psi(\lambda)|\psi(\lambda+d\lambda)\rangle|^2 \quad (2.43)$$

$$= \mathrm{Re}\{\langle\partial_\mu\psi(\lambda)|\partial_\nu\psi(\lambda)\rangle - \langle\psi(\lambda)|\partial_\mu\psi(\lambda)\rangle\langle\partial_\nu\psi(\lambda)|\psi(\lambda)\rangle\}\, d\lambda^\mu d\lambda^\nu. \quad (2.44)$$

The distance ds^2, that plays the role of the interval in general relativity [129], is equal to 1 if the two infinitesimally close states have no overlap, and equal to 0 if they are identical. It therefore indeed provides a measure of the proximity between two states. From this, one can define the gauge-invariant tensor $Q_{\mu\nu}$, known as the Quantum Geometric Tensor [47]

$$Q_{\mu\nu} = \langle\partial_\mu\psi|\partial_\nu\psi\rangle - \langle\partial_\mu\psi|\psi\rangle\langle\psi|\partial_\nu\psi\rangle. \quad (2.45)$$

This tensor is deeply fundamental in that it characterizes the geometry of the state space. It is Hermitian and complex, and can therefore be decomposed into a real and an imaginary part:

$$Q_{\mu\nu} = g_{\mu\nu} + \frac{i}{2}F_{\mu\nu}. \quad (2.46)$$

[2] Proof: since $|\psi\rangle$ is normalized by assumption, $\partial_\sigma(\langle\psi|\psi\rangle) = 0 \Leftrightarrow \langle\partial_\sigma\psi|\psi\rangle = -\langle\psi|\partial_\sigma\psi\rangle = -(\langle\partial_\sigma\psi|\psi\rangle)^*$. The complex number $\langle\partial_\sigma\psi|\psi\rangle$ being equal to the opposite of its complex conjugate, it therefore can only be purely imaginary.

The tensor $F_{\mu\nu}$ is called the Berry curvature and encodes the entire topology of the system. It is important to note that this tensor is related to the adiabatic gauge potential in the case where $|\psi\rangle$ is an eigenstate of H. By defining the Berry connection $A_\mu = \langle\psi|\partial_\mu\psi\rangle$, one has

$$F_{\mu\nu} = \partial_\mu A_\nu - \partial_\nu A_\mu. \tag{2.47}$$

This equation recalls the relation between the electromagnetic field tensor and the vector potential. Indeed, in classical electromagnetism, the electromagnetic field is defined as the antisymmetric derivative of the vector potential A_μ in exactly the same way. The formal parallel between the two expressions is not a coincidence: Berry geometry is literally an abelian $U(1)$ gauge theory, defined not on spacetime but in the parameter space of the Hamiltonian. The Berry connection A_μ therefore plays the role of a gauge potential, and the curvature $F_{\mu\nu}$ is its associated field. This geometric perspective is particularly illuminating: when the state $|\psi(\lambda)\rangle$ is slowly transported along a closed path in parameter space, the accumulated phase is nothing other than the integral of the Berry connection [102],

$$\gamma = \oint A_\mu \, d\lambda^\mu, \tag{2.48}$$

which, by Stokes' theorem, can be rewritten as the flux of the curvature tensor through a surface Σ bounded by this path. Thus, the Berry geometric phase is directly interpreted as a curvature flux, just like magnetic flux in electromagnetism. This analogy extends even further: if the parameter space has a nontrivial structure (for example, a compact surface such as the Bloch sphere), the integral of the curvature over the entire manifold yields a discrete topological invariant, the Chern number, which plays a central role in condensed-matter physics [124, 130–132].

The tensor $g_{\mu\nu}$, called the metric tensor or Fubini-Study metric, is the distance measure we were looking for:

$$ds^2 = g_{\mu\nu} d\lambda^\mu d\lambda^\nu. \tag{2.49}$$

This object encodes the entire Riemannian geometry induced on the manifold of quantum states by the immersion $\lambda \mapsto |\psi(\lambda)\rangle$. It is a genuine metric in the mathematical sense: it is symmetric, positive definite, and, crucially, gauge invariant. It therefore endows the parameter space with a rich differential structure, allowing one to define notions such as the length of a trajectory, geodesics, and an associated Levi-Civita connection [129].

A particularly convenient form of the tensor $g_{\mu\nu}$ can be obtained. By rewriting the quantum geometric tensor in terms of the eigenstates of the Hamiltonian, using

$$\langle n|\partial_\mu m\rangle = \frac{\langle n|\partial_\mu H|m\rangle}{E_m - E_n} \tag{2.50}$$

one can show that

$$g_{\mu\nu} = \mathrm{Re} \sum_{m\neq n} \frac{\langle n|\partial_\mu H|m\rangle\langle m|\partial_\nu H|n\rangle}{(E_m - E_n)^2}. \tag{2.51}$$

This expression is simpler to compute but requires knowledge of the full spectrum of the Hamiltonian.

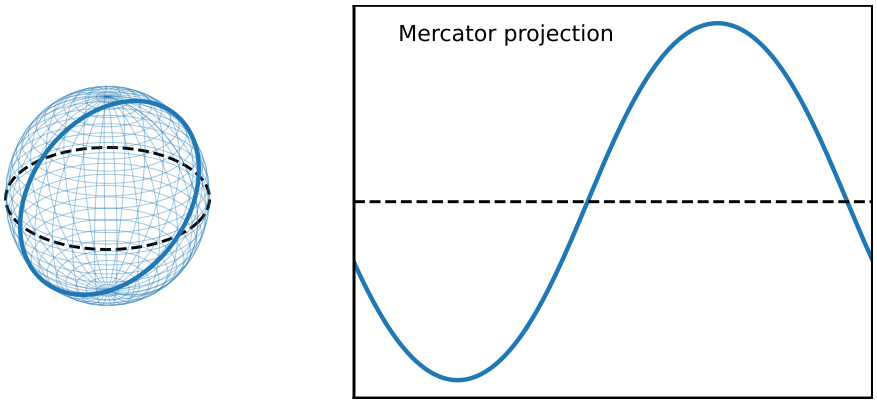

FIGURE 2.3: Illustration of the concept of a geodesic. On a curved surface such as the sphere (left), the notion of a straight line is replaced by that of a geodesic. The equator (dotted line) is a geodesic, as is the blue trajectory. When these same curves are projected onto a flat map using the Mercator projection (right), the blue trajectory appears as a sinusoidal curve, whereas the equator remains a straight line. This comparison illustrates that the shape of a straight line depends intrinsically on the underlying geometry: what is geodesic in a curved manifold is not necessarily so in its flat representation.

2.3.2 Geodesics

Geodesics are the curves that generalize the idea of a "straight line" when moving in a curved space. On a surface such as a sphere, there are no straight lines in the usual sense: geodesics then play the role of the most rectilinear possible paths, i.e., those that locally minimize the distance traveled or, more generally, those that naturally follow the geometry of the space. In general relativity as well as in differential geometry, geodesics thus describe the free motion of a particle, guided not by forces but by the curvature of the (space-)time manifold [129].

Let us now examine the deep relation between the metric and the adiabatic error. For time-dependent parameters λ^μ, one may analyse how the infinitesimal distance ds^2 behaves under an infinitesimal temporal variation.

$$v^2 \equiv \frac{ds^2}{dt^2} = g_{\mu\nu}\dot{\lambda}^\mu\dot{\lambda}^\nu, \tag{2.52}$$

where $\dot{\lambda}^\mu \equiv d\lambda^\mu/dt$ denotes the rate at which the control parameters are varied. This expression represents the speed at which the state moves in projective space. Concretely, if one wishes to follow an eigenstate while minimizing excitations as much as possible, one must choose the trajectory $\lambda(t)$ that minimizes, at every instant, the quantity $g_{\mu\nu}\dot{\lambda}^\mu\dot{\lambda}^\nu$.

This naturally motivates the definition of a geodesic path in parameter space. A geodesic path is one whose total length

$$\ell[\lambda(t)] = \int \sqrt{g_{\mu\nu}\dot{\lambda}^\mu\dot{\lambda}^\nu}\, dt \tag{2.53}$$

is minimized among all trajectories connecting two given points in parameter space. The fundamental aspect of this construction is that $\ell[\lambda(t)]$ does not depend on time itself, but only on the path traced in parameter space. Thus, the geodesic trajectory constitutes the "smoothest" possible way to evolve the quantum state in projective

space, minimizing the infinitesimal variation measured by ds^2.

To make this concept explicit, let us introduce the Christoffel symbols associated with the metric $g_{\mu\nu}$:

$$\Gamma^{\mu}_{\nu\rho} = \frac{1}{2} g^{\mu\sigma} \left(\partial_\nu g_{\rho\sigma} + \partial_\rho g_{\nu\sigma} - \partial_\sigma g_{\nu\rho} \right), \tag{2.54}$$

where $g^{\mu\nu}$ is the inverse of $g_{\mu\nu}$, defined such that $g^{\mu\nu} g_{\nu\alpha} = \delta^{\mu}_{\alpha}$, using the Kronecker symbols δ^{α}_{β}. The Christoffel symbols, which are not tensors but connections, tell us how vectors change when transported along the curved manifold. Definition (2.54) is called the Levi-Civita connection, and it is the unique connection that guarantees that, locally, the space appears flat [129, 133].

The geodesics then satisfy the differential equation

$$\ddot{\lambda}^{\mu} + \Gamma^{\mu}_{\nu\rho} \dot{\lambda}^{\nu} \dot{\lambda}^{\rho} = 0, \tag{2.55}$$

which is the direct analogue of the geodesic equation in general relativity. This equation encapsulates the following principle: the covariant acceleration along a geodesic path is zero. Intuitively, it corresponds to the path that follows the curvature described by the metric tensor. Depending on the geometry of the manifold, the notion of a straight line is no longer the same as in Euclidean geometry. An ant walking in a single direction on the surface of a sphere will feel as though it never changes direction. From your point of view, however, it traces out a circle that is clearly not a straight line (see Fig. 2.3).

The second term, proportional to the Christoffel symbols, describes how the straight-line trajectory is affected by the curvature of the space in the various directions. This term accounts for the acceleration experienced by the coordinate system λ^{μ} due to the curvature of the manifold, truly capturing Coriolis-type effects. If the curvature is zero, i.e. $\Gamma^{\mu}_{\nu\rho} = 0$, no force alters the trajectory and λ^{μ} describes uniform motion: $\ddot{\lambda}^{\mu} = 0$, a straight line.

A final notion important for what follows is the energy associated with a curve. By describing the physics of the system through the action

$$\mathcal{S}[\lambda(t)] = \int g_{\mu\nu} \dot{\lambda}^{\mu} \dot{\lambda}^{\nu} \, dt, \tag{2.56}$$

It can be shown that making the action (2.56) extremal, that is, satisfying the Euler-Lagrange equations, amounts to imposing that the λ^{μ} satisfy the geodesic equation (2.55) [119, 126]. From this, since the Lagrangian

$$\mathcal{L}(\lambda^{\mu}, \dot{\lambda}^{\nu}) = g_{\mu\nu} \dot{\lambda}^{\mu} \dot{\lambda}^{\nu}, \tag{2.57}$$

being purely kinetic, the mechanical energy of coincides the Hamiltonian H describing the system. One thus obtains that the Lagrangian (2.57) is equal to the energy of the system. Moreover, one can show that if λ^{μ} satisfies the geodesic equation, then

$$\frac{dH}{dt} = \frac{d}{dt} (g_{\mu\nu} \dot{\lambda}^{\mu} \dot{\lambda}^{\nu}) = 0. \tag{2.58}$$

In other words, the quantity H is conserved along any affinely parametrized geodesic.

This conservation follows from the time invariance of the action: since the Lagrangian does not depend explicitly on the parameter t, the temporal homogeneity of the system implies, via Noether's theorem, the conservation of energy.

2.3.3 Geodesics and energy variance

We now show a very important property of geodesics, which will allow us to establish one of the central results of this thesis. For once, let us start from the Schrödinger equation and differentiate the system's state $|\psi(t)\rangle$ a second time with respect to time:

$$\frac{d^2|\psi(t)\rangle}{dt^2} = -\frac{i}{\hbar}\dot{H}(t)|\psi(t)\rangle - \frac{i}{\hbar}H\frac{d|\psi(t)\rangle}{dt} \tag{2.59}$$

$$= -\frac{i}{\hbar}\dot{H}(t)|\psi(t)\rangle - \frac{H(t)^2}{\hbar^2}|\psi(t)\rangle \tag{2.60}$$

We want to compute the distance between two states separated by an infinitesimal time increment dt:

$$\langle\psi(t)|\psi(t+dt)\rangle \approx 1 + \langle\psi|\dot{\psi}\rangle\, dt + \langle\psi|\ddot{\psi}\rangle\, dt^2, \tag{2.61}$$

using the notation $|\dot{\psi}\rangle \equiv d|\psi(t)\rangle/dt$. By inserting expression (2.60), we obtain

$$\langle\psi(t)|\psi(t+dt)\rangle = 1 - \frac{i}{\hbar}\langle H\rangle\, dt - \frac{i}{\hbar}\langle\dot{H}\rangle\, dt^2 - \frac{1}{\hbar^2}\langle H^2\rangle\, dt^2, \tag{2.62}$$

where we have used the notation $\langle H\rangle \equiv \langle\psi(t)|H|\psi(t)\rangle$. With a bit of algebra, one can see that the terms in $\langle\dot{H}\rangle$ simplifies. The norm of the overlap is then:

$$|\langle\psi(t)|\psi(t+dt)\rangle|^2 = 1 - \frac{1}{\hbar^2}\left(\langle H^2\rangle - \langle H\rangle^2\right) dt^2 \tag{2.63}$$

$$= 1 - \frac{(\Delta E)^2}{\hbar^2}\, dt^2, \tag{2.64}$$

with $\Delta E^2 = \langle H^2\rangle - \langle H\rangle^2$ the energy variance of the system. From this, using the definition of the interval (Eq. 2.49), we obtain the key result [119]:

$$\frac{ds^2}{dt^2} = \frac{\Delta E^2}{2\hbar^2} = g_{\mu\nu}\dot{\lambda}^\mu\dot{\lambda}^\nu \tag{2.65}$$

The quantum metric encodes the energy fluctuations during a parameterized evolution. As we have shown, geodesics satisfy $\delta(g_{\mu\nu}\dot{\lambda}^\mu\dot{\lambda}^\nu) = 0$. Consequently, along a geodesic, the energy variance $(\Delta E)^2$ is constant.

2.4 Geodesic counterdiabatic driving

Counterdiabatic driving provides a systematic scheme for exactly compensating the inertial terms so as to force the system's evolution to remain adiabatic, without presupposing the time dependence of the control parameter $\lambda(t)$. However, we have shown in the previous section that this parameter can be optimized independently of the CD term, in such a way as to minimize the local infidelity and, more precisely, to reduce the instantaneous probability of exciting the system out of the eigenstate in which it was initially prepared. The study of the geometric properties of geodesics has indeed revealed that such an optimal path corresponds to a trajectory along which the energy

variance is kept constant throughout the evolution.

At first sight, these two optimization approaches (one based on the exact cancellation of nonadiabatic transitions, the other on the geometric minimization of excitations) appear to rely on conceptually distinct principles. However, comparing them suggests the existence of a deeper underlying structure. In this section, we develop the consequences of using them jointly and analyze how their combination gives rise to a unified protocol, which we refer to as Geodesic Counterdiabatic Driving (GCD) [49, 50]. This protocol enables us to connect, within a single theoretical framework, geometric optimality and dynamical suppression of nonadiabatic excitations.

2.4.1 Time-independent counterdiabatic term

Under suitable conditions, we will establish a direct connection between the counterdiabatic Hamiltonian elements and the statement that if the parameters $\lambda^\mu(t)$ follow a geodesic, then the quantity $g_{\mu\nu}\dot{\lambda}^\mu\dot{\lambda}^\nu$ remains constant along the path. From the definition (2.51) of $g_{\mu\nu}$,

$$\dot{\lambda}^\mu\dot{\lambda}^\nu g_{\mu\nu} = \dot{\lambda}^\mu\dot{\lambda}^\nu \sum_{m\neq n} \frac{\langle m|\partial_\mu H|n\rangle\langle n|\partial_\nu H|m\rangle}{(E_n - E_m)^2} \tag{2.66}$$

$$= \sum_{m\neq n} \frac{\langle m|\dot{H}|n\rangle\langle n|\dot{H}|m\rangle}{(E_n - E_m)^2}, \tag{2.67}$$

where we have used the fact that H depends on time through the parameters λ^μ. Let us now expand the square of the counterdiabatic Hamiltonian, starting from its definition (2.26):

$$(H_{\mathrm{CD}})^2 = \left(i\hbar \sum_{n,m\neq n} \frac{\langle m|\dot{H}|n\rangle}{E_n - E_m} |m\rangle\langle n| \right)^2 \tag{2.68}$$

$$= -\hbar^2 \left(\sum_{n,m\neq n} \frac{\langle m|\dot{H}|n\rangle}{E_n - E_m} |m\rangle\langle n| \right) \left(\sum_{q,p\neq q} \frac{\langle p|\dot{H}|q\rangle}{E_q - E_p} |p\rangle\langle q| \right) \tag{2.69}$$

$$= -\hbar^2 \sum_{n,m\neq n} \sum_{q\neq n} \frac{\langle m|\dot{H}|n\rangle\langle n|\dot{H}|q\rangle}{(E_n - E_m)(E_q - E_n)} |m\rangle\langle q| \tag{2.70}$$

Thus, one can identify the diagonal elements of $(H_{\mathrm{CD}})^2$ as

$$\langle m|H_{\mathrm{CD}}^2|m\rangle = -\hbar^2 g_{\mu\nu}\dot{\lambda}^\mu\dot{\lambda}^\nu. \tag{2.71}$$

For parameters $\lambda^\mu(t)$ following a geodesic in parameter space, the diagonal elements of H_{CD}^2 are therefore formally equal to a constant. In other words, imposing that the parametric trajectory be geodesic amounts to selecting a dynamics for which the diagonal elements of $(H_{\mathrm{CD}})^2$ remains strictly constant. This is far from a trivial property: it demonstrates that geometric optimality and the exact suppression of nonadiabatic transitions are not merely compatible, but deeply interconnected within a single unified framework.

This result establishes a direct connection between two a priori distinct geometric approaches and, above all, makes it possible for the first time to define time-independent

counterdiabatic driving elements. This time-invariant character opens the way to considerably simplified protocols, in which the temporal complexity of the components of H_{CD} can be absorbed into the definition of the driving functions $\lambda^{\mu}(t)$.

2.4.2 Quantum speed limit

The Mandelstam-Tamm bound states that the characteristic time Δt required for a quantum system to evolve from one state to another, in the particular case where the final state is orthogonal to the initial state [51, 134], cannot be smaller than

$$\Delta t \geq \frac{\pi\hbar}{2\Delta E}, \tag{2.72}$$

where $\Delta E^2 = \langle H^2\rangle - \langle H\rangle^2$ is the energy variance of the system. This fundamental result provides an operational definition of the quantum speed limit (QSL), namely the maximum speed at which a quantum system can evolve under the influence of an external perturbation. The QSL thus establishes a direct connection between energy dispersion and the minimal evolution time, emphasizing that no protocol can surpass this limit imposed by quantum mechanics itself.

We have shown with equation (2.65) that the energy variance ΔE^2 is closely related to the quantity $g_{\mu\nu}\dot{\lambda}^{\mu}\dot{\lambda}^{\nu}$, which is equal to a constant denoted by Ω when the parameters λ^{μ} follow a geodesic in parameter space. In particular, we have also connected this constant to the diagonal elements of the operator $(H_{\mathrm{CD}})^2$. Consequently, the QSL can be rewritten in terms of the norm of the counterdiabatic Hamiltonian [50]:

$$|\Omega| \geq \frac{\pi\hbar}{2\Delta t}. \tag{2.73}$$

This relation imposes an immediate constraint on the admissible value of Ω. Clearly, the shorter the protocol duration Δt, the larger Ω must be: the faster one goes, the greater the inertia that must be compensated, and therefore the larger the norm of the counterdiabatic term must be.

2.5 Applications to Landau-Zener model

The Landau-Zener model is truly a textbook example for studying adiabaticity in an exactly solvable quantum system. Since its introduction in the early 1930s by Landau, Zener, Stückelberg, and Majorana [38–41], it has become the canonical reference for describing nonadiabatic transitions in a two-level system subjected to a linear variation of an external parameter [48, 88, 135–137]. Its formal simplicity, combined with the wealth of the dynamics it captures, makes it a privileged analytical tool for understanding avoided crossings, diabatic transitions, and the fundamental mechanisms governing how a system adapts to a changing Hamiltonian.

Landau-Zener model is written as

$$H = \lambda(t)\sigma_z + J\sigma_x, \tag{2.74}$$

where $\lambda(t)$ is the control parameter that depends on time t, and J is a coupling term. This Hamiltonian can be diagonalized analytically, and its eigenvalues are

$$E_{\pm} = \pm\sqrt{\lambda(t)^2 + J^2}. \tag{2.75}$$

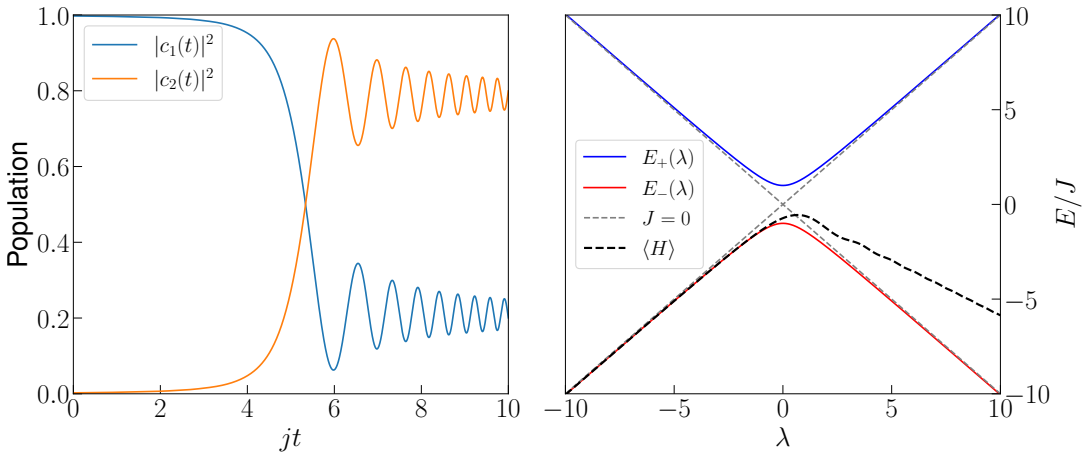

FIGURE 2.4: Left panel: Time evolution of the populations in the canonical basis for the Landau-Zener Hamiltonian with a driving $\lambda(t) = 10(2t/T - 1)$ and $jT = 10$. One observes that the population inversion is not perfect and results in a superposed state, because the total ramp time T is not sufficiently long: the system is outside the adiabatic regime. Right panel: Instantaneous eigenenergies as a function of λ. When a coupling J exists between the two states, an avoided crossing appears at $\lambda = 0$. In particular, the black dotted curves show that the system's energy over time does not perfectly follow the instantaneous eigenenergies.

In Fig. (2.4)(b), the energies (2.75) are shown as functions of λ. One observes the lifting of degeneracy at $\lambda = 0$ when $J \neq 0$, producing an avoided crossing. If the driving is adiabatic, the system's state remains in the instantaneous eigenstate of the Hamiltonian and therefore continuously follows the energy branch on which it was initially prepared. In other words, if the system is prepared in the ground state for $\lambda(t) \ll 0$ and the variation of $\lambda(t)$ is sufficiently slow, the evolution remains confined to the branch $E_-(t)$, even when passing through the region of maximal coupling around $\lambda = 0$. In this regime, the dynamics is deterministic, and the occupation of the excited state remains negligible throughout the evolution.

Conversely, if the variation of $\lambda(t)$ is too fast, the evolution is no longer adiabatic and the system cannot perfectly follow the instantaneous minimal-energy branch, as can be seen in the populations depicted in Fig.2.4. This phenomenon is precisely described by the Landau-Zener formula, which predicts the transition probability

$$P_{\mathrm{LZ}} = \exp\left(-\frac{\pi J^2}{\hbar|\dot{\lambda}|}\right) \tag{2.76}$$

highlighting that nonadiabatic transitions are more likely when the coupling J is small or when the sweep velocity $|\dot{\lambda}|$ is large. The dynamics of the system's state thus reflects this trade-off between adiabaticity and the speed at which the avoided crossing is traversed.

In order to go beyond the adiabatic theorem, the use of counterdiabatic terms makes it possible to accelerate the driving of the system while suppressing undesired transitions between eigenstates [138, 139]. In the case of the Landau-Zener model, this additional term can be determined analytically thanks to the simple structure of the Hamiltonian. From the spectrum of the Hamiltonian (2.74), it is straightforward to

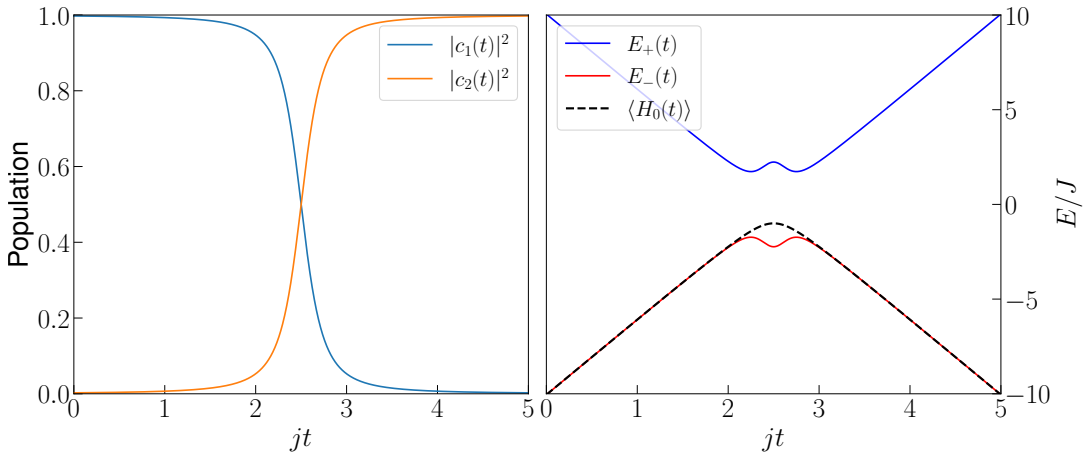

FIGURE 2.5: Left panel: Time evolution of the populations in the canonical basis for the Landau-Zener Hamiltonian driven by the linear protocol $\lambda = 10(2t/T - 1)$ with $jT = 5$, to which the counterdiabatic term H_{CD} is added. In contrast with the purely linear driving case, one observes here a perfectly adiabatic population inversion: the system remains locked to the desired instantaneous eigenstate throughout the evolution, without residual oscillations. Right panel: Instantaneous eigenenergies $E_\pm(t)$ of the total Hamiltonian $H(t) + H_{\mathrm{CD}}(t)$ as functions of time. The counterdiabatic term "opens up" the avoided crossing, allowing the system's state (black dotted curve) to faithfully follow the instantaneous eigenenergies of H.

obtain

$$H_{\mathrm{CD}} = -\frac{J\dot{\lambda}}{2(\lambda(t)^2 + J^2)}\sigma_y \tag{2.77}$$

$$\equiv \Omega(t)\sigma_y. \tag{2.78}$$

This term, which points along the transverse direction σ_y, exactly compensates the evolution of the instantaneous eigenvector when $\lambda(t)$ varies in time. In its absence, the nonadiabatic coupling responsible for Landau-Zener transitions can emerge. The eigenenergies of the total Hamiltonian $H + H_{\mathrm{CD}}$ are now

$$E_\pm = \pm\sqrt{\lambda(t)^2 + J^2 + \Omega(t)^2}. \tag{2.79}$$

Figure 2.5(a) shows the populations as a function of time for the total Hamiltonian $H + H_{\mathrm{CD}}$. As a result of the counterdiabatic terms, diabatic transitions are cancelled and the system's state strictly follows the evolution of the eigenstate of the initial Hamiltonian in which it was initially prepared. In the right panel, the eigenenergies are depicted and in particular, one can see the effect of the CD terms : the gap is "widened" arount the avoided crossing to ensure adiabaticity.

Another, more geometric point of view arises from the Fubini-Study metric associated with the family of eigenstates of the Hamiltonian. From the single non-zero component of the metric tensor, we have

$$g = \frac{J^2}{4(\lambda(t)^2 + J^2)^2}, \tag{2.80}$$

associated with $\lambda(t)$, it is possible to solve the geodesic equation for this parameter and obtain

$$\lambda(t) = J\tan\left(\alpha_i + (\alpha_f - \alpha_i)\, t/T\right), \tag{2.81}$$

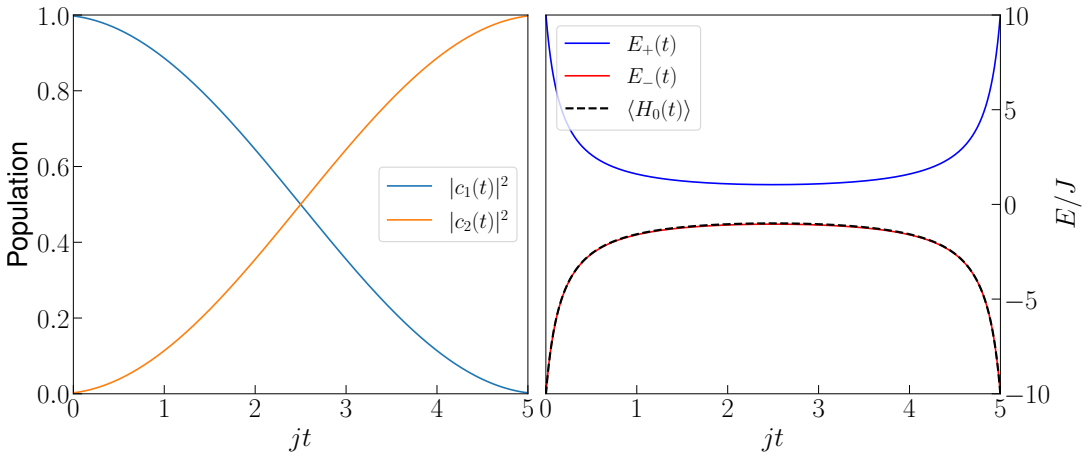

FIGURE 2.6: Left panel: Populations in the canonical basis as a function of time for the geodesic protocol (2.81) assisted by the counterdiabatic term H_{CD}, for $jT = 5$. One observes a perfectly monotonic population inversion, free of oscillations: the system's state follows exactly the targeted instantaneous eigenstate, with a fidelity close to unity throughout the evolution. In particular, the population inversion occurs less abruptly than in the case of a linear driving. Right panel: Instantaneous eigenenergies $E_{\pm}(t)$ of the total Hamiltonian $H + H_{\mathrm{CD}}$. The geodesic protocol smooths the avoided crossing, while the CD term ensures that the gap is enlarged by a time-independent quantity Ω. The mean value $\langle H\rangle$ (black dotted curve) follows the instantaneous eigenlevels perfectly.

where $\alpha_{i,f} = \tan^{-1}(\lambda_{i,f}/J)$, and where λ_i and λ_f are respectively the values of the parameter λ at $t = 0$ and $t = T$ [48]. This geodesic protocol corresponds to the evolution that minimizes the geometric length of the path followed in the space of eigenstates. Intuitively, it is the "straightest" possible path in the state manifold, ensuring that the rate of change of the eigenvectors is distributed optimally throughout the protocol.

The geodesic protocol (2.81) naturally leads to an evolution in which the energy levels are traversed rapidly for values of λ far from the avoided crossing, but much more slowly when the system approaches the critical region around $\lambda = 0$. This modulation of the speed directly reflects the structure of the metric: the curvature is maximal near the avoided crossing, which forces the evolution to slow down in order to optimally adjust the trajectory in parameter space.

A remarkable result emerges when inserting expression (2.81) into the counterdiabatic Hamiltonian: the CD protocol associated with this geodesic becomes

$$\Omega = \frac{\alpha_f - \alpha_i}{2T}, \tag{2.82}$$

that is, a quantity strictly constant in time. In other words, the highly inhomogeneous geometric curvature of the Landau-Zener model translates, after introducing the CD term and choosing the geodesic, into a perfectly uniform transverse control field. This time-independent additional term constitutes the Geodesic Counterdiabatic Driving. In particular, if $\lambda_{i,f}$ are sufficiently large compared with J, the associated angles satisfy asymptotically

$$\alpha_i \to -\pi/2 \qquad\qquad \alpha_f \to \pi/2 \tag{2.83}$$

In this case, the elements of the CD term can be rewritten in the compact form

$$\Omega = \frac{\pi}{2T}. \tag{2.84}$$

This result shows that the strength of the required transverse field depends only on the total protocol time in the case of a geodesic driving.

Figure 2.6 shows once again the populations as a function of time, when the Landau-Zener Hamiltonian is driven by a geodesic counterdiabatic protocol. In particular, one can see that the population inversion is indeed "smoother" than in the linear driving case. In the right panel, eigenenergies are depicted and it becomes clear that the role of the tangent function is to modify energies fast far away from the avoided crossing, and to be really slow around the latter.

Finally, by identifying $\Delta t = T$ and reintroducing the constant $\hbar$ explicitly, one finds that the geodesic counterdiabatic protocol saturates the quantum speed limit (2.73):

$$\Omega = \frac{\pi\hbar}{2T} \tag{2.85}$$

This means that the chosen trajectory constitutes, in this model, the dynamically fastest path allowed by quantum mechanics to connect the initial and final eigenstates. The GCD protocol is therefore not only geometrically optimal: it is also time-optimal, achieving the fastest theoretically possible state conversion.

3

NOON states creation via geodesic counterdiabatic driving

NOON states are entangled states between two modes, in which all N particles of a system are in a superposition composed of these two modes. In full generality, a NOON state can be written as $|N,0\rangle + e^{i\varphi}|0,N\rangle$, where measuring the population of one of the two modes immediately fixes the population present in the other. This type of state, of great interest for metrology [140–145], has been realized using superconducting qubits, photons, and phonons [6, 7, 146]. Various strategies and protocols on how to prepare such NOON states with bosonic quantum gases have been proposed [16–25], using the interaction between the atoms of the gas as a key ingredient. However, their creation using ultracold atoms remains to be achieved due to the lack of a sufficiently fast generation protocol.

The protocol we propose here builds on the phenomenon of collective tunneling. When a gas of bosons is trapped in an optical lattice, the system is described by the Bose-Hubbard Hamiltonian which offers a wide range of controllable parameters such as the lattice depth, the hopping rate, or the on-site interaction between particles. In a specific parameter regime, known as the self-trapping regime, sequential hopping (allowing particles to tunnel one by one) is suppressed. As a consequence, the dynamics allow for collective tunneling, in which all particles tunnel together as a whole. From this mechanism, the NOON state $|N,0\rangle + |0,N\rangle$ naturally emerges at half the tunneling time, where the probabilities of finding all N particles in either mode are equal. The problem with this method alone, however, is that the characteristic timescale of collective tunneling grows exponentially with the number of particles, preventing the experimental realization of a NOON state with ultracold atoms.

A particularly promising approach was recently proposed [35, 36], using the phenomenon of collective tunneling [26–29, 31] to generate the entangled state, together with a chaos-assisted tunneling mechanism [32] to accelerate collective tunneling and thereby shorten the entanglement time. This method significantly reduced the time required to obtain a NOON state, yet the exponential dependence of the entanglement time on the particle number remains.

Our method accelerates the collective tunneling process through the use of a third mode whose energy is varied so as to adiabatically cross the energies of the two other modes, thereby creating a NOON state in accordance with the adiabatic theorem (see Fig. 3.1). If the system is in a parameter regime corresponding to the self-trapping regime, and if all particles are initially placed in a mode that is energetically detuned from the others while being symmetrically coupled to them, then the adiabatic driving of this third mode will enable the creation of a NOON state, provided that the conditions for applying the adiabatic theorem are satisfied.

3.1 Three-site Bose-Hubbard Model

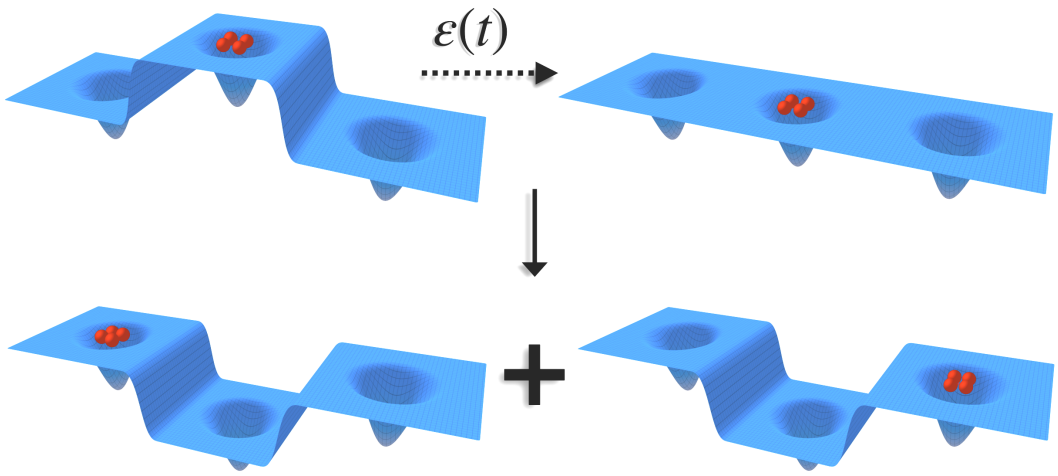

FIGURE 3.1: Schematic representation of the proposed protocol. Initially, all bosons are placed in a mode that is energetically at the top of the spectrum. Subsequently, the energy of this mode is lowered via the controlled on-site energy $\varepsilon(t)$ in order to achieve an avoided crossing with another energy level corresponding to the coherent superposition of the states $|N,0,0\rangle$ and $|0,0,N\rangle$. A NOON state $|N,0,0\rangle + |0,0,N\rangle$ is thus obtained at the end of this adiabatic transition process.

As described in Section I, the dynamics of ultracold atoms trapped in an optical lattice are described by the Bose-Hubbard model. In our system, we employ a three-site Bose-Hubbard model describing a set of N bosons trapped in an optical lattice in which each sublattice consists of three sites, with a central site symmetrically connected to the two others. The Hamiltonian describing such a system is written as

$$\hat{H}(t) = \frac{U}{2}\hat{a}_c^\dagger\hat{a}_c^\dagger\hat{a}_c\hat{a}_c + \varepsilon(t)\hat{a}_c^\dagger\hat{a}_c + \frac{U}{2}\sum_{i=1}^{2}\hat{a}_i^\dagger\hat{a}_i^\dagger\hat{a}_i\hat{a}_i - J\sum_{i=1}^{2}(\hat{a}_i^\dagger\hat{a}_c + \hat{a}_c^\dagger\hat{a}_i) \tag{3.1}$$

In this system, a central well (denoted by the letter c) is symmetrically coupled to two other wells via a real hopping amplitude J. The total particle number (obtained via the operator $\hat{N} = \sum_{i=c,1,2}\hat{a}_i^\dagger\hat{a}_i$) is conserved, which allows one to define the dimension $\mathcal{D}^{(3)}(\mathcal{H})$ of the Hilbert space $\mathcal{H}$ spanned by the eigenvectors of $\hat{H}(t)$:

$$\mathcal{D}^{(3)}(\mathcal{H}) = \frac{(N+1)(N+2)}{2} \tag{3.2}$$

where N is the total number of particles. In the Fock basis $|n_1, n_c, n_2\rangle$, the states are defined by the number of bosons occupying the energy level associated with the

left well (n_1), the central well (n_c), or the right well (n_2). In particular, particles may tunnel by passing through the central well. The hopping terms therefore take the form $\mathcal{J}_{n_c,n_i} = -J\sqrt{n_c(n_i+1)}$ when a particle moves from the center to well i, or $\mathcal{J}_{n_i,n_c} = -J\sqrt{n_i(n_c+1)}$ when it moves from well i to the central well. Particles interact whenever they occupy the same energy level, through interaction terms proportional to U, and the on-site energy of the central level, which may vary in time, is defined through the function $\varepsilon(t)$.

If $\varepsilon = 0$ and $J = 0$, the particles are trapped in the wells in which they reside. In this parameter regime, the Hamiltonian matrix is diagonal in the Fock basis, meaning that the eigenstates of the Hamiltonian are states characterized by fixed particle numbers in the different energy levels of the system. In particular, these energy levels are fully determined by

$$\epsilon(n_1, n_c, n_3) = \frac{U}{2}\left(n_1(n_1-1) + n_c(n_c-1) + n_2(n_2-1)\right). \tag{3.3}$$

For repulsive interactions ($U > 0$), the Fock states in which all particles occupy the same well ($|N,0,0\rangle$, $|0,N,0\rangle$, and $|0,0,N\rangle$) lie at the top of the spectrum and are separated from nearby states in which one particle occupies a different energy level (e.g. $|N-1,1,0\rangle$). The gap separating these states is

$$\epsilon(N,0,0) - \epsilon(N-1,1,0) = U(N-1). \tag{3.4}$$

When the hopping is slightly nonzero, i.e. $U/J \gg 1$, the eigenstates of the Hamiltonian are no longer exactly the Fock states, but remain perturbatively very close to them. Likewise, the eigenenergies of the system will differ slightly from those given in Eq. (3.3).

3.1.1 Self-trapping regime

The self-trapping regime lies in a parameter region where $NU/J \gg 1$, with the hopping term being nonzero but still small compared to the interaction term. The states in which all N particles occupy the same well are still isolated, but there remains a nonzero probability for tunneling to occur. In particular, only collective tunneling is allowed. Owing to the gap $U(N-1)$ protecting the states $|N,0,0\rangle$, $|0,N,0\rangle$, and $|0,0,N\rangle$ from the others, the particles can only tunnel together as a whole toward another well.

In Fig. 3.2, we show the spectrum of the Hamiltonian (3.1) for $N = 10$ particles as a function of the ratio NU/J. The self-trapping regime manifests itself through the disappearance of the "level spaghetti" present at large values of J. As the ratio NU/J increases, the energy levels become increasingly ordered and converge toward the Fock states, which are the eigenstates of the Hamiltonian for $J = 0$. In this context, the three highest energy eigenstates (corresponding to states where all particles are localized in the same well) are isolated from the rest of the spectrum by a protective gap given by $U(N-1)$. Thus, if the system is initially prepared in one of these three states, the dynamics are restricted to a subspace of the full Hilbert space.

This phenomenon is characterized by an almost complete absence of population in the intermediate states, resulting in an effective three-state dynamics in the case of a three-site Bose-Hubbard Hamiltonian. When the different well energies are brought into resonance, collective tunneling can occur and, halfway through the evolution over

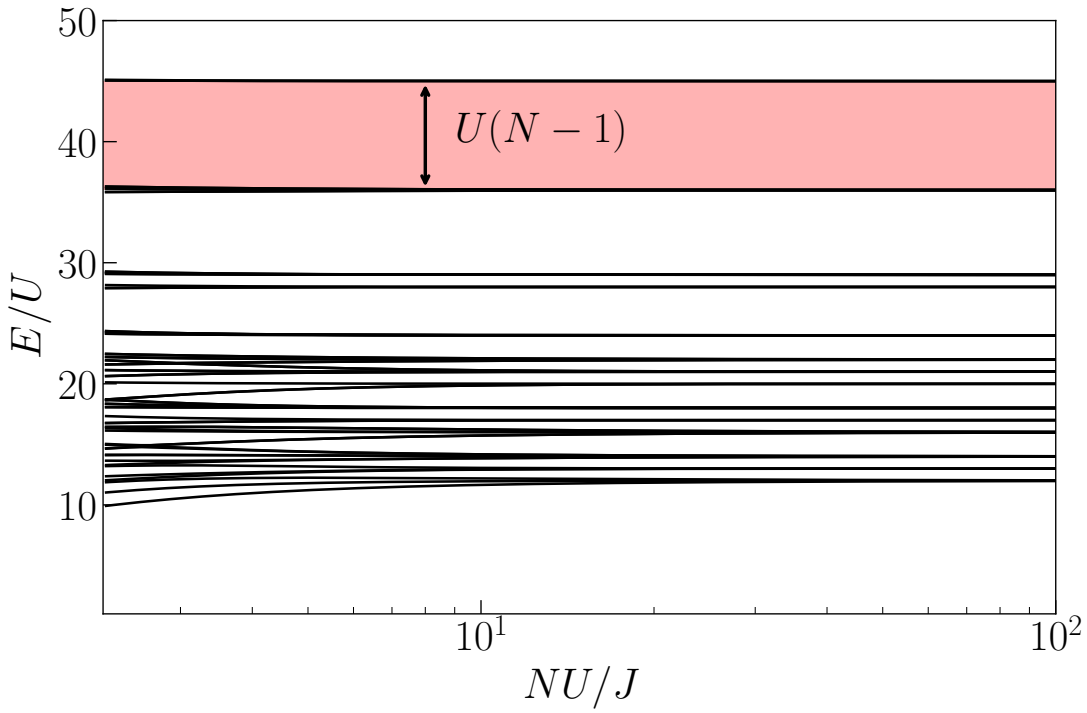

FIGURE 3.2: Evolution of the energy levels of the Bose-Hubbard Hamiltonian (3.1) as a function of NU/J for $N = 10$ and $\varepsilon = 0$. For small values of the ratio NU/J, the spectrum appears as a level spaghetti, and most levels interact with one another. When the self-trapping regime is reached ($NU/J \gg 1$), the levels become "frozen" at the energies corresponding to the Fock states. In particular, a protective gap of amplitude $\simeq U(N-1)$ isolates the three highest energy levels from the rest of the spectrum.

one tunneling period, produces a NOON state. We will show that this dynamics can be controlled by means of adiabatic driving, allowing one to tune the resonance between the wells so as to induce tunneling at the desired moment.

3.1.2 Adiabatic driving

Within the framework of the Bose-Hubbard Hamiltonian, the on-site energies ε_i of the sites i can be controlled. In particular, in our method only the energy of the central well has to be modified in order to induce a crossing between the energies of the different sites, since the energies of the two outer wells remain strictly equal by symmetry. The goal is therefore to create an avoided crossing among these three energies. In this subsection, we introduce the adiabatic driving of the three-site Bose-Hubbard Hamiltonian by applying a linear driving of the form

$$\varepsilon(t) = -a(2t/T - 1) \tag{3.5}$$

to the energy of the central well. A linear driving of this form allows the energy of the central well to evolve from an initial value $\varepsilon(t = 0) = a$ to a final value $\varepsilon(t = T) = -a$. With this driving protocol, we may initially place the energy of the central site well above the other levels and isolate it from the rest of the spectrum if $|a|$ is sufficiently large. In particular, as explained in the previous subsection, in the self-trapping regime the states in which all particles occupy the same site are energetically isolated from the rest of the spectrum. Consequently, if the initial energy of the central well is $\varepsilon(0) = a$, the highest energy level in the spectrum corresponds to the state $|0, N, 0\rangle$ in the limit $NU \gg J$.

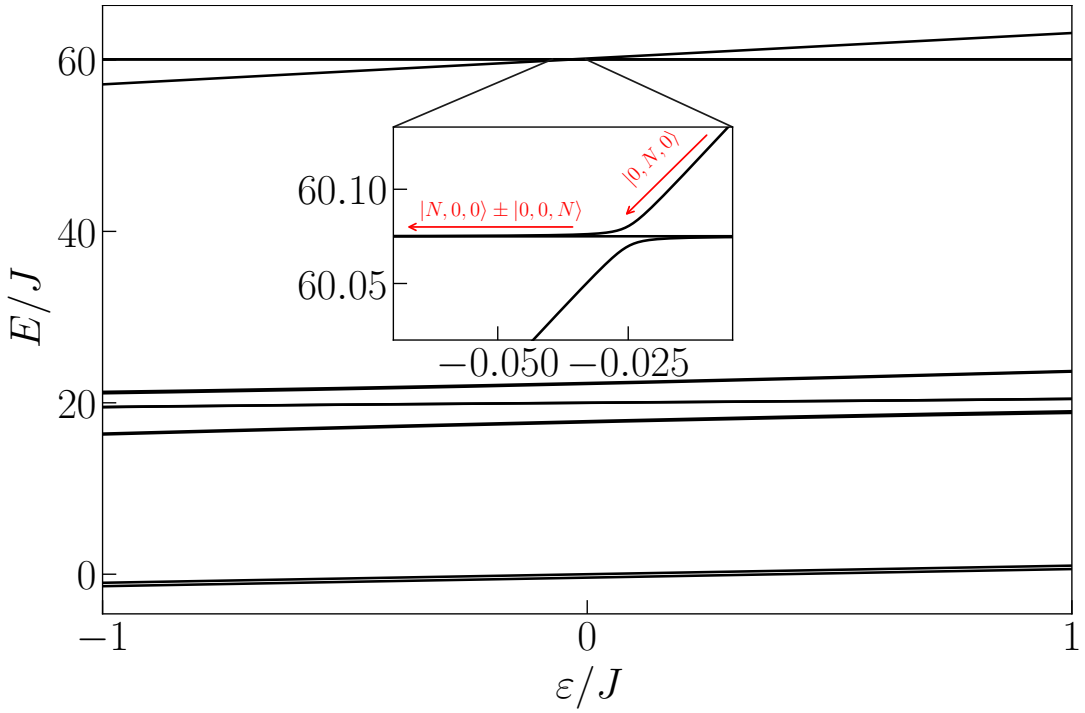

FIGURE 3.3: Evolution of the spectrum of the Hamiltonian (3.1) as a function of the bias ε for $N = 3$ particles and $U = 20J$. While the three states of interest, $|N, 0, 0\rangle$, $|0, N, 0\rangle$, and $|0, 0, N\rangle$, are isolated thanks to the self-trapping regime, an avoided crossing occurs when the driving parameter ε approaches zero. If the system is driven adiabatically and initially prepared in the state $|0, N, 0\rangle$, the creation of a NOON state $|N, 0, 0\rangle + |0, 0, N\rangle$ is achieved after the adiabatic passage through the avoided crossing.

Over time, the energy of the central well decreases according to $\varepsilon(t)$. In particular, if the energies of the other wells are fixed to $\varepsilon_1 = \varepsilon_2 = 0$, then the resonance between the energy levels occurs halfway through the protocol, i.e. at $t = T/2$. At this moment, the three sites are in resonance and collective tunneling can take place. Indeed, if the particles are initially all in the central well, collective tunneling will occur at resonance symmetrically toward the two outer wells. Because the bosons cannot choose a preferred site if the two are energetically indistinguishable, the tunneling must occur symmetrically between the two levels, thereby generating a NOON state. It is then necessary to continue the driving and detune the central well from the two others in order to freeze the dynamics and prevent any oscillatory evolution between the different energy levels. From this point, since the outer wells are not directly coupled to each other, the system's evolution is frozen in the state induced by the adiabatic tunneling.

In Fig. 3.3, the eigenenergies of the Hamiltonian (3.1) are plotted as a function of the value of ε, which varies linearly in time according to Eq. (3.5), for $N = 3$ particles and an interaction strength $U = 20J$. Around resonance, an avoided crossing (visible in the inset) appears between the state in which all bosons occupy the central well and the symmetric and antisymmetric NOON superpositions. In particular, in the three levels of interest, only the antisymmetric superposition $|N, 0, 0\rangle - |0, 0, N\rangle$ is unaffected by the driving. The presence of this avoided crossing enables the creation of a NOON state through adiabatic driving. In this situation, the state of the system will follow the time evolution of the eigenvector $|m(t)\rangle$ of the Hamiltonian (3.1) in

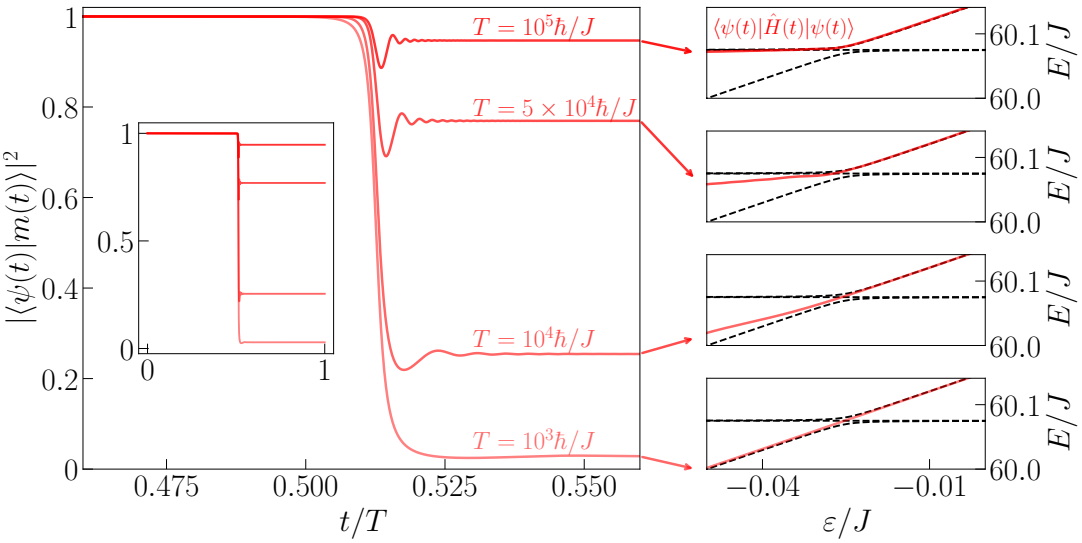

FIGURE 3.4: Overlap between the system's state $|\psi(t)\rangle$ and the eigenstate $|m(t)\rangle$ of the Hamiltonian (3.1) corresponding to the highest initial energy, asymptotically identifiable with the Fock state $|0, N, 0\rangle$, for $N = 3$ particles, $U = 20J$, and a linear driving (3.5), as a function of the normalized time t/T. The figure is zoomed in around the time $t/T \approx 1/2$, but an inset shows the overall shape of the evolution, which becomes abrupt near the avoided crossing. For different values of the total protocol time, the adiabatic criterion is more or less satisfied depending on the magnitude of T. The fidelity remains close to 1 for a total time $T = 10^5\hbar/J$, but drops to nearly zero for $T = 10^3\hbar/J$. In particular, the diabatic transition can be observed in the spectrum, since the energy associated with the system's state, $\langle\psi(t)|\hat{H}(t)|\psi(t)\rangle$, does not follow the parametric evolution of the eigenstate in which the system is initially prepared.

which it is initially prepared, namely the state asymptotically close to $|0, N, 0\rangle$.

To quantify how closely the system's state $|\psi(t)\rangle$ follows the evolution of the eigenstate $|m(t)\rangle$ of the Hamiltonian (3.1) associated with the highest energy, Fig. 3.4 shows the fidelity $|\langle\psi(t)|m(t)\rangle|^2$ as a function of the normalized time t/T for different values of T, with $N = 3$ and $U = 20J$. This scalar product directly measures the distance between the two states, and in particular, the adiabatic theorem tells us that in the adiabatic limit, this quantity must remain equal to 1. In the case of a relatively slow protocol, for example with a total time $T = 10^5\hbar/J$, the fidelity at the end of the protocol is close to unity, indicating that we indeed follow the evolution of the eigenvector. This can be observed by tracking the energy associated with the state $|\psi(t)\rangle$ throughout the evolution. Comparing the quantity $\langle\psi(t)|\hat{H}(t)|\psi(t)\rangle$ with the instantaneous eigenenergies of the Bose-Hubbard Hamiltonian (3.1) clearly shows that an adiabatic state transition occurs when the system evolves sufficiently slowly.

The adiabatic theorem can therefore indeed be used to induce the creation of an entangled state of the form $|N, 0\rangle + |0, N\rangle$ in a system described by the Bose-Hubbard Hamiltonian in the self-trapping regime. However, the time required to achieve adiabaticity remains far too long in the case of linear driving, and in particular is of the same order of magnitude as the collective tunneling timescale. The goal now is to apply the various optimization methods developed in Chapter II to accelerate the entanglement generation in the system.

3.2 Reduced model

In the self-trapping regime, the particles can no longer tunnel independently. It is clearly visible in the spectrum of the Bose-Hubbard Hamiltonian that the states in which all particles occupy the same level are isolated from the rest of the spectrum. In particular, an energy gap proportional to $\approx U(N-1)/J$ allows one to define a reduced Hamiltonian describing the three-level dynamics that appear in the time evolution of the populations.

The reduced Hamiltonian in the Fock basis $(|N,0,0\rangle, |0,N,0\rangle, |0,0,N\rangle)$ is given by

$$H_{\text{red}}(U,J,\varepsilon(t)) = \begin{pmatrix} \mathcal{E} & -\mathcal{J} & 0 \\ -\mathcal{J} & \tilde{\mathcal{E}} + \mathcal{N}\varepsilon(t) & -\mathcal{J} \\ 0 & -\mathcal{J} & \mathcal{E} \end{pmatrix} \tag{3.6}$$

where $\mathcal{E} = \mathcal{E}(U,J)$, $\tilde{\mathcal{E}} = \tilde{\mathcal{E}}(U,J)$, $\mathcal{N}(U,J) = N + \delta N(U,J)$ and $\mathcal{J} = \mathcal{J}(U,J)$ are to be obtained using perturbation theory for $NU/J \gg 1$. These functions describe how the energies of the three states of interest are perturbatively modified by the presence of a coupling J. The diagonal element $\tilde{\mathcal{E}}$ differs from $\mathcal{E}$ because the central level is symmetrically coupled to the other two, while the latter only couples to the central well. However, as long as we remain within the perturbative regime where the interaction is significantly larger than the hopping, this effect is rather weak and $\tilde{\mathcal{E}}$ will have a value very close to $\mathcal{E}$. Consequently, for $\varepsilon(t) = 0$ the three levels are very close, and the effective coupling between them is extremely small. In this regime, an adiabatic driving method can be used to steer the system towards a NOON state.

The energy levels corresponding to the eigenvalues of the Hamiltonian (3.6) can be calculated analytically:

$$E_{\pm} = \frac{\mathcal{E} + \tilde{\mathcal{E}} + \mathcal{N}\varepsilon(t) \pm \sqrt{8\mathcal{J}^2 + (\tilde{\mathcal{E}} - \mathcal{E} + \mathcal{N}\varepsilon(t))^2}}{2}, \tag{3.7}$$

$$E_0 = \mathcal{E}. \tag{3.8}$$

In particular, the gap $|E_+ - E_-| = \sqrt{8\mathcal{J}^2 + (\tilde{\mathcal{E}} - \mathcal{E} + \mathcal{N}\varepsilon(t))^2}$ determines the time required to tunnel from the state $|0,N,0\rangle$ to the superposition $(|N,0,0\rangle + |0,0,N\rangle)/\sqrt{2}$ when it reaches its minimal value. At resonance, where $\mathcal{N}\varepsilon(t) = -(\tilde{\mathcal{E}} - \mathcal{E})$, the gap takes the form

$$|E_+ - E_-| = 2\sqrt{2}\,\mathcal{J}. \tag{3.9}$$

The transition frequency between two states is directly related to the timescale on which collective tunneling can occur [35]. In particular, the time required to tunnel from one state to the other is given by

$$\tau = \frac{\pi\hbar}{|E_+ - E_-|} \tag{3.10}$$

Thus, knowing the value of the effective coupling $\mathcal{J}$ between the states that form the basis in which the reduced Hamiltonian (3.6) is expressed provides a good approximation of the time required for collective tunneling. The definition of this reduced Hamiltonian will greatly simplify all calculations. Indeed, we will be able to obtain all quantities needed for the application of the geodesic counterdiabatic driving on this subspace of the Hilbert space. However, knowledge of the perturbative functions $\tilde{\mathcal{E}}$, $\mathcal{E}$, and $\mathcal{J}$

is necessary in order to obtain any analytic solution usable in terms of the physical parameters U, J, and ε.

3.2.1 Perturbation theory

To describe the system as accurately as possible, the functions $\tilde{\mathcal{E}}$, $\mathcal{E}$, and $\mathcal{J}$ can be determined by considering the effect of the intermediate states on the three states of interest in the Fock basis. In fact, we will examine how the probabilities of individual tunneling events affect these states. The perturbative approach can be interpreted as bosons tunneling individually and returning to their initial site. Similar to Feynman diagrams, considering higher-order perturbation theory amounts to including more "virtual" paths. Thus, at second order the system has time to tunnel into another state and return, corresponding to one boson making a round trip. At fourth order, it has time to visit two different states before returning to the initial one, or to make two round trips.

For an initial state in which all particles are in one of the outer wells, we would therefore have, at second order, the path

$$|N,0,0\rangle \longrightarrow |N-1,1,0\rangle \longrightarrow |N,0,0\rangle$$

in which one boson from the left well tunnels into the central well and then returns to its initial site. If we consider a fourth-order process in perturbation theory, there are two different paths the system may take:

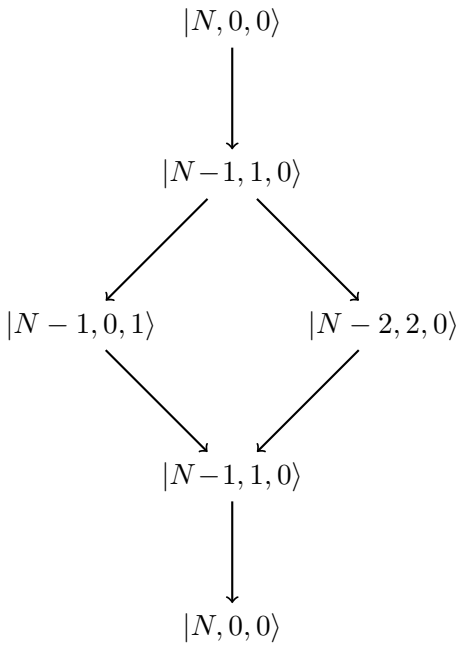

In this case, once one boson has reached the central well, a second one may join it before both return to their original site. But since the central well is also connected to the right well, the first boson may instead visit the right site before returning to the central and then to the left. Aside from those two trajectories, the system can also do two round trips, corresponding to twice the path associated with the second order of perturbation theory. Each tunneling event is associated with a probabilistic weight, and it is possible to define Feynman-like rules for computing the tunneling amplitudes.

Perturbative energies

In the case of nonzero hopping, the coupling to the other states of the many-body spectrum slightly modifies the eigenenergies of the system. These modifications are collected in the three perturbative functions that we will calculate using perturbation theory. Let us first compute the energy functional $\mathcal{E}(U,J)$ of the outer wells. We denote the interaction energy shifted by the driving term ε as

$$E_{n_1,n_c,n_2} = \frac{U}{2}\sum_{i=1}^{2} n_i(n_i-1) + n_c(n_c-1) + n_c\varepsilon. \tag{3.11}$$

As it will be useful for later, we consider complex hopping terms as $\mathcal{J}_{n_i,n_c} = J\sqrt{n_i(n_c+1)}$ and $\mathcal{J}^*_{n_c,n_i} = J^*\sqrt{n_c(n_i+1)}$, where n_i are the number of particles in site i, and n_c in the central site. Using the stationary Schrödinger equation, we end up with a system of coupled equations

$$E\Psi_{N,0,0} = E_{N,0,0}\Psi_{N,0,0} - \mathcal{J}_{N,0}\Psi_{N-1,1,0} \tag{3.12}$$

$$E\Psi_{N-1,1,0} = E_{N-1,1,0}\Psi_{N-1,1,0} - \mathcal{J}^*_{1,N-1}\Psi_{N,0,0} - \mathcal{J}_{N-1,1}\Psi_{N-2,2,0} - \mathcal{J}^*_{1,0}\Psi_{N-1,0,1} \tag{3.13}$$

$$E\Psi_{N-2,2,0} = E_{N-2,2,0}\Psi_{N-2,2,0} - \mathcal{J}^*_{2,N-2}\Psi_{N-1,1,0} - \mathcal{J}_{N-2,2}\Psi_{N-3,3,0} - \mathcal{J}^*_{2,0}\Psi_{N-2,1,1} \tag{3.14}$$

$$E\Psi_{N-1,0,1} = E_{N-1,0,1}\Psi_{N-1,0,1} - \mathcal{J}_{1,0}\Psi_{N-1,1,0} - \mathcal{J}_{N-1,0}\Psi_{N-2,1,1} \tag{3.15}$$

$$\dots$$

$$E\Psi_{0,0,N} = E_{0,0,N}\Psi_{0,0,N} - \mathcal{J}_{N,0}\Psi_{0,1,N-1} \tag{3.16}$$

Where E is the exact energy of $|N,0,0\rangle$.

The goal is to solve Eq. (3.12), which describes the energy of the state $|N,0,0\rangle$ (strictly equal to that of the state $|0,0,N\rangle$). To do so, one must substitute the expressions of the intermediate-state wavefunctions into one another so that, ultimately, Eq. (3.12) takes the form

$$E\Psi_{N,0,0} = (E_{N,0,0} + \mathcal{E}(U,J))\Psi_{N,0,0} + \mathcal{J}(U,J)\Psi_{0,N,0}. \tag{3.17}$$

In this expression, it is clear that the energy of the state $|N,0,0\rangle$ (represented by its wavefunction $\Psi_{N,0,0}$) is equal to the sum of the interaction energy $E_{N,0,0} = UN(N-1)/2$ and a perturbative contribution $\mathcal{E}(U,J)$ coming from the other states, as well as an effective coupling with the state $|0,N,0\rangle$. At second order, only a single round trip to the central well is possible. Thus, we need only consider the additional equation (3.13), neglect the terms involving $\Psi_{N-2,2,0}$ and $\Psi_{N-1,0,1}$, and substitute the expression of $\Psi_{N-1,1,0}$ into Eq. (3.12). By identifying the perturbative contribution, we obtain

$$\mathcal{E}^{(2)}(U,J) = \frac{\mathcal{J}_{N,0}\mathcal{J}^*_{1,N-1}}{E_{N,0,0} - E_{N-1,1,0}}, \tag{3.18}$$

which is the contribution of the state closest to $|N,0,0\rangle$, namely $|N-1,1,0\rangle$, to its energy.

We can go further and consider the fourth order of perturbation theory, which is composed of the paths

$$|N,0,0\rangle \leftrightarrow |N-1,1,0\rangle \leftrightarrow |N-2,2,0\rangle,$$
$$|N,0,0\rangle \leftrightarrow |N-1,1,0\rangle \leftrightarrow |N-1,0,1\rangle,$$
$$|N,0,0\rangle \leftrightarrow |N-1,1,0\rangle \leftrightarrow |N,0,0\rangle,$$

representing several trajectories. The first describes a bosonic particle moving from the left well to the central site, then a second particle joining it before both return to their initial site. The second trajectory considers the possibility that the first particle tunnels a second time, this time from the central site to the right site. Finally, the third trajectory accounts for two round trips of a particle between the left well and the central site. By solving for the considered trajectories, we obtain

$$\mathcal{E}^{(4)}(U,J) = \frac{\mathcal{J}_{N,0}\,\mathcal{J}^*_{1,N-1}}{E^{(2)} - \dfrac{\mathcal{J}_{N-1,1}\,\mathcal{J}^*_{2,N-2}}{E_{N,0,0}-E_{N-2,2,0}} - \dfrac{|\mathcal{J}_{1,0}|^2}{E_{N,0,0}-E_{N-1,0,1}}} \tag{3.19}$$

where $E^{(2)} = E_{N,0,0} - E_{N-1,1,0} + \mathcal{E}^{(2)}(U,J)$. Expanding for $E \gg |J|^2, \varepsilon$ yields

$$\begin{aligned}\mathcal{E}^{(4)}(U,J) =& \frac{N|J|^2}{(N-1)U} + \frac{N|J|^4}{(N-1)^2(N-2)U^3} \\ &+ N\varepsilon\left(\frac{|J|^2}{(N-1)^2U^2} + \frac{|J|^4(3N^2-7N+3)}{(N-1)^4(N-2)^2U^4}\right),\end{aligned} \tag{3.20}$$

which is therefore the correction to the energies of the outer wells at fourth order in perturbation theory. The last term, proportional to ε, reflects the modification of the energies due to the motion of the central well. Indeed, since the energy difference between the central site and the outer sites appears in the denominator of each term, the bias applied to the energy of the central site shows up in the correction to the energies of the outer sites.

The sixth order can also be calculated and will be used as a reference for comparing the efficiency of the other orders. It is given here for completeness, although it was not used in the simulations:

$$\begin{aligned}\mathcal{E}^{(6)} =& \frac{N|J|^2}{U(N-1)} + \frac{N|J|^2\varepsilon}{U^2(N-1)^2} + \frac{N|J|^4}{(N-1)^2(N-2)U^3} + \frac{N|J|^4\varepsilon(3N^2-7N+3)}{(N-1)^4(N-2)^2U^4} \\ &+ \frac{N|J|^6(2N^3-6N^2+N+5)}{(N-1)^5(N-2)^2(N-3)U^5} - \frac{N|J|^6\varepsilon}{(2N^2-9N-9)^2(N-1)^6(N-2)^3U^6} \\ &\times(16N^8-250N^7+1570N^6-515N^5+9425N^4-9155N^3-3351N^2+1104N-918)\end{aligned} \tag{3.21}$$

The central well, being symmetrically connected to the two others, does not have the same energy. In particular, already at second order, a particle may tunnel either to the left well or to the right well before returning. The energy shift will therefore be twice that of the outer wells, since the two paths are indistinguishable. However, at fourth order, loops appear and may allow the system to pass through states different from those visited during the first half of the trajectory. For example, a particle may tunnel to the left well, and then a second particle may tunnel to the right well. From this state, one may return to the initial state (with only one particle in the left well)

or proceed to the state with the particle in the right well. The different possible paths are therefore no longer only round trips, but may also pass through states that were not visited previously.

The time-independent Schrödinger equation for the central well at the fourth order of perturbation theory is therefore different:

$$E^{(4)}\Psi_{0,N,0} = E_{0,N,0}\Psi_{0,N,0} - \mathcal{J}^*_{N,0}(\Psi_{1,N-1,0} + \Psi_{0,N-1,1}) \tag{3.22}$$

$$E^{(2)}\Psi_{1,N-1,0} = E_{1,N-1,0}\Psi_{1,N-1,0} - \mathcal{J}_{1,N-1}\Psi_{0,N,0} - \mathcal{J}^*_{N-1,1}\Psi_{2,N-2,0} - \mathcal{J}^*_{N-1,0}\Psi_{1,N-2,1} \tag{3.23}$$

$$E^{(2)}\Psi_{0,N-1,1} = E_{0,N-1,1}\Psi_{0,N-1,1} - \mathcal{J}_{1,N-1}\Psi_{0,N,0} - \mathcal{J}^*_{N-1,1}\Psi_{0,N-2,2} - \mathcal{J}^*_{N-1,0}\Psi_{1,N-2,1} \tag{3.24}$$

$$E^{(0)}\Psi_{1,N-2,1} = E_{1,N-2,1}\Psi_{1,N-2,1} - \mathcal{J}_{1,N-2}(\Psi_{1,N-1,0} + \Psi_{0,N-1,1}) \tag{3.25}$$

$$E^{(0)}\Psi_{2,N-2,0} = E_{2,N-2,0}\Psi_{2,N-2,0} - \mathcal{J}_{2,N-2}\Psi_{1,N-1,0} \tag{3.26}$$

$$E^{(0)}\Psi_{0,N-2,2} = E_{0,N-2,2}\Psi_{0,N-2,2} - \mathcal{J}_{2,N-2}\Psi_{0,N-1,1}, \tag{3.27}$$

where $E^{(4)}$, $E^{(2)}$ and $E^{(0)} = E_{0,N,0}$ are the energies of $|0, N, 0\rangle$ respectively at fourth, second and zeroth order of perturbation theory. In the last three equations, terms are neglected in order to restrict the expansion to fourth order in perturbation theory.

Solving these equations can be lengthy due to the number of terms involved. However, it is possible to reduce the system by using the symmetry between the outer wells with respect to the central well, since their energies are strictly equal. Indeed, by defining the states

$$\Psi_1 \equiv \Psi_{1,N-1,0} + \Psi_{0,N-1,1} \tag{3.28}$$

$$\Psi_2 \equiv \Psi_{2,N-2,0} + \Psi_{0,N-2,2}, \tag{3.29}$$

with their associated energies $E_1 = E_{1,N-1,0} = E_{0,N-1,1}$ and $E_2 = E_{2,N-2,0} = E_{0,N-2,2}$, the number of equations is drastically reduced. This redefinition amounts to folding the perturbative graph symmetrically with respect to the vertical axis:

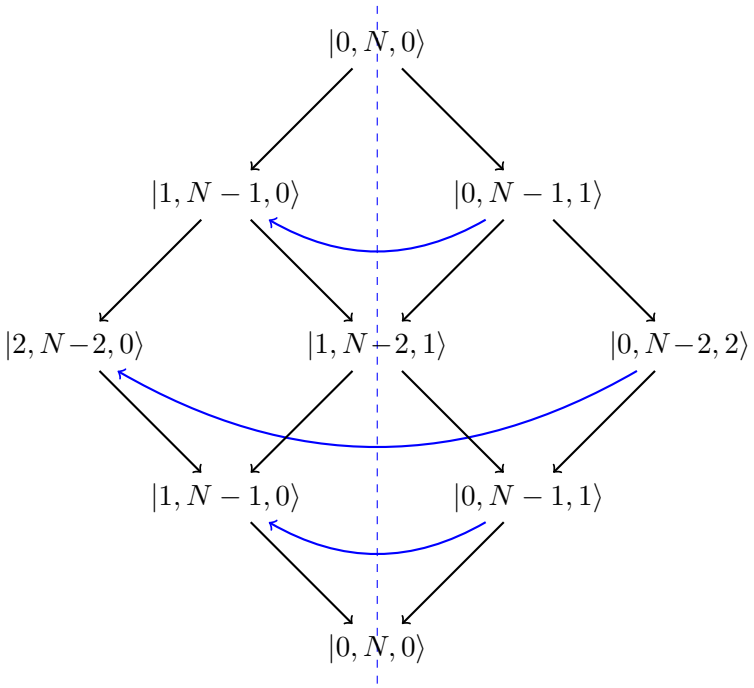

The system of equations, restricted to fourth order, then reduces to

$$(E^{(4)} - E_{0,N,0})\Psi_{0,N,0} = -\mathcal{J}^*_{N,0}\Psi_1 \tag{3.30}$$

$$(E^{(2)} - E_1)\Psi_1 = -2\mathcal{J}_{1,N-1}\Psi_{0,N,0} - \mathcal{J}^*_{N-1,1}\Psi_2 - 2\mathcal{J}^*_{N-1,0}\Psi_{1,N-2,1} \tag{3.31}$$

$$(E^{(0)} - E_{1,N-2,1})\Psi_{1,N-2,1} = -\mathcal{J}_{1,N-2}\Psi_1 \tag{3.32}$$

$$(E^{(0)} - E_2)\Psi_2 = -\mathcal{J}_{2,N-2}\Psi_1. \tag{3.33}$$

By solving the full set, the fourth-order correction term can be identified as:

$$\tilde{\mathcal{E}}^{(4)}(U,J) = \frac{2\mathcal{J}^*_{N,0}\mathcal{J}_{1,N-1}}{E^{(2)} - E_1 + \dfrac{2\mathcal{J}^*_{N,0}\mathcal{J}_{1,N-1}}{E_{0,N,0} - E_1} - \dfrac{\mathcal{J}^*_{N-1,1}\mathcal{J}_{2,N-2}}{E_{0,N,0} - E_2} - \dfrac{2\mathcal{J}^*_{N-1,1}\mathcal{J}_{1,N-2}}{E_{0,N,0} - E_{1,N-2,1}}} \tag{3.34}$$

Once again, we expand around $E \gg |J|^2, \varepsilon$ and obtain

$$\begin{aligned}\tilde{\mathcal{E}}^{(4)}(U,J) =& \frac{2NJ^2}{U(N-1)} - \frac{2NJ^4(N^2-6N+7)}{(N-1)^3(N-2)(2N-3)U^3} \\ &- N\varepsilon\left(\frac{2J^2}{U^2(N-1)} + \frac{2J^4(25N^3-123N^2+201N-109)}{(N-1)^4(2N^3-7N+6)^2U^4}\right).\end{aligned} \tag{3.35}$$

As expected, the second-order perturbative correction for the central well is equal to twice that of the outer wells. However, since the fourth-order term includes loops and paths that are more complex than simply the sum of individual trajectories, it is no longer equal to $2\mathcal{E}$.

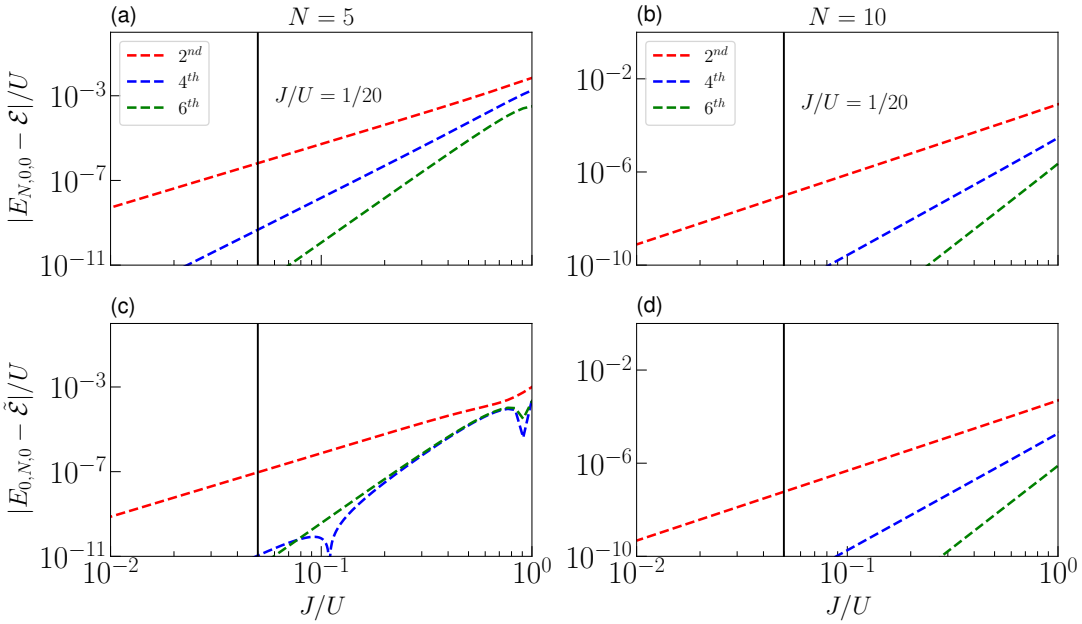

FIGURE 3.5: Convergence of the perturbative expansions for the two highest energies in the Bose-Hubbard model (3.1) as a function of J/U. Panels (a),(b) display the relative deviation for the external wells $|E_{N,0,0} - \mathcal{E}|$ for $N = 5$ and $N = 10$, respectively, while panels (c),(d) show the deviation for the central well $|E_{0,N,0} - \tilde{\mathcal{E}}|$. The red, blue, and green dashed lines correspond to the 2nd, 4th, and 6th order expansions. The black vertical line indicates the regime $J/U = 1/20$, which is used in our simulations.

Similarly to the outer sites, the sixth order is given for reference:

$$\begin{aligned}\tilde{\mathcal{E}}^{(6)} &= \frac{2N|J|^2}{U(N-1)} - \frac{2N|J|^2\varepsilon}{U^2(N-1)^2} - \frac{2N|J|^4(N^2-6N+7)}{(N-1)^3(N-2)(2N-3)U^3} \\ &- \frac{2N|J|^4\varepsilon(25N^3-123N^2+201N-109)}{(N-1)^4(2N^2-7N+6)^2U^4} \\ &- \frac{2N|J|^6(12N^6-124N^5+381N^4-80N^3-1602N^2+2804N-1455)}{(2N-3)^2(N-3)(N-2)^2(N-1)^5(3N-7)U^5} \\ &+ \frac{2N|J|^6\varepsilon}{(3N-7)^2(N-3)^2(N-2)^3(N-1)^6(2N-3)^3U^6}(48N^{12}-1248N^{11}+14978N^{10} \\ &- 110137N^9+548649N^8-1923443N^7+4781377N^6-8313943N^5-9733925N^4 \\ &- 7041789N^3+2460637N^2+96384N-247230).\end{aligned} \tag{3.36}$$

To compare the different orders and their validity, Fig. 3.5 shows the modulus of the differences between the well energies and their perturbative approximations at various orders, for the three-site Bose-Hubbard model, as a function of the ratio J/U. Panels (a) and (b) compare the energy of an outer well for $N = 5$ and $N = 10$, respectively, while panels (c) and (d) correspond to the central well. One can see from Fig. 3.5 that, already at fourth order in perturbation theory, the accuracy is better than 10^{-8}.

The time-independent Schrödinger equation (3.12) also allows us to extract the effective coupling between $|N,0,0\rangle$ and $|0,N,0\rangle$, which, by symmetry, will be the same as that between the central-well state and $|0,0,N\rangle$. Perturbatively, we examine the probability that all particles tunnel one by one to the other site. We consider only the

most direct path, namely

$$|N,0,0\rangle \longrightarrow |N-1,1,0\rangle \longrightarrow \cdots \longrightarrow |1,N-1,0\rangle \longrightarrow |0,N,0\rangle$$

We thus obtain

$$\mathcal{J}(U,J) = \frac{\mathcal{J}_{N,0}\mathcal{J}_{N-1,1}\cdots\mathcal{J}_{1,N-1}}{(E^{(0)}-E_{N-1,1,0})(E^{(0)}-E_{N-2,2,0})\ldots(E^{(0)}-E_{1,N-1,0})} \tag{3.37}$$

$$= \frac{NJ^N}{(N-1)!\,U^{N-1}}. \tag{3.38}$$

The effective coupling scales exponentially with the number of particles N, and follows a power-law dependence with respect to the interaction U.

In the case of a two-site Bose-Hubbard Hamiltonian, as presented in Chapter I, the difference between the two highest energies is equal to $2\mathcal{J}$. In this case, the estimate of the tunneling time (3.10) becomes

$$\tau_{L=2} = \frac{\pi\hbar}{2\mathcal{J}} \tag{3.39}$$

$$\approx 1.2\times 10^5\hbar/J. \tag{3.40}$$

for $U = 20J$ and $N = 5$, which indeed matches what is observed in the two-well resonant system. In particular, the NOON state appearing halfway through the tunneling time is obtained at $\tau_{L=2}/2 \approx 6\times 10^5\hbar/J$. This first result confirms that the effective coupling obtained perturbatively captures the collective tunneling phenomenon sufficiently well.

For $\varepsilon = 0$, the expressions of $\tilde{\mathcal{E}}(U,J)$, $\mathcal{E}(U,J)$, and $\mathcal{J}(U,J)$ determine the reduced Hamiltonian describing the static system. For a nonzero bias ε, a final step allows us to absorb the dependence on this parameter into a shifted particle number $\mathcal{N}$. We wish the resonance condition $\tilde{\mathcal{E}} = \mathcal{E}$ (i.e. the moment when the energy gap is minimal) to occur at $\varepsilon = 0$, which requires shifting the driving function ε since only the central well is driven. The resonance condition is $\tilde{\mathcal{E}} + N\varepsilon = \mathcal{E}$. By writing the perturbative functions as a sum of coefficients associated with their expansions in powers of J^2/U, namely

$$\mathcal{E} = \sum_{i=0}^{2} \alpha_i \frac{J^{2i}}{U^{2i-1}} + \beta N\varepsilon \tag{3.41}$$

$$\tilde{\mathcal{E}} = \sum_{i=0}^{2} \tilde{\alpha}_i \frac{J^{2i}}{U^{2i-1}} + \tilde{\beta} N\varepsilon + N\varepsilon \tag{3.42}$$

with the coefficients

$$\alpha_0 = \tilde{\alpha}_0 = N(N-1)/2 \tag{3.43}$$

$$\alpha_1 = \frac{N}{N-1} \tag{3.44}$$

$$\tilde{\alpha}_1 = 2\alpha_1 \tag{3.45}$$

$$\alpha_2 = \frac{N}{(N-1)^2(N-2)} \tag{3.46}$$

$$\tilde{\alpha}_2 = -\frac{2N(N^2-6N+7)}{(N-1)^3(N-2)(2N-3)}, \tag{3.47}$$

we have, at the resonance,

$$\sum_{i=0}^{2} \frac{J^{2i}}{U^{2i-1}}(\tilde{\alpha}_i - \alpha_i) + (\tilde{\beta} - \beta + 1)N\varepsilon = 0, \tag{3.48}$$

Defining

$$\mathcal{N}(U,J) = N\left(1 - \frac{3J^2}{(N-1)^2U^2} - \frac{(12N^4 - 14N^3 - 123N^2 + 303N - 191)J^4}{(N-1)^4(2N^3 - 7N + 6)^2U^4}\right) \tag{3.49}$$

yields the resonance to occur when $\tilde{\mathcal{E}} - \mathcal{E} + \mathcal{N}\varepsilon = 0$. This transformation allows us to avoid dealing explicitly with the energy modification introduced by ε and to incorporate it instead into a slightly modified particle number $\mathcal{N}(U,J)$. This will become important later when defining effective parameters for the full Bose-Hubbard system.

3.2.2 Disorder and different couplings

The main assumption in the previous developments relies on perfect symmetry between the wells. In general, such a condition may be difficult to achieve. For example, uncertainties may exist in the on-site energies of the wells, and there may be a difference between the two outer wells in our case. Here, we also study the impact of a well-depth fluctuation as well as of different couplings between the wells. We therefore consider a coupling $\mathcal{J}$ between the central well and the left well, and a coupling $\mathcal{G}$ with the right well. The energies are then written as $E_{n_0,n_1,n_2} = \sum_{i=0}^{2} n_i(\varepsilon_i + U(n_i - 1)/2)$, where the ε_i are the on-site energies of the different wells. The equations for the fourth-order corrections of the central well then become

$$(E^{(4)} - E_{0,N,0})\Psi_{0,N,0} = -\mathcal{J}_{N,0}\Psi_{1,N-1,0} - \mathcal{G}_{N,0}\Psi_{0,N-1,1} \tag{3.50}$$

$$(E^{(2)} - E_{1,N-1,0})\Psi_{1,N-1,0} = -\mathcal{J}_{1,N-1}\Psi_{0,N,0} - \mathcal{J}_{N-1,1}\Psi_{2,N-2,0} - \mathcal{G}_{N-1,0}\Psi_{1,N-2,1} \tag{3.51}$$

$$(E^{(2)} - E_{0,N-1,1})\Psi_{0,N-1,1} = -\mathcal{G}_{1,N-1}\Psi_{0,N,0} - \mathcal{G}_{N-1,1}\Psi_{0,N-2,2} - \mathcal{J}_{N-1,0}\Psi_{1,N-2,1} \tag{3.52}$$

$$(E^{(0)} - E_{2,N-2,0})\Psi_{2,N-2,0} = -\mathcal{J}_{2,N-2}\Psi_{1,N-1,0} \tag{3.53}$$

$$(E^{(0)} - E_{0,N-2,2})\Psi_{0,N-2,2} = -\mathcal{G}_{2,N-2}\Psi_{0,N-1,1} \tag{3.54}$$

$$(E^{(0)} - E_{1,N-2,1})\Psi_{1,N-2,1} = -\mathcal{J}_{1,N-2}\Psi_{1,N-1,0} - \mathcal{G}_{1,N-2}\Psi_{0,N-1,1} \tag{3.55}$$

where $\mathcal{J}_{n_i,n_j}$ was already defined, and $\mathcal{G}_{n_i,n_j} = G\sqrt{n_i(n_j+1)}$ is the probabilistic weight associated with the motion of a particle between the central well and the right well. For the sake of simplicity, we take the couplings to be real, but the extension to complex hopping is straightforward, replacing J^2 and G^2 by $|J|^2$ and $|G|^2$, respectively. Solving these equations leads to the following correction:

$$\begin{aligned}\tilde{\mathcal{E}}^{(4)} =& \frac{\mathcal{J}_{N,0}\mathcal{J}_{1,N-1}}{E^{(0)}-E_{1,N-1,0}} - \frac{\mathcal{J}_{N,0}\mathcal{J}_{1,N-1}}{(E^{(0)}-E_{1,N-1,0})^2} \\ &\times\left(\frac{\mathcal{J}_{N,0}\mathcal{J}_{1,N-1}}{E^{(0)}-E_{1,N-1,0}}+\frac{\mathcal{G}_{N,0}\mathcal{G}_{1,N-1}}{E^{(0)}-E_{0,N-1,1}}-\frac{\mathcal{J}_{N-1,1}\mathcal{J}_{2,N-2}}{E^{(0)}-E_{2,N-2,2}}-\frac{\mathcal{G}_{N-1,1}\mathcal{G}_{1,N-2}}{E^{(0)}-E_{1,N-2,1}}\right) \\ &+\frac{\mathcal{G}_{N,0}\mathcal{G}_{1,N-1}}{E^{(0)}-E_{0,N-1,1}} - \frac{\mathcal{G}_{N,0}\mathcal{G}_{1,N-1}}{(E^{(0)}-E_{0,N-1,1})^2} \\ &\times\left(\frac{\mathcal{J}_{N,0}\mathcal{J}_{1,N-1}}{E^{(0)}-E_{1,N-1,1}}+\frac{\mathcal{G}_{N,0}\mathcal{G}_{1,N-1}}{E^{(0)}-E_{0,N-1,1}}-\frac{\mathcal{G}_{N-1,1}\mathcal{G}_{2,N-2}}{E^{(0)}-E_{0,N-2,2}}-\frac{\mathcal{J}_{N-1,0}\mathcal{J}_{1,N-2}}{E^{(0)}-E_{1,N-2,1}}\right) \\ &+\frac{\mathcal{J}_{N,0}\mathcal{G}_{N-1,0}\mathcal{G}_{1,N-2}\mathcal{J}_{1,N-1}}{(E^{(0)}-E_{1,N-1,0})(E^{(0)}-E_{0,N-1,1})(E^{(0)}-E_{1,N-2,1})} \\ &+\frac{\mathcal{G}_{N,0}\mathcal{J}_{N-1,0}\mathcal{J}_{1,N-2}\mathcal{G}_{1,N-1}}{(E^{(0)}-E_{1,N-1,0})(E^{(0)}-E_{0,N-1,1})(E^{(0)}-E_{1,N-2,1})}.\end{aligned} \tag{3.56}$$

In this form, it is clear that each term corresponds to a different trajectory in Hilbert space. For instance, the term proportional to $\mathcal{J}^2_{N,0}\mathcal{J}^2_{1,N-1}$ corresponds to a particle starting from the central well and performing two round trips to the left well. For the outer wells, the expression is much simpler due to the presence of only one single loop in the perturbative diagram, as opposed to three in the case of the central well. We have

$$\begin{aligned}\mathcal{E}^{(4)} =& \frac{\mathcal{J}_{N,0}\mathcal{J}_{1,N-1}}{E^{(0)}-E_{N-1,1,0}} - \frac{\mathcal{J}_{N,0}\mathcal{J}_{1,N-1}}{(E^{(0)}-E_{N-1,1,0})^2} \\ &\times\left(\frac{\mathcal{J}_{N,0}\mathcal{J}_{1,N-1}}{E^{(0)}-E_{N-1,1,0}}-\frac{\mathcal{J}_{N-1,1}\mathcal{J}_{2,N-2}}{E^{(0)}-E_{N-2,2,0}}-\frac{\mathcal{G}_{1,0}\mathcal{G}_{1,0}}{E^{(0)}-E_{N-1,0,1}}\right).\end{aligned} \tag{3.57}$$

From Eqs. (3.56) and (3.57), it is possible to include the energy differences between the central well and the outer wells, thereby capturing the notion of disorder between sites. To picture the behavior of disorder, we consider small deviations on the hopping ($G \to J + \delta J/2$, $J \to J - \delta J/2$) and on onsite energies of external wells ($E_{N,0,0} - E_{0,0,N} = N(\delta\epsilon_1 - \delta\epsilon_2)$). We can then develop expressions (3.56) and (3.57) to obtain, to the second order of disorder, the energies for the central well ($\tilde{\mathcal{E}^{(2)}}$), for the left ($\mathcal{E}^{(2)}_1$) and right ($\mathcal{E}^{(2)}_2$) wells:

$$\begin{aligned}\tilde{\mathcal{E}}^{(2)} \approx& \frac{2NJ^2}{U(N-1)} + \frac{NJ^2}{(N-1)^2U^2}(\delta\epsilon_1+\delta\epsilon_2) + \frac{NJ^2}{(N-1)^3U^3}(\delta\epsilon_1^2+\delta\epsilon_2^2) \\ &-\frac{NJ}{(N-1)^2U^2}(\delta\epsilon_1+\delta\epsilon_2)\delta J + \frac{N}{2U(N-1)}\delta J^2\end{aligned} \tag{3.58}$$

$$\begin{aligned}\mathcal{E}^{(2)}_1 \approx& \frac{NJ^2}{U(N-1)} - \frac{NJ^2}{(N-1)^2U^2}\delta\epsilon_1 + \frac{NJ^2}{(N-1)^3U^3}\delta\epsilon_1^2 - \frac{NJ}{(N-1)U}\delta J \\ &+\frac{NJ}{(N-1)^2U^2}\delta\epsilon_1\delta J + \frac{N}{4U(N-1)}\delta J^2\end{aligned} \tag{3.59}$$

$$\mathcal{E}_2^{(2)} \approx \frac{NJ^2}{U(N-1)} - \frac{NJ^2}{(N-1)^2U^2}\delta\epsilon_2 + \frac{NJ^2}{(N-1)^3U^3}\delta\epsilon_2^2 + \frac{NJ}{(N-1)U}\delta J - \frac{NJ}{(N-1)^2U^2}\delta\epsilon_2\delta J + \frac{N}{4U(N-1)}\delta J^2 \tag{3.60}$$

To give a concrete example, we consider a symmetrical detuning around the energy of the central well, that has the form $\delta\epsilon_1 = -\delta\epsilon_2 = \delta\epsilon/2$:

$$\tilde{\mathcal{E}}^{(2)} \approx \frac{2NJ^2}{U(N-1)} + \frac{NJ^2}{2(N-1)^3U^3}\delta\epsilon^2 + \frac{N}{2(N-1)U}\delta J^2 - \frac{NJ}{(N-1)^2U^2}\delta J\delta\epsilon, \tag{3.61}$$

$$\mathcal{E}_1^{(2)} \approx \frac{NJ^2}{U(N-1)} - \frac{NJ^2}{2(N-1)^2U^2}\delta\epsilon + \frac{NJ^2}{4(N-1)^3U^3}\delta\epsilon^2 - \frac{NJ}{U(N-1)}\delta J + \frac{NJ}{2(N-1)^2U^2}\delta J\delta\epsilon + \frac{N}{(N-1)^2U^2}\delta J^2, \tag{3.62}$$

$$\mathcal{E}_2^{(2)} \approx \frac{NJ^2}{U(N-1)} + \frac{NJ^2}{2(N-1)^2U^2}\delta\epsilon + \frac{NJ^2}{4(N-1)^3U^3}\delta\epsilon^2 + \frac{NJ}{U(N-1)}\delta J + \frac{NJ}{2(N-1)^2U^2}\delta J\delta\epsilon + \frac{N}{(N-1)^2U^2}\delta J^2. \tag{3.63}$$

This yields a quantitative information on the extent to which the presence of disorder can be tolerated without affecting the effectiveness of the protocol.

3.2.3 GCD with reduced Hamiltonian

With the reduced Hamiltonian and its perturbative functions now determined up to fourth order, we can explicitly calculate the geodesic control as well as the counter-diabatic Hamiltonian describing the adiabatic driving of the states of interest. It is important to note that the explicit and exact calculation of these functions would have been impossible for the full Bose-Hubbard system since it would require the analytical knowledge of the entire spectrum at each time. Although approximation methods for the counterdiabatic term exist, it is difficult to target precisely the matrix elements that are relevant for adiabatic driving. Here, thanks to the self-trapping regime, the dynamics of the physical system can be captured by a reduced model in which analytical calculations can be carried out without significant difficulty.

Metric tensor and geodesic equation

To determine the geometry of the parametric space spanned by the system under study, it is necessary to examine how the curvature of the manifold behaves as a function of the coordinate ε. Let us first compute the metric tensor associated with the reduced Hamiltonian H_{red}:

$$\begin{aligned} g^{(n)} &= \sum_{m\neq n} \frac{\langle m|\partial_\varepsilon H_{\text{red}}|n\rangle\langle n|\partial_\varepsilon H_{\text{red}}|m\rangle}{(E_n - E_m)^2} \\ &= \frac{4N^2\mathcal{J}^2}{\left(8\mathcal{J}^2 + (\tilde{\mathcal{E}} - \mathcal{E} + \mathcal{N}\varepsilon)^2\right)^2} \end{aligned} \tag{3.64}$$

The metric of the system encodes its geometry and, in particular, makes it possible to identify whether singularities in the curvature of the manifold are present, which is not the case here. As we have shown, if the quantity $g^{(n)}\dot{\varepsilon}^2$ can be identified with a constant c, then the affine parametrization $\varepsilon(t)$ follows a geodesic of the parameter space. Let us expand this condition:

$$\begin{aligned} \frac{4N^2\mathcal{J}^2\dot{\varepsilon}^2}{\left(8\mathcal{J}^2+(\tilde{\mathcal{E}}-\mathcal{E}+\mathcal{N}\varepsilon)^2\right)^2} &= c \\ 2N\mathcal{J}\int \frac{d\varepsilon}{8\mathcal{J}^2+\left(\tilde{\mathcal{E}}-\mathcal{E}+\mathcal{N}\varepsilon\right)^2} &= \sqrt{c}\int dt \\ \text{Arctan}\left(\frac{\tilde{\mathcal{E}}-\mathcal{E}+\mathcal{N}\varepsilon}{2\sqrt{2}\mathcal{J}}\right) &= \sqrt{2c}\ t+A \end{aligned} \tag{3.65}$$

By fixing $\varepsilon(t=0)\equiv\varepsilon_i$ and $\varepsilon(t=T)\equiv\varepsilon_f$, we obtain the geodesic control:

$$\mathcal{N}\varepsilon(t) = 2\sqrt{2}\mathcal{J}\tan\left((\alpha_f-\alpha_i)t/T+\alpha_i\right)-(\tilde{\mathcal{E}}-\mathcal{E}), \tag{3.66}$$

where $\alpha_{i,f}=\text{Arctan}\left((\tilde{\mathcal{E}}-\mathcal{E}+\mathcal{N}\varepsilon_{i,f)}/2\sqrt{2}\mathcal{J}\right)$ allows to ensure that the tangent decreases fast enough relatively to the amplitude of the gap $\mathcal{J}$. Indeed, the narrower the avoided crossing, the faster one has to enter the "plateau" region of the tangent to avoid any excitation.

This function describes a rapid temporal evolution far from the central gap and a very slow evolution near it, ensuring that the adiabaticity condition is satisfied where the energy levels are closest. The geodesic path is specifically designed to minimize energy variance during the system's evolution. By aligning the driving protocol with the metric tensor's structure, the fluctuations in energy are reduced, especially near the avoided crossing, where the gap is smallest. The probability for non-adiabatic transitions is minimized, insuring a smooth controlled evolution.

Counterdiabatic Hamiltonian

Although geodesic control is by essence the optimal way to drive a system adiabatically, it remains constrained by the limitations of the adiabatic theorem. To overcome this limit, adding a counterdiabatic Hamiltonian that cancels the residual inertial term allows the dynamics to be greatly accelerated, thereby bypassing the adiabatic theorem. The counterdiabatic Hamiltonian can be calculated analytically for the reduced Hamiltonian by diagonalizing it. We obtain, after expressing it in the Fock basis,

$$H_{\text{CD}}(t) = i\hbar\Omega(t)\begin{pmatrix} 0 & 1 & 0 \\ -1 & 0 & -1 \\ 0 & 1 & 0 \end{pmatrix} \tag{3.67}$$

with

$$\Omega(t) = \frac{\mathcal{N}\mathcal{J}\dot{\varepsilon}(t)}{8\mathcal{J}^2+(\mathcal{N}\varepsilon(t)+\tilde{\mathcal{E}}-\mathcal{E})^2} \tag{3.68}$$

This Lorentzian function describes matrix elements whose amplitude grows with the driving speed $\dot{\varepsilon}$. Its maximum Ω_{max} is located at $\mathcal{N}\varepsilon=-(\tilde{\mathcal{E}}-\mathcal{E})$ and, in the case of a

linear driving of the form (3.5), is given by

$$\Omega_{\max} = -\frac{a\mathcal{N}}{4\mathcal{J}T}. \tag{3.69}$$

Geodesic counterdiabatic driving

Given the form of the counterdiabatic Hamiltonian, it is clear that the relation linking the diagonal elements of H_{CD}^2 to the geodesic condition is satisfied. By substituting the expression of the geodesic control ε into Eq. (3.68), the matrix elements of the counterdiabatic Hamiltonian reduce to a constant. Indeed, expression (3.68) can be rewritten as

$$\Omega = \frac{\mathcal{N}\mathcal{J}}{8\mathcal{J}^2 + \tan^2(\alpha_i + (\alpha_f - \alpha_i)t/T)} \times \frac{2\sqrt{2}\mathcal{J}(\alpha_f - \alpha_i)}{\mathcal{N}T\cos^2(\alpha_i + (\alpha_f - \alpha_i)t/T)}. \tag{3.70}$$

Recalling that the tangent can be written as the ratio of a sine to a cosine, the expression for Ω reduces to

$$|\Omega| = \frac{\sqrt{2}\pi}{4T}, \tag{3.71}$$

given that $\alpha_f - \alpha_i \approx -\pi$. The speed of evolution experienced when the driving protocol follows a geodesic of the parameter space exactly compensates the inertial term responsible for diabatic transitions. In Fig. 3.6, several curves of $\varepsilon(t)$ and of the elements of H_{CD} are shown as functions of time for different particle numbers. As expected, the variations of $\varepsilon(t)$ are very large far from the avoided crossing (that is, at the beginning and end of the protocol) while the elements of the counterdiabatic Hamiltonian grow quickly as the gap is approached. In particular, recalling that H_{CD} can be written as $H_{\mathrm{CD}} = \dot{\varepsilon}\mathcal{A}_\varepsilon$, and by plotting $\dot{\varepsilon}$ and $\mathcal{A}_\varepsilon$ separately, one observes that these quantities exactly compensate each other (see Fig. 3.6 panel (c)).

Thus, the reduced Hamiltonian equipped with the geodesic counterdiabatic term takes the form :

$$H_{\mathrm{red}}(U, J, \varepsilon(t)) + H_{\mathrm{CD}} = \begin{pmatrix} \mathcal{E} & -\mathcal{J} + i\hbar\Omega & 0 \\ -\mathcal{J} - i\hbar\Omega & \tilde{\mathcal{E}} + \mathcal{N}\varepsilon(t) & -\mathcal{J} - i\hbar\Omega \\ 0 & -\mathcal{J} + i\hbar\Omega & \mathcal{E} \end{pmatrix}, \tag{3.72}$$

where the function $\varepsilon(t)$ satisfies the geodesic equation $g^{(n)}\dot{\varepsilon}(t)^2 = \text{const}$. This reduced Hamiltonian makes it possible to understand several important aspects introduced by the GCD protocol. First, one can diagonalize this Hamiltonian and determine the three eigenenergies E_-, E_0, and E_+ in the basis of the states $|N,0,0\rangle$, $|0,N,0\rangle$, and $|0,0,N\rangle$. Setting $\hbar = 1$, we have:

$$E_\pm = \frac{\tilde{\mathcal{E}} + \mathcal{E} + \mathcal{N}\varepsilon(t) \pm \sqrt{8(\mathcal{J}^2 + \Omega^2) + (\tilde{\mathcal{E}} - \mathcal{E} + \mathcal{N}\varepsilon(t))^2}}{2} \tag{3.73}$$

$$E_0 = \mathcal{E}. \tag{3.74}$$

The eigenvalue E_0 corresponds to the antisymmetric superposition $|N,0,0\rangle - |0,0,N\rangle$, which does not participate in the dynamics of the driven system. The two other energies correspond respectively to the initial state $|0,N,0\rangle$, where all particles occupy the central well and are isolated from the two others, and to the NOON state $|N,0,0\rangle + |0,0,N\rangle$.

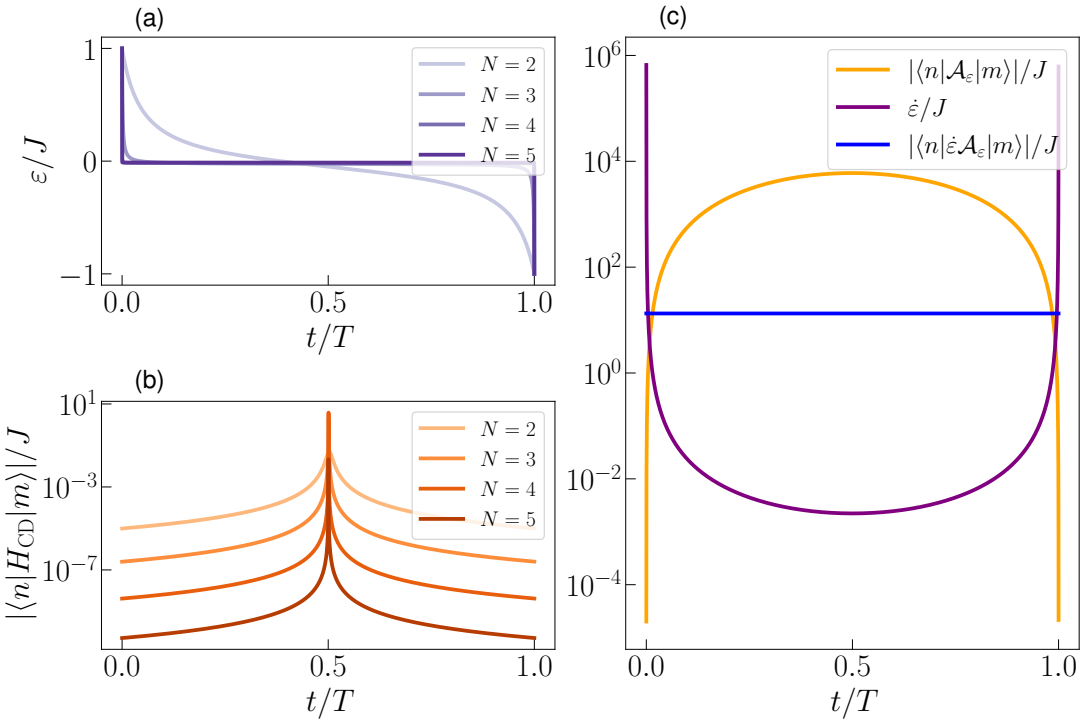

FIGURE 3.6: Components of the geodesic counterdiabatic protocol for different particle numbers and $U = 20J$. (a) Geodesic driving (3.66) as a function of the normalized time t/T. The tangent function, whose amplitude is directly proportional to the gap $\mathcal{J}$, must become increasingly sharply peaked as the gap becomes smaller. (b) Off-diagonal elements of the counterdiabatic Hamiltonian (3.67) for a linear driving (3.5), whose peaks occur exactly at the avoided crossing at $t/T \approx 1/2$. (c) For $N = 4$ particles, the off-diagonal elements of the adiabatic gauge potential $\mathcal{A}_\varepsilon = H_{\mathrm{CD}}/\dot{\varepsilon}$ (orange), the time derivative $\dot{\varepsilon}$ of the geodesic driving (purple), and the off-diagonal elements of $H_{\mathrm{CD}} = \dot{\varepsilon}\mathcal{A}_\varepsilon$ (blue) are shown on the same plot. In the case of geodesic driving, the different components of the counterdiabatic Hamiltonian perfectly compensate each other, resulting in a H_{CD} whose matrix elements remain constant in time.

The spectrum also informs us about the nature of the gap and its behavior under the GCD protocol. The minimal distance $|E_+ - E_-| = \sqrt{8(\mathcal{J}^2 + \Omega^2)}$ appears when the geodesic driving satisfies $\mathcal{N}\varepsilon(t) = -(\tilde{\mathcal{E}} - \mathcal{E})$. Moreover, the gap is broadened by an amount proportional to Ω, and we can now compare the two gaps to highlight the effect of adding GCD relative to simple adiabatic driving of the system:

$$\frac{\sqrt{8(\mathcal{J}^2 + \Omega^2)}}{2\sqrt{2}|\mathcal{J}|} = \left(1 + \frac{\Omega^2}{\mathcal{J}^2}\right)^{1/2}. \tag{3.75}$$

Thus, as soon as $\Omega \neq 0$, the gap is enlarged due to the action of the counterdiabatic Hamiltonian. Since the time required for adiabaticity is inversely proportional to the energy separation between the involved states, the GCD protocol accelerates the process and induces the entangled state $|N, 0, 0\rangle + |0, 0, N\rangle$ more rapidly. In particular, because this widening of the gap is directly caused by $\Omega \sim 1/T$, the effect of the GCD protocol is directly proportional to the total protocol time. The shorter the driving duration, the larger the amplitude of Ω will be. This observation leads us to consider several constraints that must be imposed on the driving, depending on experimental conditions. Notably, when this procedure is applied in a many-body context, it is necessary to ensure that the gap enlargement does not couple the

isolated states to other states (such as, for example, those in which only a single particle has tunneled to another well) which would result in leaving the self-trapping regime.

In this section, we have developed the Hamiltonian (3.6), which describes a two-level system symmetrically coupled to a third level with a different energy. A time-dependent driving is applied to the central well, bringing its energy from the top of the spectrum down to the bottom, producing an avoided crossing around the midpoint of the protocol. By following a geodesic trajectory in parameter space, the avoided crossing is parametrized so as to be as smooth as possible, thereby minimizing the risk of unwanted transitions caused by the inertia of the evolving system. Moreover, the addition of counterdiabatic terms proportional to Ω widens the gap so as to maintain adiabaticity, regardless of the evolution speed. Since this widening is proportional to the temporal variation of the central site's energy, the combination with a geodesic protocol makes the inertial term time-independent.

3.3 NOON state generation

The previous section enabled the development of the GCD protocol on the reduced Hamiltonian, which describes the system when it is placed in the self-trapping regime. In the ideal limit, no other state of the many-body spectrum contributes, and the dynamics are entirely restricted to three states. However, in a situation closer to experimental reality, coupling to intermediate states still exists and may impose certain limitations on the use of the proposed protocol. In particular, since the counterdiabatic Hamiltonian is defined in the basis of the states $|N,0,0\rangle$, $|0,N,0\rangle$, and $|0,0,N\rangle$, its direct transcription into the full many-body system would induce nonlocal couplings between the previously listed states. These couplings occur only perturbatively and cannot be used to emulate the terms required for counterdiabatic driving. Therefore, to generate NOON states in the real physical system, it will be necessary to emulate the action of the counterdiabatic term through experimentally accessible parameters in the Bose-Hubbard Hamiltonian, namely the interaction U, the onsite energy ε, and the tunneling rate J.

3.3.1 Implementation into the many-body system

To capture the action of the geodesic counterdiabatic driving, we assume a Bose-Hubbard model

$$\begin{aligned}\hat{H}(t) =& \frac{U_{\text{eff}}}{2}\hat{a}_c^\dagger\hat{a}_c^\dagger\hat{a}_c\hat{a}_c + \varepsilon_{\text{eff}}(t)\hat{a}_c^\dagger\hat{a}_c + \frac{U_{\text{eff}}}{2}\sum_{i=1}^{2}\hat{a}_i^\dagger\hat{a}_i^\dagger\hat{a}_i\hat{a}_i - \sum_{i=1}^{2}(J_{\text{eff}}\,\hat{a}_i^\dagger\hat{a}_c + J_{\text{eff}}^*\hat{a}_c^\dagger\hat{a}_i) \\ &+ \varepsilon_{\text{eff}}(t)\hat{a}_c^\dagger\hat{a}_c \end{aligned} \tag{3.76}$$

whose parameters $U_{\text{eff}}, J_{\text{eff}}, J_{\text{eff}}^*$, and ε_{eff} differ from U, J, and ε. In the self-trapping regime, the system described by Hamiltonian (3.76) can be characterized by the reduced Hamiltonian

$$H_{\text{red}}(U_{\text{eff}}, J_{\text{eff}}, \varepsilon_{\text{eff}}(t)) = \begin{pmatrix} \mathcal{E} & -\mathcal{J} & 0 \\ -\mathcal{J} & \tilde{\mathcal{E}} + \mathcal{N}\varepsilon(t) & -\mathcal{J} \\ 0 & -\mathcal{J} & \mathcal{E} \end{pmatrix} \tag{3.77}$$

where $\mathcal{E} = \mathcal{E}(U_{\text{eff}}, J_{\text{eff}})$, $\tilde{\mathcal{E}} = \tilde{\mathcal{E}}(U_{\text{eff}}, J_{\text{eff}})$, $\mathcal{N}(U_{\text{eff}}, J_{\text{eff}}) = N + \delta N(U_{\text{eff}}, J_{\text{eff}})$ and $\mathcal{J} = \mathcal{J}(U_{\text{eff}}, J_{\text{eff}})$ are obtained using perturbation theory for $NU/J \gg 1$. In these effective

parameters, we want to encapsulate the action of the counterdiabatic term by identifying the equations that constrain their expressions, that is, by identifying

$$H_{\text{red}}(U, J, \varepsilon(t)) + H_{\text{CD}} \stackrel{!}{=} H_{\text{red}}\left(U_{\text{eff}}, J_{\text{eff}}, \varepsilon_{\text{eff}}(t)\right). \tag{3.78}$$

The aim of this approach is to identify the values of U_{eff}, J_{eff}, and $\varepsilon_{\text{eff}}(t)$ that strictly satisfy the following equalities:

$$\mathcal{E}(U_{\text{eff}}, J_{\text{eff}}) = \mathcal{E}(U, J) \tag{3.79}$$
$$\tilde{\mathcal{E}}(U_{\text{eff}}, J_{\text{eff}}) + \mathcal{N}(U_{\text{eff}}, J_{\text{eff}})\varepsilon(U_{\text{eff}}, J_{\text{eff}}, t) = \tilde{\mathcal{E}}(U, J) + \mathcal{N}(U, J)\varepsilon(U, J, t) \tag{3.80}$$
$$\mathcal{J}(U_{\text{eff}}, J_{\text{eff}}) = \mathcal{J}(U, J) - i\Omega \tag{3.81}$$
$$\mathcal{J}^*(U_{\text{eff}}, J_{\text{eff}}) = \mathcal{J}(U, J) + i\Omega \tag{3.82}$$

Of course, the last two equations are equivalent for $\mathcal{J}(U_{\text{eff}}, J_{\text{eff}}) \in \mathbb{C}$.

Using the expressions of the perturbative functions developed in the previous section, Eq. (3.81) can be rewritten as

$$\begin{aligned} \frac{N J_{\text{eff}}^N}{(N-1)! U_{\text{eff}}^{N-1}} &= \frac{N J^N}{(N-1)! U^{N-1}} - i\Omega \\ \Leftrightarrow J_{\text{eff}} &= U_{\text{eff}}^{(N-1)/N} \left[\frac{J^N}{U^{N-1}} - i\frac{(N-1)!\Omega}{N} \right]^{1/N}. \end{aligned} \tag{3.83}$$

Using the definition of the perturbative functions (3.41) and (3.42), equation (3.79) yields

$$U_{\text{eff}} = \frac{\displaystyle\sum_{i=0}^{2} \alpha_i \frac{J^{2i}}{U^{2i-1}}}{\displaystyle\sum_{j=0}^{2} \alpha_j \frac{|J_{\text{eff}}|^{2j}}{U_{\text{eff}}^{2j}}} \tag{3.84}$$

In particular, the modulus of the effective hopping can be rewritten so as to reveal hidden dependence on U_{eff}:

$$|J_{\text{eff}}|^2 = U_{\text{eff}}^{(2N-2)/N} \left[\left(\frac{J^N}{U^{N-1}} \right)^2 + \left(\frac{(N-1)!\Omega}{N} \right)^2 \right]^{1/N}. \tag{3.85}$$

and writing

$$B^2 = \left[\left(\frac{J^N}{U^{N-1}} \right)^2 + \left(\frac{(N-1)!\Omega}{N} \right)^2 \right]^{1/N}, \tag{3.86}$$

one can obtain a self-consistent expression to determine U_{eff}:

$$U_{\text{eff}} = \frac{\displaystyle\sum_{i} \alpha_i \frac{J^{2i}}{U^{2i-1}}}{\displaystyle\sum_{j} \alpha_j \, U_{\text{eff}}^{-2j/N} B^{2j}} \tag{3.87}$$

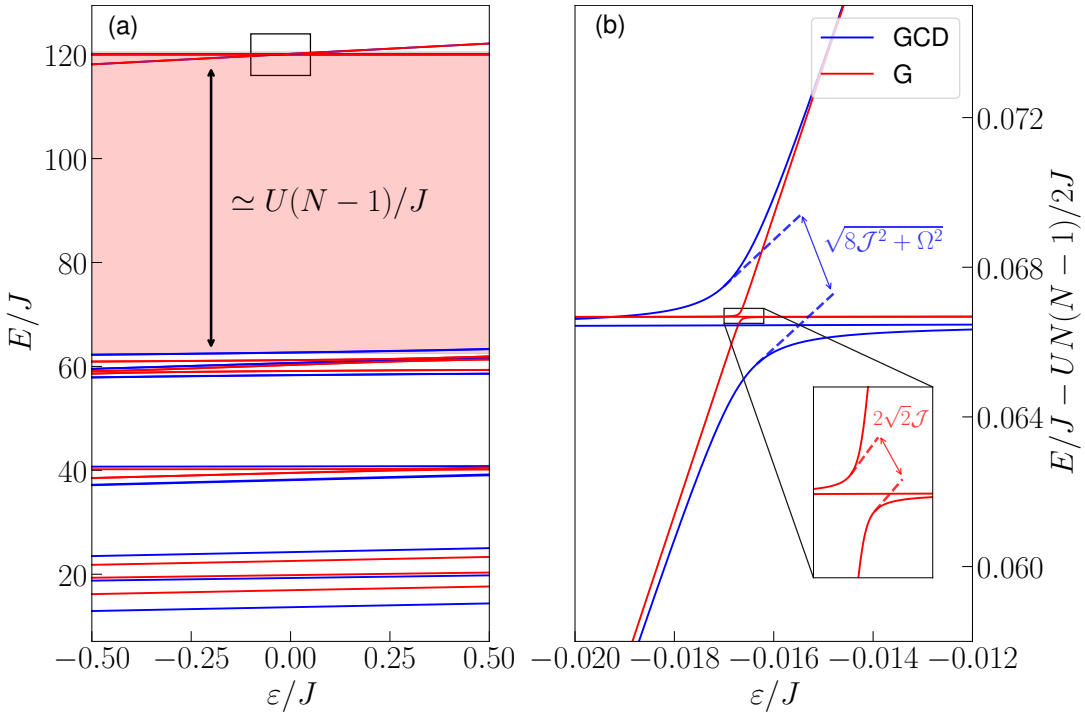

FIGURE 3.7: Spectrum of the Hamiltonian (3.76) in the case of geodesic counterdiabatic driving (GCD, blue) and geodesic driving only (G, red), for $N = 4$ particles, $T = 10^3\hbar/J$, and $U = 20J$. In panel (a), one clearly verifies the existence of the protective gap $\simeq U(N-1)/J$. A black rectangle highlights the region zoomed in panel (b). One indeed observes a widening of the avoided crossing in the case of a GCD protocol compared to simple geodesic driving. As a result, the adiabatic driving is greatly simplified and allows the adiabatic creation of NOON states much more rapidly.

which can be solved iteratively. Finally, thanks to Eqs. (3.85) and (3.87), we can determine the remaining parameter:

$$\varepsilon_{\text{eff}}(t) = \sum_{i=0} \frac{\tilde{\alpha}_i}{\mathcal{N}(U_{\text{eff}}, J_{\text{eff}})} \left[\frac{J^{2i}}{U^{2i-1}} - \frac{|J_{\text{eff}}|^{2i}}{U_{\text{eff}}^{2i-1}} \right] + \frac{\mathcal{N}(U,J)}{\mathcal{N}(U_{\text{eff}}, J_{\text{eff}})} \varepsilon(t). \tag{3.88}$$

Thus, Eqs. (3.85), (3.87), and (3.88) analytically determine the adjustment of the physical parameters required to emulate the counterdiabatic Hamiltonian within the full Bose-Hubbard system (3.76).

It is important to emphasize that these expressions are valid for any perturbative order, the only necessary ingredients being the coefficients α_i and $\tilde{\alpha}_i$. The use of a geodesic control enables the definition of the GCD protocol and, in particular, allows U_{eff} and J_{eff} to be defined as time-independent. Clearly, such an economy of control resources is crucial when the goal of the study is to devise an experimentally realizable method. Likewise, the effective geodesic driving ε_{eff} differs from the original parameter ε only by a time-independent shift.

3.3.2 Spectrum

The use of GCD on the Bose-Hubbard Hamiltonian, through the effective parameters U_{eff}, J_{eff}, and $\varepsilon_{\text{eff}}(t)$, makes it possible to encapsulate the action of a counterdiabatic Hamiltonian acting on the Hilbert subspace defined by the states $|N,0,0\rangle$, $|0,N,0\rangle$,

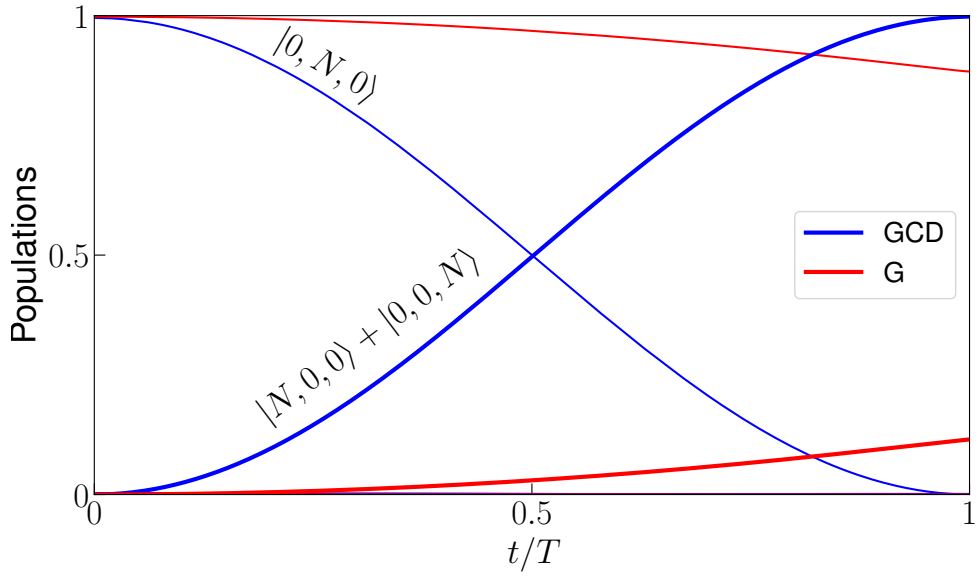

FIGURE 3.8: Detection probabilities for a fixed total protocol time $T = 3 \times 10^3 \hbar/J$. Thick curves indicates the probability of finding the system in the state $|\text{NOON}\rangle = (|N,0,0\rangle + |0,0,N\rangle)/\sqrt{2}$, while thin curves relates to the probability of measuring the state $|0,N,0\rangle$. One can observe a nearly perfect transition with the GCD method, in contrast to method G, which only attains about 10% of population inversion.

and $|0,0,N\rangle$. The action of an HCD widens the gap occurring at the avoided crossing, which is inversely proportional to the time required to reach adiabaticity, that is, the time needed for the system to evolve along the eigenvectors of the Hamiltonian that defines it. We now proceed to study the structure of the spectrum of Hamiltonian (3.76).

In Fig. 3.7, the spectrum of Hamiltonian (3.76) is shown for the effective parameters (blue, GCD) and for the case where $U_{\text{eff}} = U$, $\text{Re}\{J_{\text{eff}}\} = J$, $\text{Im}\{J_{\text{eff}}\} = 0$, and $\varepsilon_{\text{eff}} = \varepsilon$, i.e., when only geodesic driving (G) is considered (red). The effect of GCD is most clearly observed in the zoomed-in view of Fig. 3.7(b), where the avoided crossing in blue is significantly larger than the one in red. This difference can be easily understood within the reduced model focusing on the states of interest. The minimum gap (i.e. when $\mathcal{N}\varepsilon = -(\tilde{\mathcal{E}} - \mathcal{E})$) has the expression $\sqrt{8(\mathcal{J}^2 + \Omega^2)}$ in the case of GCD driving. It is evident that the action of Ω, which is inversely proportional to the total protocol time T, dictates the widening of the gap. The ratio of the level spacing at the minimum gap between G and GCD driving is $\sqrt{\mathcal{J}^2/(\mathcal{J}^2 + \Omega^2)}$.

As a reminder, the three-state dynamics are only possible thanks to the protective gap (3.4). Since this gap is proportional to $\simeq U(N-1)$, it is necessary that the modification of the energy levels (and in particular, the widening of the gap) remain smaller than the protective gap, otherwise the system would leave the self-trapping regime.

3.3.3 Dynamics

The dynamics generated by Hamiltonian (3.76) for $N = 4$ and $U = 20J$ are shown in Fig. 3.8, for geodesic driving (G, red) and for the GCD protocol (blue), where the initial state of the system is $|\psi(0)\rangle = |0,N,0\rangle$. Only the initial state and the NOON superposition $|N,0,0\rangle + |0,0,N\rangle$ appear in the time evolution, consistent with the self-trapping regime. In particular, one observes that a NOON state with a fidelity

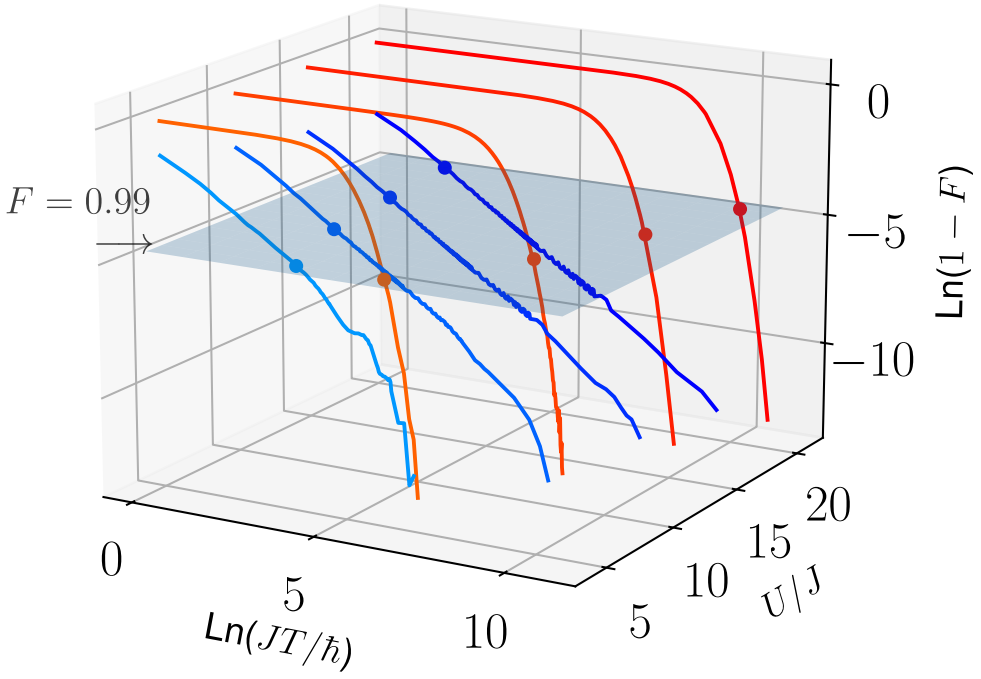

FIGURE 3.9: Infidelity $1-F$ as a function of the protocol time T for $N = 4$ and $U/J = 5, 10, 15$ and 20. The fidelity F is defined as the closeness of the system state to the NOON state at the end of the driving protocol. The GCD method (blue curves) achieves a NOON state for $U = 20J$ with a fidelity $F > 0.99$ after $T \simeq 10\hbar/J$, whereas the G method (red curves) requires a significantly longer time exceeding $T \simeq 3 \times 10^4\hbar/J$. The plane related to a fidelity of $F = 0.99$ is depicted in blue and color dots mark its intersection with the infidelity curves.

close to 1 is obtained after a time $T = 3 \times 10^3\hbar/J$ using the GCD protocol, whereas only about $\approx 10\%$ of the population reaches the NOON state when using the initial parameters U, J, and ε. We will show next that the GCD protocol can be a lot faster while still guaranteeing close to unit purities for the obtained NOON state.

If we define the fidelity as the overlap between the final state of the system and the NOON state, $F = |\langle \text{NOON}|\psi(T)\rangle|^2$, we can determine the time required to reach given fidelity thresholds for the purity of the obtained NOON state. In particular, we can analyze how the fidelity as a function of the total protocol time T behaves with respect to the interaction-to-hopping ratio U/J, and therefore with respect to the self-trapping regime. Figure 3.9 displays the numerically computed infidelity $1 - F$ as a function of the total protocol time $JT/\hbar$ for $N = 4$ and different values of U/J. This infidelity is defined as $1 - F$, with $F = |\langle \text{NOON}|\psi(T)\rangle|^2$ and $|\text{NOON}\rangle = (|N, 0, 0\rangle + |0, 0, N\rangle)/\sqrt{2}$, where $|\psi(t)\rangle$ is the time-dependent state vector of the system starting from $|\psi(0)\rangle = |0, N, 0\rangle$. We observe that the fidelity $F = 0.99$ is reached much more rapidly with the GCD protocol than with simple geodesic driving. In particular, the separation between the times at which each protocol reaches the $F = 0.99$ plateau provides a direct measure of how much more efficient one protocol is compared to the other.

To quantify the impact of counterdiabatic driving, we define by T_G and T_{GCD} the protocol time needed to reach the fidelity $F = 0.99$ with the geodesic protocol (G) and the combined geodesic and counterdiabatic driving (GCD), respectively. For $N = 4$ and $U/J = 20$, a protocol speed gain factor $T_G/T_{GCD} \simeq 10^4$ is obtained.

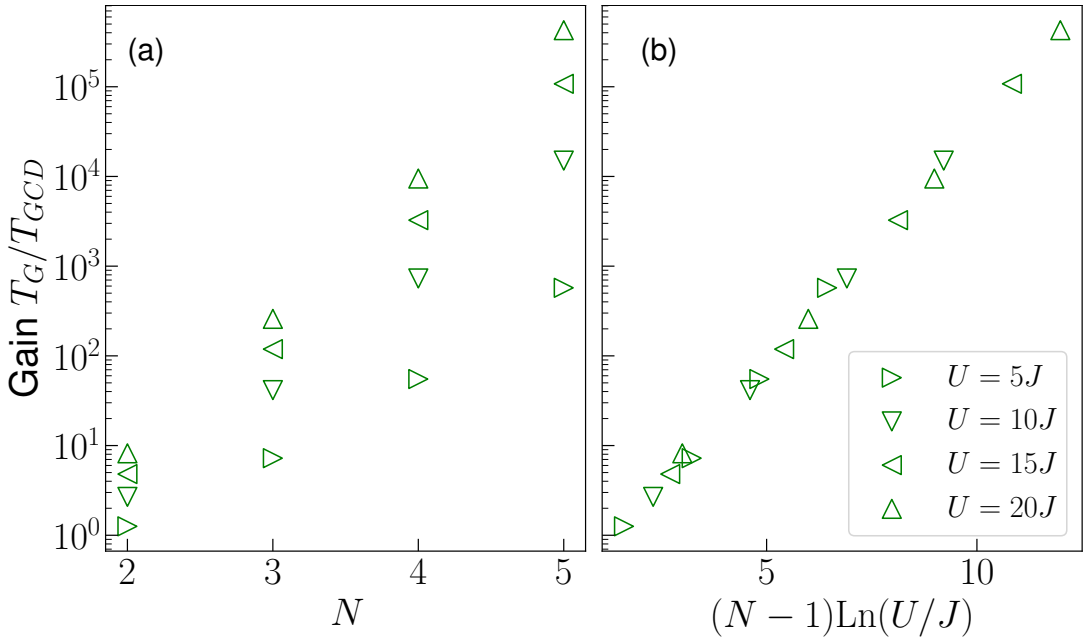

FIGURE 3.10: (a),(b) Gain ratio between the times required to achieve a fidelity of $F = 0.97$ using the G and GCD methods for various interaction strengths, as a function of the number of particles. We find an exponential increase in efficiency $T_G/T_{GCD} \sim (U/J)^{N-1}$ when using the GCD method compared to the G method.

3.3.4 Parameter dependence

In order to study how the gain T_G/T_{GCD} behaves as a function of the relevant parameters of our system, we compare the time required to obtain a NOON state with purity 0.99 for different particle numbers N, as well as for various values of the ratio U/J characterizing the self-trapping regime. The purpose of this analysis is to understand what acceleration of the procedure can realistically be expected, and in particular how deep into the self-trapping regime one must be.

In Fig. 3.10(a), several values of the gain are shown as a function of the particle number N for different values of the ratio U/J on a logarithmic scale. In panel (b), these points are plotted as a function of $(N-1)\mathrm{Ln}(U/J)$, revealing a straight line in the graph. This collapse of the points demonstrates that the ratio T_G/T_{GCD} behaves as an exponential function of N and as a power law in the interaction strength U, confirming the early intuition developed using the reduced Hamiltonian.

The exponential dependence of the gain on particle number is particularly important, as it shows that the exponential growth of the entanglement time originally present in the collective tunneling mechanism can be significantly mitigated through the use of the GCD protocol. Whereas it becomes experimentally difficult to adiabatically manipulate large particle numbers due to the extremely long timescales required for adiabaticity, the implementation of a counterdiabatic protocol combined with geodesic driving counteracts this exponential growth.

3.4 Ultracold atoms in a star-shaped optical lattice

In this section, we extend the framework previously developed for the creation of NOON states in two-mode systems in order to address the generation of more exotic multimode entangled states. Among these states, a particularly representative example is the triple-NOON state, defined as the superposition $|N,0,0\rangle + |0,N,0\rangle + |0,0,N\rangle$, which constitutes a natural generalization of the NOON state to three modes and illustrates the emergence of high-dimensional multipartite entanglement [36, 147–150]. Such states have attracted increasing interest in various contexts, notably in artificial optical lattices or triangular superlattices, where suitable geometric configurations open the way to a richer exploration of multimode entanglement as well as new strategies for generating non-classical quantum states [7, 151, 152].

However, the aim of this section goes beyond a simple adaptation of the NOON-state creation protocol to triple-NOON states. We highlight a fundamental structural property of the Bose-Hubbard model when it is defined on a so-called star-like lattice, i.e., a geometry in which a central site is connected in a strictly symmetric manner to a set of L peripheral sites [153–155]. This symmetry, still largely underexploited in the literature, turns out to be a key ingredient for reducing the problem to an effective dynamics equivalent to that of a two-level system, and this independently of the total number of outer sites. In other words, the Hilbert space associated with the L peripheral modes can be contracted into a single collective mode, such that the complexity of the system no longer depends on L. This reduction not only enables an analytical understanding of the system's dynamics, but also allows the techniques of geodesic counterdiabatic driving developed for the bimodal NOON state to be directly transferred.

Thanks to this symmetry, we will show that the procedure for generating NOON states can be extended to the creation of multimode states such as triple-, quadruple-, or quintuple-NOON states, by exploiting the fact that each of these states corresponds to the coherent distribution of all particles into the equivalent modes of the lattice. The geometric formalism introduced in the previous chapter will remain central, but it will here be applied in an effective space whose structure is radically simplified by the symmetry of the lattice.

To simplify the notation in the developments that follow, we introduce a useful convention regarding Fock states. The central site, when it contains N particles, will be written in the form $|N;0,0,0,\ldots\rangle$, where the semicolon explicitly separates the occupation of the central site from those of the L outer sites. However, it is crucial to keep in mind that this central site is symmetrically coupled to all of the L peripheral sites, and that this symmetry will dictate all of the analytical reductions and results presented in this chapter.

3.4.1 (L+1)-sites Bose-Hubbard model

The natural generalization of Hamiltonian (3.1) to describe a larger number of outer sites considers a central well with an onsite energy $\varepsilon(t)$, symmetrically coupled to a set of L outer sites. The particles in the same site interact with a strenght U and can tunnel from the central site to outer wells (or the inverse path) with a hopping rate J.

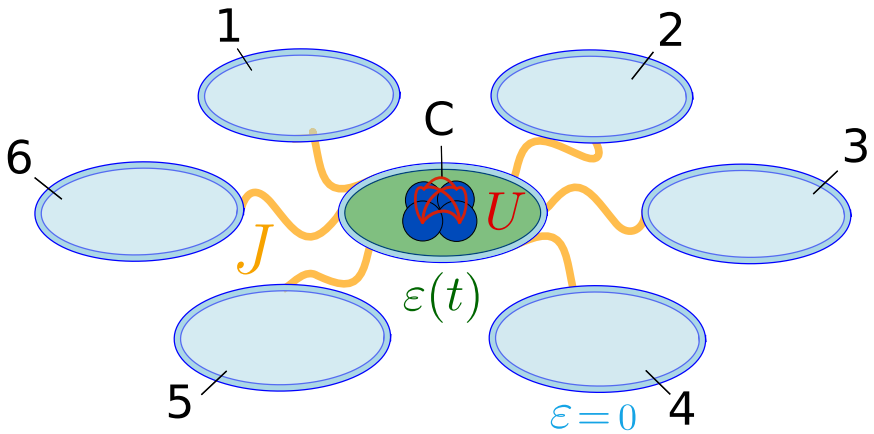

FIGURE 3.11: Schematic representation of the star-shaped Bose-Hubbard model for $L = 6$ and a central initially populated well. The bosons can tunnel from the central well to any of the outer wells with a hopping rate J. Particles localized in the same well present an interaction U. Initially, all bosons are localized in the central well, whose energy ε is isolated far from the rest of the spectrum. Over time, the energy of the central well is varied by a function $\varepsilon(t)$ to induce an adiabatic transfer of the system's state to the desired coherent superposition $|\text{L-NOON}\rangle$. At the end of the protocol, the central well is again isolated from the rest of the spectrum, leaving only the entangled state across all L wells.

Such a system is described by the Bose-Hubbard Hamiltonian

$$\hat{H}(t) = \frac{U}{2}\sum_{i=1}^{L}\hat{a}_i^\dagger\hat{a}_i^\dagger\hat{a}_i\hat{a}_i - J\sum_{i=1}^{L}\left(\hat{a}_c^\dagger\hat{a}_i + \hat{a}_i^\dagger\hat{a}_c\right) + \frac{U}{2}\hat{a}_c^\dagger\hat{a}_c^\dagger\hat{a}_c\hat{a}_c + \varepsilon(t)\hat{a}_c^\dagger\hat{a}_c. \tag{3.89}$$

This Hamiltonian is invariant under permutations of the outer sites because all their energies are equal, but the central well (denoted by the letter c) has a nonzero onsite energy. Figure 3.11 shows such a system for $L = 6$, where six outer sites are symmetrically coupled to a site with energy $\varepsilon(t)$.

The structure of the spectrum of Hamiltonian (3.89) has the same form as that of the three-site Hamiltonian (3.1), still with a conserved total number of particles N. The dimension $\mathcal{D}^{(L)}(\mathcal{H})$ of the Hilbert space $\mathcal{H}$ is given by [8, 10, 12],

$$\mathcal{D}^{(L)}(\mathcal{H}) = \frac{(N+L)!}{N!\,L!}. \tag{3.90}$$

When all hopping is forbidden ($J = 0$), the particles are confined to their respective sites and the different eigenenergies of the Hamiltonian result solely from the interaction between bosons on the same site:

$$\epsilon(n_c; n_1, n_2, ...) = \frac{U}{2}\left(\sum_{i=1}^{L} n_i(n_i - 1) + n_c(n_c - 1)\right) \tag{3.91}$$

where n_c is the number of particles in the central well, and the n_i are the number of particles in site i. In the case of zero hopping, Eq. (3.91) gives the exact energies of the system, and the eigenvectors are the Fock states. In this context, the states in which all particles are localized in the same well, whether it is the central site or one of the outer ones, are isolated from the rest of the spectrum and protected by a gap of the form

$$\epsilon(N; 0, 0, \ldots) - \epsilon(N-1; 1, 0, \ldots) = U(N-1). \tag{3.92}$$

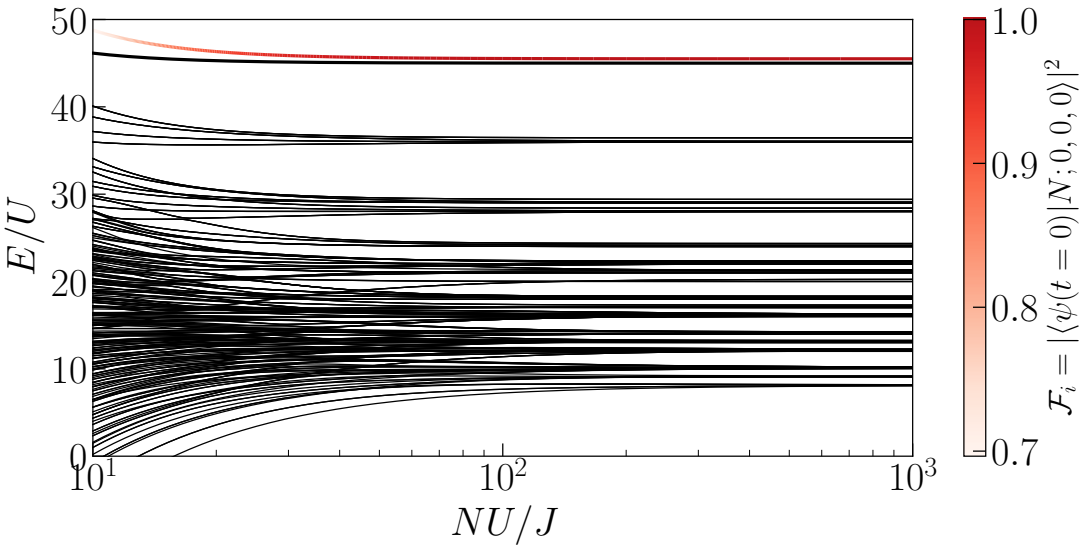

FIGURE 3.12: (a) Spectrum as a function of NU/J for $N = 10$, $L = 3$ and $\varepsilon = 0$. It is clearly possible to define a self-trapping regime, within which several effectively separable states in the energy spectrum can be identified. In these subsystems, the size of the Hilbert space is significantly reduced, allowing for the determination of a simplified Hamiltonian. The validity of the approximation can be quantified via the overlap $F_i = |\langle\psi(t=0)|N;0,0,0\rangle|^2$, depicted in a red fade, between the initial state $|\psi(0)\rangle$ and the Fock state having all the bosons located in the central well.

With the aim of defining a reduced Hamiltonian describing the dynamics occurring among the $L+1$ levels, the hopping will be taken to be slightly nonzero so as to preserve the properties that are convenient for us (in particular, the gap (3.92)) while still allowing the populations to move collectively between the sites.

3.4.2 Self-trapping regime

As in the three-site case, we will consider a regime where the hopping is nonzero but small compared to the interaction: $NU/J \gg 1$. In particular, for $\varepsilon = 0$ it is possible to quantify how deep we are in the self-trapping regime by projecting the eigenvector of Hamiltonian (3.89) associated with the highest energy onto the Fock state in which all particles are located in the central well. Indeed, if the levels of interest are sufficiently isolated from the rest of the spectrum, they must be close to the corresponding Fock states.

As an example, let us consider the case where a central well is surrounded by $L = 3$ wells symmetrically coupled to it. Figure 3.12 illustrates the evolution of the energy levels as a function of the ratio NU/J, for $L = 3$ and $N = 10$. Beyond a certain value of this ratio, the highest-energy levels become completely isolated from the rest of the spectrum, and we enter the self-trapping regime. This parameter region can be characterized by the proximity of the highest-energy eigenstate of Hamiltonian (3.89) in which the system is prepared at $t = 0$ to the Fock state $|N;0,0,0\rangle$ corresponding to all bosons being in the central well. In this figure, one observes that the overlap $|\langle\psi(t=0)|N;0,0,0\rangle|^2$ is already close to unity for a ratio $NU/J \approx 50$ with $N = 10$. It is therefore clear that the isolation of the relevant states becomes increasingly achievable with a large number of particles.

In particular, a gap of width $U(N-1)$ protects the system's highest energy levels

from the influence of other states, allowing its temporal evolution to be restricted to the states nearest to the initial condition. In this self-trapping regime, an adiabatic driving can be applied to the central well to induce energy level crossings and create a gap that enables the generation of entangled states.

3.5 Generalized reduced model

In the self-trapping regime for L outer sites, it is possible to describe the dynamics with a reduced model involving only two levels, for any L. Indeed, since the phenomenon of collective tunneling does not distinguish any outer site from the others, the particles must tunnel collectively and symmetrically toward the L sites. Consequently, if their energies are the same and if they are all coupled in the same way to the central well, there is no reason to treat them differently. This intuition is strongly supported by the results obtained in the case $L = 2$ studied in this chapter previously. In Fig. 3.7, one sees that only two of the three top energy levels are involved in the adiabatic driving. The antisymmetric superposition is not involved in the driving and does not participate in the dynamics. Similarly, in Fig. 3.8, the populations of the two outer wells are inevitably identical due to the symmetry of the system. Thus, in no case is it possible to distinguish the outer sites.

In this context, it becomes clear that there exists a fundamental symmetry in the type of systems described by Hamiltonian (3.89) in the self-trapping regime, which will allow us to generalize the reduced Hamiltonian obtained in the previous chapter.

3.5.1 Perturbation theory

With the aim of modeling the reduced dynamics occurring during the time evolution of the Bose-Hubbard Hamiltonian (3.89) in the self-trapping regime $NU/J \gg 1$, we will determine the various matrix elements of the reduced Hamiltonian.

The symmetry of the system rests on two different states: the first, in which all bosons are in the central well, and the second, in which all bosons occupy a superposed state over the L sites, a state $|\text{L-NOON}\rangle \equiv (|0; N, 0, \ldots\rangle + |0; 0, N, \ldots\rangle + \ldots)/\sqrt{L}$. Hence, in view of the symmetry of the system, the reduced Hamiltonian can be written in the two-state basis $\{|N; 0, 0, \ldots\rangle, (|0; N, 0, \ldots\rangle + |0; 0, N, \ldots\rangle + \ldots)/\sqrt{L}\}$ as

$$H_{\text{red}}(U, J, t) = \begin{pmatrix} \tilde{\mathcal{E}} + \mathcal{N}\varepsilon(t) & -\sqrt{L}\,\mathcal{J} \\ -\sqrt{L}\,\mathcal{J} & \mathcal{E} \end{pmatrix}, \tag{3.93}$$

where $\mathcal{E} = \mathcal{E}(U, J)$, $\tilde{\mathcal{E}} = \tilde{\mathcal{E}}(U, J)$, $\mathcal{N}(U, J) = N + \delta N(U, J)$ and $\mathcal{J} = \mathcal{J}(U, J)$ are to be obtained using perturbation theory for $NU/J \gg 1$. Once again, since the central well is connected to L other sites, its energy $\tilde{\mathcal{E}}$ is perturbatively different from that of the outer wells $\mathcal{E}$. The effective coupling $\mathcal{J}$ is modified only by a factor $\sqrt{L}$, which arises from the normalized definition of the vector $|\text{L-NOON}\rangle$.

The calculation of the perturbative functions will have the same structure as for the case $L = 2$. In particular, the intuition developed regarding the symmetry between the states $|N - 1; 1, 0\rangle$ and $|N - 1; 0, 1\rangle$ had led us to define a wavefunction $\Psi_1 \equiv \Psi_{N-1;1,0} + \Psi_{N-1;0,1}$, which greatly simplified the calculations. In fact, we were

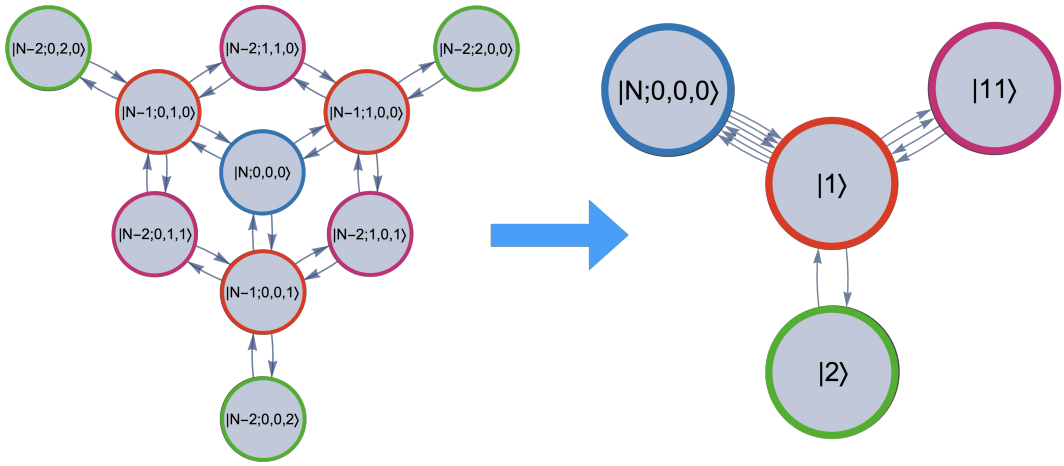

FIGURE 3.13: Perturbative diagram of the energy corrections to the state $|N;0,0,0\rangle$, for $L = 3$, at fourth order. Each path contributes to the state's energy in the manner of a Feynman path integral. Each arrow represents a possible transition path and carries a probabilistic amplitude proportional to J/U. The correction to the energy of the state $|N;0,0,0\rangle$ is given by the sum over all paths of length p (where p corresponds to the desired perturbative order) that start at and return to this state. The number of such paths (24 for $|N;0,0,0\rangle$ in this example) is determined by the p^{th} power of the adjacency matrix associated with the diagram. The irreducible form of the adjacency matrix provides the most efficient reduction of the system of equations via the states $|i\rangle \equiv |N-i;i,0,0\rangle + |N-i;0,i,0\rangle + |N-i;0,0,i\rangle$, for $i = 1, 2$ and $|11\rangle \equiv |N-2;1,1,0\rangle + |N-2;1,0,1\rangle + |N-2;0,1,1\rangle$.

already working with the underlying symmetry associated with the outer wells.

In Fig. 3.13, we illustrate the perturbative diagram for the case $L = 3$ at fourth order of perturbation theory. The diagram on the left shows all the states through which the system can pass during a fourth-order perturbative process, which can only involve four transitions. Such a diagram is called an adjacency graph, which is a way of representing an adjacency matrix. The latter encodes the connections between the nodes of a graph and, in particular, makes it possible to determine the number of possible paths with a given number of allowed steps via the power of the matrix. Thus, the diagram on the left was constructed from the adjacency matrix A, which, in the basis $\{|N;0,0,0\rangle,\ |N-1;1,0,0\rangle,\ |N-1;0,1,0\rangle,\ |N-1;0,0,1\rangle,\ |N-2;2,0,0\rangle,\ |N-2;0,2,0\rangle,\ |N-2;0,0,2\rangle,\ |N-2;1,1,0\rangle,\ |N-2;1,0,1\rangle,\ |N-2;0,1,1\rangle\}$, takes the form

$$A = \begin{pmatrix} 0 & 1 & 1 & 1 & 0 & 0 & 0 & 0 & 0 & 0 \\ 1 & 0 & 0 & 0 & 1 & 0 & 0 & 1 & 1 & 0 \\ 1 & 0 & 0 & 0 & 0 & 1 & 0 & 1 & 0 & 1 \\ 1 & 0 & 0 & 0 & 0 & 0 & 1 & 0 & 1 & 1 \\ 0 & 1 & 0 & 0 & 0 & 0 & 0 & 0 & 0 & 0 \\ 0 & 0 & 1 & 0 & 0 & 0 & 0 & 0 & 0 & 0 \\ 0 & 0 & 0 & 1 & 0 & 0 & 0 & 0 & 0 & 0 \\ 0 & 1 & 1 & 0 & 0 & 0 & 0 & 0 & 0 & 0 \\ 0 & 1 & 0 & 1 & 0 & 0 & 0 & 0 & 0 & 0 \\ 0 & 0 & 1 & 1 & 0 & 0 & 0 & 0 & 0 & 0 \end{pmatrix}.$$

This matrix is read as follows. The diagonal element corresponding to $|N;0,0,0\rangle$ indicates that there is no one-step path connecting this vector to itself. On the other

hand, the three elements in the row corresponding to this state indicate that it is possible, in one step, to move to the nodes $|N-1;1,0,0\rangle$, $|N-1;0,1,0\rangle$, and $|N-1;0,0,1\rangle$. In the case of our perturbative diagram, the matrix is symmetric because any path can be taken in either direction, and in particular it must be possible to perform a back-and-forth transition in order to account for the modification of the energies of $|N;0,0,0\rangle$ by the perturbative expansion.

The number of paths connecting two nodes in a given number of steps p is given by the power of the matrix $(A)^p$. Thus, for fourth order, we have

$$(A)^4 = \begin{pmatrix} 24 & 0 & 0 & 0 & 8 & 8 & 8 & 16 & 16 & 16 \\ 0 & 24 & 20 & 20 & 0 & 0 & 0 & 0 & 0 & 0 \\ 0 & 20 & 24 & 20 & 0 & 0 & 0 & 0 & 0 & 0 \\ 0 & 20 & 20 & 24 & 0 & 0 & 0 & 0 & 0 & 0 \\ 8 & 0 & 0 & 0 & 4 & 2 & 2 & 6 & 6 & 4 \\ 8 & 0 & 0 & 0 & 2 & 4 & 2 & 6 & 4 & 6 \\ 8 & 0 & 0 & 0 & 2 & 2 & 4 & 4 & 6 & 6 \\ 16 & 0 & 0 & 0 & 6 & 6 & 4 & 12 & 10 & 10 \\ 16 & 0 & 0 & 0 & 6 & 4 & 6 & 10 & 12 & 10 \\ 16 & 0 & 0 & 0 & 4 & 6 & 6 & 10 & 10 & 12 \end{pmatrix}.$$

There are therefore 24 paths that connect $|N;0,0,0\rangle$ with itself, each of exactly 4 steps long.

Even more powerfully, it is possible to obtain the way to fold the graph, as done for the case $L = 2$, through the irreducible representations (irreps) of the matrix. Irreps are the elementary building blocks from which any representation of a group can be decomposed. A representation is said to be irreducible when it is impossible to find a non-trivial invariant subspace: it can no longer be simplified or reduced into smaller blocks. Thus, decomposing a representation into irreps amounts to expressing the action of a group in its simplest form, much like factorizing a matrix into independent elementary blocks. This is exactly what we can do by identifying that the matrix is invariant under the symmetry group S_3, which permutes the three "arms" visible in the diagram (3.13). In this case, one can rewrite the matrix A in the irreducible representation M in the basis $\{|N;0,0,0\rangle, |1\rangle, |11\rangle, |2\rangle\}$, where

$$|1\rangle = |N-1;1,0,0\rangle + |N-1;0,1,0\rangle + |N-1;0,0,1\rangle \tag{3.94}$$

$$|2\rangle = |N-2;2,0,0\rangle + |N-2;0,2,0\rangle + |N-2;0,0,2\rangle \tag{3.95}$$

$$|11\rangle = |N-2;1,1,0\rangle + |N-2;1,0,1\rangle + |N-2;0,1,1\rangle. \tag{3.96}$$

The matrix M has then the form

$$M = \begin{pmatrix} 0 & 3 & 0 & 0 \\ 3 & 0 & 2 & 1 \\ 0 & 2 & 0 & 0 \\ 0 & 1 & 0 & 0 \end{pmatrix},$$

whose adjacency graph is the diagram on the right of Fig. 3.13. We see that there are three paths connecting $|N;0,0,0\rangle$ to $|1\rangle$, two connecting $|1\rangle$ to $|11\rangle$ and only one connecting $|1\rangle$ to $|2\rangle$. In this way, we have been able to reduce the number of required equations while keeping track of the coefficients that arise from the folding. In particular, by generalizing this procedure, it is possible to extract the coefficients

for L outer sites.

Perturbative functions

We now compute the function $\tilde{\mathcal{E}}$ describing the perturbative modification of the energy of the central well in the case of L outer wells. By applying the folding of the perturbative diagram, we define the following states

$$\Psi_1 = \Psi_{N-1;1,0,0,\dots} + \Psi_{N-1,0,1,0,\dots} + \dots, \tag{3.97}$$
$$\Psi_2 = \Psi_{N-2;2,0,0,\dots} + \Psi_{N-2;0,2,0,\dots} + \dots, \tag{3.98}$$
$$\Psi_{11} = \Psi_{N-2;1,1,0,\dots} + \Psi_{N-2;1,0,1,\dots} + \dots. \tag{3.99}$$

From this, the time-independent Schrödinger equation gives, for the fourth order of perturbation theory,

$$(E^{(4)} - E_{N;0,0,\dots})\Psi_{N;0,0,\dots} = -\mathcal{J}_{N,0}\Psi_1 \tag{3.100}$$
$$(E^{(2)} - E_{N-1;1,0,\dots})\Psi_1 = -L\mathcal{J}_{1,N-1}\Psi_{N;0,0,\dots} - \mathcal{J}_{N-2,2}\Psi_2 - 2\mathcal{J}_{N-1,0}\Psi_{11} \tag{3.101}$$
$$(E^{(0)} - E_{N-2;2,0,..})\Psi_2 = -\mathcal{J}_{2,N-2}\Psi_1 \tag{3.102}$$
$$(E^{(0)} - E_{N-2;1,1,\dots})\Psi_{11} = -(L-1)\mathcal{J}_{1,N-2}\Psi_1. \tag{3.103}$$

Solving for $\Psi_{N;0,0,,\dots}$, and expanding for $U \gg J, \varepsilon$, we obtain

$$\tilde{\mathcal{E}}^{(4)} = \frac{NLJ^2}{U(N-1)} - \frac{NLJ^4(L(N-2)^2-(N-1)^2)}{(N-1)^3(N-2)(2N-3)U^3} - \frac{NLJ^2\varepsilon}{(N-1)^2U^2} - \frac{NLJ^4\varepsilon((N-1)^2(19+N(8N-25)) - L(N-2)(16+N(4N-17)))}{(N-1)^4(N-2)^2(2N-3)^2U^4}. \tag{3.104}$$

Similarly, for the energy of one of the outer sites, we define the state

$$\Psi_1' = \Psi_{0;N-1,1,0,\dots} + \Psi_{0;N-1,0,1,\dots} + \dots. \tag{3.105}$$

Considering once again the Schrödinger equation at fourth order of perturbation theory, we have

$$(E^{(4)} - E_{0;N,0,0,\dots})\Psi_{0;N,0,0,\dots} = -\mathcal{J}_{N,0}\Psi_{1;N-1,0,0,\dots} \tag{3.106}$$
$$(E^{(2)} - E_{1;N-1,0,0,\dots})\Psi_{1;N-1,0,0,\dots} = -\mathcal{J}^*_{1,N-1}\Psi_{0;N,0,0,\dots} - \mathcal{J}^*_{1,0}\Psi_1' - \mathcal{J}_{N-1,1}\Psi_{2;N-2,0,0,\dots} \tag{3.107}$$
$$(E^{(0)} - E_{0;N-1,1,0,\dots})\Psi_1' = -(L-1)\mathcal{J}_{1,0}\Psi_{1;N-1,0,0,\dots} \tag{3.108}$$
$$(E^{(0)} - E_{2;N-2,0,0,\dots})\Psi_{2;N-2,0,0,\dots} = -\mathcal{J}_{2,N-2}\Psi_{1;N-1,0,0,\dots}. \tag{3.109}$$

Once solved for $\Psi_{0;N,0,0,,\dots}$, and expanded for $U \gg J, \varepsilon$, we obtain

$$\mathcal{E}^{(4)} = \frac{NJ^2}{U(N-1)} - \frac{NJ^4(N-L(N-2)-3)}{(N-1)^3(N-2)U^3} + \frac{NJ^2\varepsilon}{U^2(N-1)} + \frac{NJ^4\varepsilon\left(2L(N-2)^2 - N(N-9)+13\right)}{(N-1)^4(N-2)^2U^4} \tag{3.110}$$

The effective coupling $\mathcal{J}$ between the outer wells and the central well has no reason to change, since it involves only the tunneling between one well and another. It is

therefore still given by

$$\mathcal{J} = \frac{NJ^N}{(N-1)!\,U^{N-1}}. \tag{3.111}$$

As in the three-site case, in order to encapsulate the energy shift due to the motion of the central well, we define

$$\mathcal{N} = N\Bigg(1 - \frac{(L-1)J^2}{(N-2)^2U^2} + \frac{J^4}{(-1+N)^4(6-7N+2N^2)^2U^4} \tag{3.112}$$

$$\times \Big((3-2N)^2(13+(-9+N)N) + L^2(-2+N)^2(16+N(-17+4N)) \tag{3.113}$$

$$+ L(-91+N(231+N(-223+(97-16N)N)))\Big)\Bigg). \tag{3.114}$$

Thus, the reduced Hamiltonian (3.93) is complete and defined at fourth order for an arbitrary number L of outer sites. The resonance between the central well and the outer wells occurs at the moment when the driving function satisfies

$$\mathcal{N}\varepsilon(t) = -(\tilde{\mathcal{E}} - \mathcal{E}). \tag{3.115}$$

3.5.2 Geodesic counterdiabatic driving

Now that the reduced Hamiltonian has been determined perturbatively, it is possible to compute the quantities required to accelerate the adiabatic driving, using the geodesic counterdiabatic driving method developed earlier. In the context of the reduced Hamiltonian (3.93), the only nonzero component of the metric tensor (2.51) describing the geometry of the parameter space takes the form

$$g = \frac{2N^2L\mathcal{J}^2}{(4L\mathcal{J}^2 + (\tilde{\mathcal{E}} - \mathcal{E} + \mathcal{N}\varepsilon(t)^2)^2}. \tag{3.116}$$

The geodesic equation then makes it possible to determine the optimal trajectory to follow, which will minimize the instantaneous infidelity and thus enable fast adiabatic driving:

$$\mathcal{N}\varepsilon(t) = 2\sqrt{L}\,\mathcal{J}\tan(\alpha_i + (\alpha_f - \alpha_i)t/T) - (\tilde{\mathcal{E}} - \mathcal{E}) \tag{3.117}$$

where $\alpha_{i,f} = \tan^{-1}[(\tilde{\mathcal{E}} - \mathcal{E} + \varepsilon(t = t_{i,f}))/2\sqrt{L}\,\mathcal{J}]$ must be close to $\pm\pi/2$ to approach the asymptote of the tangent. This function yields a fast temporal evolution when the system is far from the central gap, and slows down significantly in its vicinity, thereby ensuring that the adiabaticity condition is best fulfilled precisely where the energy levels come closest. The geodesic trajectory is constructed to minimize the energy variance throughout the evolution. By matching the driving protocol to the structure imposed by the metric tensor, energy fluctuations are suppressed, particularly near the avoided crossing where the gap reaches its minimum. As a result, the likelihood of non-adiabatic transitions is reduced, leading to a smooth and well-controlled evolution.

The GCD protocol requires the calculation of the counterdiabatic terms associated with the Hamiltonian (3.93). Using definition (2.26), one obtains

$$\hat{H}_{\mathrm{CD}}(t) = \frac{\mathcal{N}\sqrt{L}\,\mathcal{J}\dot{\varepsilon}(t)}{4L\mathcal{J}^2 + (\tilde{\mathcal{E}} - \mathcal{E} + \mathcal{N}\varepsilon(t))^2}\hat{\sigma}_y \tag{3.118}$$

which we will denote as $\hat{H}_{\mathrm{CD}}(t) = \Omega(t)\hat{\sigma}_y$ where $\hat{\sigma}_y$ is the Pauli matrix. The new

factor $\sqrt{L}$ that was not present in Eq. (3.67) comes from the normalization of the state $|\mathrm{L-NOON}\rangle$. Substituting the explicit expression of $\varepsilon(t)$ into Eq. (3.118) yields the GCD protocol :

$$\Omega = \frac{\alpha_f - \alpha_i}{2T}. \tag{3.119}$$

The elements of $\hat{H}_{\mathrm{CD}}$ are, as anticipated, independent of time and also of the number of sites considered. The norm of $\hat{H}_{\mathrm{CD}}$ therefore depends solely on the total protocol time T, given that $\alpha_f - \alpha_i \approx -\pi$.
This result is justified by the form of $\hat{H}_{\mathrm{CD}}$. As we demonstrated in chapter 2, a relationship linking the counterdiabatic Hamiltonian and the metric tensor exist, namely through

$$\langle n|\hat{H}^2_{\mathrm{CD}}|n\rangle = -\hbar^2 g^{(n)}\dot{\varepsilon}(t)^2. \tag{3.120}$$

Thus, since $\hat{\sigma}_y^2 = \hat{1}$, any $\hat{H}_{\mathrm{CD}}$ proportional to $\hat{\sigma}_y$ will have time-independent elements if the driving $\varepsilon(t)$ satisfies the geodesic equation $g^{(n)}\dot{\varepsilon}^2 = \text{const}$.

The reduced Hamiltonian driving the system along its eigenstates in full adiabaticity is written as $H_{\mathrm{red}} + H_{\mathrm{CD}}$. The spectrum of this two-level Hamiltonian can be calculated exactly, and the energies are expressed as:

$$2E_{\pm} = \tilde{\mathcal{E}} + \mathcal{E} + \mathcal{N}\varepsilon(t) \pm \sqrt{4(L\mathcal{J}^2 + \Omega^2) + (\tilde{\mathcal{E}} - \mathcal{E} + \mathcal{N}\varepsilon(t))^2}. \tag{3.121}$$

Hence, the minimal gap will be expressed as $2\sqrt{L\mathcal{J}^2 + \Omega^2}$. It is then possible to estimate the time savings achieved with the use of the GCD protocol by comparing the minimal gap sizes:

$$T_G/T_{GCD} \sim \left(1 + \frac{\Omega^2}{L\mathcal{J}^2}\right)^{1/2}. \tag{3.122}$$

With Eq. (3.111), we can therefore conclude that the proposed method must exhibit, compared to geodesic driving alone, a time-saving gain that behaves as

$$T_G/T_{GCD} \sim \sqrt{1 + \left(\frac{\pi(N-1)!}{2\sqrt{L}NT}\frac{U^{N-1}}{J^N}\right)^2} \tag{3.123}$$

The exponential dependence of the gain on the particle number in the proposed protocol is of crucial importance for any implementation that is of interest for quantum metrology, where N should be as large as possible.

Reaching quantum speed limit

The Mandelstam-Tamm bound states that the standard time Δt for energy to transition from one system state to another cannot be smaller than $\pi\hbar/2\Delta E$ [51], in the case of a final state that is orthogonal to the initial one [134]. This fundamentally significant result provides a definition of the quantum speed limit, which is the maximum rate at which a system can evolve under an external perturbation. Applying this limit for our system and reintroducing the constant $\hbar$, we find that the minimum time follows the inequality

$$T \geq \frac{\pi\hbar}{2|\Omega|}. \tag{3.124}$$

This inequality imposes a constraint on the minimal value of Ω, which aligns precisely with the expression obtained earlier :

$$|\Omega| = \frac{\pi\hbar}{2T}. \tag{3.125}$$

We can thus conclude that the GCD protocol saturates the quantum speed limit.

3.6 Creating L-NOON states with GCD

In this section, we show how the GCD protocol overcomes enables the fast and robust creation of multi-mode NOON states. By dynamically reshaping the spectral gap, the GCD method provides a powerful and versatile tool for engineering L-NOON states in systems with an arbitrary number of modes.

As in the three modes case, to obtain an experimentally relevant protocol it is necessary to emulate the action of the counterdiabatic Hamiltonian through the physical parameters of the system, namely the interaction U, the hopping J, and the driving ε. Various ways to emulate H_{CD} were proposed [44, 123, 134, 156, 157]. Here, we define effective parameters U_{eff}, J_{eff}, and $\varepsilon_{\mathrm{eff}}$ through the identification

$$H_{\mathrm{red}}(U, J, \varepsilon(t)) + H_{\mathrm{CD}} \overset{!}{=} H_{\mathrm{red}}\left(U_{\mathrm{eff}}, J_{\mathrm{eff}}, \varepsilon_{\mathrm{eff}}(t)\right). \tag{3.126}$$

The equations constraining the parameters can be fully determined via the same path that was developped in Chapter III. In particular, by writing

$$\tilde{\mathcal{E}}(U, J) = \sum_{i=0}^{2} \tilde{\alpha}_i \frac{J^{2i}}{U^{2i-1}} \tag{3.127}$$

$$\mathcal{E}(U, J) = \sum_{i=0}^{2} \alpha_i \frac{J^{2i}}{U^{2i-1}}, \tag{3.128}$$

where the perturbative coefficients are given by

$$\alpha_0 = N(N-1)/2 = \tilde{\alpha}_0 \tag{3.129}$$

$$\alpha_1 = N/(N-1) = \tilde{\alpha}_1/L \tag{3.130}$$

$$\alpha_2 = -\frac{N(N - L(N-2) - 3)}{(N-1)^3(N-2)} \tag{3.131}$$

$$\tilde{\alpha}_2 = -\frac{NL(L(N-2)^2 - (N-1)^2)}{(N-1)^3(N-2)(2N-3)}. \tag{3.132}$$

Injecting the α_i and $\tilde{\alpha}_i$ coefficients in the definitions that were given in the case $L = 2$ (3.85, 3.87 and 3.88) yields the correct expressions of the effective parameters, up to the fourth order of perturbation theory. The only difference is coming from the L factor in the definitions of the coefficients.

The strength of this result lies in the fact that, thanks to the GCD protocol, it becomes possible to accelerate the adiabatic creation of states using physical parameters that remain constant over time. Thus, in the self-trapping regime, the Bose-Hubbard

Hamiltonian can be written as:

$$\hat{H}(t) = \frac{U_{\text{eff}}}{2}\sum_{i=1}^{L}\hat{a}_i^\dagger\hat{a}_i^\dagger\hat{a}_i\hat{a}_i - \sum_{i=1}^{L}\left(J_{\text{eff}}\,\hat{a}_c^\dagger\hat{a}_i + J_{\text{eff}}^*\,\hat{a}_i^\dagger\hat{a}_c\right) + \frac{U_{\text{eff}}}{2}\hat{a}_c^\dagger\hat{a}_c^\dagger\hat{a}_c\hat{a}_c + \varepsilon_{\text{eff}}(t)\hat{a}_c^\dagger\hat{a}_c, \tag{3.133}$$

which will describe an adiabatic temporal evolution along the eigenstates of the Hamiltonian (3.89), requiring only a modulation of the energy of the central well. Note that a complex hopping matrix element $J_{\text{eff}} \neq J_{\text{eff}}^*$ is required, which could be in practice implemented by a static gauge field creating a phase $\phi = \tan^{-1}(\Omega\hbar/\mathcal{J})$ between sites via, for example, Floquet engineering [15, 123, 124, 158–162].

Globally, the overall structure of the spectrum is only slightly altered, as the action of the counterdiabatic term primarily focuses on widening the gap. However, there are limitations. Since the effective parameters depend on Ω, which is itself inversely proportional to T, a protocol time that is too short may lead to complications. Indeed, proceeding too quickly would mean significantly altering the parameters and thus potentially deviating from the self-trapping regime. In particular, if the energy levels of interest are modified too strongly, they could become closer to the rest of the spectrum and thus exhibit interferences even with states lying a priori farther away in energy. The only contribution depending on the driving speed is Ω, which must be compared to the initial separation between the considered levels and the states $|N-1;1,0,...\rangle, |N-1;0,1,...\rangle, ...$, proportional to $U(N-1)/J$. Thus, knowing the expression of Ω in the case of geodesic counterdiabatic driving, we obtain a bound on the protocol time required to remain in the self-trapping regime:

$$T \gg \frac{\pi J}{2U(N-1)}. \tag{3.134}$$

Therefore, although the quantum speed limit is reached for the reduced Hamiltonian, some fundamental limitations remain for the full Hamiltonian.

3.6.1 Triple-NOON states

To illustrate the effectiveness of the developed technique, we apply the protocol to the creation of highly entangled triple-NOON states, corresponding to the superposition

$$|3\text{-NOON}\rangle = (|N,0,0\rangle + |0,N,0\rangle + |0,0,N\rangle)/\sqrt{3}. \tag{3.135}$$

Producing such a state in our setup requires considering a system with $L = 3$ sites arranged such that a single central site is coupled to the three outer wells. The on-site energy of this central well is dynamically controlled according to the GCD protocol introduced previously, and its time dependence is engineered to drive the system adiabatically toward the entangled superposition $|3\text{-NOON}\rangle$. At the beginning of the evolution, the atoms occupy the central site exclusively, i.e., the system is prepared in the asymptotic Fock state $|N;0,0,0\rangle$.

Spectrum

Figure 3.14(a) provides a global view of the many-body spectrum of the Bose-Hubbard Hamiltonian as a function of the driving parameter ε/J. The comparison between the geodesic ramp (red curves) and the GCD optimized (blue curves) highlights the

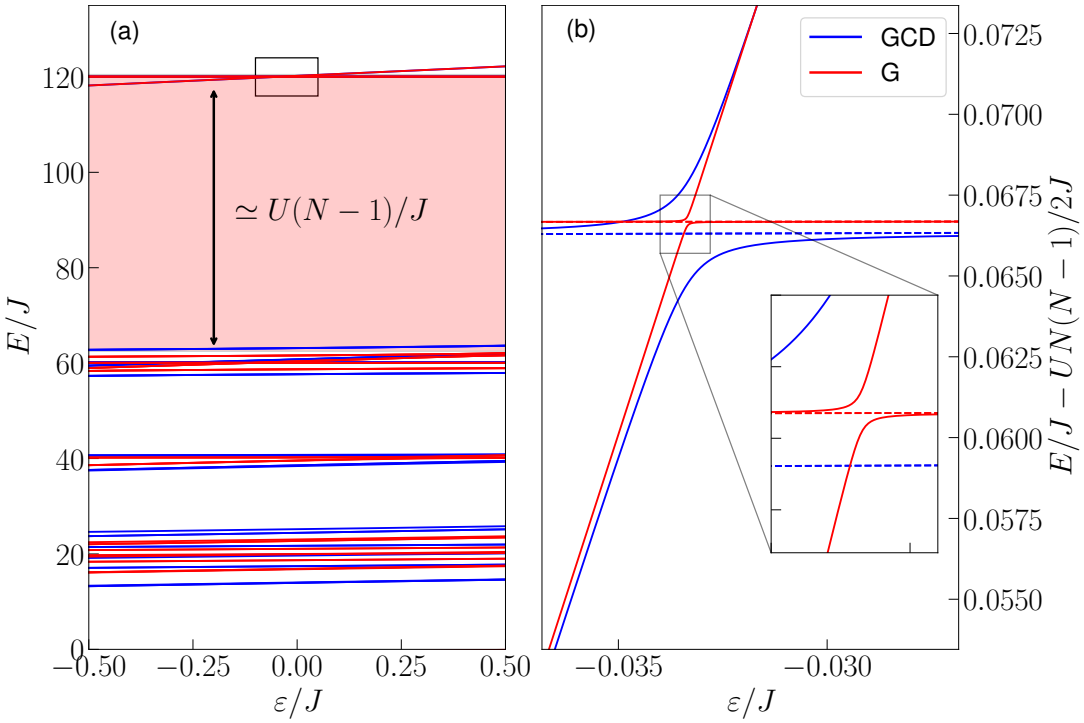

FIGURE 3.14: (a) Spectrum of the Bose-Hubbard Hamiltonian for $L = 3$, under geodesic driving (G, red curves) and geodesic counterdiabatic driving (GCD, blue curves) as a function of the parameter ε/J, for $U = 20J$, $T = 10^3\hbar/J$ and $N = 4$. The states of interest, namely those where all particles are in the same level, are protected by a gap of value $U(N-1)/J$ from the rest of the spectrum, enabling the definition of a reduced system. A black rectangle highlights the avoided crossing region. (b) Zoom into the avoided crossing region. The gap is significantly widened due to the GCD protocol, allowing much faster adiabatic creation of triple-NOON states.

qualitative change in the structure of the relevant avoided crossings. Whereas the usual protocol leads to narrow avoided crossings that impose stringent adiabaticity constraints, the GCD protocol actively reshapes these crossings by modifying the instantaneous slope of the energy bias. This spectral deformation is central to enhancing the robustness and speed of the adiabatic evolution.

A closer inspection of the relevant avoided crossing region is shown in Fig. 3.14(b). The zoom-in reveals how the GCD trajectory stretches and smooths the avoided crossing, effectively increasing its minimum gap. As a consequence, the system follows the desired adiabatic path with significantly reduced non-adiabatic transitions. This enlargement of the gap is precisely what allows one to accelerate the preparation of the triple-NOON state without compromising fidelity. The dashed horizontal lines in the inset indicate the antisymmetric superpositions that are not involved in the time evolution of the system.

Dynamics

Figure 3.15(a) shows the time evolution of the populations in the initial Fock state $|N;0,0,0\rangle$ and in the target state $|3\text{-NOON}\rangle$ for a total protocol duration $T = 10^3\hbar/J$. The contrast between the two driving methods is striking. Under the GCD protocol (blue curves), the population is smoothly transferred from the initial configuration to the desired triple-NOON superposition, reaching a final fidelity extremely close to unity. In other words, the system remains faithfully locked to the instantaneous

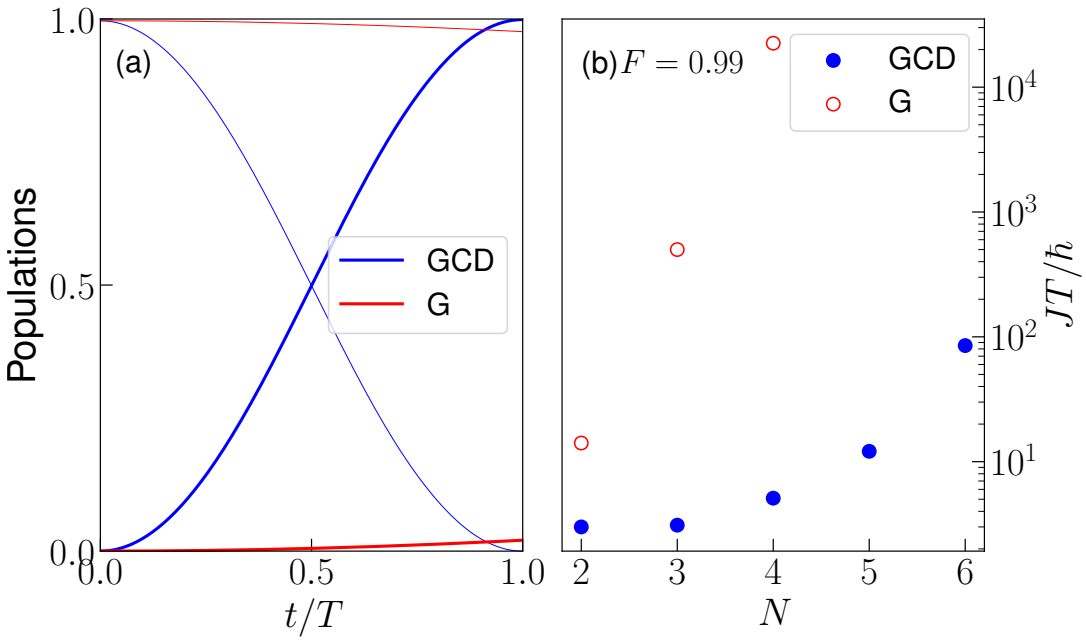

FIGURE 3.15: (a) Population of the states $|N;0,0,0\rangle$ (thin lines) and $|3\text{-NOON}\rangle$ (thick lines) over time, for a total protocol time $T = 10^3\hbar/J$, $U = 20J$ and $N = 4$. Population inversion is complete with the GCD protocol, whereas it does not even reach 10% with simple geodesic driving (G). (b) Various values of the time required to create a triple-NOON state with G and GCD driving for different numbers of particles N, with a fixed $U = 20J$ and a fixed fidelity $F = 0.99$. An exponential growth in creation time is observed with the G protocol, while it is effectively mitigated with the GCD protocol, achieving experimentally feasible creation times.

eigenstate engineered by the GCD trajectory throughout the entire evolution. By contrast, the standard G protocol (red curves) fails to induce a significant population transfer: almost the entire population remains trapped in the initial state, and only a negligible fraction reaches the 3-NOON state. This illustrates the bottleneck imposed by the narrow avoided crossings encountered in the geodesic-only protocol, which prevent an adiabatic following unless unrealistically long evolution times are used. The comparison visible in panel (a) thus highlights the ability of GCD to unlock transitions that are otherwise dynamically frozen.

To further quantify the advantage of the optimized trajectory, Fig. 3.15(b) presents the minimum duration required to achieve a final fidelity of 0.99 in the triple-NOON state as a function of the particle number N. For the standard G protocol, the required time rapidly exhibits an exponential scaling with N, reflecting the shrinking energy gaps and increasing fragility of the adiabatic path as the system size grows. This exponential behaviour renders the protocol practically unusable for preparing NOON states. On the other hand, the GCD protocol dramatically mitigates this scaling: the required times remain orders of magnitude smaller and increase much more slowly for small N. This improvement directly originates from the gap-enhancing mechanism of GCD, which reshapes the avoided crossings and suppresses diabatic transitions even for relatively large particle numbers.

A concrete illustration is provided by the case $N = 4$. Achieving a fidelity of 0.99 requires a time approximately equal to $10^4\hbar/J$ with the standard G protocol for $U = 20J$ while with the GCD protocol the same state can be produced in merely $5\hbar/J$, placing high-fidelity NOON-state generation well within experimentally accessible

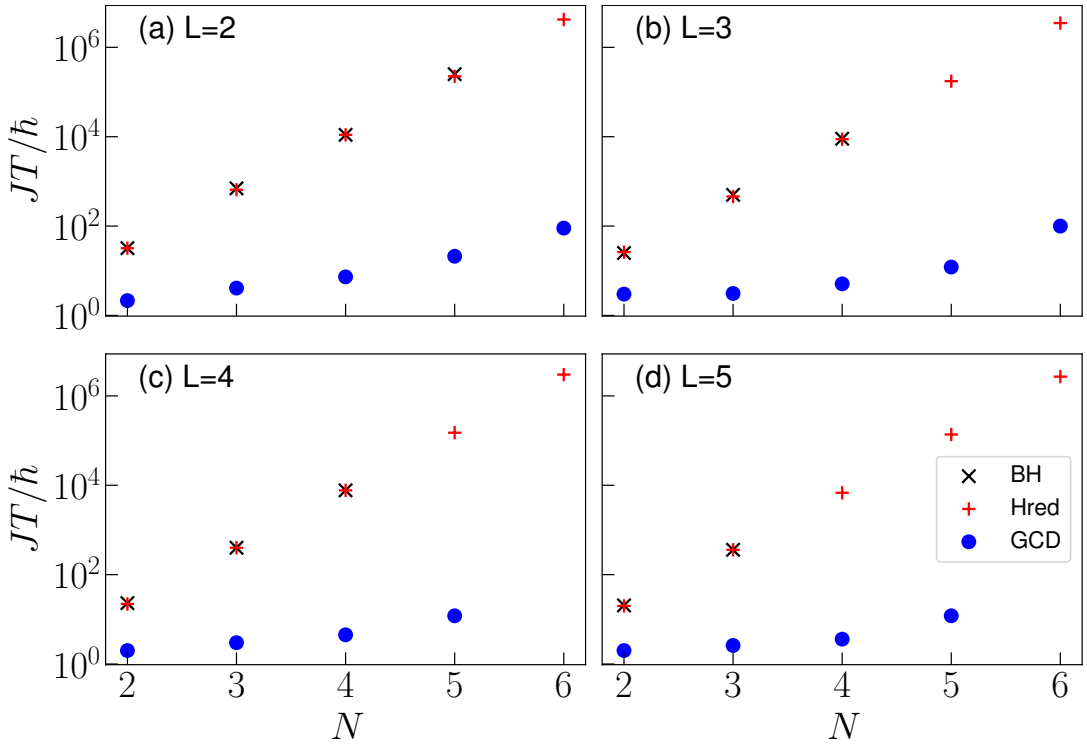

FIGURE 3.16: Protocol time $JT/\hbar$ required to achieve 99% fidelity of the state (a) NOON, (b) 3-NOON, (c) 4-NOON, and (d) 5-NOON, in logarithmic scale, for a geodesic driving (Bose-Hubbard system in black (x), reduced system in red (+), and for the geodesic counterdiabatic driving (GCD protocol in blue), with a fixed value of $NU/J = 60$. Clearly, the GCD protocol allows for a gain of several orders of magnitude in the time required to create an L-NOON state. In particular, the exponential dependence of T on the number of particles is very clearly visible.

timescales.

3.6.2 L-NOON states

Figure 3.16 illustrates the remarkable generality of the GCD protocol when extended to systems with an arbitrary number of wells L. Since the method is defined for any dimensionality of the Bose-Hubbard Hamiltonian, the generation of more exotic entangled states, such as 4-NOON or 5-NOON states, follows naturally from the same principles used for the triple-NOON case. For each $L \in \{2, 3, 4, 5\}$, the figure reports the minimum evolution time required to reach a fidelity of 0.99 with the target $|\text{L-NOON}\rangle$ state, for different numbers of particles. Due to increasing numerical complexity of the protocol, only a few points are computed for the geodesic driving only (black "×"), and are to be compared with those obtained using the reduced Hamiltonian (3.93) (red "+"). As one can conclude that the reduced model indeed captures the good values, one can expect the full BHM to follow the same dependence as the one obtained with the reduced model.

The comparison between the geodesic driving ("×" and "+") and the complete GCD protocol (blue) demonstrates unequivocally that the counterdiabatic-assisted trajectory enables the creation of large multi-mode NOON states orders of magnitude faster than a simple geodesic protocol lacking counterdiabatic corrections. This advantage

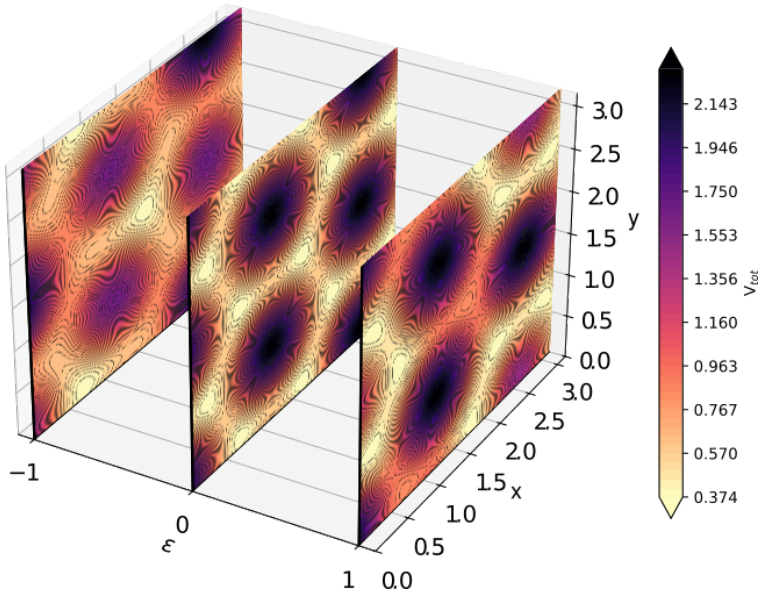

FIGURE 3.17: Schematic representation of a hexagonal optical lattice of depth V_{tot}, in which the proposed protocol could be used to generate triple-NOON states. A triangular lattice is superposed on the latter in order to have control on the depth of the central well. Initially, the bosons are trapped in one of the highest-energy wells ($\varepsilon = 1$), effectively isolating the particles from other energy levels. The protocol then provides a method for modifying the optical lattice to control the energy of the central well using an additional external field.

becomes especially striking for states with many modes. For example, the state

$$|5\text{-NOON}\rangle = (|0; N, 0, 0, 0, 0\rangle + |0; 0, N, 0, 0, 0\rangle + ... + |0; 0, 0, 0, 0, N\rangle)/\sqrt{5}, \quad (3.136)$$

can be produced by the GCD protocol in times that remain well within experimentally feasible ranges, even for particle numbers where the Bose-Hubbard Hilbert space becomes prohibitively large for direct numerical simulations.

A key observation emerging from Fig. 3.16 is that the time required to generate a high-fidelity $|\text{L-NOON}\rangle$ state depends only weakly on the number of wells L. This behavior is readily understood from the structure of the reduced Hamiltonian (3.93): the effective coupling between the initial Fock state and the NOON state is modified only by a factor of $\sqrt{L}$ when transitioning from $L = 1$ to arbitrary L. Since the total protocol duration scales inversely with this coupling, one expects only a mild dependence on L, as compared to the exponential dependence on the total number of particles N.

Interestingly, the protocol time can even decrease slightly with increasing L, as the enhanced effective coupling accelerates the adiabatic passage toward the NOON manifold. In practical terms, this means that the creation of highly entangled states involving a larger number of modes does not impose additional dynamical constraints and may in fact be accomplished more rapidly.

3.6.3 Experimental realization

Although the theoretical framework presents no fundamental obstacle to extending the protocol to larger numbers of particles or wells, certain experimental constraints must be taken into account. First, perturbation theory is inherently limited by the chosen

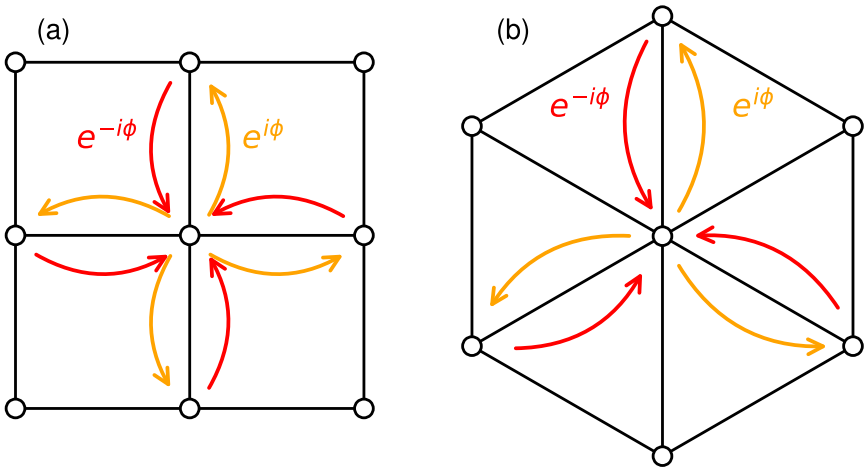

FIGURE 3.18: Examples of different geometries that could be used to realize the proposed method within (a) square and (b) trigonal lattices. In order to implement the complex hopping defined by Eq. (3.81), it is necessary that a phase $\pm\phi$ exists between the sites. Specifically, all hoppings from the central site to the outer wells must carry the same phase sign, and the opposite phase sign applies for hoppings from the outer wells back to the central site.

maximum order. The larger the number of bosons involved in the system, the greater the precision required in determining the energy splitting to ensure adiabatic evolution. Additionally, it is necessary to maintain an almost perfect symmetry among the L outer wells, a condition that becomes increasingly difficult to satisfy as N increases.

The method proposed here is readily extensible numerically, as the only required parameters can be obtained through straightforward diagonalization of the Bose-Hubbard Hamiltonian. The precision on the energy splitting can therefore reach machine-level accuracy for any number L of outer wells. However, the experimental realization of such a system may become increasingly challenging as L grows. Several well-known lattice geometries can be employed to generate exotic states, such as triangular ($L = 3$) [14] (see also Fig. 3.17), square ($L = 4$) [10], or hexagonal ($L = 6$) lattices [15].

Another challenge, particularly within optical lattice setups, is to realize, via Floquet engineering [15, 123, 124, 158–162] or related techniques, a complex hopping in the effective parameters of the Bose-Hubbard model. In our protocol, the same phase is required from the central site to all other sites, which does not correspond to a simple Peierls phase with alternating signs. Figure 3.18 illustrates two possible cases for state creation: (a) a 4-NOON state in a square lattice and (b) a 3-NOON state in a triangular lattice, together with the associated phases required to emulate the action of the counterdiabatic Hamiltonian. Our GCD approach mitigates the experimental difficulty, since it relies on time-independent parameters.

The larger L becomes, the more problematic it is to neglect couplings between the outer wells. Still, one can quickly see that the presence of such couplings introduces only minor complications. Indeed, if an effective coupling $\mathcal{J}'$ between the L outer wells is considered, the system can still be reduced to an effective two-level description. The energy of the outer wells will be shifted by a factor $-(L-1)\mathcal{J}'$, leading to a slight modification of Eq. (3.87) in the form of a constant shift that has no impact on the determination of the effective parameters. Since all outer wells are equally coupled to one another, this coupling acts as an internal energy for the $|\text{L-NOON}\rangle$ state.

4

NOON states of vortices

The Bose-Hubbard system employed throughout this thesis describes a collection of bosonic particles confined to L discrete sites, which, in the context of an optical lattice, correspond to the minima of the periodic potential forming the lattice structure. Beyond this standard spatial interpretation, the quantization of energy levels within a single optical trap also allows one to introduce an alternative notion of "sites", associated with the different orbital states accessible to the particles.

In this chapter, we exploit this latter perspective to show that, by means of an anisotropic harmonic confinement, an effective vortex model can be mapped onto the Bose-Hubbard model. In such a description, the bosons acquire a well-defined angular momentum, which characterizes their rotational dynamics.

4.1 Ultracold atoms in a 2D harmonic trap

Let us consider a ensemble of N bosons trapped in an anisotropic harmonic potential with angular frequencies $(\omega_x, \omega_y, \omega_z)$, arranged such that the system is confined to the (x, y) plane with a slight anisotropy, i.e., $\omega_x \approx \omega_y \ll \omega_z$. The single-particle Hamiltonian describing a particle trapped in such a potential is written as

$$H_{\mathrm{HO}} = -\frac{\hbar^2}{2m}\nabla^2 + \frac{m}{2}(\omega_x^2 x^2 + \omega_y^2 y^2 + \omega_z^2 z^2). \tag{4.1}$$

This Hamiltonian is composed of a kinetic term $-\hbar^2\nabla^2/2m$ and a potential term determining how a massive particle is influenced by the type of trap described above.

Given the absence of coupling terms between the different components x, y, and z, the eigenfunctions $\psi(x, y, z)$ of this Hamiltonian, satisfying the eigenvalues equation $H(x, y, z)\psi(x, y, z) = E(x, y, z)\psi(x, y, z)$, are separable:

$$\psi(x, y, z) = \phi(x)\phi(y)\phi(z). \tag{4.2}$$

By separation of variables, the constraint on each function ϕ can be obtained directly:

$$\Big(-\frac{\hbar^2}{2m}\nabla^2 + \frac{1}{2}m\omega_x^2 x^2\Big)\phi(x) = E_x\phi(x). \tag{4.3}$$

The solutions $\phi(x)$ are those of the harmonic oscillator and are well known in terms of Hermite polynomials

$$H_n(x) = (-1)^n e^{x^2} \frac{d^n}{dx^n} e^{-x^2} \tag{4.4}$$

and are given by:

$$\phi_{n_x}(x) = \frac{1}{\sqrt{2^{n_x} n_x!}} \left(\frac{m\omega_x}{\pi\hbar}\right)^{1/4} e^{-m\omega_x x^2/2\hbar} H_{n_x}\left(\sqrt{\frac{m\omega_x}{\hbar}} x\right), \tag{4.5}$$

for $n \in \mathbb{N}$. The energies associated with the eigenfunctions (4.5) are

$$E_{n_x} = \hbar\omega_x(n_x + 1/2). \tag{4.6}$$

According to the initial assumptions, we consider the system to be in its ground state along the z axis, i.e., $n_z = 0$. As for the x and y components, we consider the p bands [163, 164], denoted ϕ_{n_x,n_y}, with n_x and n_y taking values 0 or 1, but not simultaneously. In this case, the eigenfunctions in the (x, y) plane can be written as

$$\phi_{10}(x,y) = \sqrt{\frac{2}{\pi}} \frac{m}{\hbar} \left(\omega_x^3 \omega_y\right)^{1/4} x \exp\left\{-\frac{m}{2\hbar}\left(\omega_x x^2 + \omega_y y^2\right)\right\} \tag{4.7}$$

$$\phi_{01}(x,y) = \sqrt{\frac{2}{\pi}} \frac{m}{\hbar} \left(\omega_x \omega_y^3\right)^{1/4} y \exp\left\{-\frac{m}{2\hbar}\left(\omega_x x^2 + \omega_y y^2\right)\right\}, \tag{4.8}$$

with their respective eigenvalues

$$E_{10} = \frac{3}{2}\hbar\omega_x + \frac{1}{2}\hbar\omega_y + \frac{1}{2}\hbar\omega_z \tag{4.9}$$

$$E_{01} = \frac{1}{2}\hbar\omega_x + \frac{3}{2}\hbar\omega_y + \frac{1}{2}\hbar\omega_z. \tag{4.10}$$

These functions are plotted in Fig. 4.1. In particular, the two modes ϕ_{10} and ϕ_{01} describe the wavefunctions of the first two excited states. Most importantly, their superpositions $\psi_\pm = \phi_{10} \pm i\phi_{01}$ genuinely describe a vortex. Indeed, by examining the phase of the function $\psi_\pm$, one finds that it rotates in the (x, y) plane in the clockwise $(+)$ and counterclockwise $(-)$ directions. When we consider the natural many-body extension of Hamiltonian (4.1), we will in fact describe, through these eigenfunctions, a set of bosons rotating clockwise or counterclockwise.

It is important to note that the energy difference between the two modes is

$$\Delta = E_{01} - E_{10} = \hbar(\omega_y - \omega_x). \tag{4.11}$$

For a purely isotropic trap, the two states of the p band are degenerate. However, in the presence of an anisotropy $\omega_x \neq \omega_y$, this degeneracy is lifted. It is precisely this energy splitting that enables quantum control of the state, allowing the creation of a NOON state composed of the vortices introduced above.

4.1.1 Many-body Hamiltonian

In full generality, the Hamiltonian describing the many-body system is composed of a kinetic term H_0 and an interaction term H_{int}. By defining the field operators $\hat{\psi}(\mathbf{r})$ and $\hat{\psi}^\dagger(\mathbf{r})$, which respectively annihilate and create a particle at position $\mathbf{r}$, the full

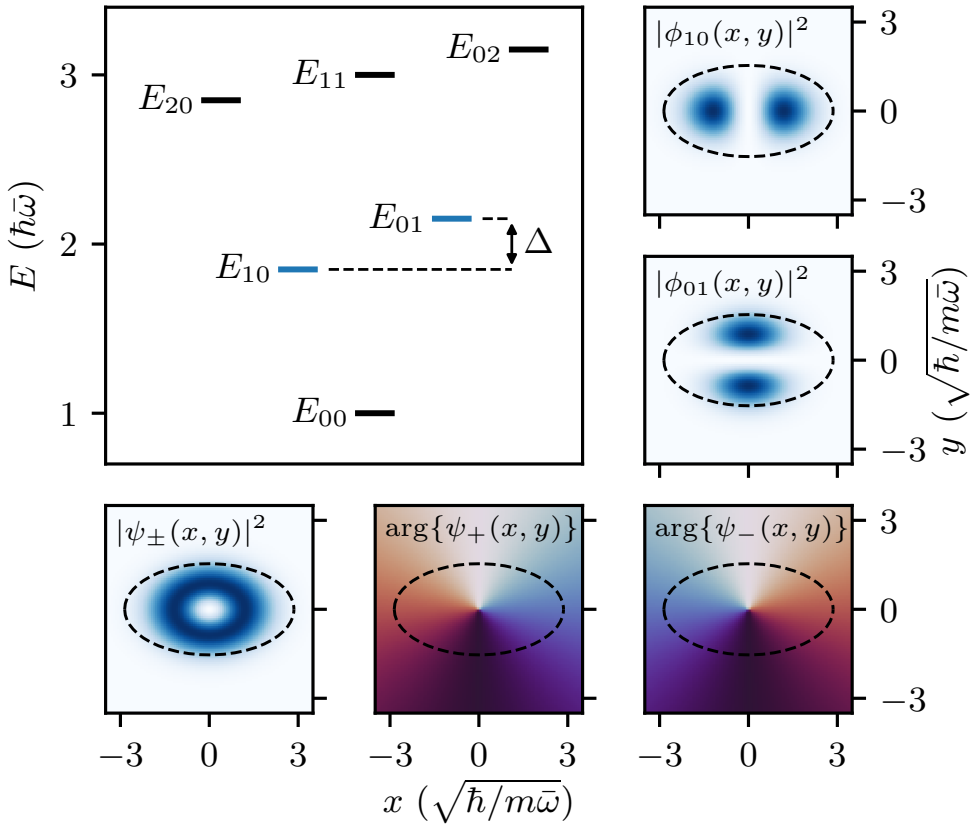

FIGURE 4.1: **One-body subspace.** Top left: First six levels E_{n_x,n_y} of the 2D quantum harmonic oscillator with anisotropy Δ, with levels of interest $|\phi_{10}\rangle$ and $|\phi_{01}\rangle$ in blue. Five remaining panels: $|\phi_{10}(x,y)|^2$, $|\phi_{01}(x,y)|^2$ and their vortex superpositions $|\psi_\pm(x,y)|^2$ (see text) with their phase (curling in opposite direction). The dashed line corresponds to the iso-potential $U(x,y) = 2\hbar\bar{\omega}$, with $\bar{\omega} = (\omega_x + \omega_y)/2$.

Hamiltonian describing the system can be written as

$$\hat{H} = \hat{H}_0 + \hat{H}_{\text{int}} \tag{4.12}$$

$$= \int_{-\infty}^{\infty} d^2\mathbf{r}\ \psi^\dagger(\mathbf{r})\hat{H}_{\text{HO}}\psi(\mathbf{r}) + \frac{g}{2}\int_{-\infty}^{\infty} d^2\mathbf{r}\ \psi^\dagger(\mathbf{r})\psi^\dagger(\mathbf{r})\psi(\mathbf{r})\psi(\mathbf{r}), \tag{4.13}$$

Here, $g = 4\pi\hbar^2 a_s/m$ is the interaction parameter [72], with a_s the s-wave scattering length. By defining $\hat{a}_x$ and $\hat{a}_y$ as the annihilation operators of a boson in the p band (and their respective complex conjugates as creation operators), the field operator can be decomposed in terms of known orbitals:

$$\hat{\psi}(\mathbf{r}) = \hat{\psi}(x,y)\phi_0(z) \tag{4.14}$$

$$= \big[\hat{a}_x\phi_{10}(x,y) + \hat{a}_y\phi_{01}(x,y)\big]\phi_0(z). \tag{4.15}$$

In fact, decomposing the field operators in the basis of the p orbitals means that we study the case where the bosons are already excited into the first excited state above the ground state. In this basis, creating a boson in the p_x orbital corresponds to a wavefunction ϕ_{10}: the state is excited along the x axis and in the ground state along the y axis, and similarly for the p_y orbital.

The kinetic Hamiltonian $\hat{H}_0$ can be rewritten quite straightforwardly in the basis

of the p orbitals, since we know that the functions ψ_{n_x,n_y,n_z} are eigenfunctions of the Hamiltonian, associated with the energies

$$E_{n_x,n_y,n_z} = \hbar(\omega_x(n_x + 1/2) + w_y(n_y + 1/2) + w_z(n_z + 1/2)). \tag{4.16}$$

From this, by substituting the expression (4.15) into the Hamiltonian $\hat{H}_0$, we obtain

$$\hat{H}_0 = E_{10}\hat{n}_x + E_{01}\hat{n}_y + \hbar\omega_z\hat{N}, \tag{4.17}$$

where $\hat{n}_x = \hat{a}_x^\dagger\hat{a}_x$, $\hat{n}_y = \hat{a}_y^\dagger\hat{a}_y$, and $\hat{N} = \hat{n}_x + \hat{n}_y$ are respectively the number of particles in the p_x orbital, the p_y orbital, and the total number of particles. This first term of the Hamiltonian tells us that the energy of the system is determined by the number of particles in each band. The last term of $\hat{H}_0$ is simply a constant energy shift, proportional to the total number of particles weighted by the frequency ω_z, and will be ignored in the following.

The interaction term is not as straightforward to compute. Nevertheless, by expanding the field operators, one obtains

$$\begin{aligned}\hat{H}_{\text{int}} = \frac{g}{2}\int_{-\infty}^{\infty} dz\,|\phi_0(z)|^4 \int_{-\infty}^{\infty} dxdy\,\big(\hat{a}_x^\dagger\hat{a}_x|\phi_{10}|^4 + \hat{a}_y^\dagger\hat{a}_y|\phi_{01}|^4 + \\ (\hat{a}_x^{\dagger 2}\hat{a}_y^2 + \hat{a}_y^{\dagger 2}\hat{a}_x^2)|\phi_{10}|^2|\phi_{0,1}|^2 + 4\hat{a}_x^\dagger\hat{a}_x\hat{a}_y^\dagger\hat{a}_y|\phi_{10}|^2|\phi_{01}|^2\big)\end{aligned} \tag{4.18}$$

By evaluating the integrals and defining the two-body interaction energy as

$$U = \frac{3}{2}\sqrt{\frac{m\hbar}{2\pi}}\,a_s\sqrt{\omega_x\omega_y\omega_z}, \tag{4.19}$$

one finally obtains the interaction Hamiltonian

$$\hat{H}_{\text{int}} = \frac{U}{2}(n_x^2 + n_y^2) + \frac{U}{6}(\hat{a}_x^{\dagger 2}\hat{a}_y^2 + \hat{a}_y^{\dagger 2}\hat{a}_x^2) + \frac{2U}{3}\hat{n}_x\hat{n}_y. \tag{4.20}$$

The emergence of vortices becomes clear by defining the angular momentum operator along the z axis as

$$\hat{L}_z = -i(\hat{a}_x^\dagger\hat{a}_y - \hat{a}_y^\dagger\hat{a}_x). \tag{4.21}$$

From there, by expanding $\hat{L}_z^2$, the interaction Hamiltonian can be rewritten as

$$\hat{H}_{\text{int}} = -\frac{U}{6}\hat{L}_z^2 + \frac{NU}{2}\left(N - \frac{1}{3}\right), \tag{4.22}$$

where the second term is constant and can therefore be eliminated by redefining the global energy scale. At the end of the derivation, the many-body Hamiltonian reads

$$\hat{H} = -\frac{U}{6}\hat{L}_z^2 + E_{10}\hat{n}_x + E_{01}\hat{n}_y. \tag{4.23}$$

The form of the Hamiltonian (4.23) already contains a wealth of information, but it can be made even more transparent by working in its eigenbasis. For a small anisotropy Δ compared to the interaction strength U, the eigenstates of the Hamiltonian (4.23) are well approximated by Fock states built from the creation and annihilation operators $\hat{a}_\pm^\dagger$ and $\hat{a}_\pm$, which correspond to vortex modes rotating clockwise (+) and counterclockwise

$(-)$:

$$\hat{a}_{\pm} = \frac{\hat{a}_x \pm i\hat{a}_y}{\sqrt{2}} \tag{4.24}$$

$$\hat{a}^{\dagger}_{\pm} = \frac{\hat{a}^{\dagger}_x \pm i\hat{a}^{\dagger}_y}{\sqrt{2}}, \tag{4.25}$$

while simultaneously defining the particle number operators in each mode as $\hat{n}_{\pm} = \hat{a}^{\dagger}_{\pm}\hat{a}_{\pm}$. In this basis, the angular momentum operator takes a very simple form as the population imbalance between the $(+)$ and $(-)$ modes :

$$\hat{L}_z = \hat{a}^{\dagger}_{+}\hat{a}_{+} - \hat{a}^{\dagger}_{-}\hat{a}_{-} \tag{4.26}$$

Indeed, angular momentum is generated by the difference in the number of particles rotating clockwise $(+)$ and counterclockwise $(-)$. If fewer particles rotate in one direction than in the other, the resulting angular momentum is determined by the direction with the larger particle population.

The two terms proportional to $\hat{n}_x = \hat{a}^{\dagger}_x\hat{a}_x$ and $\hat{n}_y = \hat{a}^{\dagger}_y\hat{a}_y$ take on a different form:

$$E_{10}\hat{n}_x + E_{01}\hat{n}_y = \frac{\hat{N}}{2}\left(E_{10} + E_{01}\right) + \frac{E_{10} - E_{01}}{2}\left(\hat{a}^{\dagger}_{+}\hat{a}_{-} + \hat{a}^{\dagger}_{-}\hat{a}_{+}\right). \tag{4.27}$$

The first term on the right-hand side is again nothing but a global energy shift, indicating once more that part of the energy is fixed by the total particle number. The second term, however, is much more interesting. Indeed, recalling that we defined the anisotropy Δ as the energy difference between the orbitals, $E_{01} - E_{10} = \hbar(\omega_y - \omega_x)$, this term can be identified as a coupling between the two modes, generated by the anisotropy of the trap.

By expanding $\hat{L}_z^2 = (\hat{a}^{\dagger}_{+}\hat{a}_{+} - \hat{a}^{\dagger}_{-}\hat{a}_{-})^2 = 2(\hat{n}_{+}^2 + \hat{n}_{-}^2) - \hat{N}^2$ and neglecting constant terms, the full Hamiltonian can finally be written as [163, 164]:

$$\hat{H} = -\frac{U}{3}\left(\hat{n}_{+}^2 + \hat{n}_{-}^2\right) - \frac{\Delta}{2}\left(\hat{a}^{\dagger}_{+}\hat{a}_{-} + \hat{a}^{\dagger}_{-}\hat{a}_{+}\right). \tag{4.28}$$

For a repulsive interaction U (i.e. $U > 0$), the first term of Hamiltonian (4.28) describes an attractive interaction between particles occupying the same mode. Bosons rotating in a given direction attract other bosons rotating in the same direction and repel vortices with the opposite circulation, a well-known behavior in systems carrying angular momentum. The anisotropy Δ plays the role of a coupling term between the two rotational modes, tending to mix bosons with opposite angular momentum and favoring superpositions of vortex states with opposite directions of rotation.

4.1.2 Bose-Hubbard model of vortices

Hamiltonian (4.28) is completely equivalent to a two-site Bose-Hubbard Hamiltonian, describing bosons trapped in two modes, with an interaction strength $-U/3$ and a hopping amplitude $\Delta/2$. In the vortex basis, adding a diagonal term is straightforward and allows one to define a Bose-Hubbard system of the familiar form, namely with an

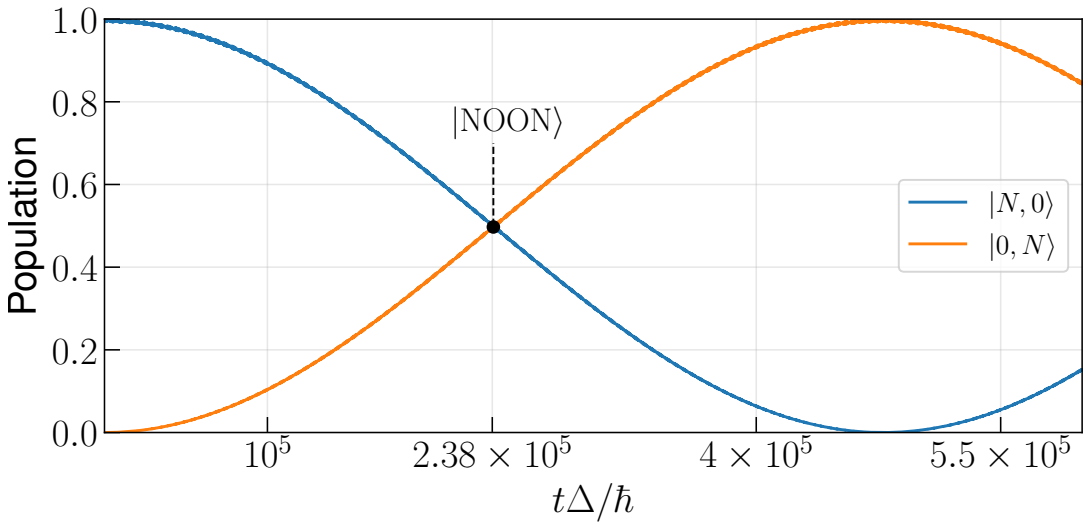

FIGURE 4.2: Populations of the Fock states $|N,0\rangle$ and $|0,N\rangle$ for $N = 5$ and $U = 10\Delta$, whose evolution is governed by the Bose-Hubbard Hamiltonian (4.29). Collective tunneling suppresses sequential tunneling and allows all particles to tunnel together, producing a NOON state at half the total tunneling time.

onsite energy ε that may depend on time, $\varepsilon(t)$:

$$\hat{H} = -\frac{U}{3}\left(\hat{a}_+^{\dagger 2}\hat{a}_+^2 + \hat{a}_-^{\dagger 2}\hat{a}_-^2\right) - \frac{\Delta}{2}\left(\hat{a}_+^\dagger\hat{a}_- + \hat{a}_-^\dagger\hat{a}_+\right) + \varepsilon(t)\left(\hat{a}_+^\dagger\hat{a}_+ - \hat{a}_-^\dagger\hat{a}_-\right). \quad (4.29)$$

We thus once again obtain a Hamiltonian whose physical parameters U, Δ, and ε are controllable and allow one to define different parametric regimes. In particular, for a ratio $NU \gg \Delta$, we recover the self-trapping regime that has been used throughout this thesis. In this case, we are able to isolate the states $|N,0\rangle$ and $|0,N\rangle$ from the rest of the spectrum.

Naturally, this comes with the central phenomenon at the heart of the geodesic counterdiabatic protocol: collective tunneling between the states in which all particles occupy the same mode. This means that, over time, if all bosons initially rotate in the same direction, after a certain time they will all rotate in the opposite direction, and so on. Since sequential tunneling is suppressed by the self-trapping regime, only the states $|N,0\rangle$ and $|0,N\rangle$ participate in the dynamics. Thus, halfway through the tunneling time, the state of the system is found in a coherent superposition $|N,0\rangle + |0,N\rangle$, namely a NOON state. It is therefore possible to naturally create a NOON state using vortices of bosonic particles.

Figure 4.2 shows the populations of the different states of the many-body system (4.29) in the Fock basis. Initially, if the system is prepared in the state $|N,0\rangle$, only collective tunneling is possible during the time evolution of the system. Indeed, after a certain time, the entire population is transferred to the state $|0,N\rangle$, without other intermediate states (such as $|N-1,1\rangle$, for example) having any significant influence during the time evolution. This phenomenon is cyclic when the energies of the two sites are resonant, and allows for the periodic creation of NOON states. However, as for the other systems studied in this thesis, the tunneling time is extremely long and must be reduced for any experimental realization with ultracold atoms.

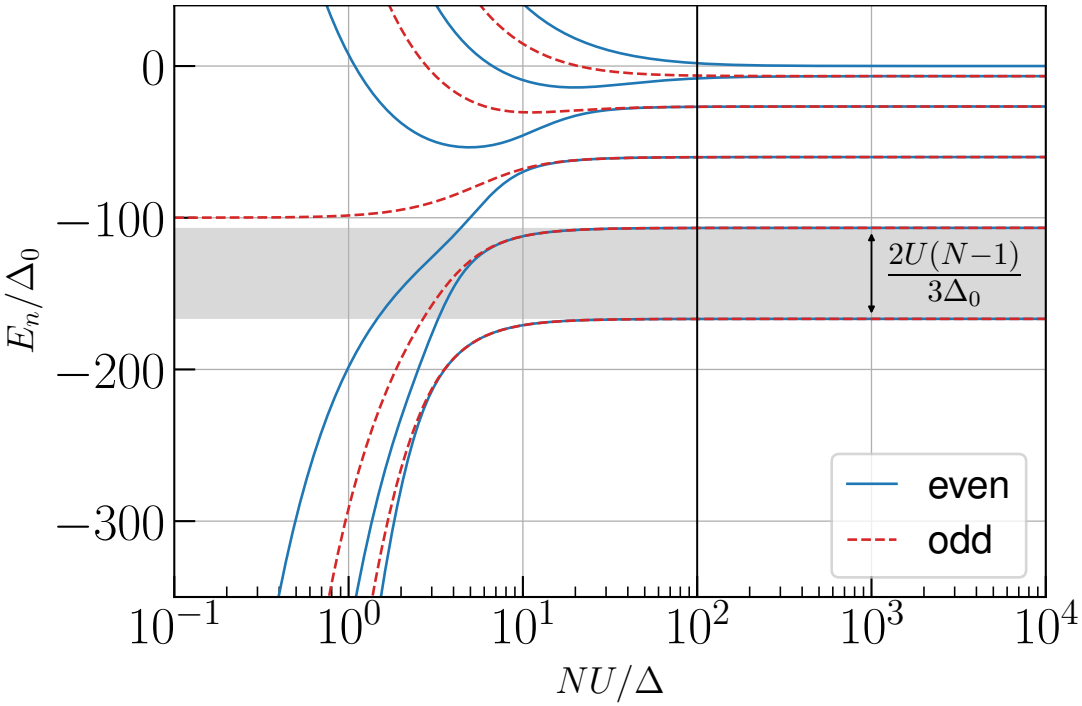

FIGURE 4.3: Spectrum of the Hamiltonian (4.29) as a function of the ratio NU/Δ, for $N = 10$ particles. The energies corresponding to the symmetric states (solid blue) and antisymmetric states (dashed red) become degenerate beyond a certain value of NU/Δ, which can be identified as the lower bound of the self-trapping region. The gap between the energies of $|N,0\rangle, |0,N\rangle$ and $|N-1,1\rangle, |1,N-1\rangle$ at large NU/Δ is shown in gray.

4.1.3 Self-trapping regime

Since the Hamiltonian (4.29) is fully equivalent to a Bose-Hubbard Hamiltonian of the type investigated throughout this thesis, all previous discussions concerning the existence and characterization of a self-trapping parameter regime remain directly applicable. In the present context, this regime plays a crucial role, as it enables the energetic isolation of the two vortex states, denoted $(+)$ and $(-)$, from the remainder of the many-body spectrum. This spectral separation provides a well-defined subspace in which the vortex dynamics can be analyzed independently of higher-lying excitations.

Figure (4.3) shows the spectrum of Hamiltonian (4.29) as a function of NU/Δ, with energies normalized by Δ_0 defined such that $U/\Delta_0 = 20$. For the regime $NU/\Delta \gg 1$, the levels can be identified with the energies of the Fock states, and there is an exact degeneracy between even and odd states. In particular, once the self-trapping regime is reached, a gap of amplitude $2U(N-1)/3\Delta_0$ isolates the states $|N,0\rangle$ and $|0,N\rangle$ from the rest of the spectrum.

4.2 Reduced model

As suggested by the population dynamics shown in Fig. 4.2, the evolution of the system can be reduced to a subspace containing only the states $|N,0\rangle$ and $|0,N\rangle$ in a self-trapping parameter regime. Since the intermediate states appear only through small contributions, their effects will be expressed perturbatively. We therefore define

a two-level reduced Hamiltonian

$$H_{\text{red}} = \begin{pmatrix} N\varepsilon(t) & -\mathcal{J} \\ -\mathcal{J} & -N\varepsilon(t) \end{pmatrix}. \tag{4.30}$$

In this case, owing to the perfect symmetry between the two wells, there is no correction to the onsite energies. Indeed, unlike situations where a central well is coupled to L outer wells, the left well cannot be distinguished from the right one when $\varepsilon = 0$. As a consequence, there is only a single matrix element to determine, namely the effective coupling between the states in which all particles occupy the same site, being mediated by intermediate states.

In particular, given the clear correspondence between the Hamiltonians of the different systems studied throughout this thesis, the effective coupling $\mathcal{J}$ is obtained by performing the substitutions $J \to \Delta/2$ and $U \to 2U/3$, and is given by

$$\mathcal{J}(U, \Delta) = -\frac{N(\Delta/2)^N}{(N-1)!(2U/3)^{N-1}}. \tag{4.31}$$

Knowing the expression of the effective coupling allows us to solve the evolution of the undriven system and to obtain a first indication of the system's dynamics. In particular, the time required to invert the population is known, and the time at which the NOON state is obtained corresponds to half of this value:

$$\tau_{\text{NOON}} = \frac{\pi\hbar}{4\mathcal{J}} \tag{4.32}$$

For the parameters used in Fig. 4.2, namely $N = 5$ and $U = 10\Delta$, we obtain

$$\tau_{\text{NOON}} = 2.38 \times 10^5\, \hbar/\Delta \tag{4.33}$$

which is consistent with the value obtained for the full system.

4.2.1 GCD with reduced Hamiltonian

In this subsection, we compute the ingredients required for the application of geodesic counterdiabatic driving to the system defined by the Hamiltonian (4.30). In order to determine the most suitable driving function, we calculate the different components of the geodesic counterdiabatic driving. For the reduced Hamiltonian (4.30), the metric tensor takes the following form

$$g = \frac{N^2\mathcal{J}^2}{2\left(\mathcal{J}^2 + (N\varepsilon)^2\right)^2}$$

which, along with the geodesic condition, yields the optimal time parametrization for ε:

$$N\varepsilon(t) = \mathcal{J}\tan(\alpha_i + (\alpha_f - \alpha_i)t/T) \tag{4.34}$$

where $\alpha_{i,f} = \tan^{-1}(N\varepsilon_{i,f}/\mathcal{J})$ must be close to $\pm\pi/2$ in order to approach the tangent asymptote and ensure that the states $|N, 0\rangle$ and $|0, N\rangle$ are initially well decoupled.

This form of the geodesic driving can be readily interpreted from Eq. (3.117) for $L = 1$, noting that there is only a single outer site. The factor of 2 disappears because, in the reduced Hamiltonian (3.93), only the central well is subject to the driving. In

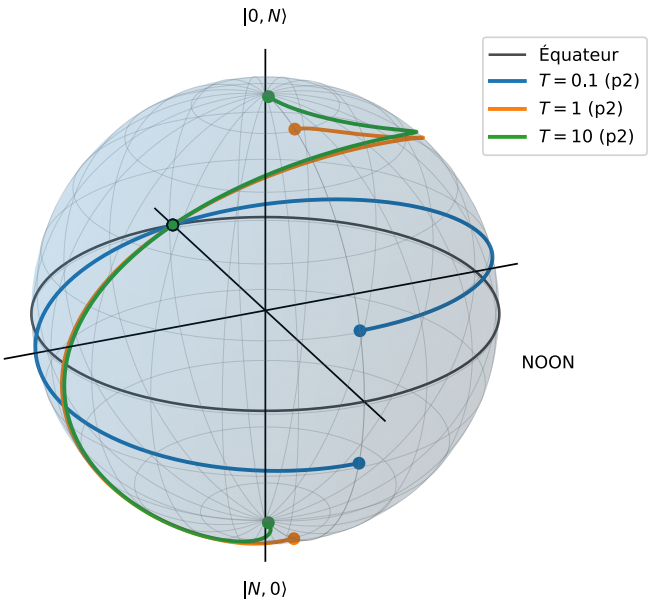

FIGURE 4.4: Evolution of the populations projected onto the Bloch sphere of the system reduced to two modes (Eq. (4.30)) for different total protocol times T, with $N = 5$ and $U = 10\Delta$, the azimuthal angle $\phi(t)$ evolving as $2\pi t/T$. The faster the evolution, the farther the initial and final states are from the Fock states located at the poles. The equator corresponds to the NOON state $|N, 0\rangle + |0, N\rangle$.

the system (4.30) studied here, both wells are modified by the functions $\pm\varepsilon(t)$; it is therefore natural that the rate of change is divided by two.

In the eigenbasis of the Bose-Hubbard Hamiltonian (4.29), the counterdiabatic Hamiltonian takes the form

$$\hat{H}_{\mathrm{CD}}(t) = \frac{N\mathcal{J}\dot{\varepsilon}(t)}{2(\mathcal{J}^2 + (N\varepsilon(t))^2}\,\hat{\sigma}_y \tag{4.35}$$

which we denote $\hat{H}_{\mathrm{CD}}(t) = \Omega(t)\hat{\sigma}_y$. Thus, defining a new Hamiltonian $\hat{H} + \hat{H}_{\mathrm{CD}}$ removes all off-diagonal elements in the eigenbasis, protecting the system state from any unwanted diabatic transitions.

By inserting the expression of the geodesic driving (4.34) into the definition of the counterdiabatic terms (4.35), one obtains the constant amplitude of the GCD protocol:

$$\Omega = \frac{\alpha_f - \alpha_i}{2T} \tag{4.36}$$

The norm of the counterdiabatic term is therefore fully determined by the total evolution time T, since $\alpha_f - \alpha_i \approx \pi$. The gap $\sqrt{\mathcal{J}^2 + (N\varepsilon(t))^2 + \Omega^2}$ is thus broadened by the last term, which is inversely proportional to T. Hence, the NOON time (4.32) at resonance $\varepsilon = 0$ for a total evolution time $T \ll \hbar/\mathcal{J}$ is given by

$$\begin{aligned}\tau_{\mathrm{NOON}} &= \frac{\pi\hbar}{4\sqrt{\mathcal{J}^2 + \Omega^2}} \\ &\approx T/2.\end{aligned} \tag{4.37}$$

The result (4.36) is intrinsically connected to the notion of a quantum speed limit.

Indeed, the relation linking counterdiabatic control to geodesic driving arises through the diagonal elements of the CDH: $\langle n|H_{\mathrm{CD}}^2|n\rangle = -\hbar^2 g^{(n)}\dot{\varepsilon}(t)^2$. In our case, and more generally for a two-level system, the squared norm of the counterdiabatic Hamiltonian, namely Ω^2, can therefore be directly related to the geodesic condition, which requires that the quantity $g^{(n)}\dot{\varepsilon}(t)^2 = \Delta E^2$ remain constant in time. Thus, by linking Ω^2 to ΔE^2 and expanding the Mandelstam-Tamm bound for the system under consideration, one finds that the GCD protocol saturates the quantum speed limit due to expression (4.36).

4.3 Entangling vortices

4.3.1 Implementation into the many-body system

To apply the protocol to the full system, one must define an effective complex hopping that incorporates the action of the counterdiabatic term. Using the identification

$$H_{\mathrm{red}}(U,\Delta,\varepsilon(t)) + H_{\mathrm{CD}} \overset{!}{=} H_{\mathrm{red}}\left(U,\Delta_{\mathrm{eff}},\varepsilon(t)\right), \tag{4.38}$$

we can define a complex Δ_{eff} such that

$$\Delta_{\mathrm{eff}}/2 = \left[(\Delta/2)^N - i\frac{\pi(2U/3)^{N-1}(N-1)!}{2NT}\right]^{1/N} \tag{4.39}$$

Thus, in the self-trapping regime, the Hamiltonian describing the system under the GCD protocol can be written as

$$\begin{aligned}\hat{H} = &-\frac{U}{3}\left(\hat{a}_+^{\dagger 2}\hat{a}_+^2 + \hat{a}_-^{\dagger 2}\hat{a}_-^2\right) - \frac{1}{2}\left(\Delta_{\mathrm{eff}}\,\hat{a}_+^\dagger\hat{a}_- + \Delta_{\mathrm{eff}}^*\,\hat{a}_-^\dagger\hat{a}_+\right)\\ &+\varepsilon(t)(\hat{a}_+^\dagger\hat{a}_+ - \hat{a}_-^\dagger\hat{a}_-),\end{aligned} \tag{4.40}$$

which describes an adiabatic time evolution along the eigenvectors of the Hamiltonian (4.29), requiring only a temporal modulation of the energies of the two modes.

Figure 4.5(a) shows the spectrum of the Hamiltonian (4.40) in the case of GCD driving (blue) and of purely geodesic driving (with $\mathrm{Re}\Delta_{\mathrm{eff}} = \Delta$ and $\mathrm{Im}\Delta_{\mathrm{eff}} = 0$, red), for $N = 4$, $U = 10\Delta$, and $T = 1000\hbar/\Delta$. The spectrum is slightly modified in the presence of GCD driving; in particular, a zoom (Fig. 4.5(b)) reveals that the gap separating the initial state $|N,0\rangle$ from the final state $|0,N\rangle$ is enlarged, allowing for adiabatic driving beyond the typical timescale set by the adiabatic theorem. This is visible in panel (c), where the populations of the states $|N,0\rangle$ and $|0,N\rangle$ are shown as a function of time. In particular, the GCD protocol indeed enables population inversion, whereas purely geodesic driving fails to do so. A NOON state $(|N,0\rangle + |0,N\rangle)/\sqrt{2}$ is obtained at half of the total protocol time, i.e., at $t \approx 500\hbar/\Delta$.

4.3.2 Emulating counterdiabatic driving with Floquet engineering

The need to introduce a complex coupling Δ_{eff} may, however, pose practical difficulties. An alternative definition can be obtained by adding an oscillating term to the Bose-Hubbard Hamiltonian, emulating the additional complex phase [45, 46]. One can show that such an alternative construction is possible at the cost of producing larger

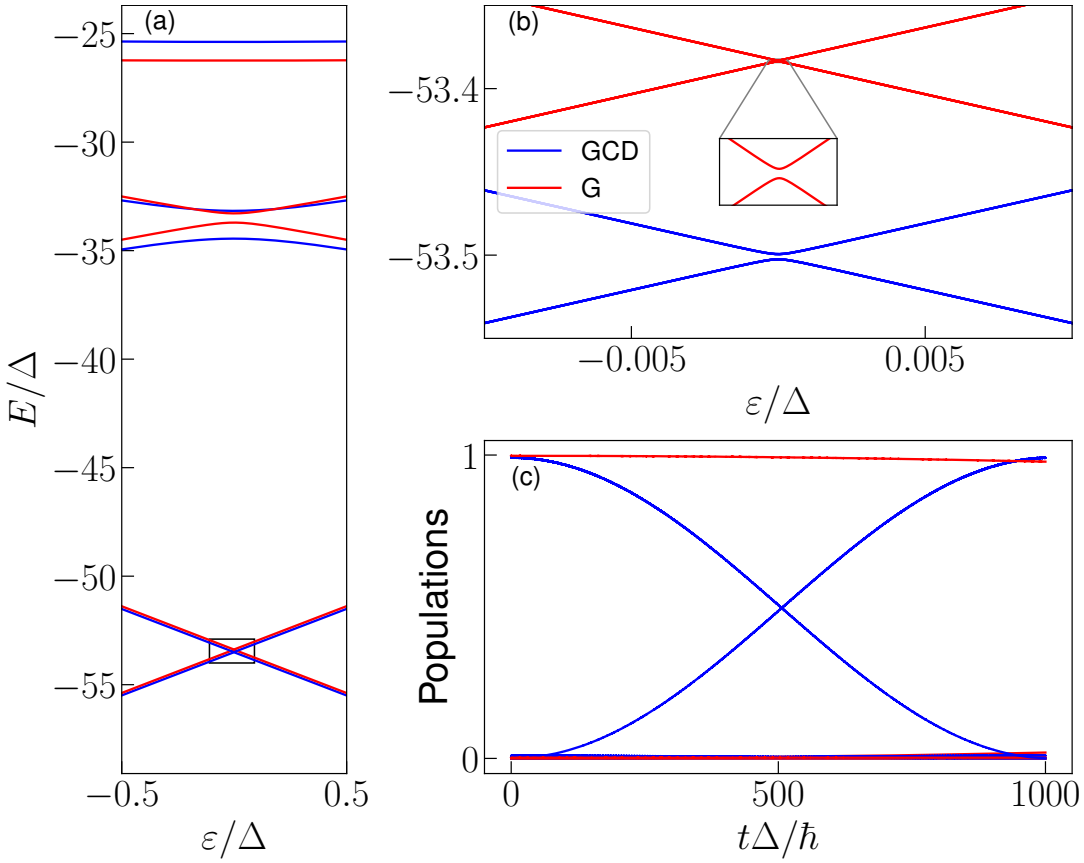

FIGURE 4.5: (a) Spectrum of the Bose-Hubbard Hamiltonian under geodesic driving (red) and geodesic counterdiabatic (GCD) driving (blue), for $N = 4$ particles, $U = 10\Delta$, and $T = 10^3\hbar/\Delta$. A rectangle highlights the gap of interest between the states $|N, 0\rangle$ and $|0, N\rangle$, which are isolated from the rest of the spectrum by a gap proportional to $2U(N-1)/3$. (b) Zoom on the avoided crossings for the two different protocols, G and GCD. The gap under GCD is significantly enlarged, enabling faster adiabatic driving. (c) Time evolution of the populations of the states $|N, 0\rangle$ and $|0, N\rangle$ for a total time $T = 10^3\hbar/\Delta$. A population inversion is achieved within the GCD protocol, allowing for the creation of a NOON state at time $t = T/2$, whereas the inversion is not achieved without counterdiabatic driving (G).

oscillation amplitudes in the population dynamics over time. Let us consider a Bose-Hubbard Hamiltonian as defined in Eq. (4.29), to which we add an oscillating term

$$\hat{h}(t) = A\sin(\omega t)(\hat{a}_+^\dagger \hat{a}_- + \hat{a}_-^\dagger \hat{a}_+) + B\cos(\omega t)(\hat{a}_+^\dagger \hat{a}_+ - \hat{a}_-^\dagger \hat{a}_-). \tag{4.41}$$

At first order in the Magnus-Floquet expansion [45, 46], this Hamiltonian is equivalent to

$$\hat{h}(t) \approx i\frac{AB}{\omega}(\hat{a}_+^\dagger \hat{a}_- + \hat{a}_-^\dagger \hat{a}_+) \tag{4.42}$$

which allows us to identify, by comparison with the Hamiltonian (4.40), the complex term to be emulated

$$\frac{AB}{\omega} = \mathrm{Im}\left\{\Delta_{\mathrm{eff}}\right\}. \tag{4.43}$$

Fixing $B = A$, we obtain the condition

$$A = \sqrt{\omega\,\mathrm{Im}\left\{\Delta_{\mathrm{eff}}\right\}} \tag{4.44}$$

The frequency $\omega \equiv \omega_{\mathrm{FM}}$ should ideally lie in a parametric regime where it is sufficiently large compared to characteristic frequencies of the system. We may therefore define three characteristic frequencies scales of the system: the adiabatic frequency $\omega_{\mathrm{GCD}} \sim \sqrt{\mathcal{J}^2 + \Omega^2} \sim 1/T$, which sets the timescale required to adiabatically invert the population; the many-body frequency $\omega_{\mathrm{MB}} \sim 2U(N-1)/3\hbar$, arising from the energy difference between the states $|N, 0\rangle$ and $|N-1, 1\rangle$; and finally the Floquet-Magnus frequency

$$\omega_{\mathrm{FM}} = \frac{A^2}{\mathrm{Im}\{\Delta_{\mathrm{eff}}\}}. \tag{4.45}$$

It is necessary that ω_{GCD} be the smallest frequency in the system, despite the acceleration of the adiabatic process enabled by the GCD protocol. The excitation frequency to the nearest many-body states, ω_{MB}, must be sufficiently large to remain completely decoupled from the adiabatic driving (in other words, to stay in the self-trapping regime). The emulation frequency ω_{FM} must be well separated from the other system frequencies to avoid unwanted couplings.

Finally, all internal frequencies must remain sufficiently small compared to the average trapping frequency, which isolates the p band from the s and d bands. These requirements can be expressed as

$$\omega_{\mathrm{GCD}} \ll \omega_{\mathrm{MB}} \ll \omega_{\mathrm{FM}} \ll \bar{\omega}, \tag{4.46}$$

such a regime ensures that the different timescales at which the relevant physical processes occur remain well separated.

Figure 4.6(a) compares the population dynamics obtained using the Bose-Hubbard Hamiltonian with a complex coupling Δ_{eff} (red curves) and using the oscillating terms added via the Hamiltonian $\hat{h}(t)$ (blue curves). In a parametric regime where the Floquet-Magnus expansion frequency is sufficiently large to be fully decoupled from the other characteristic frequencies of the system, the dynamics produced by the two methods are, on average, the same. However, larger oscillations are expected when the evolution is governed by $\hat{H}(U, \Delta) + \hat{h}(t)$. In particular, the different frequencies present in the system are visible at different resolution scales, as shown in the insets. In panel 4.6(b), the first zoom reveals oscillations arising from many-body couplings with other states in the system's spectrum. A beating phenomenon is observed, corresponding to the proximity between the excitation frequencies connecting neighboring states. Denoting by E_{n_+,n_-} the energy of the state with n_+ (respectively n_-) bosons in the clockwise (respectively anticlockwise) mode, the two frequencies are written

$$\omega_{\mathrm{MB1}} = E_{N,0} - E_{N-1,1} = 2U(N-1)/3 \tag{4.47}$$

$$\omega_{\mathrm{MB2}} = E_{N-1,1} - E_{N-2,2} = 2U(N-3)/3. \tag{4.48}$$

The proximity of these two frequencies gives rise to the observed beats phenomenon, visible in both the red and blue curves, through the ratio

$$\omega_{\mathrm{MB1}}/\omega_{\mathrm{MB2}} = (N-1)/(N-3). \tag{4.49}$$

Inset 4.6(c) shows the third and largest frequency, corresponding to the Floquet-Magnus expansion used to emulate the complex coupling via oscillating terms. Once the three main frequencies of the system are sufficiently well separated in magnitude, they no longer interfere with the physical processes associated with each of them.

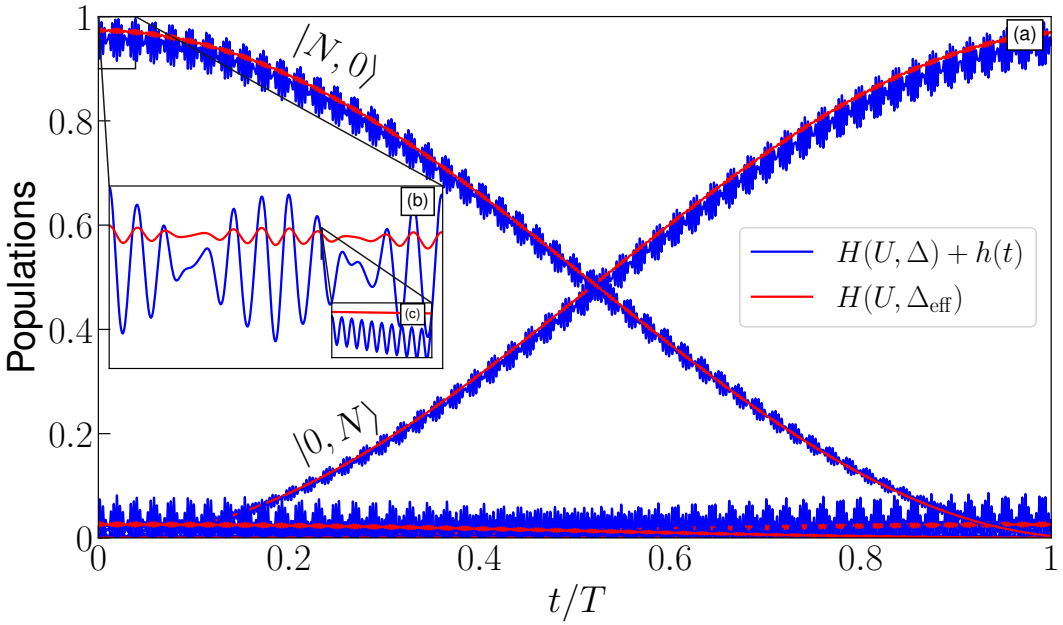

FIGURE 4.6: Time evolution of the populations in the case of geodesic counterdiabatic driving (4.40, red) and in the case where the complex hopping is emulated by a Hamiltonian composed of oscillating terms (4.41, blue). The three characteristic frequencies of the system are visible in each plot, namely ω_{GCD}, associated with the adiabatic evolution, ω_{MB}, associated with many-body transitions (inset (b)), and the frequency ω_{FM} related to the emulation of the complex terms. The average dynamics are the same in both cases, thus allowing one to reproduce a perfectly adiabatic evolution without resorting to complex hopping.

4.3.3 Experimental feasibility and order-of-magnitude estimates

The question that now arises is whether the typical frequency values considered in this work, and in particular the hierarchy (4.46), are plausible within a realistic experimental setting. In the article [165], the authors investigate a bosonic gas of rubidium 87 confined in a quasi two-dimensional harmonic potential, realized using a one-dimensional optical lattice. The trapping frequencies associated with the three spatial directions are

$$\omega_x/2\pi = 11\,\mathrm{Hz}, \tag{4.50}$$
$$\omega_y/2\pi = 130\,\mathrm{Hz}, \tag{4.51}$$
$$\omega_z/2\pi = 3600\,\mathrm{Hz}, \tag{4.52}$$

which corresponds to a very strong confinement along the z axis, ensuring the quasi two-dimensional character of the system, and to a pronounced anisotropy in the transverse (x, y) plane. In this configuration, the total number of rubidium 87 atoms trapped in each optical well is of the order of $N \sim 10^5$.

For the atomic species ^{87}Rb, the contact interaction can be rewritten in terms of the s-wave scattering length, $a_s \simeq 5.29 \times 10^{-9}\,\mathrm{m}$, and the atomic mass $m = 1.44 \times 10^{-25}\,\mathrm{kg}$ [12]. By inserting these values together with the experimental trapping frequencies

into the expression (4.19), one obtains an effective interaction strength

$$U/\hbar \simeq 4.19\,\mathrm{rad/s}. \tag{4.53}$$

The anisotropy associated with the trap is given by $\Delta = \hbar(\omega_y - \omega_x)$, which leads to the numerical value

$$\Delta/\hbar \simeq 7.48 \times 10^2\,\mathrm{rad/s}. \tag{4.54}$$

At first glance, this anisotropy appears to be much larger than the two-body interaction scale. However, it should be recalled that the self-trapping regime is a collective phenomenon, whose relevant criterion involves the total number of particles. The appropriate quantity to consider is therefore the ratio NU/Δ. Under the experimental conditions of [165], one finds

$$\frac{NU}{\Delta} \approx 560, \tag{4.55}$$

indicating that the self-trapping regime is largely satisfied in this experimental setup. As an order-of-magnitude estimate, a ratio $U/\Delta \approx 10$ could already be achieved for a particle number of the order of $N \sim 10^3$. The self-trapping regime may also be reached by reducing the anisotropy Δ, for instance by choosing a trapping frequency ω_x closer to ω_y.

For the previously established values, the frequency hierarchy (4.46) can also be fixed for an arbitrary GCD protocol duration $T = 100\,\hbar/\Delta$ and for $N = 10$. In this case, the different characteristic frequencies of the system read

$$\omega_{\mathrm{GCD}} \sim 1/T = \Delta/(100\hbar) \approx 7.5\,\mathrm{rad/s}, \tag{4.56}$$

$$\omega_{\mathrm{MB}} \sim 2U(N-1)/\hbar \approx 72\,\mathrm{rad/s}, \tag{4.57}$$

$$\bar{\omega} \approx 2\pi \times 440\,\mathrm{rad/s}. \tag{4.58}$$

These order-of-magnitude estimates confirm that the parameter regime considered here is compatible with experimentally accessible conditions, while allowing for a clear separation between the different timescales of the problem. The hierarchy (4.46) therefore provides a consistent framework for analyzing the dynamics induced by the GCD protocol.

5

Metrology with NOON states

Metrology is the science of measurement. Far from being limited to the construction of equivalent land parcels or other geographical analyses, metrology is fundamentally the discipline that establishes the link between physical theory and experiment. Without experimental verification of theoretical results, physics would be nothing more than a minimalist branch of mathematics, devoid of any connection to reality. Confronting mathematical developments and results with the data provided by nature makes it possible to discard fanciful physical theories in favor of models that genuinely allow for an accurate description of reality.

Advances in metrology also drive progress in physics. A paradigmatic example is the measurement of gravitational waves in 2016 [166], which validated a century-old theoretical prediction [129], representing a remarkable technical achievement by reaching a measurement precision of the order of 10^{-18}, corresponding to the thickness of a human hair relative to the distance to nearby stars. Slightly earlier, in 2012, it was the Brout-Englert-Higgs boson [167, 168], whose lifetime is of the order of 10^{-22} s, that was detected at the LHC through its decays into quarks.

Metrology does not solely serve to confirm previously established theories. The history of physics, and more particularly that of quantum physics, abounds with cases in which a measurement finds no explanation within existing mathematical frameworks and calls for the development of new theoretical results to achieve a rational understanding. Beyond advancing fundamental science, the development of such mathematical tools has led to the emergence of new technologies with a tangible impact on everyday life (one may cite, for instance, the GPS system, which must account for the time shift induced by the gravitational field). In this context, the development of metrology at the quantum scale finds its natural motivation: the more negligible external perturbations become, the more precise measurements can be achieved.

In particular, a branch of metrology known as parameter estimation is widely used in conjunction with purely quantum states [169]. Within this framework, a known initial quantum state is employed as a probe. The state of the system then evolves deterministically according to the Schrödinger equation and, if a perturbation depending on a parameter θ is present, acquires a phase during its evolution. Once the final state is obtained, by comparing it with a system initially prepared in the same state but which has not undergone any phase shift, information about the parameter θ can be extracted. In particular, determining the parameter exactly is not always possible; however, it is possible to extract sufficient information to make use of inference

statistics in order to estimate the parameter.

In this chapter, we will detail the mathematical theory of parameter estimation and apply it to quantum theory. In particular, we will show that NOON states are optimal for phase-difference estimation. We will also present the results obtained by Humphreys [170], which provide the optimal population of multi-NOON states for the simultaneous phase estimation of a set of L sites. Finally, we will apply vortex NOON states to the measurement of infinitesimal rotations and show that our results indicate that a measurement of the Earth's rotation would be possible using such states.

5.1 Parameter estimation

In what follows, we introduce the density operator formalism, which provides a complete description of quantum systems, in particular when some uncertainty remains about the prepared state. In the case of pure states, if the system is prepared in the state $|\psi\rangle$, the density operator $\hat{\rho}$ is defined by

$$\hat{\rho} = |\psi\rangle\langle\psi|. \tag{5.1}$$

This operator is Hermitian, positive semi-definite, and has unit trace, properties that guarantee its probabilistic interpretation. It contains the full set of physically accessible information about the system; in particular, the expectation value of an observable $\hat{A}$ can be obtained directly from the trace

$$\langle\hat{A}\rangle = \langle\psi|\hat{A}|\psi\rangle = \mathrm{Tr}[\hat{\rho}\hat{A}]. \tag{5.2}$$

The time evolution of the density operator is entirely determined by the system dynamics. In the case of an isolated quantum system, this evolution is governed by the Schrödinger equation applied to the states $|\psi_i\rangle$. As a consequence, the density operator obeys the von Neumann equation

$$i\hbar\frac{d\hat{\rho}}{dt} = \left[\hat{H}, \hat{\rho}\right], \tag{5.3}$$

where $\hat{H}$ is the Hamiltonian of the system and $[\cdot,\cdot]$ denotes the commutator. This equation constitutes the analogue, for the density operator, of the Schrödinger equation for state vectors.

The formal solution of this equation can be expressed using the unitary time-evolution operator $\hat{U}(t) = \exp\left(-i\hat{H}t/\hbar\right)$, leading to

$$\hat{\rho}(t) = \hat{U}(t)\,\hat{\rho}(0)\,\hat{U}^{\dagger}(t). \tag{5.4}$$

This evolution preserves the fundamental properties of the density operator, in particular its trace and its positivity, thereby ensuring the consistency of the probabilistic interpretation at all times.

This formalism proves to be particularly well suited for the study of composite systems or situations involving coupling to an environment, for which a description in terms of state vectors becomes insufficient. It therefore provides a natural framework

for the analysis of decoherence phenomena and non-unitary dynamics.

This formalism is also especially appropriate when the evolution of the system depends on an unknown parameter. Let us assume that the system is initially in the state $\hat{\rho}$ and that it evolves according to a unitary transformation $U(\theta)$ parametrized by an unknown real number θ. By measuring the final state $\hat{\rho}(\theta)$, we obtain a measurement outcome that itself depends on θ, and we wish to estimate the value of this parameter from the measurement results. The most general measurement operation is described by a set of positive operator-valued measure (POVM) elements $\hat{E}(\varepsilon)$ associated with the measurement outcome ε, which are non-negative and satisfy the completeness relation $\sum \hat{E}(\varepsilon) = \hat{\mathbb{I}}$.

One then defines the likelihood, that is, the conditional probability of observing the outcome ε for a given value of θ:

$$P(\varepsilon|\theta) = \mathrm{Tr}[\hat{E}(\varepsilon)\hat{\rho}(\theta)] \tag{5.5}$$

In full generality, let us assume that our system $\hat{\rho}$ is composed of m subsystems

$$\hat{\rho} = \hat{\rho}^{(1)} \otimes \hat{\rho}^{(2)} \otimes \ldots \otimes \hat{\rho}^{(m)} \tag{5.6}$$

and that we perform local measurements that are independent of one another, that is,

$$\hat{E}(\varepsilon) = \hat{E}^{(1)}(\varepsilon_1) \otimes \hat{E}^{(2)}(\varepsilon_2) \otimes \ldots \otimes \hat{E}^{(m)}(\varepsilon_m) \tag{5.7}$$

In this case, the likelihood becomes the product of the individual measurements:

$$P(\boldsymbol{\varepsilon}|\theta) = \prod_{i=1}^{m} \mathrm{Tr}[\hat{E}^{(i)}(\varepsilon_i)\, \rho^{(i)}(\theta)]. \tag{5.8}$$

It is customary to define the log-likelihood, which is simply the natural logarithm of the likelihood:

$$L(\boldsymbol{\varepsilon}|\theta) = \ln P(\boldsymbol{\varepsilon}|\theta). \tag{5.9}$$

The measurement of the observable yields a set of random outcomes $\boldsymbol{\varepsilon}$ that depend on the unknown variable θ. We aim to define a function that will **estimate** the value of θ, that is, a function that associates an estimate of θ with each set of measurement outcomes. An **estimator** Θ must therefore be close to the true value of θ in order to provide a good estimate.

A very popular choice of estimator is the maximum-likelihood estimator, which consists in maximizing the probability of observing $\boldsymbol{\varepsilon}$ given θ. An estimator can be characterized by its mean value $\langle\Theta\rangle_\theta$ and its variance $(\Delta\Theta)^2_\theta$:

$$\langle\Theta\rangle_\theta = \sum_{\boldsymbol{\varepsilon}} P(\boldsymbol{\varepsilon}|\theta)\Theta(\boldsymbol{\varepsilon}), \tag{5.10}$$

$$(\Delta\Theta)^2_\theta = \sum_{\boldsymbol{\varepsilon}} P(\boldsymbol{\varepsilon}|\theta)\left(\Theta(\varepsilon) - \langle\Theta\rangle_\theta\right)^2. \tag{5.11}$$

In particular, an estimator is said to be unbiased if its statistical mean coincides with the true value of the parameter:

$$\langle\Theta(\boldsymbol{\varepsilon})\rangle_\theta = \theta. \tag{5.12}$$

The search for an unbiased estimator, thus satisfying $\partial_\theta \langle \Theta \rangle_\theta = 1$, is therefore essential in order to estimate a random variable accurately. The natural question that follows the definition of an estimator is the following: how precise can an estimator be? This limit is formalized by the Cramér-Rao bound.

5.1.1 Cramér-Rao lower bound

The Cramér-Rao bound [171, 172] provides a lower bound on the variance of an estimator. It states that, at best, only a limited precision can be achieved. It is expressed as

$$(\Delta\Theta)_\theta^2 \geq \frac{\partial_\theta \langle \Theta \rangle_\theta}{F(\theta)}, \tag{5.13}$$

where

$$F(\theta) = \langle (\partial_\theta L(\varepsilon|\theta))^2 \rangle_\theta \tag{5.14}$$

is the **classical Fisher information**. This quantity measures the sensitivity of the measurement outcome distribution to variations of the parameter θ. The stronger the dependence of $P(\varepsilon|\theta)$ on θ, the larger the Fisher information and the smaller the minimal achievable variance. The Fisher information is additive, which implies that, in the case of a large number of independent repetitions of the experiment, the variance decreases inversely with the number of measurements. Moreover, the maximum-likelihood estimator is asymptotically efficient: it saturates the Cramér-Rao bound in the limit of an infinite number of data points, which justifies its widespread use in estimation protocols.

In particular, one can show that there exists an upper bound on the classical Fisher information, known as the **quantum Fisher information** (QFI, denoted F_Q) [173, 174] :

$$F_Q(\theta) = \max F(\theta), \tag{5.15}$$

where the maximization is performed over the set of measurements $\hat{E}_\varepsilon$. In fact, this upper bound implies that there exists (under certain conditions [169]) at least one measurement operation for which the Cramér-Rao bound can be saturated. In the particular case of a pure state $\hat{\rho}(\theta) = |\psi_\theta\rangle\langle\psi_\theta|$, the quantum Fisher information takes a particularly interesting form:

$$F_Q(\theta) = 4 \left(\langle \partial_\theta \psi_\theta | \partial_\theta \psi_\theta \rangle - |\langle \psi_\theta | \partial_\theta \psi_\theta \rangle|^2 \right), \tag{5.16}$$

which is reminiscent of the definition of the metric tensor 2.51. This resemblance is ultimately quite natural: the quantum Fisher information quantifies the sensitivity of the state to variations of the parameter to be estimated, just as the metric tensor describes how the eigenstates of the Hamiltonian vary under small changes of a parameter λ. Searching for the optimal scaling of F_Q with respect to the parameter to be estimated amounts to minimizing the statistical distances between states.

In the case of a pure state, the QFI satisfies a very interesting identity. Let us assume that the dependence of the state on θ is generated by a unitary evolution

$$|\psi_\theta\rangle = e^{-i\theta\hat{H}} |\psi_0\rangle, \tag{5.17}$$

where $\hat{H}$ is the generator of the transformation. In this case, $|\partial_\theta \psi\rangle = -i\hat{H}|\psi_\theta\rangle$, and one finds

$$\langle \partial_\theta \psi_\theta | \partial_\theta \psi_\theta \rangle = \langle \hat{H}^2 \rangle \tag{5.18}$$

$$\langle \psi_\theta | \partial_\theta \psi_\theta \rangle = -i\langle \hat{H} \rangle. \tag{5.19}$$

We thus obtain

$$F_Q(\theta) = 4(\Delta \hat{H})^2_\theta, \tag{5.20}$$

showing that the ultimate precision of the estimation is directly related to the fluctuations of the generator in the initial state.

Using Eq. (5.20), the Cramér-Rao bound can be manipulated so as to resemble the Heisenberg uncertainty principle:

$$(\Delta\Theta)^2_\theta \, (\Delta H)^2_\theta \geq \frac{1}{4}. \tag{5.21}$$

When this bound is saturated, it is referred to as the Heisenberg limit. It is, however, important to emphasize that, in contrast to the usual uncertainty principle relating two non-commuting observables, this inequality here connects the uncertainty on the estimated parameter Θ to the fluctuations of the generator $\hat{H}$ of the transformation encoding this parameter.

In a many-body context, the notion of the Heisenberg limit is often associated with the scaling of the precision with the number of particles N. For separable states, the fluctuations of the generator grow at most linearly with N, which leads to the standard quantum limit $(\Delta\Theta)\theta \sim 1/\sqrt{N}$. In contrast, for entangled states it is possible to obtain a QFI scaling as N^2, thereby allowing one to reach the Heisenberg limit $(\Delta\Theta)\theta \sim 1/N$. NOON states allow this limit to be achieved for phase estimation.

5.2 L-NOON states for phase estimation

In this section, we will show that NOON states constitute a central resource in quantum metrology due to their ability to encode phase information with an enhanced sensitivity that scales as N rather than $\sqrt{N}$.

5.2.1 NOON states as optimal states for metrology

Let us consider a system initially prepared in a two-mode NOON state, which evolves within a Mach-Zehnder interferometer. The latter is composed of two ideal beam splitters, separated by a region in which a relative phase θ is acquired between the two arms of the interferometer. The overall evolution can be described as a sequence of unitary operations acting on the quantum state.

After the first beam splitter, the state is subjected to a relative phase evolution generated by the population difference between the two modes. This unitary transformation is implemented through the generator $\hat{G} = (\hat{n}_a - \hat{n}_b)/2$, where $\hat{n}_a$ and $\hat{n}_b$ are respectively the particle number operators in modes a and b. The state of the system then transforms as

$$|\psi_\theta\rangle = e^{-i\theta\hat{G}}|\text{NOON}\rangle. \tag{5.22}$$

One observes that the relative phase is amplified by a factor N, which is a direct signature of the enhanced sensitivity of NOON states. The second beam splitter then converts this relative phase into a measurable population difference between the two output modes. The detection probabilities consequently exhibit oscillations as a function of θ with a period reduced by a factor N, a phenomenon known as phase super-resolution [175]. In particular, by computing

$$\langle \hat{G} \rangle = 0, \qquad (\Delta \hat{G})^2 = N^2/4, \tag{5.23}$$

one verifies that the quantum Fisher information is given by

$$F_Q = N^2, \tag{5.24}$$

thereby reaching the Heisenberg limit for the Cramér-Rao bound. NOON states therefore allow a $1/N$ scaling for the minimal achievable variance of the estimator, demonstrating a significant advantage for quantum metrology.

Metrological sensitivity and NOON purity

The next natural question is to assess to what extent a NOON state must be prepared with high fidelity in order to retain a significant metrological advantage. In practice, experimental imperfections inevitably lead to degraded states, either through population imbalances or through the presence of spurious components in Fock space. It is therefore essential to quantify the impact of these deviations on the phase resolution.

A first example consists in considering a "nearly NOON" state, in which one particle is transferred from one mode to the other:

$$|\psi\rangle = \frac{1}{\sqrt{2}} \left(|N-1, 1\rangle + |1, N-1\rangle \right). \tag{5.25}$$

Although this state retains a macroscopic superposition structure, the occupations of the two modes are no longer extreme. Using the same phase generator,

$$\hat{G} = (\hat{n}_a - \hat{n}_b)/2 \tag{5.26}$$

we obtain for the QFI :

$$F_Q = (N-2)^2. \tag{5.27}$$

The Heisenberg-type scaling is therefore still present, indicating that the state remains strongly entangled. However, the prefactor N is reduced, reflecting an effective decrease in the fluctuations of the generator. This loss of sensitivity becomes particularly significant for small values of N, where each particle plays a crucial role.

A second type of imperfection that is frequently encountered corresponds to an amplitude imbalance between the two components of the NOON state, leading to a state of the form

$$|\psi\rangle = a|N, 0\rangle + b|0, N\rangle, \tag{5.28}$$

where $|a|^2 + |b|^2 = 1$. In that case, the QFI is

$$F_Q = 4N^2 |a|^2 |b|^2. \tag{5.29}$$

This expression clearly shows that the quantum Fisher information is maximized when

the two components are equally weighted, that is, for $a = b = 1/\sqrt{2}$. Any asymmetry between the amplitudes leads to a reduction of the QFI, which becomes drastic when one component dominates, reflecting a gradual transition toward a classical state localized in a single mode.

These two examples complementarily illustrate that the metrological advantage of NOON states relies not only on their entangled nature, but also on a precise balance between the different components of the superposition. They show that, although Heisenberg scaling may persist in the presence of imperfections, the absolute sensitivity remains fragile and strongly dependent on the quality of state preparation.

5.2.2 Multimode NOON states for multiple phase estimation

Up to this point, we have considered the estimation of a single parameter, typically a relative phase acquired in a two-mode interferometer. However, many physical situations (both in optics and in atomic interferometry) involve the simultaneous estimation of several independent phases, for instance in multimode interferometers or complex optical networks.

The work by Humphreys [170] fits precisely within this context and shows that multipartite entanglement not only improves the precision of single-phase estimation, but also provides a collective quantum advantage in the simultaneous estimation of multiple parameters.

Let us consider an interferometer with $L+1$ modes, in which L independent phases $\boldsymbol{\theta} = (\theta_1, \ldots, \theta_L)$ are encoded relative to a reference mode, which we denote by the index c. The initial state of the system is a $|\text{L-NOON}\rangle$ state, which we denote as

$$|\psi_0\rangle = \frac{1}{\sqrt{L+1}} \sum_{\mu=1}^{L} \alpha_\mu \, |0, 0, \ldots, \underbrace{N}_{\mu^{\text{th}} \text{ mode}}, \ldots, 0\rangle \equiv \frac{1}{\sqrt{L+1}} \sum_{\mu=1}^{L} \alpha_\mu \, |N_\mu\rangle. \tag{5.30}$$

The unitary operator can be written as

$$\hat{U}(\boldsymbol{\theta}) = \exp\left(-i \sum_{\mu=1}^{L} \theta_\mu \hat{G}_\mu \right) \tag{5.31}$$

where $\hat{G}_k = \hat{n}_k - \hat{n}_c$ is the generator associated with the phase θ_k.

For a pure quantum state, the Quantum Fisher Information matrix $F_{\mu\nu}$ associated with the estimation of the phases θ_μ is given by

$$F_{\mu\nu} = 4\text{Re}\left\{ \langle \partial_\mu \psi | \partial_\nu \psi \rangle - \langle \partial_\mu \psi | \psi \rangle \langle \psi | \partial_\nu \psi \rangle \right\}, \tag{5.32}$$

where the derivatives $\partial_\mu \equiv \partial / \partial \theta_\mu$ act on the L independent phase parameters indexed by $\mu, \nu \in \{1, \ldots, L\}$. The QFI matrix fully characterizes the ultimate sensitivity of the state with respect to multi-parameter phase estimation [174, 176, 177] and provides a fundamental lower bound on the achievable variances through the quantum Cramér-Rao inequality [173]. In particular, the total estimation error for the collection

of phases is bounded by [170]

$$|\Delta\boldsymbol{\theta}|^2 = \sum_{k=1}^{L} \delta\theta_k^2 \geq \mathrm{Tr}[F_{\mu\nu}^{-1}]. \tag{5.33}$$

which holds for any unbiased estimator. Minimizing this bound is therefore equivalent to optimizing the structure of the state, in particular the relative amplitudes a and b, in order to maximize its sensitivity to the encoded phases.

Let us assume that the system is in a state

$$|\psi\rangle = \alpha\left(|0, N, \ldots, 0, 0\rangle + |0, 0, N, \ldots, 0\rangle + \ldots + |0, 0, \ldots, 0, N\rangle\right) \tag{5.34}$$

$$+\beta\,|N, 0, \ldots, 0, 0\rangle, \tag{5.35}$$

where the N particles are either fully localized in one of the L probed modes or concentrated in the reference mode. The coefficients α and β satisfy the normalization condition

$$L\alpha^2 + \beta^2 = 1, \tag{5.36}$$

which allows β to be expressed as a function of α, which we assume to be real without loss of generality. This state constitutes a continuous interpolation between a symmetric multimode NOON superposition and a state localized in the reference mode. It therefore provides a natural framework to study the trade-off between multipartite entanglement and asymmetric amplitude weighting in the context of the simultaneous estimation of multiple phases. In this case, the QFI associated with the phase parameters $\boldsymbol{\theta} = (\theta_1, \ldots, \theta_L)$ can be written as

$$F_{\mu\nu} = 4N^2(\alpha^2\delta_{\mu,\nu} - \alpha^4). \tag{5.37}$$

To quantify the overall precision of the multiparameter estimation, we consider the trace of the inverse of the quantum Fisher information matrix, $\mathrm{Tr}[F_{\mu\nu}^{-1}]$, which provides a lower bound on the total mean-square variance. Minimizing this quantity with respect to the parameter α makes it possible to identify the optimal state in the metrological sense. One then shows that the minimum is achieved for

$$\alpha = \frac{1}{\sqrt{L + \sqrt{L}}}, \tag{5.38}$$

which allows one to obtain the optimal state. In this case, the minimal variance is given by

$$|\Delta\boldsymbol{\theta}|^2 = \frac{L\left(1 + \sqrt{L}\right)^2}{4N^2}. \tag{5.39}$$

This result clearly highlights a global Heisenberg-type scaling, proportional to $1/N^2$, confirming that the considered state makes it possible to fully exploit quantum resources for the simultaneous estimation of multiple parameters.

Application to triple-NOON states

In this section, we illustrate the metrological usefulness of the triple-NOON states generated by our protocol by explicitly computing the Quantum Fisher Information (QFI) associated with phase estimation in our four-mode geometry in the case of the Bose-Hubbard model (3.89) for $L = 3$.

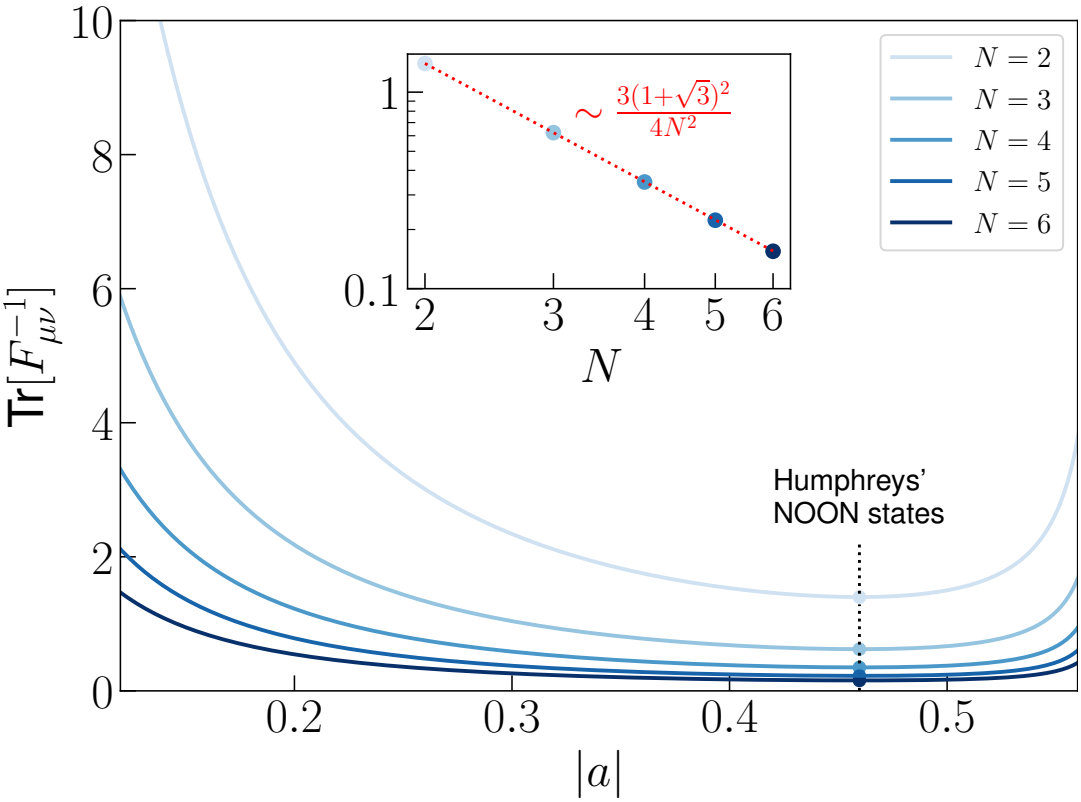

FIGURE 5.1: Evolution of the total phase variance for the state $|\psi(\theta_1, \theta_2, \theta_3)\rangle$ as a function of the population root of the $|3\text{-NOON}\rangle$ state for different particle numbers N. This graph highlights the minimum of $|\Delta\boldsymbol{\theta}|^2$ predicted by Humphreys [170] at $a = 1/\sqrt{L + \sqrt{L}}$. In the inset, minimal values of $\mathrm{Tr}[F_{\mu\nu}^{-1}]$ are plotted as a function of the number of particles to confirm the Heisenberg scaling of $\sim 1/N^2$ for pure NOON states, which occurs when the GCD protocol is fully implemented

We consider the situation in which each of the three outer wells acquires an independent phase shift relative to the central reference well. The resulting state of the system can be written as

$$|\psi(\theta_1, \theta_2, \theta_3)\rangle = b|N; 0, 0, 0\rangle + a(e^{i\theta_1 N}|0; N, 0, 0\rangle + e^{i\theta_2 N}|0; 0, N, 0\rangle + e^{i\theta_3 N}|0; 0, 0, N\rangle). \tag{5.40}$$

where the three parameters θ_1, θ_2, and θ_3 represent the accumulated phases in the three arms of the interferometer. The coefficients a and b quantify the relative population of the NOON manifold and the central Fock state. Their time evolution is governed by the dynamics shown in Fig. 3.15, and thus encapsulates the progressive formation of the triple-NOON state during the GCD protocol.

Figure 5.1 displays the behavior of the Quantum Fisher Information as a function of the amplitude $|a|$ for several particle numbers N, allowing us to quantify how the metrological performance evolves during the preparation of the $|3\text{-NOON}\rangle$ state. For each value of N, the trace of the inverse QFI matrix, $\mathrm{Tr}[F_{\mu\nu}^{-1}]$, exhibits a characteristic minimum that reflects the point of maximal sensitivity to the three phase parameters. This minimum corresponds precisely to the balance between the NOON component and the reference mode that yields optimal multiparameter estimation.

As indicated by the markers in Fig. 5.1, the dynamically generated state approaches the value of $|a|$ predicted by Humphreys [170] for achieving the lowest possible total phase uncertainty in a three-arm interferometer. The corresponding state represents the configuration that saturates the quantum Cramér-Rao bound for simultaneous estimation of three phases.

The inset of Fig. 5.1 further highlights that the final value of the total phase variance, $|\Delta\boldsymbol{\theta}|^2 = \mathrm{Tr}[F_{\mu\nu}^{-1}]$, follows the expected Heisenberg scaling with particle number. Specifically, our protocol achieves a precision consistent with the theoretical scaling

$$\frac{3(1+\sqrt{3})^2}{4N^2} \tag{5.41}$$

demonstrating that the generated $|3\text{-NOON}\rangle$ states possess the full metrological power anticipated for ideal multimode NOON states. This confirms not only the correctness of the state produced by the GCD method but also its practical relevance for high-precision, multiparameter quantum sensing.

5.3 NOON states of vortices for rotation sensing

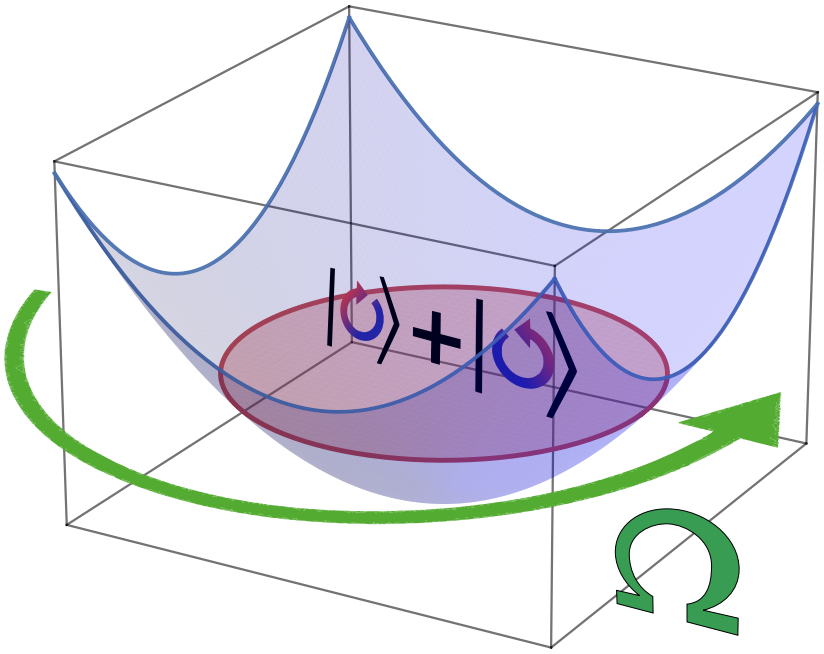

FIGURE 5.2: Schematic representation of the proposed protocol for metrology with vortex NOON states. The aim is to use the superposed state to detect whether an external rotation Ω acts on the laboratory frame. Owing to the enhanced sensitivity of NOON states, such a superposition can, in principle, enable the measurement of Earth's rotation through the growing imbalance in population between the two counter-rotating components.

In Chapter 4, we demonstrated the possibility of creating vortex NOON states within experimentally achievable times. We now present a metrological protocol that takes advantage of the extreme sensitivity of NOON states. The idea is as follows: thanks to the GCD, we know that the NOON state must appear at half of the chosen protocol time T. Can one identify the failure to observe a NOON state at $T/2$ and

relate this failure to an external rotation acting as a constant perturbation?

Let us examine what happens in the reduced system (4.30) when an external rotation of the laboratory is present (see Fig. 5.2). In the Fock-state basis defined by the number of bosons rotating clockwise (+) or anticlockwise (−), we have

$$H_{\text{red}} = \begin{pmatrix} N(\varepsilon(t)+\Omega_R) & -\mathcal{J} \\ -\mathcal{J} & -N(\varepsilon(t)+\Omega_R) \end{pmatrix}, \tag{5.42}$$

where Ω_R is the amplitude of the unknown rotation. The gap between the two eigenenergies E_+ and E_- of the reduced system is modified by the presence of Ω_R:

$$|E_+ - E_-| = \sqrt{\mathcal{J}^2 + N^2(\varepsilon(t)+\Omega_R)^2}. \tag{5.43}$$

Whereas the geodesic driving $\varepsilon(t)$ is specifically designed so that the rate of change of the system is minimal where the energy gap is minimal, the presence of the external rotation alters this situation. Indeed, the minimum of the gap no longer occurs at $\varepsilon(t) = 0$ but rather at

$$\varepsilon(t) = -\Omega_R, \tag{5.44}$$

which results in a temporal shift of the gap minimum. Knowing the expression of $\varepsilon(t)$ as the geodesic driving (4.34), one can isolate the time at which the resonance between the two modes occurs in Eq. (5.44), bearing in mind that the constants $\alpha_{i,f}$ tend respectively toward $\pm\pi/2$:

$$\frac{t}{T} = \frac{1}{2} + \frac{\tan^{-1}\left(\frac{N\Omega_R}{\mathcal{J}}\right)}{\pi}. \tag{5.45}$$

In the absence of an external rotation ($\Omega_R = 0$), the resonance indeed occurs at half of the total protocol time T. In the case $\Omega_R > 0$, the GCD protocol does not have sufficient time to be fully completed, and the population is therefore not entirely transferred. This results in a reduced fidelity. From this failure to create the NOON state arises the possibility of measuring the external rotation. If one knows exactly at which time a NOON state should be obtained with a measurement probability close to unity, then the observation of a less pure state serves as an indicator of an external rotation.

In Fig. 5.3, one indeed observes that the final fidelity (and thus the ability of the GCD protocol to invert the population) decreases as a function of Ω_R. More concretely, for a total protocol time $T = 2 \times 10^3 \hbar/\Delta$, the fidelity begins to drop for $\Omega_R \approx 5 \times 10^{-4}\Delta$. This means that for such a value of T, the sensitivity window of the protocol lies roughly in the range $[10^{-4}, 10^{-3}]$. By increasing T, this window shifts toward smaller values of Ω_R. Indeed, the slower the evolution, the more time the external rotation has to affect the system. There is therefore a trade-off to be found between creating the state rapidly and operating within a window that allows one to observe a drop in the measurement probability in the region of Ω_R of interest.

Another possibility to improve the precision window would be to increase the number of particles. The reduced Hamiltonian (4.30) allows us to gain insight into what happens in parametric regimes that become too computationally demanding to study numerically in the case of the many-body Hamiltonian (4.29). In Fig. 5.4, we show the mean value at the end of the GCD protocol, for different values of T, of the

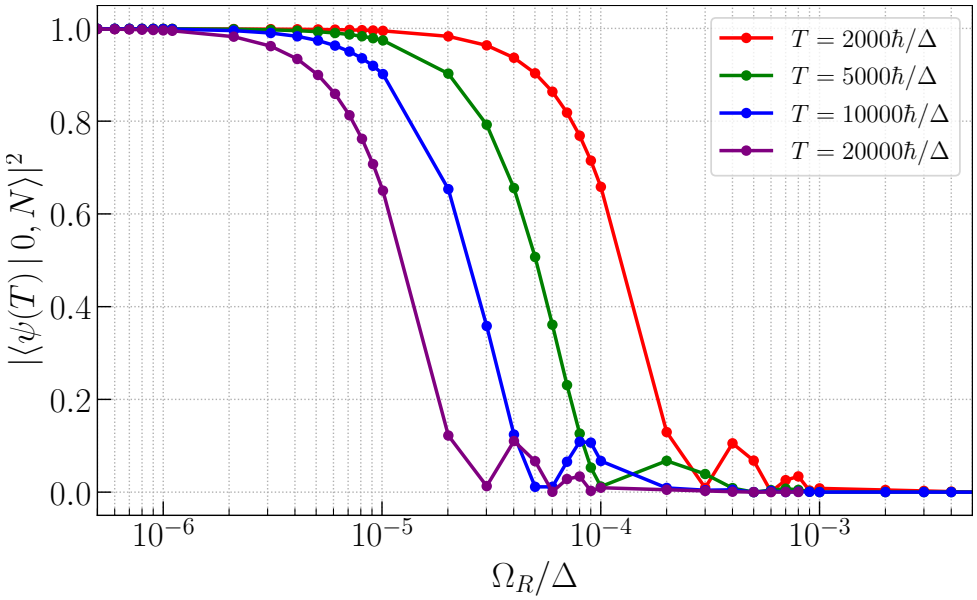

FIGURE 5.3: Overlap between the final state of the system $|\psi(T)\rangle$ and the Fock state $|0, N\rangle$ as a function of the amplitude of the external rotation Ω_R, for different total protocol times T, with $N = 5$ in the case of the Bose-Hubbard Hamiltonian (4.29). At the end of the GCD protocol, the population is perfectly inverted when the external rotation is weak, but it approaches zero when the rotation is too strong. This drop is weighted by the total protocol time: the faster the inversion, the less sensitive the system is to small values of Ω_R.

operator $\hat{J}_z$, defined as

$$\hat{J}_z = \frac{\hat{n}_+ - \hat{n}_-}{2}, \tag{5.46}$$

from the particle number operators $\hat{n}_\pm$ in the $(\pm)$ modes, for a total number of $N = 100$ particles. For small values of Ω_R or relatively short times, the mean value of $\hat{J}_z$ is negative and indicates that the majority of the population occupies the $(-)$ state. A transition then occurs, up to the point where population inversion is no longer achieved and a majority of the population remains in the $(+)$ mode. The transition region makes it possible to identify the amplitude of the unknown rotation Ω_R.

5.3.1 Measuring Earth's rotation

In this subsection, we estimate the magnitude of the Earth's rotation in units relevant to the laboratory frame and to the atomic species considered. As a reminder, in Chapter 4 we assumed a bosonic gas confined in a two-dimensional harmonic trap with a small anisotropy $\Delta = \hbar(\omega_y - \omega_x)$ between the in-plane trapping frequencies (ω_x, ω_y). The relevant physical quantity is therefore the frequency scale $\Delta/\hbar$, which naturally sets the energy splitting between the two modes of interest.

The formation of vortices in a Bose-Einstein condensate of ^{87}Rb confined in a magnetic trap was demonstrated in a closely related experimental setup [178]. In that work, the trapping frequencies are

$$\omega_z/2\pi = 11.7\,\text{Hz}, \tag{5.47}$$

$$\omega_\perp/2\pi = 219\,\text{Hz}, \tag{5.48}$$

corresponding to a strong confinement in the transverse (x, y) plane and a weak axial

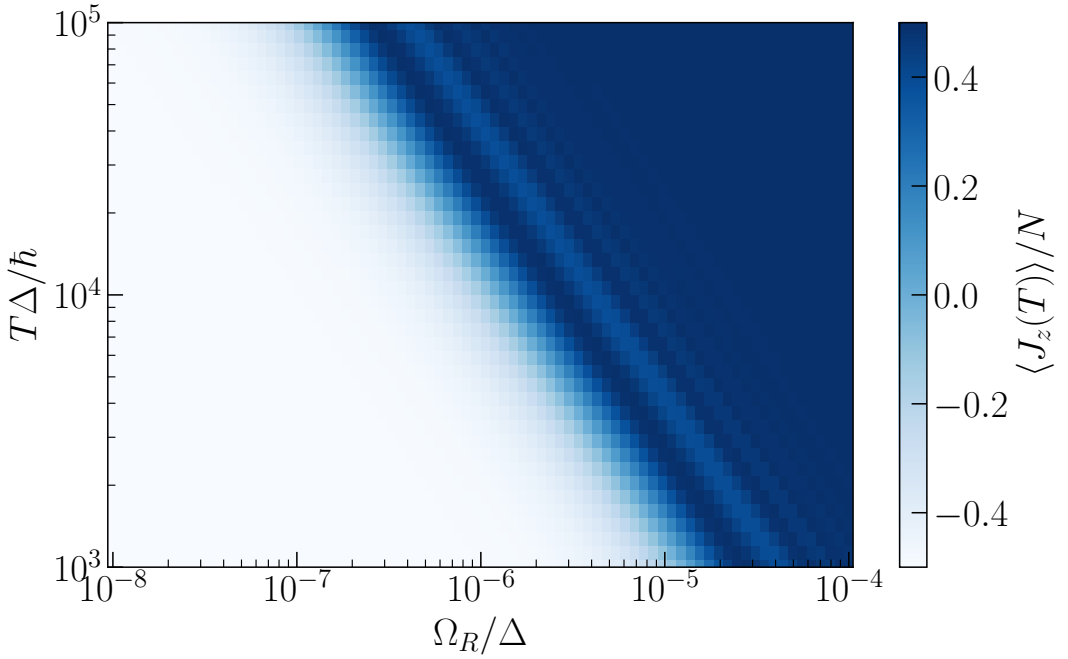

FIGURE 5.4: Heatmap of the mean value of the operator $\hat{J}_z$ as a function of the total protocol time T and the amplitude of the external rotation Ω_R. When the system is initially prepared in the (+) state and the GCD protocol is applied, the drop in fidelity associated with the failure of population inversion makes it possible to identify, within a given window, the amplitude of the external rotation that prevents the proper execution of the entanglement protocol.

confinement along z, such that $\omega_z \ll \omega_x \simeq \omega_y$. By contrast, the protocol proposed in this work requires a strong confinement along the z direction, with $\omega_z \gg \omega_x, \omega_y$. This difference in geometry does not affect the order-of-magnitude estimates presented here, since the relevant energy scales are entirely determined by the in-plane anisotropy $\Delta/\hbar$ and by the external rotation frequency.

The in-plane anisotropy is parametrized through the coefficients ϵ_x and ϵ_y according to

$$\omega_{x,y}^2 = \omega_\perp^2\, \epsilon_{x,y}. \tag{5.49}$$

In Ref. [178], these parameters take the values $\epsilon_x = 0.03$ and $\epsilon_y = 0.09$. From these values, the anisotropy frequency can be expressed as

$$\frac{\Delta}{\hbar} = \omega_\perp\left(\sqrt{\epsilon_y} - \sqrt{\epsilon_x}\right) \approx 1.7 \times 10^2\,\mathrm{rad/s}, \tag{5.50}$$

which corresponds to an energy splitting $\Delta \simeq 2 \times 10^{-32}\,\mathrm{J}$.

This anisotropy must now be compared to the external rotation Ω_R that one aims to measure. Assuming that the rotation corresponds to the Earth's rotation, the associated angular frequency is

$$\omega_R = 7 \times 10^{-5}\,\mathrm{rad\,s^{-1}}, \tag{5.51}$$

leading to a perturbation amplitude

$$\frac{\Omega_R}{\hbar} = \omega_R. \tag{5.52}$$

In dimensionless form, the relative strength of the perturbation induced by the Earth's rotation is therefore

$$\frac{\Omega_R}{\Delta} = \frac{\omega_R}{\Delta/\hbar} \sim 10^{-7}. \tag{5.53}$$

For a system of $N = 100$ particles, the analysis based on the reduced Hamiltonian indicates that the effect of such a weak perturbation can be resolved over a total protocol duration on the order of

$$T \sim 10^5\, \hbar/\Delta. \tag{5.54}$$

Using the numerical estimate $\Delta/\hbar \simeq 1.7 \times 10^2\,\mathrm{rad/s}$, this corresponds to a protocol duration of approximately

$$T \sim 6 \times 10^2\,\mathrm{s}, \tag{5.55}$$

that is, a timescale of several minutes. While such a duration remains relatively long for realistic experimental conditions, it already represents a substantial improvement when compared to the intrinsic timescale of collective tunneling, which increases extremely rapidly with the particle number. For instance, for $N = 5$ particles and $\Delta/\hbar \simeq 1.7 \times 10^2\,\mathrm{rad/s}$, the characteristic collective tunneling time is on the order of a few tens of minutes. By contrast, for $N = 100$ particles, this timescale exceeds the age of the Universe by many orders of magnitude, rendering the collective tunneling completely inaccessible experimentally.

In this perspective, a protocol duration of only a few minutes appears remarkably short. Several strategies may further reduce the required timescale. In particular, increasing the effective anisotropy Δ directly shortens the protocol duration. In addition, although the intrinsic collective tunneling time grows rapidly with N, the sensitivity of the protocol to external perturbations also increases with the particle number through collective many-body effects, allowing one to reach favorable signal-to-noise ratios without relying on the exponentially slow tunneling dynamics.

6

Conclusion

In this manuscript, we have studied the creation of highly entangled states within several many-body systems. In particular, we have proposed a new method allowing one to accelerate the generation of many-body entanglement with the aim of creating NOON states of bosons trapped in optical lattices, as well as of bosons exhibiting rotation in two opposite orientations. In conclusion to this journey, let us emphasize the lessons learned during this thesis.

First, we developed a new quantum control method based on shortcuts to adiabaticity. In the current state of the art, quantum state manipulation is generally performed in two different ways. In the first case, state manipulation is optimized so as to reach the target state as fast as possible while avoiding excessive excitation of the system. In this approach, the emphasis is placed on the shape of the controls applied to the system. In the second case, one attempts to cancel the consequences of an overly fast driving by means of new controls, which sometimes do not represent a physical variable initially present in the system. In this thesis, we constructed a new control method, the geodesic counterdiabatic driving, which is based on the combined use of both methods. By positioning oneself on the optimal parametric path for the studied system and by calculating the form of the terms that must be canceled in order to remain on the desired path, the two methods merge to form a robust quantum control protocol that does not require any time dependence in the new terms. We first showed that geodesic counterdiabatic driving makes it possible to facilitate the adiabatic control of Landau-Zener-type systems, and to reach the quantum speed limit under certain conditions.

Next, we showed that it is possible to analytically construct a reduced Hamiltonian from perturbation theory, which allows one to simulate the dynamics of a star-shaped Bose-Hubbard Hamiltonian with L outer sites connected to a central site. In the self-trapping regime, particles can only undergo collective tunneling between the sites of the lattice, and these dynamics can be simulated by an effective coupling between the states in which all particles occupy the same energy level. In particular, we identified a fundamental symmetry of this type of system by highlighting the formal equivalence between the outer sites. Owing to their symmetric couplings to the central well, it is possible to simulate the dynamics of the full system simply by means of a two-level reduced Hamiltonian.

Reducing the system to a subspace of the global Hilbert space makes it possible to facilitate greatly the analytical calculations of the various functions required for the

application of the GCD method, and provides valuable information about the behavior of the energy gap separating the states we seek to control. Once the desired quantities have been calculated within the reduced Hamiltonian, we have shown that it is possible to encapsulate the action of the GCD protocol within the controllable physical parameters of the Bose-Hubbard Hamiltonian. The absence of time dependence in the new controls makes it possible to reduce the experimental resources generally required by shortcuts to adiabaticity. Once the new parameters are encoded in the many-body system, the generation of L-mode NOON states becomes possible on a timescale that is compatible with experimental reality.

Whereas the Bose-Hubbard Hamiltonian generally describes an ensemble of bosons trapped within an optical lattice, whose geometry affects the dynamics, we showed that it is possible to define a vortex system that fits within this type of model. By considering a gas of bosons confined in a two-dimensional harmonic trap with a slight anisotropy, this system can be rewritten as a Bose-Hubbard model describing bosons carrying angular momentum corresponding to either clockwise or counterclockwise rotation. From there, the application of the GCD protocol made it possible to demonstrate the creation of NOON states composed of N bosons rotating in opposite directions. This state is of clear interest in metrology, where the sensitivity to asymmetry between the two rotations could allow the measurement of very weak external perturbations, potentially on the order of the Earth's rotation with respect to a laboratory.

All the studies presented in this manuscript lead to the conclusion that the geodesic counterdiabatic driving protocol makes it possible to create a wide variety of different entangled states within diverse many-body systems, and to do so on experimentally realistic timescales.

This work raises new questions concerning two aspects. First, while GCD is effective for systems exhibiting an avoided crossing between two energy levels, its extension to triple avoided crossings still needs to be investigated. For example, it would be interesting to study to what extent, if two avoided crossings are sufficiently well separated, the GCD protocol still allows one to define a counterdiabatic Hamiltonian with time-independent elements. In particular, is it possible to generalize the definition of GCD? Could one find a more fundamental connection between geodesics in parameter space and the adiabatic gauge potential? As this new method represents the first manifestation of a counterdiabatic driving whose elements are time-independent, many questions and open issues regarding the conditions of applicability naturally arise.

The second aspect concerns the generated NOON states and their experimental realization. Although perturbation theory pushed to sixth order makes it possible to limit the truncation error to below 10^{-11}, experimental conditions and the required precision on the energy levels may become problematic. However, the GCD method could be perfectly suited to a numerical extension. Indeed, all the coefficients to be obtained could be extracted from the system's spectrum. A routine could be developed to compute, at higher orders, the elements of the reduced Hamiltonian and to refine the precision of the protocol, sufficiently to compensate for losses arising from experimental reality.

In particular, one of the conditions of the protocol relies on the symmetry between the outer sites. Perfect symmetry between the different wells of an optical lattice can be difficult to achieve, and potentially constitutes the primary source of imprecision

generated within an experimental setup capable of implementing the GCD protocol. This difficulty could be resolved in the context of discrete time crystals, where such symmetry is guaranteed by construction [179–181]. In this case, the modes are located on the resonance islands of phase space [32–34]. The method to be applied is an adiabatic transfer from a central state symmetrically coupled to all other resonant modes, which is localized at the center of the main regular island in phase space; the goal is thus to construct a nonlinear resonance centered around the central well, enabling symmetric tunneling to all other modes. This method could potentially be implemented in single optical lattice wells subjected to periodic modulation.

Bibliography

[1] A. Einstein, B. Podolsky, and N. Rosen, "Can Quantum-Mechanical Description of Physical Reality Be Considered Complete?", Phys. Rev. **47**, 777–780 (1935).

[2] A. Aspect, J. Dalibard, and G. Roger, "Experimental Test of Bell's Inequalities Using Time-Varying Analyzers", Phys. Rev. Lett. **49**, 1804–1807 (1982).

[3] R. Horodecki, P. Horodecki, M. Horodecki, and K. Horodecki, "Quantum entanglement", Rev. Mod. Phys. **81**, 865–942 (2009).

[4] H. Bernien, B. Hensen, W. Pfaff, G. Koolstra, M. S. Blok, L. Robledo, T. H. Taminiau, M. Markham, D. J. Twitchen, L. Childress, and R. Hanson, "Heralded entanglement between solid-state qubits separated by three metres", Nature **497**, 86–90 (2013).

[5] F. Dolde, I. Jakobi, B. Naydenov, N. Zhao, S. Pezzagna, C. Trautmann, J. Meijer, P. Neumann, F. Jelezko, and J. Wrachtrup, "Room-temperature entanglement between single defect spins in diamond", Nature Physics **9**, 139–143 (2013).

[6] C. Song, K. Xu, W. Liu, C.-P. Yang, S.-B. Zheng, H. Deng, Q. Xie, K. Huang, Q. Guo, L. Zhang, P. Zhang, D. Xu, D. Zheng, X. Zhu, H. Wang, Y.-A. Chen, C.-Y. Lu, S. Han, and J.-W. Pan, "10-Qubit Entanglement and Parallel Logic Operations with a Superconducting Circuit", Phys. Rev. Lett. **119**, 180511 (2017).

[7] J. Zhang, M. Um, D. Lv, J.-N. Zhang, L.-M. Duan, and K. Kim, "NOON States of Nine Quantized Vibrations in Two Radial Modes of a Trapped Ion", Phys. Rev. Lett. **121**, 160502 (2018).

[8] I. Bloch, "Ultracold quantum gases in optical lattices", Nature Physics **1**, 23–30 (2005).

[9] C. Foot, Atomic Physics, Oxford Master Series in Physics (OUP Oxford, 2005).

[10] I. Bloch, J. Dalibard, and W. Zwerger, "Many-body physics with ultracold gases", Rev. Mod. Phys. **80**, 885–964 (2008).

[11] S. Fölling, S. Trotzky, P. Cheinet, M. Feld, R. Saers, A. Widera, T. Müller, and I. Bloch, "Direct observation of second-order atom tunnelling", Nature **448**, 1029–1032 (2007).

[12] D. Jaksch, C. Bruder, J. I. Cirac, C. W. Gardiner, and P. Zoller, "Cold bosonic atoms in optical lattices", Phys. Rev. Lett. **81**, 3108–3111 (1998).

[13] G.-B. Jo, J. Guzman, C. K. Thomas, P. Hosur, A. Vishwanath, and D. M. Stamper-Kurn, "Ultracold Atoms in a Tunable Optical Kagome Lattice", Phys. Rev. Lett. **108**, 045305 (2012).

[14] P. Windpassinger and K. Sengstock, "Engineering novel optical lattices", Reports on Progress in Physics **76**, 086401 (2013).

[15] G. Jotzu, M. Messer, R. Desbuquois, M. Lebrat, T. Uehlinger, D. Greif, and T. Esslinger, "Experimental realization of the topological Haldane model with ultracold fermions", Nature **515**, 237–240 (2014).

[16] J. I. Cirac, M. Lewenstein, K. Mølmer, and P. Zoller, "Quantum superposition states of Bose-Einstein condensates", Phys. Rev. A **57**, 1208–1218 (1998).

[17] D. Gordon and C. M. Savage, "Creating macroscopic quantum superpositions with Bose-Einstein condensates", Phys. Rev. A **59**, 4623–4629 (1999).

[18] A. Sørensen, L.-M. Duan, J. I. Cirac, and P. Zoller, "Many-particle entanglement with Bose–Einstein condensates", Nature **409**, 63–66 (2001).

[19] A. Micheli, D. Jaksch, J. I. Cirac, and P. Zoller, "Many-particle entanglement in two-component Bose-Einstein condensates", Phys. Rev. A **67**, 013607 (2003).

[20] K. W. Mahmud, H. Perry, and W. P. Reinhardt, "Phase engineering of controlled entangled number states in a single component Bose–Einstein condensate in a double well", J. Phys. B: At. Mol. Opt. Phys **36**, L265 (2003).

[21] N. Teichmann and C. Weiss, "Coherently controlled entanglement generation in a binary Bose-Einstein condensate", EPL **78**, 10009 (2007).

[22] U. R. Fischer and M.-K. Kang, ""Photonic" Cat States from Strongly Interacting Matter Waves", Phys. Rev. Lett. **115**, 260404 (2015).

[23] A. A. Bychek, D. N. Maksimov, and A. R. Kolovsky, "NOON state of Bose atoms in the double-well potential via an excited-state quantum phase transition", Phys. Rev. A **97**, 063624 (2018).

[24] L. Pezzè, M. Gessner, P. Feldmann, C. Klempt, L. Santos, and A. Smerzi, "Heralded Generation of Macroscopic Superposition States in a Spinor Bose-Einstein Condensate", Phys. Rev. Lett. **123**, 260403 (2019).

[25] D. Schneider Grün, K. Wittmann Wilsmann, L. Ymai, J. Links, and A. Foerster, "Protocol designs for NOON states", Commun Phys **5** (2022).

[26] G. J. Milburn, J. Corney, E. M. Wright, and D. F. Walls, "Quantum dynamics of an atomic Bose-Einstein condensate in a double-well potential", Phys. Rev. A **55**, 4318–4324 (1997).

[27] A. Smerzi, S. Fantoni, S. Giovanazzi, and S. R. Shenoy, "Quantum Coherent Atomic Tunneling between Two Trapped Bose-Einstein Condensates", Phys. Rev. Lett. **79**, 4950–4953 (1997).

[28] M. P. Strzys, E. M. Graefe, and H. J. Korsch, "Kicked Bose-Hubbard systems and kicked tops—destruction and stimulation of tunneling", New J. Phys. **10**, 013024 (2008).

[29] L. D. Carr, D. R. Dounas-Frazer, and M. A. Garcia-March, "Dynamical realization of macroscopic superposition states of cold bosons in a tilted double well", EPL **90**, 10005 (2010).

[30] H. Zhang, Y.-K. Wang, Y. Zheng, H.-T. Bai, and B. Yang, "Observation of Coherent Quantum Tunneling of a Massive Atomic Cluster with 435 u", arXiv:2502.06246 (2025).

[31] A. N. Salgueiro, A. de Toledo Piza, G. B. Lemos, R. Drumond, M. C. Nemes, and M. Weidemüller, "Quantum dynamics of bosons in a double-well potential: Josephson oscillations, self-trapping and ultralong tunneling times", Eur. Phys. J. D **44**, 537–540 (2007).

[32] S. Tomsovic and D. Ullmo, "Chaos-assisted tunneling", Phys. Rev. E **50**, 145–162 (1994).

[33] O. Brodier, P. Schlagheck, and D. Ullmo, "Resonance-Assisted Tunneling in Near-Integrable Systems", Phys. Rev. Lett. **87**, 064101 (2001).

[34] C. Eltschka and P. Schlagheck, "Resonance- and chaos-assisted tunneling in mixed regular-chaotic systems", Phys. Rev. Lett. **94**, 014101 (2005).

[35] G. Vanhaele and P. Schlagheck, "NOON states with ultracold bosonic atoms via resonance- and chaos-assisted tunneling", Phys. Rev. A **103**, 013315 (2021).

[36] G. Vanhaele, A. Bäcker, R. Ketzmerick, and P. Schlagheck, "Creating triple-NOON states with ultracold atoms via chaos-assisted tunneling", Phys. Rev. A **106**, L011301 (2022).

[37] M. Born and V. Fock, "Beweis des Adiabatensatzes", Zeitschrift für Physik **51**, 165–180 (1928).

[38] L. Landau, "Zur Theorie der Energieubertragung. II", Physikalische Zeitschrift der Sowjetunion **2**, 46 (1932).

[39] C. Zener, "Non-adiabatic crossing of energy levels", Proc. R. Soc. Lond. A **137**, 696–702 (1932).

[40] E. Stückelberg, "Theorie der unelastischen Stösse zwischen Atomen", Helv. Phys. Acta **5**, 369 (1932).

[41] E. Majorana, "Atomi orientati in campo magnetico variabile", Il Nuovo Cimento (1924-1942) **9**, 43–50 (1932).

[42] D. Guéry-Odelin, A. Ruschhaupt, A. Kiely, E. Torrontegui, S. Martínez-Garaot, and J. G. Muga, "Shortcuts to adiabaticity: Concepts, methods, and applications", Rev. Mod. Phys. **91**, 045001 (2019).

[43] M. V. Berry, "Transitionless quantum driving", J. Phys. A: Math. Theor. **42**, 365303 (2009).

[44] F. Petiziol, B. Dive, F. Mintert, and S. Wimberger, "Fast adiabatic evolution by oscillating initial Hamiltonians", Phys. Rev. A **98**, 043436 (2018).

[45] P. W. Claeys, M. Pandey, D. Sels, and A. Polkovnikov, "Floquet-Engineering Counterdiabatic Protocols in Quantum Many-Body Systems", Phys. Rev. Lett. **123**, 090602 (2019).

[46] F. Petiziol, F. Mintert, and S. Wimberger, "Quantum control by effective counterdiabatic driving", EPL **145**, 15001 (2024).

[47] J. P. Provost and G. Vallee, "Riemannian structure on manifolds of quantum states", Commun. Math. Phys. **76**, 289–301 (1980).

[48] M. Tomka, T. Souza, S. Rosenberg, and A. Polkovnikov, "Geodesic Paths for Quantum Many-Body Systems", arXiv:1606.05890 (2016).

[49] S. Dengis, S. Wimberger, and P. Schlagheck, "Accelerated creation of NOON states with ultracold atoms via counterdiabatic driving", Phys. Rev. A **111**, L031301 (2025).

[50] S. Dengis, S. Wimberger, and P. Schlagheck, "Multimode NOON-state generation with ultracold atoms via geodesic counterdiabatic driving", Phys. Rev. A **112**, 042610 (2025).

[51] L. Mandelstam and I. Tamm, "The Uncertainty Relation Between Energy and Time in Non-Relativistic Quantum Mechanics", J. Phys (USSR) **9**, 249 (1945).

[52] A. Einstein, "Über einen die Erzeugung und Verwandlung des Lichtes betreffenden heuristischen Gesichtspunkt", Annalen der Physik **17**, 132–148 (1905).

[53] L. de Broglie, "Waves and quanta", Nature **112**, 540 (1923).

[54] W. Heisenberg, "Über quantentheoretische Umdeutung kinematischer und mechanischer Beziehungen", Zeitschrift für Physik **33**, 879–893 (1925).

[55] E. Schrödinger, "An undulatory theory of the mechanics of atoms and molecules", Physical Review **28**, 1049–1070 (1926).

[56] C. J. Davisson and L. H. Germer, "Diffraction of electrons by a crystal of nickel", Physical Review **30**, 705–740 (1927).

[57] L. D. Landau and E. M. Lifshitz, Statistical physics, part 1, 3rd ed., Vol. 5, Course of Theoretical Physics (Pergamon Press, 1980).

[58] S. N. Bose, "Planck's law and the light quantum hypothesis", Zeitschrift für Physik **26**, 178–181 (1924).

[59] A. Einstein, "Quantentheorie des einatomigen idealen Gases", Sitzungsberichte der Preussischen Akademie der Wissenschaften, 3–14 (1925).

[60] S. Chu, "Nobel Lecture: The manipulation of neutral particles", Rev. Mod. Phys. **70**, 685–706 (1998).

[61] H. F. Hess, "Evaporative cooling of magnetically trapped and compressed spin-polarized hydrogen", Phys. Rev. B **34**, 3476–3479 (1986).

[62] M. H. Anderson, J. R. Ensher, M. R. Matthews, C. E. Wieman, and E. A. Cornell, "Observation of Bose-Einstein Condensation in a Dilute Atomic Vapor", Science **269**, 198–201 (1995).

[63] K. B. Davis, M. .-. Mewes, M. R. Andrews, N. J. van Druten, D. S. Durfee, D. M. Kurn, and W. Ketterle, "Bose-Einstein Condensation in a Gas of Sodium Atoms", Phys. Rev. Lett. **75**, 3969–3973 (1995).

[64] C. C. Bradley, C. A. Sackett, J. J. Tollett, and R. G. Hulet, "Evidence of Bose-Einstein Condensation in an Atomic Gas with Attractive Interactions", Phys. Rev. Lett. **75**, 1687–1690 (1995).

[65] D. G. Fried, T. C. Killian, L. Willmann, D. Landhuis, S. C. Moss, D. Kleppner, and T. J. Greytak, "Bose-Einstein Condensation of Atomic Hydrogen", Phys. Rev. Lett. **81**, 3811–3814 (1998).

[66] A. Robert, O. Sirjean, A. Browaeys, J. Poupard, S. Nowak, D. Boiron, C. I. Westbrook, and A. Aspect, "A Bose-Einstein Condensate of Metastable Atoms", Science **292**, 461–464 (2001).

[67] M. Lu, N. Q. Burdick, S. H. Youn, and B. L. Lev, "Strongly dipolar bose-einstein condensate of dysprosium", Phys. Rev. Lett. **107**, 190401 (2011).

[68] A. L. Gaunt, T. F. Schmidutz, I. Gotlibovych, R. P. Smith, and Z. Hadzibabic, "Bose-Einstein Condensation of Atoms in a Uniform Potential", Phys. Rev. Lett. **110**, 200406 (2013).

[69] F. Wang, X. Li, D. Xiong, and D. Wang, "A double species ^{23}Na and ^{87}Rb Bose–Einstein condensate with tunable miscibility via an interspecies Feshbach resonance", Journal of Physics B: Atomic, Molecular and Optical Physics **49**, 015302 (2015).

[70] T. M. Bersano, J. Hou, S. Mossman, V. Gokhroo, X.-W. Luo, K. Sun, C. Zhang, and P. Engels, "Experimental realization of a long-lived striped Bose-Einstein condensate induced by momentum-space hopping", Phys. Rev. A **99**, 051602 (2019).

[71] V. Bagnato, D. E. Pritchard, and D. Kleppner, "Bose-Einstein condensation in an external potential", Phys. Rev. A **35**, 4354–4358 (1987).

[72] F. Dalfovo, S. Giorgini, L. P. Pitaevskii, and S. Stringari, "Theory of Bose-Einstein condensation in trapped gases", Rev. Mod. Phys. **71**, 463–512 (1999).

[73] M. P. A. Fisher, P. B. Weichman, G. Grinstein, and D. S. Fisher, "Boson localization and the superfluid-insulator transition", Phys. Rev. B **40**, 546–570 (1989).

[74] M. Greiner, O. Mandel, T. Esslinger, T. W. Hänsch, and I. Bloch, "Quantum phase transition from a superfluid to a mott insulator in a gas of ultracold atoms", Nature **415**, 39–44 (2002).

[75] C. J. Pethick and H. Smith, Bose-Einstein Condensation in Dilute Gases, 2nd ed. (Cambridge University Press, 2008).

[76] L. D. Landau and E. M. Lifshitz, Quantum Mechanics: Non-Relativistic Theory, 3rd ed., Vol. 3, Course of Theoretical Physics (Pergamon Press, 1977).

[77] F. Williams, Nuclear and Particle Physics (Clarendon Press, 1991).

[78] L. Pitaevskii and S. Stringari, Bose-Einstein Condensation and Superfluidity (Oxford University Press, 2016).

[79] C. Chin, R. Grimm, P. Julienne, and E. Tiesinga, "Feshbach resonances in ultracold gases", Rev. Mod. Phys. **82**, 1225–1286 (2010).

[80] A. L. Fetter and J. D. Walecka, Quantum theory of many-particle systems (McGraw-Hill, 1971).

[81] D. R. Hartree, "The Wave Mechanics of an Atom with a Non-Coulomb Central Field. Part I. Theory and Methods", Mathematical Proceedings of the Cambridge Philosophical Society **24**, 89–110 (1928).

[82] E. P. Gross, "Structure of a quantized vortex in boson systems", Il Nuovo Cimento **20**, 454–477 (1961).

[83] L. P. Pitaevskii, "Vortex lines in an imperfect Bose gas", Soviet Physics JETP **13**, 451–454 (1961).

[84] T. Tsuzuki, "Nonlinear waves in the Pitaevskii-Gross equation", Journal of Low Temperature Physics **4**, 441–457 (1971).

[85] A. A. Michelson, "On the Application of Interference Methods to Spectroscopic Measurements", Philosophical Magazine **31**, 338–346 (1891).

[86] W. Pauli, "Zur Frage der theoretischen Deutung der beobachteten Molekülspektren", Zeitschrift für Physik **23**, 117–122 (1924).

[87] A. Corney, Atomic and laser spectroscopy (Oxford University Press, 2006).

[88] C. Cohen-Tannoudji, J. Dupont-Roc, and G. Grynberg, Atom-Photon Interactions: Basic Processes and Applications (Wiley, 1998).

[89] D. Budker and M. Romalis, "Optical magnetometry", Nature Physics **3**, 227–234 (2007).

[90] D. E. Pritchard, "Cooling Neutral Atoms in a Magnetic Trap for Precision Spectroscopy", Phys. Rev. Lett. **51**, 1336–1339 (1983).

[91] W. Petrich, M. H. Anderson, J. R. Ensher, and E. A. Cornell, "Stable, Tightly Confining Magnetic Trap for Evaporative Cooling of Neutral Atoms", Phys. Rev. Lett. **74**, 3352–3355 (1995).

[92] R. Grimm, M. Weidemüller, and Y. B. Ovchinnikov, "Optical Dipole Traps for Neutral Atoms", Advances In Atomic, Molecular, and Optical Physics **42**, 95–170 (2000).

[93] F. Bloch, "Über die Quantenmechanik der Elektronen in Kristallgittern", Zeitschrift für Physik **52**, 555–600 (1929).

[94] G. H. Wannier, "The structure of electronic excitation levels in insulating crystals", Phys. Rev. **52**, 191–197 (1937).

[95] T. Pudlik, H. Hennig, D. Witthaut, and D. K. Campbell, "Tunneling in the self-trapped regime of a two-well Bose-Einstein condensate", Phys. Rev. A **90**, 053610 (2014).

[96] M. Albiez, R. Gati, J. Fölling, S. Hunsmann, M. Cristiani, and M. K. Oberthaler, "Direct observation of tunneling and nonlinear self-trapping in a single bosonic josephson junction", Phys. Rev. Lett. **95**, 010402 (2005).

[97] R. Gati and M. K. Oberthaler, "A bosonic Josephson junction", Journal of Physics B **40**, R61–R89 (2007).

[98] P. Cheinet, S. Trotzky, M. Feld, U. Schnorrberger, M. Moreno-Cardoner, S. Fölling, and I. Bloch, "Counting Atoms Using Interaction Blockade in an Optical Superlattice", Phys. Rev. Lett. **101**, 090404 (2008).

[99] A. P. Itin and P. Schmelcher, "Semiclassical spectrum of small Bose-Hubbard chains: A normal-form approach", Phys. Rev. A **84**, 063609 (2011).

[100] D. Leibfried, R. Blatt, C. Monroe, and D. Wineland, "Quantum dynamics of single trapped ions", Rev. Mod. Phys. **75**, 281–324 (2003).

[101] J. I. Cirac and P. Zoller, "Goals and opportunities in quantum simulation", Nature Physics **8**, 264–266 (2012).

[102] M. V. Berry, "Quantal phase factors accompanying adiabatic changes", Proc. Roy. Soc. Lond. A **392**, 45–57 (1984).

[103] M. V. Berry, "Quantum Phase Corrections from Adiabatic Iteration", Proc. R. Soc. Lond. A **414**, 31–46 (1987).

[104] Y. Aharonov and D. Bohm, "Significance of Electromagnetic Potentials in the Quantum Theory", Phys. Rev. **115**, 485–491 (1959).

[105] Y. Aharonov and D. Bohm, "Further Considerations on Electromagnetic Potentials in the Quantum Theory", Phys. Rev. **123**, 1511–1524 (1961).

[106] A. Tonomura, N. Osakabe, T. Matsuda, T. Kawasaki, J. Endo, S. Yano, and H. Yamada, "Evidence for Aharonov-Bohm effect with magnetic field completely shielded from electron wave", Phys. Rev. Lett. **56**, 792–795 (1986).

[107] R. Unanyan, L. Yatsenko, K. Bergmann, and B. Shore, "Laser-induced adiabatic atomic reorientation with control of diabatic losses", Optics Communications **139**, 48–54 (1997).

[108] M. Fleischhauer, R. Unanyan, B. W. Shore, and K. Bergmann, "Coherent population transfer beyond the adiabatic limit: generalized matched pulses and higher-order trapping states", Phys. Rev. A **59**, 3751–3760 (1999).

[109] R. Lim and M. V. Berry, "Superadiabatic tracking of quantum evolution", J. Phys. A: Math. Gen. **24**, 3255 (1991).

[110] X. Chen, A. Ruschhaupt, S. Schmidt, A. del Campo, D. Guéry-Odelin, and J. G. Muga, "Fast Optimal Frictionless Atom Cooling in Harmonic Traps: Shortcut to Adiabaticity", Phys. Rev. Lett. **104**, 063002 (2010).

[111] X. Chen, A. Ruschhaupt, S. Schmidt, A. del Campo, D. Guéry-Odelin, and J. G. Muga, "Fast Optimal Frictionless Atom Cooling in Harmonic Traps: Shortcut to Adiabaticity", Phys. Rev. Lett. **104**, 063002 (2010).

[112] A. del Campo, "Shortcuts to Adiabaticity by Counterdiabatic Driving", Phys. Rev. Lett. **111**, 100502 (2013).

[113] S. Martínez-Garaot, E. Torrontegui, X. Chen, and J. G. Muga, "Shortcuts to adiabaticity in three-level systems using Lie transforms", Phys. Rev. A **89**, 053408 (2014).

[114] T. Opatrný and K. Mølmer, "Partial suppression of nonadiabatic transitions", New Journal of Physics **16**, 015025 (2014).

[115] S. Deffner, C. Jarzynski, and A. del Campo, "Classical and Quantum Shortcuts to Adiabaticity for Scale-Invariant Driving", Phys. Rev. X **4**, 021013 (2014).

[116] M. Demirplak and S. Rice, "Adiabatic Population Transfer with Control Fields", J. Phys. Chem. A **107** (2003).

[117] M. Demirplak and S. A. Rice, "On the consistency, extremal, and global properties of counterdiabatic fields", J. Chem. Phys. **129**, 154111 (2008).

[118] D. Sels and A. Polkovnikov, "Minimizing irreversible losses in quantum systems by local counterdiabatic driving", PNAS **114**, E3909–E3916 (2017).

[119] M. Kolodrubetz, D. Sels, P. Mehta, and A. Polkovnikov, "Geometry and nonadiabatic response in quantum and classical systems", Physics Reports **697**, 1–87 (2017).

[120] C. W. Duncan, P. M. Poggi, M. Bukov, N. T. Zinner, and S. Campbell, "Taming Quantum Systems: A Tutorial for Using Shortcuts-To-Adiabaticity, Quantum Optimal Control, and Reinforcement Learning", PRX Quantum **6**, 040201 (2025).

[121] L. Prielinger, A. Hartmann, Y. Yamashiro, K. Nishimura, W. Lechner, and H. Nishimori, "Two-parameter counter-diabatic driving in quantum annealing", Phys. Rev. Res. **3**, 013227 (2021).

[122] G. B. Mbeng and W. Lechner, "Rotated ansatz for approximate counterdiabatic driving", arXiv:2207.03553.

[123] F. Petiziol, S. Wimberger, A. Eckardt, and F. Mintert, "Nonperturbative Floquet engineering of the toric-code Hamiltonian and its ground state", Phys. Rev. B **109**, 075126 (2024).

[124] N. Goldman and J. Dalibard, "Periodically Driven Quantum Systems: Effective Hamiltonians and Engineered Gauge Fields", Phys. Rev. X **4**, 031027 (2014).

[125] M. Bukov, L. D'Alessio, and A. Polkovnikov, "Universal high-frequency behavior of periodically driven systems: from dynamical stabilization to Floquet engineering", Advances in Physics **64**, 139–226 (2015).

[126] M. Kolodrubetz, V. Gritsev, and A. Polkovnikov, "Classifying and measuring geometry of a quantum ground state manifold", Phys. Rev. B **88**, 064304 (2013).

[127] A. Carlini, A. Hosoya, T. Koike, and Y. Okudaira, "Time-optimal quantum evolution", Phys. Rev. Lett. **96**, 060503 (2006).

[128] J. C. Budich and B. Trauzettel, "From the adiabatic theorem of quantum mechanics to topological states of matter", physica status solidi (RRL) – Rapid Research Letters **7**, 109–129 (2013).

[129] C. W. Misner, K. S. Thorne, and J. A. Wheeler, Gravitation (W. H. Freeman and Company, San Francisco, 1973).

[130] M. Aidelsburger, M. Lohse, C. Schweizer, M. Atala, J. T. Barreiro, S. Nascimbène, N. R. Cooper, I. Bloch, and N. Goldman, "Measuring the Chern number of Hofstadter bands with ultracold bosonic atoms", Nature Physics **11**, 162–166 (2014).

[131] N. Goldman, J. C. Budich, and P. Zoller, "Topological quantum matter with ultracold gases in optical lattices", Nature Physics **12**, 639–645 (2016).

[132] N. R. Cooper, J. Dalibard, and I. B. Spielman, "Topological bands for ultracold atoms", Rev. Mod. Phys. **91**, 015005 (2019).

[133] P. Petersen, Riemannian geometry, Vol. 171, Graduate Texts in Mathematics (Springer, New York, 2000).

[134] S. Deffner and S. Campbell, "Quantum speed limits: from Heisenberg's uncertainty principle to optimal quantum control", Journal of Physics A: Mathematical and Theoretical **50**, 453001 (2017).

[135] B. Damski, "The Simplest Quantum Model Supporting the Kibble-Zurek Mechanism of Topological Defect Production: Landau-Zener Transitions from a New Perspective", Phys. Rev. Lett. **95**, 035701 (2005).

[136] N. V. Vitanov, A. A. Rangelov, B. W. Shore, and K. Bergmann, "Stimulated Raman adiabatic passage in physics, chemistry, and beyond", Rev. Mod. Phys. **89**, 015006 (2017).

[137] O. V. Ivakhnenko, S. N. Shevchenko, and F. Nori, "Nonadiabatic LZSM transitions, dynamics, and interference", Physics Reports **995**, 1–89 (2023).

[138] Z. Sun, L. Zhou, G. Xiao, D. Poletti, and J. Gong, "Finite-time Landau-Zener processes and counterdiabatic driving in open systems: Beyond Born, Markov, and rotating-wave approximations", Phys. Rev. A **93**, 012121 (2016).

[139] K. Nishimura and K. Takahashi, "Counterdiabatic Hamiltonians for multistate Landau-Zener problem", SciPost Physics **5**, 029 (2018).

[140] C. L. Degen, F. Reinhard, and P. Cappellaro, "Quantum sensing", Rev. Mod. Phys. **89**, 035002 (2017).

[141] L. Pezzè, A. Smerzi, M. K. Oberthaler, R. Schmied, and P. Treutlein, "Quantum metrology with nonclassical states of atomic ensembles", Rev. Mod. Phys. **90**, 035005 (2018).

[142] H. Kwon, K. C. Tan, T. Volkoff, and H. Jeong, "Nonclassicality as a Quantifiable Resource for Quantum Metrology", Phys. Rev. Lett. **122**, 040503 (2019).

[143] L. Pezzè and A. Smerzi, "Heisenberg-Limited Noisy Atomic Clock Using a Hybrid Coherent and Squeezed State Protocol", Phys. Rev. Lett. **125**, 210503 (2020).

[144] J. Ye and P. Zoller, "Essay: Quantum Sensing with Atomic, Molecular, and Optical Platforms for Fundamental Physics", Phys. Rev. Lett. **132**, 190001 (2024).

[145] C. Panda, M. Tao, M. Ceja, J. Khoury, G. Tino, and H. Müller, "Measuring gravitational attraction with a lattice atom interferometer", Nature **631**, 1–6 (2024).

[146] I. Afek, O. Ambar, and Y. Silberberg, "High-NOON States by Mixing Quantum and Classical Light", Science **328**, 879–881 (2010).

[147] Y. I. Bogdanov, M. V. Chekhova, S. P. Kulik, G. A. Maslennikov, A. A. Zhukov., C. H. Oh, and M. K. Tey, "Qutrit State Engineering with Biphotons", Phys. Rev. Lett. **93**, 230503 (2004).

[148] V. I. Shnyrkov, A. A. Soroka, and O. G. Turutanov, "Quantum superposition of three macroscopic states and superconducting qutrit detector", Phys. Rev. B **85**, 224512 (2012).

[149] F. Yao, Y.-M. Du, H. Xing, and L. Fu, "Two-parameter estimation with three-mode NOON state in a symmetric triple-well potential", Communications in Theoretical Physics **74**, 045103 (2022).

[150] Y. Maleki, "N00N State Generation by Floquet Engineering", Mathematics **13**, 1667 (2025).

[151] S. Hong, J. Ur Rehman, Y.-S. Kim, Y.-W. Cho, S.-W. Lee, H. Jung, S. Moon, S.-W. Han, and H.-T. Lim, "Quantum enhanced multiple-phase estimation with multi-mode NOON states", Nature Communications **12**, 5211 (2021).

[152] D.-H. Kim, S. Hong, Y.-S. Kim, K. Oh, S.-Y. Lee, C. Lee, and H.-T. Lim, "Distributed Quantum Sensing with Multimode $N00N$ States", Phys. Rev. Lett. **135**, 050802 (2025).

[153] I. Brunelli, G. Giusiano, F. Mancini, P. Sodano, and A. Trombettoni, "Topology induced spatial Bose–Einstein condensation for bosons on star-shaped optical networks", Journal of Physics B: Atomic, Molecular and Optical Physics **37**, 1431–1442 (2004).

[154] S. V. Isakov, K. Sengupta, and Y. B. Kim, "Bose-Hubbard model on a star lattice", Phys. Rev. B **80**, 214503 (2009).

[155] V. Pouthier, "Quantum self-trapping on a star graph", Phys. Rev. E **105**, 044304 (2022).

[156] L. S. Yagüe Bosch, T. Ehret, F. Petiziol, E. Arimondo, and S. Wimberger, "Shortcut-to-Adiabatic Controlled-Phase Gate in Rydberg Atoms", Annalen der Physik **535**, 2300275 (2023).

[157] K. Takahashi and A. del Campo, "Shortcuts to Adiabaticity in Krylov Space", Phys. Rev. X **14**, 011032 (2024).

[158] J. Dalibard, F. Gerbier, G. Juzeliūnas, and P. Öhberg, "Colloquium: Artificial gauge potentials for neutral atoms", Rev. Mod. Phys. **83**, 1523–1543 (2011).

[159] M. Aidelsburger, M. Atala, S. Nascimbène, S. Trotzky, Y.-A. Chen, and I. Bloch, "Experimental realization of strong effective magnetic fields in an optical lattice", Phys. Rev. Lett. **107**, 255301 (2011).

[160] K. Jiménez-García, L. J. LeBlanc, R. A. Williams, M. C. Beeler, A. R. Perry, and I. B. Spielman, "Peierls substitution in an engineered lattice potential", Phys. Rev. Lett. **108**, 225303 (2012).

[161] H. Miyake, G. A. Siviloglou, C. J. Kennedy, W. C. Burton, and W. Ketterle, "Realizing the Harper Hamiltonian with Laser-Assisted Tunneling in Optical Lattices", Phys. Rev. Lett. **111**, 185302 (2013).

[162] B.-Y. Sun, N. Goldman, M. Aidelsburger, and M. Bukov, "Engineering and Probing Non-Abelian Chiral Spin Liquids Using Periodically Driven Ultracold Atoms", PRX Quantum **4**, 020329 (2023).

[163] A. Isacsson and S. M. Girvin, "Multiflavor bosonic Hubbard models in the first excited Bloch band of an optical lattice", Phys. Rev. A **72**, 053604 (2005).

[164] X. Li and W. V. Liu, "Physics of higher orbital bands in optical lattices: a review", Reports on Progress in Physics **79**, 116401 (2016).

[165] Z. Hadzibabic, P. Krüger, M. Cheneau, B. Battelier, and J. Dalibard, "Berezinskii–Kosterlitz–Thouless crossover in a trapped atomic gas", Nature **441**, 1118–1121 (2006).

[166] B. P. Abbott et al. (LIGO Scientific Collaboration and Virgo Collaboration), "Observation of gravitational waves from a binary black hole merger", Phys. Rev. Lett. **116**, 061102 (2016).

[167] F. Englert and R. Brout, "Broken Symmetry and the Mass of Gauge Vector Mesons", Phys. Rev. Lett. **13**, 321–323 (1964).

[168] P. W. Higgs, "Broken symmetries and the masses of gauge bosons", Phys. Rev. Lett. **13**, 508–509 (1964).

[169] L. Pezzé and A. Smerzi, Quantum theory of phase estimation, Vol. 188, Proceedings of the International School of Physics "Enrico Fermi" (IOS Press, 2014), pp. 691–741.

[170] P. C. Humphreys, M. Barbieri, A. Datta, and I. A. Walmsley, "Quantum enhanced multiple phase estimation", Phys. Rev. Lett. **111**, 070403 (2013).

[171] C. R. Rao, "Information and the Accuracy Attainable in the Estimation of Statistical Parameters", Bulletin of the Calcutta Mathematical Society **37**, 81–91 (1945).

[172] H. Cramér, Mathematical Methods of Statistics (Princeton University Press, Princeton, 1946).

[173] C. W. Helstrom, Quantum detection and estimation theory, Vol. 123, Mathematics in Science and Engineering (Academic Press, New York, 1976).

[174] S. L. Braunstein and C. M. Caves, "Statistical distance and the geometry of quantum states", Phys. Rev. Lett. **72**, 3439–3443 (1994).

[175] Z.-Y. Zhou, S.-L. Liu, S.-K. Liu, Y.-H. Li, D.-S. Ding, G.-C. Guo, and B.-S. Shi, "Superresolving Phase Measurement with Short-Wavelength NOON States by Quantum Frequency Up-Conversion", Phys. Rev. Appl. **7**, 064025 (2017).

[176] M. G. A. Paris, "Quantum estimation for quantum technology", International Journal of Quantum Information **7**, 125–137 (2009).

[177] J. Liu, H. Yuan, X.-M. Lu, and X. Wang, "Quantum Fisher information matrix and multiparameter estimation", Journal of Physics A: Mathematical and Theoretical **53**, 023001 (2019).

[178] K. W. Madison, F. Chevy, W. Wohlleben, and J. Dalibard, "Vortex Formation in a Stirred Bose-Einstein Condensate", Phys. Rev. Lett. **84**, 806–809 (2000).

[179] F. Wilczek, "Quantum Time Crystals", Phys. Rev. Lett. **109**, 160401 (2012).

[180] K. Sacha, "Modeling spontaneous breaking of time-translation symmetry", Phys. Rev. A **91**, 033617 (2015).

[181] G. He, B. Ye, R. Gong, C. Yao, Z. Liu, K. W. Murch, N. Y. Yao, and C. Zu, "Experimental Realization of Discrete Time Quasicrystals", Phys. Rev. X **15**, 011055 (2025).